THÈSE

En vue de l'obtention du

DOCTORAT DE L'UNIVERSITÉ DE TOULOUSE

Délivré par l'Université Toulouse 3 - Paul Sabatier

Présentée et soutenue par

Sarah BROTMAN

Le 6 Decembre 2021

Couplages multi-physique et multi-échelle pour la modélisation prédictive de la combustion de matériaux énergétiques intégrés dans leur environnement

École doctorale :
GEET - Génie Electrique Electronique et Télécommunications : du système au nanosystème

Spécialité :
Micro et nano systèmes

Unité de recherche

LAAS - Laboratoire d'Analyse et d'Architecture des Systèmes

Directrice(s) ou Directeur(s) de Thèse
Alain Estève, Carole Rossi

Jury – Advisory Committee

Walter Focke	University of Pretoria, South Africa	Rapporteur
Djalal Trache	Ecole Militaire Polytechnique, Algeria	Rapporteur
Mehdi Djafari-Rouhani	University of Toulouse 3, France	Examinateur
Kyle Sullivan	Lawrence Livermore National Laboratory, USA	Examinateur
Ludovic Glavier	Ariane Group, France	Examinateur

2

Acknowledgements

Table of Contents

General Introduction

Energetic materials are a class of different types of materials, including fuels, solid propellants, explosives, or pyrotechnics, which contain a large amount of stored chemical energy that can be released on demand. Through external stimulation, principally by mechanical, electrical, thermal, or optical means, the energy stored in the molecular structure is released, initiating internal exothermic chemical reactions and potentially leading to fully autonomous "runaway" combustion. These materials can be mono-molecular, such as popular explosives like trinitrotoluene (TNT) or RDX (Royal Demolition Explosive), or composite mixtures, such as thermites.[1]

Energetic materials have been utilized historically since the 9th century AD, first developed in China during the Tang dynasty for medicinal purposes then repurposed for military use.[2,3] The commonly named "black powder" consisted of sulfur and charcoal acting as fuels in reaction with the oxidizer, saltpeter (potassium nitrate). Interest in this type of material spread throughout the world, eventually leading to the invention of dynamite, a mixture of nitroglycerin and silica, by Alfred Nobel in 1867.[4] This innovative substance provided a more powerful, yet stable alternative to black powder and was widely used in World War I. In 1893, the thermite reaction, based on a pyrotechnic composition of metal powder and metal oxide, was discovered by Hans Goldschmidt[5] and quickly utilized for welding in railway construction.[6,7] In modern times, these various categories of energetic materials have expanded from their original military uses to applications in civil and aerospatial engineering like welding, mining, propulsion systems, or fireworks.[8–12] For the past few decades, the rapidly growing academic and industrial nanotechnology domain has introduced new energetic compositions in the form of nanopowders, nanolaminates, or functionalized nanoparticles, primarily to ameliorate conventional compositions of energetic materials, while also broadening the use of these materials to further applicative fields.[13–19]

In thermite materials, particularly, in which the heat release occurs relatively slowly despite their high reaction enthalpies, the nanoscale organization of basic ingredients was expected to boost performances by reducing mass transport distances and increasing reactive interface areas, giving new opportunities in explosives, pyrotechnics, and propellants. Despite substantial gains, notably in the measured rate of combustion, limitations were also discovered. The rapid sintering of the nanostructure, during and after initiation, as this process was demonstrated to be in the time scale of the reaction, was reported as one main factor penalizing performances.

One of the most promising new applications of nanoscale research in the domain of nanothermites is the concept of PYROMEMs and/or energetic "on a chip", where integration of energetic materials into complex miniaturized systems opens new routes to practical applications, most notably in security systems such as airbags, circuit breakers, and chip destruction.[20–22] LAAS-CNRS is one such pioneer in the development of nanothermites for

MEMs. For instance, one of the main projects developed the fabrication of integrated Al:CuO nanolaminates for the next generation of microinitiators, making use of materials and synthesis approaches compatible with mass fabrication techniques of miniaturized systems.[23–27]

Beyond their high energy density, nanothermites intrinsically possess high versatility. Tunability of thermite materials performances (gas release, temperature, and flame speed) can be achieved through many pathways: compaction[28], structuring (fully dense versus powdered systems with more or less compaction, interface engineering)[29–37], 3D printing of complex 2D, 3D architectures[38,39], fuel/oxidizer ratio[40], or co-reagents. Blind prediction of performances, while necessary to reduce the trial and errors of the design stage, remains a vast challenge today. The arrival of the nanothermite era naturally motivated intensive research efforts to understand the details of combustion closer to the scale of the individual microscopic events (migrations, reactions, phase transformation, alloying, mechano-chemical mechanisms). This is a particularly difficult task both experimentally and theoretically since energetic materials, at large, exhibit this variety of basic mechanisms within very short time scales and length scales on the submicron scale. Series of experiments have been used to slow down the phenomenon (such as DSC, TGA experiments) thus opening opportunities to shed light on some mechanisms, but, unfortunately, because of the highly non-equilibrium nature of the reaction, the derived theories and mechanistic outcomes must be validated with experiments reproducing the conditions of combustion. One major example is the burn tube experiment loaded with energetic materials that allows clear observation of the burning front through high speed cameras[41]. More recently, *in-operando* experiments develop these techniques further to detect the temperature and behavior of the flame front of nanothermites, either in powder or nanolaminate form, with micron-scale resolution, providing new insights into the mechanisms of combustion.[42–44]

Despite this large effort, there are still conflicting theories for the underlying mechanisms at play. In particular, the role of gas phase versus condensed phase processes has been the subject of much controversy. The role of sintering, again, was demonstrated and proposed as one main step in the early stage of nanothermite reaction.[45] In any case, the number of potential microscopic mechanisms and their complex interplay, as well as the difficulty in trying to quantify and parametrize them, is a real challenge for producing predictive models for the *in-silico* design of nanothermites with specific performance goals. To date, no such modelling tool has been produced for particle-based nanothermite systems. Most studies rely on equilibrium thermodynamic estimates where the reaction is assumed to be completed, and all intermediates and kinetic evolution is neglected.[46,47] This type of simulation is particularly performant for the analysis of the maximum energy produced by a certain thermite, but is heavily limited by the assumption of a complete combustion reaction, and, thus, cannot elucidate the temporal evolution of such a reaction. Some recent modelling efforts have attempted to fill this gap. One approach, developed exclusively for nanolaminates that are suitable for fully dense materials, predicts full propagation performance based on condensed phase processes (diffusion/reaction).[48] In what concerns mixed nanoparticle systems, a gas phase-mediated reaction model has been proposed, focused on calculating the evolution of pressure generation.[49] However, this still leaves open the need for a particle-based model that

can analyze the temporal evolution of the propagation. One major advantage to a condensed phase driven formulation to this problem is that thermite reaction with low or no gas production could be simulated. Such an approach would not only provide a complement to the existing set of models proposed in the literature to date, but also a versatile tool with easier handling, higher computational efficiency (compared to Computational Fluid Dynamic methods) and easy transferability to a range of different thermite materials.

This thesis presents the development and exploitation of such a model that fully simulates both the initiation and propagation reaction of powder-based nanothermites with purely condensed phase mechanisms. As the project evolved over time, three main goals remained the focus for the final product.

1) A predictive model of both the initiation and propagation of the nanothermite reaction for powder-based systems implementing the recently discovered "reactive sintering" mechanism under different external heating regimes at low computational cost with flexibility to adapt to newly interesting materials.

2) A study of the influence of numerous key parameters such as the size of the experimental apparatus, particle size, stoichiometric ratio of materials, or the amount of compaction on both aspects of the reaction. This both permits an exploration of the effects of these factors for system design, as well as acts as a method of validation through comparison with experimental studies.

3) A comparison of this model with a purely gas phase approach to expound on the recent experimental works exploring the importance of reactive sintering and to contribute to the discussion within the domain on the fundamental driving mechanisms of the nanothermite combustion reaction.

The fulfillment of these goals is detailed in this manuscript, organized into five chapters following the chronological development of the project.

In a first chapter, a brief state of the art of nanothermites is presented to outline the motivation and scientific context of this project. Numerous experimental works are cited to summarize the methods of manufacturing and synthesis of nanothermites, their principal characteristics, and the effect of the nanostructure on performance in terms of the burn rate and initiation delays. This then includes an overview of the current arguments in the debate on the fundamental driving mechanisms of reaction, followed by a presentation of the existing modelisation approaches, their aims, formulations, and limitations.

Chapter 2 presents the theoretical basis for the proprosed model exclusively based on a condensed state formulation of the combustion, developed specifically for application to nanopowder thermites. As the work is explored chronologically, the first formulation is for a base model of the initiation of two nanoparticles (one fuel, one oxidizer) sintered into contact, coupled to a thermal equation. Then, the base model is expanded into a full propagation model,

which includes theoretical constructions of different macroscopic heat transfer mechanisms that were compared to find the best reproduction of experimental results. Thus, the final iteration combines the heterogeneous nanoscale mechanisms and chemical reactions with the overall macroscale propagation reaction.

In Chapter 3, the base model is utilized to investigate the importance of condensed-phase mechanisms on the initiation of these thermites, with particular insights into reactive sintering for different thermite couples and different heating rates. Results are first validated by comparison with recent experimental works and then with a purely gas phase simulation. This is supplemented by a benchmark study of the initiation of nanothermites with different varying parameters including the particle size, stoichiometric ratio, native oxide thickness, and the fuel and oxide material species.

Chapter 4 continues with the exploitation of the full self-sustaining propagation model with discussion of the probable factors that most influence the reaction rate. This begins with a presentation of the basic results for an Al:CuO system for each of the three model formulations presented in Chapter 2 in chronological order. Once the chosen system was validated, this version was then used to test the effect of varying important parameters such as the compaction rate, the material species', and the different heat transfer mechanisms also discussed previously.

Finally, this is followed by a general conclusion to summarize this work and its implications, as well as explore the perspectives for future work in this research sector. A Software Architecture Document that lays out the program implementation with the technical details necessary for use is available in Appendix A.

CHAPTER 1. State of the Art & Motivation

1.1 Introduction

At large, thermite materials have led to many industrialized applications boosted by the novel opportunities of nanoenergetic perspectives. However, many questions still remain in regards to the understanding of their process of reaction. This is coupled with a lack of analytical tools for performance predictions. In the following chapter, an overview of the current field of nanothermite work is presented. After an introduction to the theoretical basis of these materials, a state of the art of the present understanding of the effects of different parameters on the reaction, as well as hypotheses of their mechanistic processes are introduced. The final part of the chapter is devoted to a state of the art of modelling approaches and main analytical tools currently available.

1.2 Overview of Thermites & Nanothermites

The advantages of developing nanoscale materials are particularly useful when applied to the thermite reaction. The reaction entails a highly exothermic[50] reduction-oxidation reaction between a metal, acting as the fuel or reducing agent, with an intermetallic oxide, the oxidizer. The associated chemical equation can be expressed as:

$$M + AO \rightarrow MO + A + \Delta H \tag{1.1}$$

including the metal, M and the reacting metal oxide, AO, producing the corresponding MO oxide, reduced A metal and energy released ΔH.

It is evident that, by definition, a huge class of different materials can be considered for use in thermite mixtures. A large number of metals have the propensity to be oxidized exothermically, such as aluminum, boron, titanium, etc. An even greater list of metal or intermetallic oxide species can be utilized as oxidizers due to their metastability, for instance, iron oxides, copper oxide, bismuth oxide, or perovskite, to name just a few. In general, even micron-sized thermites provide reactions that remain too slow for many applications of more conventional energetic materials. On the macroscale, many thermite materials do not manage a fully self-sustained reaction and have, thus, been limited to their original applications, such as railroad welding. The development of metallic nanopowders and, more generally, the evolution of nanotechnology since the early 1990s has led to a great variety of thermite systems with diverse shapes and densities, *i.e.*, fully dense nanolaminates, ball milled nanostructures, nanopowders with different compaction, or nanowires. Nanothermites are defined as a mixture of a metallic fuel with an oxidizer, intimately mixed on the nanoscale, where each material has at least one dimension less than 100 nm. At that scale, these thermites offer larger fuel/oxidizer interface regions and shorter diffusion lengths. These advantages were expected to lead to performance enhancements by (1) shortening the time for initiation, (2) shortening the burn

times to increase reaction completeness, and, thus, increase the specific impulse, and (3) enhancing the heat transfer rates due to higher surface area of contact.[13] In certain stoichiometric and dimensional conditions, the reaction speeds have been found to be as high as 2500 m/s. However, the overall performance improvements were well below expectations, and a large research effort shifted to explore these unexpected results. Many found that the quick loss of the nanostructure of the system during the early stages of combustion likely diminishes the gains of the initial material scale.[42,51]

As such, this work concentrates on the implementation of a model for nanopowder-based thermites, while remaining applicable for use with microthermites for comparison. Thermites, and nanothermites in particular, are extremely interesting for certain applications such as integration in microsystems, civil engineering, and the aerospace industry due to the possibility of controlling the temperature, pressure, and products produced during reaction, as well as the initiation delay and burn rate.[52–55] The following provides an overview of the current understanding of the effects of major parameters of the system on these reaction characteristics.

1.2.1 Material Selection

A major parameter in the reaction mechanics of thermites in general is the selection of fuel and oxide material species. The heat of reaction and gas production for each unique fuel/oxide pairing's resultant redox reaction are major factors to take into account when selecting a nanothermite for a particular application. In 1998, Fischer *et al.* completed a large-scale study of the theoretical energy release, gas production, reaction products, and adiabatic temperatures of thermites, intermetallics, and combustible metals.[50] The choice of the fuel and oxide species can also affect the thermite performance due to the differences in diffusion coefficients of oxygen within the species, the melting temperatures, and the thermal conductivities, and, thus, play an important role in the tunability of thermites for specific applications. Some applications, such as circuit breakers for MEMS devices[56], require high gas production to pop the circuit, while the flame temperature is without real importance, whereas others require specifically gasless or nearly gasless combustion, like those used in aerospatial applications for vehicle separation[57]. Additionally, studies have shown a large importance on the oxidizer's capacity for oxygen release in the initiation delay of nanothermites.[45,58,59]

The following provides an overview of materials commonly used or under development for nanothermites over the last three decades.

a. Fuels

Many metallic species show a tendency to naturally oxidize, leading to a large variety of potential materials. The predominant fuel utilized in current nanothermites in both academic and industrial applications is aluminum. Aluminum remains the leading choice as it provides a reasonably high energetic density source of high abundance in the Earth's crust allowing for mass production at low cost. Additional species of growing interest include boron, zinc,

titanium, lithium, and magnesium, which also liberate high energy densities when oxidized; however, many suffer drawbacks of oxidization-limiting processes and slow reaction kinetics during their burn which can prevent complete combustion. Zinc and boron, in particular, have low oxygen diffusivity across their passivation shells which can lead to difficult initiations ($\sim 10^{-10}$ m/s, for boron, and $\sim 10^{-16}$ m/s, for zinc). Some studies consider combinations of these fuels to alter characteristics of reactions, such as Al:Zr reactive composites that show lower initiation delays than for either species alone.[60]

b. Oxides

There exists an even larger diversity of oxide choices current in thermite mixtures, spanning from common metallic oxides like cupric oxide (CuO), ferric oxide (Fe_2O_3), bismuth trioxide (Bi_2O_3), or tungsten trioxide (WO_3), to perovskites like lanthanum chromite ($LaCrO_3$), lanthanum ferrite ($LaFeO_3$), or lanthanum cobaltite ($LaCoO_3$)[61,62], to metal iodates including bismuth(III) iodate ($Bi(IO_3)_3$), copper iodate ($Cu(IO_3)_2$), or iron(III) iodate ($Fe(IO_3)_3$).[63] As numerous studies have revealed the oxygen diffusion and release upon decomposition of the metallic oxide as the limiting factor in the reaction initiation, Zhou $et\ al.$[58] tested the importance of the rate of oxygen release in three different nanothermite systems including Al:CuO, Al:Fe_2O_3, and Al:ZnO. Using time-of-flight mass spectrometry, a correlation is evidenced between the ease of oxygen release and the overall thermite reactivity. Nanopowders formed of a combination of 50 nm Al powder mixed with $\sim$100 nm powder of the oxides are initiated through T-Jump experiments at medium heating rates up to $\sim 10^6$ K/s. CuO and Fe_2O_3 display large oxygen releases when individual particles are heated under T-Jump conditions; this corresponds to the successfully initiated reactions of the corresponding nanothermites, where CuO releases a greater concentration of oxygen with a consistently lower initiation delay in the mixed thermite. The smaller amount of oxygen released by individual Fe_2O_3 particles correlated with moderate reactivity in the combined nanothermite. Individual ZnO particles poorly released oxygen upon heating, which also conforms to the lack of reactivity for this thermite pairing. Thus, for nanothermites under vacuum, the chosen oxide species and its rate of decomposition are extremely important parameters for the resultant reactivity.

In a similar goal, Jian $et\ al.$[59] studied ten oxidizers individually, as well as in nanothermite mixtures, to understand the role of gas phase oxygen on nanothermite initiation. CuO, Fe_2O_3, WO_3, Bi_2O_3, $AgIO_3$, $KClO_4$, SnO_2, Co_3O_4, MoO_3, and Sb_2O_3 were tested in gas release customized T-Jump experiments to find the O_2 release temperature under rapid heating. These release temperatures are then compared to initiation temperatures for respective thermite mixtures with Al fuel particles. Initiation experiments were performed with an identical

apparatus, with an addition of a PMT to allow mass spectra and optical emission information, which was used to determine initiation, defined as the onset of optical emission.
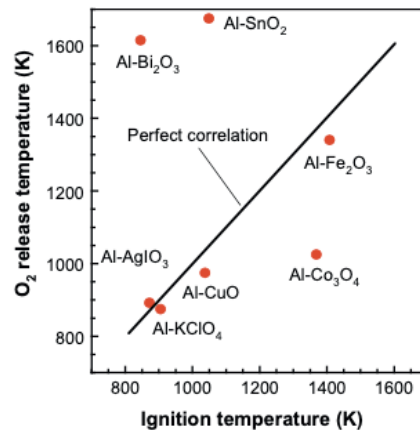
Figure 1.1: Oxygen release of different thermite couples as a function of ignition temperature. **[59]**

Almost all neat oxides were found to release O_2 gas, exclusively, except for Bi_2O_3, which also produced Bi gas, and SnO_2 and MoO_3, which were found not to produce gas. Importantly, as the main conclusion of the study, the authors point to the essential role of condensed phase processes during initiation, as some of the thermite couples, such as $Al:Co_3O_4$, release gaseous oxygen at temperatures well below initiation (see Table 1.1).

Table 1.1 : The temperatures of ignition (heating rate of $\sim 5\ 10^5$ K/s) and oxygen release from various aluminothermites for comparison with the temperature of oxygen release from the bare oxidizer nanoparticle, as detected by TOFMS. **[59]**

Nanothermite (Al + oxidizer)	Ignition Temperature (K, ± 50K)	Thermite O_2 Release Temperature (K, ± 50K)	Bare oxidizer O_2 Release Temperature (K, ± 50K)
AgIO₃	890	890	890
KClO₄	905	905	875
CuO	1040	1050	975
Fe₂O₃	1410	1400	1340
Co₃O₄	1370	1020	1030
Bi₂O₃	850	930	1620
Sb₂O₃	950	-	-
MoO₃	850	-	-
WO₃	1030	-	-
SnO₂	1050	-	1680

1.2.2 Manufacturing Methods

Production of a nanothermite begins with individual nanoparticle components, which can be accomplished by vapor-phase condensation, liquid-based chemistry, or occasionally mechanical means. As previously mentioned, aluminum remains the predominant choice for fuel, especially in nanoparticle form, because of its stability (due to its naturally formed alumina shell) and its environmental abundance. Most Al nanoparticles studied in the literature

are synthesized by vapor-phase condensation methods, specifically by electrical explosion wire. The process, based on the method discovered by Narme and Faraday in 1774 and heavily developed since for specific metal nanoparticle fabrication[64–66], involves electrical explosion with a shock-wave generation and rapid heating of the metal. This forms a plasma that is then spatially restricted through a high pressure field created by the pulse that generates metal clusters projected at supersonic speeds into the environment. This process has been extrapolated to macroscale production of a few hundreds of grams per hour.[13]

It is also possible to produce aluminum nanoparticles from condensed aluminum vapor by vaporizing a thin Al wire through the imposition of a strong electric current and collecting the particles from the walls of the explosion vessel. Through these vapor-phase condensation methods, it is possible to control the passivation layer characteristics including its thickness and material components through manipulation of the composition and concentration of the atmosphere. These vapor-phase methods permit fabrication of particles over a large scale of 40 to 100 nm by adjustment of the current and are generally simple and highly efficient.

Liquid phase methods, also termed "wet chemistry," typically call for careful mixing of different quantities of initial solutions with continuous stirring and drying phases. While this process is not very adjustable to large-scale production, it is of particular interest due to the possibility for functionalization of the particle surface for specifically desired effects on the complete thermite.[67] Mechanical manufacturing provides another fabrication pathway which allows control of the native oxide layer formation by introduction of oxygen during the milling process. Nanoparticles formed from this process are observed to have alumina present at the grain boundaries.[68]

To fabricate complete nanothermites, the two constituents are intimately mixed at the nanoscale. The most popular choice for mixing today remains one of the numerous physical processes, such as ultrasonic mixing or high-energy ball milling, but improvements in nanoscale fabrication processes have also opened chemical pathways like molecular auto-assembly, cold spray consolidation, or rapid expansion of a supercritical fluid.

The traditional method for mixing by sonication remains one of the simplest and most practiced preparation methods. To accomplish this, the nanopowder constituents are suspended in a solvent that is then placed in an ultrasonic water bath and agitated for a pre-determined time period usually around a few minutes, with a one second delay after every two seconds of sonication to prevent premature initiation. After mixing, the preparation is dried. Mixing by this method provide variable degrees of mixing, mostly due to the different morphologies of the initial particle forms. Other disadvantages are also present, such as the difficulty of larger batch mixing due to a decrease in mixing efficiency and an observed segregation of the particles during drying which can cause inhomogeneities.

High-energy ball milling, particularly, arrested reactive milling (ARM) is an effective preparation method to form highly dense metastable intermolecular composites. In this process, nanoparticles are loaded at ambient temperature with milling balls then milled at several

hundred rounds per hour. This begins a mechanical initiation of the exothermic reaction, increasing the temperature and pressure within the mixing environment, that is arrested before the self-sustaining reaction begins. Pressures can reach up to 5GPa and the temperature is externally restrained by a cooling jacket filled with water or liquid nitrogen (called cryogenic milling). The final product is a microscale pellet with nanoscaled structural features that approaches the theoretical maximum density. ARM is advantageous due to its flexibility, versatility, and low cost, but presents disadvantages in the necessary safety precautions to prevent full initiation during processing and the inevitable presence of reacted material in the final mixture. Interestingly, nanothermites prepared by this method show lower initiation temperatures than through traditional mixing methods; this finding has interesting implications in regards to the newly proposed theory of reactive sintering and its effect on nanopowder-based thermite initiation (see Section 1.3.3).

The desire to increase the degree of mixing for improved performance has led to the development of innovative processes such as through the use of supercritical dispersion.[69] Due to the lack of interfacial tension in supercritical fluids, homogeneous mixing of nanoparticles that usually aggregate during drying can be achieved. The thermite components are mixed in an agitated autoclave in a supercritical atmosphere, and this dispersion is either rapidly or slowly expanded by a nozzle, which destroys any formed agglomerates. The major downside to this approach is the possibility of reaction between the supercritical fluid and the fuel nanoparticles when attempting to scale up production.

Another proposition in recent studies has been molecular self-assembly, where one particle species arranges themselves autonomously or through application of external forces around the other in inorganic, aqueous, or organic solutions. Possible pathways include assembly by electrostatic forces existent between charged aerosol particles[70] or between two ligands on functionalized nanoparticles[71] or grafting strategies to bind oligonucleotides based on DNA assembly[72–76]. Characterization of these preparations have shown excellent reaction enthalpies likely due to the high level of mixing from such processes, however, these complex processes remain difficult to upscale for mass fabrication.

1.2.3 Influence of Key Parameters

a. Stoichiometry

When preparing nanothermites, the stoichiometric ratio ξ is of great importance to ensure the completeness of the reaction. It details the stoichiometry, or the relative amounts of fuel and oxide, within a thermite composition. This relationship can be expressed as:

$$\xi = \frac{\left(m_{fuel}/m_{oxide}\right)_{sample}}{\left(m_{fuel}/m_{oxide}\right)_{ST}} \tag{1.2}$$

where m_{fuel} and m_{oxide} are the respective weights for the fuel and oxides species in the sample or the stoichiometric mixture. ST represents the stoichiometric mixture that leads to a complete reaction, given by:

$$\left(m_{fuel}/m_{oxide}\right)_{ST} = \frac{xM_{fuel}}{yM_{oxide}} \tag{1.3}$$

for the proposed reaction x Fuel + y Oxide. Thus, $\xi = 1.0$ is considered the stoichiometric ratio. Mixtures with $\xi > 1.0$ are considered fuel-rich, while mixtures with $\xi < 1.0$ are considered fuel-lean. To obtain precise ratios, it is also important to account for the native oxide passivation layer on fuel particles by including a purity term, P, in percentage weight :

$$X = \frac{\xi \left(m_{fuel}/m_{oxide}\right)_{ST}}{P + \xi \left(m_{fuel}/m_{oxide}\right)_{ST}} \tag{1.4}$$

This ratio can then be manipulated to optimize the energy density of the reaction according to the desired application. Many fundamental studies have experimentally investigated the reaction characteristics as a function of the reaction stoichiometry.

A 2004 article from Granier *et al.*[77] studied the initiation delays and propagation speeds of the reactions of compressed pellets of Al:MoO$_3$ thermites in an open environment. Materials utilized included variable aluminum nanopowders with sizes ranging from 20 nm to 200 nm mechanically mixed by sonic waves in solution with rectangular sheets of MoO$_3$ roughly 1 μm long, 20 nm wide, and 10 nm thick. The final product was dried and compressed into cylindrical pellets by a standard axial press, then initiated by laser (44 mm, $\lambda = 10.6$ μm, 50 W laser) with a maximum power density of ~100 W/cm^2. The initiation delays, defined as the time between the laser emission and the first optical emission, and propagation speeds, observed by high-speed camera, as a function of the equivalence ratio were tested for Al nanoparticles of diameters 29.9 nm, 39.2 nm, and 108 nm, with these results presented in Fig. 1.2a and 1.2b, respectively.
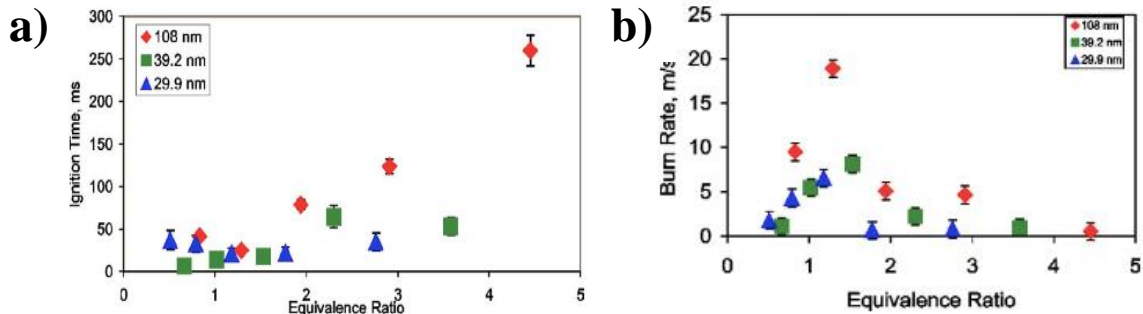
Figure 1.2: The ignition time (a) and burn rate (b) as a function of the equivalence ratio. **[77]**

Interestingly, it was observed that both the optimal ignition time (lowest) and burn rate (fastest) were not found at the perfectly stoichiometric mixture ($\xi = 1.0$) but instead for fuel-rich mixtures somewhere between $\xi = 1 - 1.5$ depending on the specific Al particle size.

Similar results were obtained by other studies[78–80] for this and other nanothermite mixtures, including a Prentice *et al.*[81] study of mixtures of 80 nm Al particles mixed in solution with two WO_3 aerogels: Aerogel 120 and Aerogel 400, named for their extraction temperatures. Observing the reaction velocity as a function of the equivalence ratio, the highest reaction speeds are determined to occur at $\xi = 1.4$.

Finally, a full spectrum analysis was completed by Dutro *et al.*[82] on the combustion behavior of $Al:MoO_3$ within an enclosed burn tube experiment. It was determined that three combustion regimes can be defined as a function of the percentage of fuel in the mixure as follows: a steady high-speed propagation for approximately 10% to 65% fuel, an oscillating and accelerating wave around 70% fuel, and a steady slow-speed propagation for ~ 75% to 85% fuel. Additionally, propagation failed for extremely fuel-lean (< 10 % fuel) and fuel-rich (> 85% fuel) mixtures.

It is important to note that most of these studies have been completed in an open environment system where ambient oxygen likely contributes to the improved performance due to interaction with the excess fuel. There are currently a limited number of specific studies on the effect of the equivalence ratio on thermite behavior in confined experimental setup. One such study by Son *et al.,*[79] however, confirms the general pattern even in closed burn tube experiments. Here, $Al:MoO_3$ mixtures of varying stoichiometric ratios (spherical nanoaluminum with sheetlike MoO_3 of approximately 30 x 200 nm) were initiated within thick-walled tubes with an inner diameter of 1.85 mm. Results of the propagation velocity as a function of the mass percentage of nano-Al (Fig. 1.3) shows that the optimal propagation velocity occurs for a slightly fuel-rich mixture.
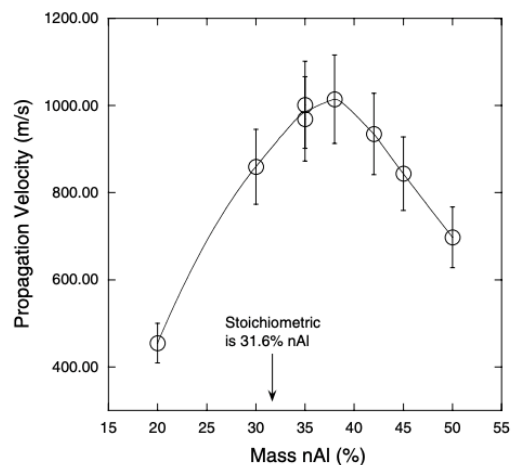
Figure 1.3: Measured propagation rate as a function of the mass fraction of nAl (%). **[79]**

Thus, it can be generally concluded that the required optimal mixture for high thermite performance, *i.e.,* a low initiation delay with a high burn rate, is fuel-rich ($\xi \cong 1.2 - 1.4.$)

b. Particle Size

Thermites reduced to the nanoscale open the opportunity for a theoretical increase in performance compared to their microscale counterparts. The effect of particle size on the combustion of isolated Al particles was studied theoretically by Huang *et al.*[83], including a literature review of numerous experimental results on this matter (Fig 1.4). Two clearly defined regimes can be established, with an exponentially inverse relationship between initiation temperature and particle size for particles less than ~10 μm, whereas performance stagnates for larger particles.
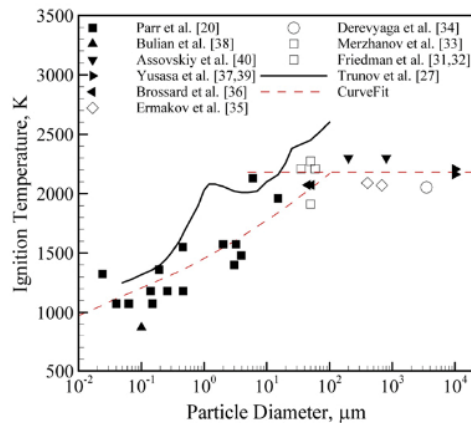
Figure 1.4: A literature review of studies on the ignition temperature as a function of particle diameter. **[83]**

It is, thus, logical to expect a similar proportionality in performance when reducing the size of particles in thermites; however, a study investigating this effect when integrated into thermites, completed by Pantoya *et al.*[84] with Al:MoO$_3$ thermites over a large range of Al
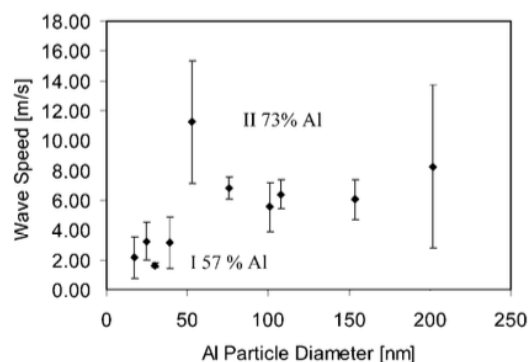
Figure 1.5: Wave speed as a function of Al particle diameter for an Al:MoO$_3$ system. **[77]**

particle diameters, raises some doubt. Al, ranging from 17 to 202 nm on the nanoscale and 3-4, 10-14, and 20 μm on the microscale, was mixed with MoO$_3$ flakes with at least one dimension under 100 nm and initiated by a 10.6 μm, 50 W laser. A direct comparison of nano vs. micro sized components was unattainable due to a preheating effect on the micron-composites. On the other hand, an assessment of nano-Al based thermites from previous experiments[77] with identical initiation setup show two evident velocity regimes according to the ratio of weight percentage of active Al to native Al$_2$O$_3$. The first regime, for an active Al

content of $\leq 57\%$, actually shows a reduction in wave speed due to the large percentage of alumina, acting as a diluent and limiting conductivity. In samples falling into the second regime, with particles of diameters from $50 - 200$ nm ($\geq 73\%$ active Al content), performance appears constant regardless of the fuel particles size. Thus, it can be understood that an equilibrium must be found between size reduction and the increasing alumina content. The authors propose that this critical limit for Al particle size falls around 50 nm.

However, another study by the same team in Texas where three Al sample sizes (44 nm, 80 nm, 121 nm) are tested with the same MoO_3 flakes as used in Ref. 77 shows a clear increase in combustion velocity inversely with the Al particle diameter.[78] A major difference between these two studies is the method of initiation; this study tests samples within a closed stainless-steel vessel and uses an electric match head for initiation. It is possible that the heating apparatus and resultant heating rate have a larger effect than previously hypothesized. Despite the difference in results, a critical limit is equally observed, potentially around 80 nm.

This difference in results where only the method of initiation is adjusted could be
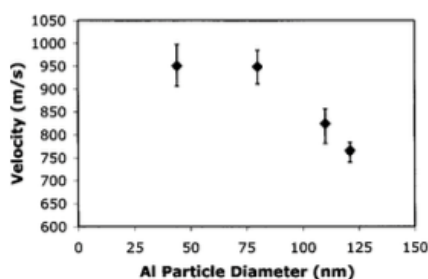
Figure 1.6: Propagation velocity as a function of Al particle diameter for an Al:MoO₃ system [**78**]

explained by a discussion proposed by Egan *et al.*[85] on the effect of particle size in laser-initiated experiments due to different absorption behavior. A CuO particle absorbs ~3 times the energy of a 532 nm laser than Al particles, thus, the CuO particles are expected to melt first, while the alumina oxide shell acts as a delay. To test this effect, isolated CuO particles were heated by the same pulse, 12 ns, which would normally be sufficient to melt the material, but this was not observed. According to Mie scattering calculations, the absorption efficiency per volume decreases with diameter for CuO particle above 175 nm. The presence of variable size aggregates within a sample or compaction density effectively causing the upper layers to "shade" the underlayers could cause a lack of size dependency in reaction speed. It is clear that, despite a general trend of higher reactivity for smaller fuel particle sizes, there is a tradeoff with other factors.

Extending this axe of questioning to both the fuel and oxidizer particle sizes, the reduction of oxidizer size was found to produce double the effect of an identical reduction in fuel size. Weismiller *et al.*[86] tested Al:CuO and Al:MoO₃ thermites while varying the two particle sizes between the nanometer and micrometer scale. The samples were tested in an acrylic burn tube (L = 8.9 cm, D_{in} = 0.32 cm, D_{out} = 0.64 cm) where the measured burn rate was calculated from position-time data, taking the average of three tests to account for errors in %TMD stability as the tubes were loaded. The resultant burn rates are presented in Fig. 1.7a (Al:CuO) and Fig. 1.7b (Al:MoO₃) for nominal particle sizes: nanoscale Al, 38 nm; microscale

Al, 2 μm; nanoscale CuO, 33 nm; microscale CuO, 2.92 μm; nanoscale MoO₃, ~50 nm; microscale MoO₃, ~ 50 μm. The best thermite performance is obtained through all nanoscale components; but on an individual basis, it is clear that nanoscale oxidizer particles show greater enhancements compared to nanoscale fuel. An additional sample was prepared for all μm-Al:CuO mixes by diluting the μm-Al with Al₂O₃ nanopowder to produce the same overall mass percentage of alumina to test the effect of the oxide shell as a diluent. The authors indeed found a similar performance for diluted μm-Al:nm CuO (230 m/s) and nm-Al:μm CuO (200 m/s); however, similarly prepared Al:MoO₃ samples were difficult to ignite and did not show strong propagation. It was thus determined that, while the oxide shell dilution can influence thermite behavior, this is not the only explanation as to why oxidizer particle size shows a stronger impact than fuel particle size.
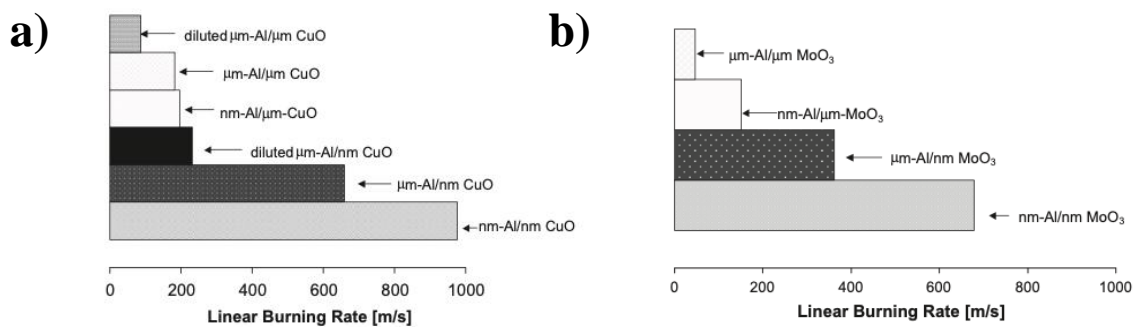
Figure 1.7: Linear burning rate of Al:CuO (a) and Al:MoO₃ (b) thermites of mixed nano and micro components as a function of particle size. **[86]**

b.   Native Oxide Shell Thickness

A more-detailed study of the effect of the thickness of the oxide shell was produced in 2010 by Chowdhury *et al.*[87] where Al:CuO thermites with varying native oxide thicknesses were rapidly heated (3.2 x 10⁵ K/s) on a platinum wire to ~1250 K by voltage pulse. Aluminum nanoparticles of nominal size ~50 nm were determined to contain ~70% active aluminum content by TGA, indicating a native oxide shell thickness equal to ~2 nm. To provide different thicknesses, some particles were oxidized at 773 K and weighed until corresponding to a thickness of ~3 and 4 nm. These particles were then mixed with < 100 nm particles of CuO and initiation was simultaneously determined by an optical signal and by the detection of Cu by mass spectrometry. A clear nearly linear effect is observed in the initiation delay as a function of the oxide shell thickness.
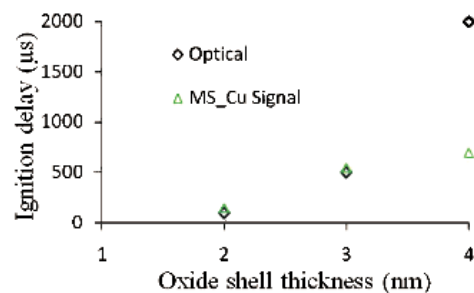
Figure 1.8: Ignition delay as a function of oxide shell thickness for an Al:CuO system. **[87]**

Recent works discovering the loss of nanostructure due to reactive sintering and coalescence of the initial nanoparticles into microscale agglomerates shows the potential flaws in the assumption that size reduction automatically leads to performance enhancements.[42,45,88] This does not deny the effect of reduced particle size on reactivity, in general, as isolated fuel particles are not in the reactive environment necessary to produce the reactive sintering effect. Instead, this implies that the reason for improvements in performance in nano- vs micro-thermites may be attributable to a combination of this and other factors, such as the degree of mixing, the melting timescale, or the wetting contact between the fuel and oxide species, which actually overcome certain detriments added by the size reduction such as the dilution from increased alumina.

c. Compaction

Compaction is an important parameter which is generally expressed in terms of the percentage of the Theoretical Mass Density (%TMD). This theoretical maximum density is the calculation of the density of the mixture as a weighted average of the bulk densities of the reactants. Thus, a highly compacted mixture has high %TMD, while a low %TMD implies a low compaction rate with a good percentage of void space.

In Pantoya $et\ al.$[84], the effect of the bulk density on combustion velocity was also explored using pellets with 76-80 nm Al and 10–14 μm MoO_3 flakes prepared at an equivalence ratio of 1.2 and initiated by laser. The results from a test on a range of 6.5 to 73 %TMD is displayed in Figure 1.9. The authors propose that the opposing dependence of nano- and micro-thermite reactivities' as a function of %TMD is due to a difference in initiation mechanisms. Microthermite reaction velocity displays a direct proportionality to the density. Assuming that this reaction is driven by diffusion, higher compaction rates will decrease the air volume and increase the pellet's thermal diffusivity, effectively increasing diffusion and, ultimately, the combustion velocity.
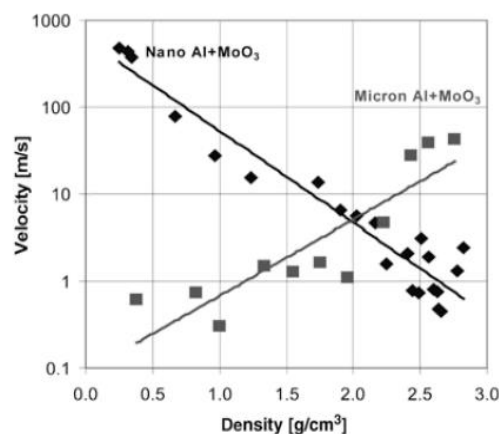
Figure 1.9: Propagation velocity as a function of mixture density for both nano and micro $Al:MoO_3$ systems. **[84]**

In contrast, the nanocomposite materials show a nearly linear reduction in reaction velocity as %TMD is increased. DSC plots of the same materials showed that the reaction in $Al:MoO_3$ thermite pellets occurs before the melting point of Al and the sublimation of MoO_3,

thus, it is hypothesized that a solid-solid diffusion pre-reaction occurs due to the high compression of materials to achieve higher compaction. This is not enough energy to cause initiation, but could remove some stored energy that would otherwise help to promote the self-propagation combustion reaction, thus reducing the combustion velocities.

In a more extensive study, Sanders *et al.*[89] tested four different nanothermite couples for the effect of compaction on their burn rates, including an open tray and two closed burn tube experiments at variable low density and 47 %TMD. Materials used include 80 nm spherical Al particles, 25 μm Bi_2O_3 rods, ~21 nm x 100 nm CuO rods, ~30 nm x 200 nm sheets of MoO_3, and 100 nm x 20 nm WO_3 platelets. The samples were first mixed in solution (hexane for MoO_3 and CuO and isopropanol for WO_3 and Bi_2O_3) by ultrasonic mixing, then subsequently dried by hot plate at ~321 K. Finally, the mixture was passed in a 355 μm sieve to avoid large agglomerations.

A metal tray with two holes for optical fibers coupled to photodiodes at a distance of 20 mm was utilized for open tray burn experiments, where each powder mixture was deposed and ignited at one end by a piezoelectric igniter. For enclosed burn experiments, the experimental setup designed by Bockmon *et al,*[78] was modified to allow direct loading of the powder, which was then vibrated by a Cleveland vibrating block to achieve a uniform density. The acrylic tube has an inner diameter of 3.2 mm, an outer diameter of 6.4 mm, and is either 88.9 or 101.6 mm long. The higher density experiments were initiated by exploding bridge wire, which allowed full preservation of the pressure within the system. For the lower density tests, a bare electric match head is used for initiation.

Table 1.2 : Reaction speed and pressure observed by Sanders *et al.* for four types of aluminothermites in three experimental setups. All reported values are the average of three tests. **[89]**

Thermite	Pressure Cell P_{avg} (psi)	Open Tray V_{avg} (m/s)	Low Density (%TMD)	Burn Tube Low Density P_{avg} (psi)	Burn Tube Low Density V_{avg} (m/s)	Burn Tube 47% TMD P_{avg} (psi)	Burn Tube 47% TMD V_{avg} (m/s)
Al/MoO$_3$	240	320	11	2700	950	6595	580
Al/Bi$_2$O$_3$	365	425	17	7750	646	5700	560
Al/WO$_3$	260	365	9	3900	925	-	-
Al/CuO	250	525	6	1900	802	-	-

Table 1.2 presents the results obtained from these three tests. Overall, the confined burn test velocities are generally 1.5 to 3 times greater than those seen in the open tray test due to the confined gases either propagating heat or reacting itself through gas-phase mechanisms. It is also apparent that the thermite reaction is complex and cannot be succinctly resumed as function of %TMD. In the open tray experiment, Al:CuO has the fastest propagation while Al:MoO$_3$ is the least performant. When confined, Al:MoO$_3$ reports instead the fastest propagation, with Al:Bi$_2$O$_3$ as the slowest.

Results were not available for two thermite couples at 47 %TMD due to premature initiation during preparation; however, a general trend can be proposed that within the confined tube system, an augmentation of the rate of compaction leads to a reduction in the speed of propagation. This corresponds to the general trend found in the previously discussed study. Additionally, it is important to note that the behavior of the $Al:Bi_2O_3$ sample, which was the only microscale oxide component, is found to produce considerably more gas while reporting a significantly slower propagation velocity, particularly at low compaction in a confined environment.

Overall, a lower compaction rate in nanothermites will increase propagation speeds; however, for specifically gasless applications, our interest rests in thermite couples and compaction rates that will favor condensed phase reactions with conductive heat transfer for propagation. At very low %TMD, large voids may induce a more gas-phased regime for initiation, as the fuel may be oxidized by environmental gasses, and propagation, as gaseous species are released. Additionally, the dominant heat transfer mechanism transitions from convective to conductive burning at around 50 %TMD.

The principal parameters of the reaction include the initiation temperature, the initiation energy and the reactivity. The initiation temperature is defined as the temperature at which the exothermic reaction starts and is sustained autonomously without external energy. The initiation energy is the external energy required, whether by mechanical, thermal, or electrical means, to reach its point of initiation. Finally, the reactivity is the decomposition or reaction rate, which can be composed of different thermodynamic and kinetic processes such as the rate of oxidation of the fuel and the rate of decomposition of the oxide for nanothermites. These three parameters are attributable to the choice of fuel and oxide species, where each combination has its own stoichiometric ratio, reaction pathway, gas production, and heats of reaction, as well as the manufacturing method.

1.2.4 Conclusion

In summary, the last three decades of research efforts in energetic materials have led to the emergence of a new family of materials, nanothermites, which have shown vast improvements in reactivity when compared to conventional energetic materials such as CHNO.[90]

The previous section presented the important parameters that have been shown to affect the reaction characteristics. The reactivity of the fabricated mixtures is dependent upon, of course, the material components (fuel and oxide species), but the size has also been shown to heavily affect the reaction characteristics. The work of Bockmon *et al.*[78] on the $Al:MoO_3$ thermite couple clearly illustrated the tendency for an inversely proportional relationship between particle size and reactivity with an increase in combustion speed from 750 to 950 m/s by decreasing the Al particle size from 121 to 80 nm. Furthermore, they showed that under ~80 nm, the combustion rate becomes independent of the Al particle size, possibly

explained by the dominance of the native oxide layer on the Al surface, which inhibits the reaction. This phenomenon will be further discussed in the next section.

However, size reduction in thermite materials can considerably affect the sensibility of the reactive materials. This is both an advantage and disadvantage as the mixtures can have amplified sensitivity to mechanical shocks or electrostatic impulses leading to accidental initiation. This adds significant difficulty to their processes of fabrication and integration into application systems.

This first section also introduced numerous methods of manufacturing available in laboratories for nanothermite production of various morphologies, of which nanopowders are the principal format. These particle-based morphologies offer a large potential for applications in pyrotechnics, welding, mining, civil engineering, and the aerospace industry.

Despite the amount of research studies and technological advancements, many unknowns remain regarding the mechanisms of reaction during the initiation and/or combustion of nanothermites. As such, analytical models are still early in their development, despite their necessity for the incorporation of these new materials in applications (prediction of performances and aging). In the subsequent section, a state of the art of the current works investigating the mechanisms of initiation and reaction of nanothermites is presented, followed by an overview of the different existent models of the initiation and combustion of nanothermites.

1.3 Fundamental Studies of the Mechanisms of Initiation/Reaction of Nanothermites

One of the principal unknowns, highly debated in the scientific community, in the pursuit to better understand and tune nanothermites is the driving mechanism of initiation. Multiple possible pathways have been proposed and studied intensively during the last ten years, including both gaseous and condensed phase mechanisms. There are three dominant theories proposed: i) A heterogeneous condensed/gas phase with fracture of the oxide shell. ii) A Melt Dispersion Method with liquid aluminum expulsion before shell fracture iii) Reactive sintering where the fuel and oxide particle are condensed and aggregated due to the exothermic redox reaction, leading to a diffusion regime for initiation which dynamically increases as sintering is operated.

In the following subsections, an overview of these three basic processes is presented. Then, the current modelling approaches available, based on some of these hypothesized mechanisms, are discussed. An improved understanding of the mechanisms at play is necessary to better analyze the current simulation packages and to improve novel models under development.

1.3.1 Heterogeneous Process with Shell Fracture and Mass Transport

One type of proposed theory for the dominant initiation regime in nanothermites involves different formulations of a heterogeneous combination of condensed and gas phase mechanisms. Multiple detailed explanations for this reaction have been hypothesized, but nearly all include a fracture of the native oxide shell surrounding the fuel particle releasing the core fuel for interaction, in either phase.

An initial work in 1992 by Rozenband *et al.*[91] developed a quantitative model for the oxidation of metal particles in a gaseous oxidant. Due to the differences in the bulk densities and linear expansion coefficients between the metal and oxidized metal species, mechanical stresses form in the native oxide layer that ultimately overcome its structure and disturb the protective nature once the equivalent stress surpasses the ultimate strength of the native oxide. The rupture of the protective oxide layer permits a rapid augmentation in the amount of interacting core metal and the gaseous oxide, explaining the sudden initiation of the runaway reaction. A corresponding temperature of native oxide disruption was also determined for common fuel species such as aluminum, with corresponding rupture temperature around 800K, magnesium around 500K, and zirconium around 550K.

This work was continued in 2004 by V. Rosenband,[92] extending the possible reasons for shell fracture to include phase or polymorphic transformations in the metal. This is first corroborated by theoretical calculations for aluminum where the equivalent stress in the shell only surpasses the critical stress limit for alumina after the melting point of Al, most likely due to the volumetric increase of the metal as it melts. This also corresponds to the high increase in reactivity for temperatures at and above the melting point of Al, where in certain experiments past this temperature, aluminum particles were observed to aggregate. The author concludes that this is likely due to the release of molten Al leaking through the tensile fractures in the outer shell of the native oxide layer. A similar effect is also observed for titanium particles due to the polymorphic transformation from αTi to βTi around 1155K, the temperature at which reactivity is seen to strongly and rapidly increase.

An in-depth study of the polymorphic phase transformations in the native alumina layer of aluminum particles during initiation was performed by Trunov *et al.*[93] as further proof of physical defects in the alumina layer causing increases in reactivity. This work divides the initiation process into four stages, as follows:

i)   Slow growth of the amorphous alumina layer until critical thickness, ~ 5 nm.
ii)   Transformation into γ-Al_2O_3, with a greater density forming crystallites that do not form a continuous layer, permitting metal aluminum to interact with the gaseous oxidizer and showing a rapid increase in the rate of oxidation, terminating in a completed shell of γ-Al_2O_3.

iii) Growth of the γ-Al_2O_3 layer limited by oxygen diffusion, which can be accompanied by phase transformations into δ-Al_2O_3 and θ-Al_2O_3, terminating in a stable α-Al_2O_3 shell.

iv) The oxide shell is completely transformed, diffusion is reduced, and the oxidation rate greatly decreases.

Experimental heating setups for aluminum powder with a diameter of 10–14 μm at a heating rate of 40 K/min correspond to theoretical TGA curves calculated based on a model corresponding to this four-stage process of initiation, where initiation occurs due to the interaction between the gaseous environment and the aluminum surface, limiting the oxidation rate to the diffusion rate of gaseous oxygen.

In 2006, Rai *et al.*[94] proposed a two-regime process for the oxidation of aluminum nanoparticles, including the diffusion of both aluminum and oxygen as important factors for initiation. A slow oxidation regime is present prior to the aluminum melting point, dominated by the diffusion of oxygen through the native oxide shell for interaction with the metal core. Once the melting point is reached, oxidation rapidly increases with diffusion of both aluminum and oxygen, possibly attributable to a fractured oxide shell. Visual characterization by TEM, as well as density analysis by DMA after oxidation of Al nanoparticles with nominal particle size from 70-80 nm showed hollow particles indicating the diffusion of metal aluminum through the oxide shell as a leading mechanism.

Zhang *et al.*[95] provided a supplementary study of this heterogeneous diffusion-based reaction theory by locating the reaction interface via thermogravimetric measurements of aluminum powder oxidation at the micro-scale (one powder at 3-4.5 μm, the other at 10–14 μm). They propose that if the limiting factor in oxidation is the aluminum diffusion through the native layer, then the reaction interface will be found inside the aluminum particle, at the meeting of the core metal and its resulting oxide. If, instead, the diffusion of the molten aluminum is faster than that of the free oxygen, then the resulting interface is on the outer surface of the particle. They model three different formulations for comparison with experimental TGA and SEM characterization:

i) Corresponding to aluminum diffusion as the limiting factor, the reaction interface is set at the interior limit between metal and its corresponding oxide.

ii) Corresponding to oxygen diffusion as the limiting factor, the reaction is set at the exterior oxide boundary which is ductile, thus there are no voids.

iii) Corresponding to oxygen diffusion as the limiting factor, the reaction is set at the exterior oxide boundary, taking into account the volumetric difference as Al melts, leaving voids between the rigid Al_2O_3 shell and shrinking Al core.

For the smaller particle size set, the second case model formulation best fits the experimental TG data indicating that the aluminum diffusion is the faster process. Additional SEM imagery after quenching shows non-ruptured particles after heating, with crystallite

formation at temperatures greater than ~1220 K, corroborating the four-stage phase changes suggested by Trunov *et al.*[93] In the case of the larger particles, the third formulation corresponds best to the data, signifying that the gaseous oxygen diffusion is also the limiting factor at this size. After quenching, the SEM images clearly show a similar crystallization, however, on hollow particles. Overall, they conclude that the third expression best fits all data, where the difference in data sets results from the point at which the growing native oxide shell becomes rigid during oxidation, at approximately 100 nm. This is not achieved by the smallest particle size distributions due to the speed at which the reaction is completed, which explains the better correlation with the second model formulation and the solid particles observed after quenching. Ultimately, the crystallite formation and preservation at high temperature observed under SEM confirm previous conclusions that grain boundary diffusion is quicker than through the oxide shell and causes increased reactivity once these temperatures are achieved.

Jian *et al.*[43] utilized time-resolved mass spectrometry of Al nanoparticles and Al:CuO nanothermites under T-Jump rapid heating to analyze the presence of aluminum vapor species including $Al_{(g)}$, $AlO_{(g)}$, $Al_2O_{2\ (g)}$, and the main oxidation product, $Al_2O_{(g)}$. An increase in concentration is found corresponding to temperature increase, with a rapid augmentation around ~2030 K. This further corroborates the diffusion of aluminum through the oxide shell under high heating rates. They also hypothesize that the large concentration increase at 2030 K, below the melting point of alumina indicates an aluminum-rich suboxide shell that thickens due to the increasing aluminum ion diffusion outward with simultaneous oxygen anion diffusion radially inward, growing the shell thickness.

Further evidence of the diffusion of aluminum was found in a 2015 study completed by Coulet *et al.*[96], where they characterized aluminum nanopowders of average particle size ~50 nm oxidized at different temperatures up to 900°C showing that, at high temperature above the melting point of aluminum, the migration of Al is faster than oxidation, leading to the creation of voids within the nanoparticle. Another article by Vorozhtsov *et al.*[97] found in 2016 that the oxidation of nanosized aluminum results in hollow oxide shells for larger particle sizes around 200 nm.

1.3.2 Melt Dispersion Method (MDM)

The Melt Dispersion Method is another proposed hypothesis for the dominant mechanism of the initiation regime defined as a mechanochemical mechanism for fast heating rates where the alumina shell on aluminum nanoparticles undergoes dynamic spallation, dispersing small clusters of liquid Al for interaction with the oxide due to tensile stresses; thus, by this mechanism, the reactivity is not limited by diffusion. This process is due to the 6% volumetric expansion as the interior Al melts, creating high internal pressure that leads to hoop stresses exceeding the theoretical strength of alumina.[98] However, after complete destruction of the oxide shell, a diffusion regime dominates the reaction.

This hypothesis was first proposed and developed by Levitas *et al.*[98] in a 2007 study establishing the theoretical solution to this phenomenon, with corresponding macroscopic

experiments determining that for a particle under a critical size, the propagation rate and initiation delay are independent of the radius. Additionally, due to this process, it can be expected that, after combustion, each Al particle will be dispersed into numerous smaller particles. This is in direct contrast to a diffusion regime, where the particle size will increase as the oxygen concentration grows, leading to oxidation of the Al into alumina, increasing the volume by 25% due to the difference in density. In a further work in 2008, Levitas *et al.*[99] explored the flame velocity as a function of the Al nanoparticle size in Al:MoO$_3$ thermites. Both the particle radius and the alumina shell thickness were varied, and it was determined that the radius alone does not control the speed of propagation. Instead, the propagation speed was primarily a function of the ratio between the particle radius (R) and the shell thickness (δ), defined as M = R/δ. Under a critical value, M = 19, the propagation speed is found to be independent of all physical parameters as well as Al content.
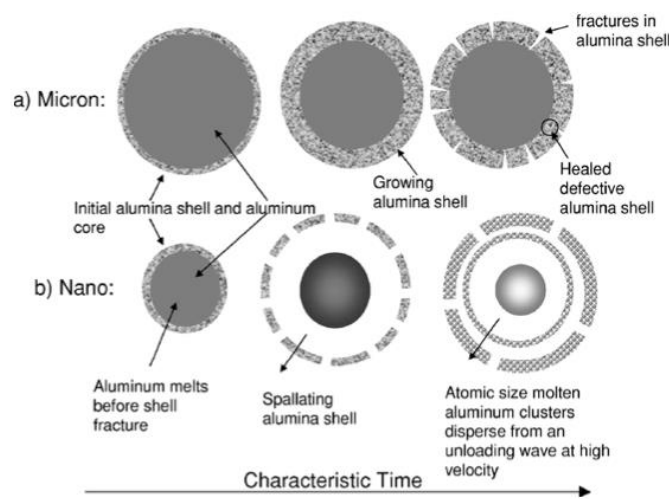
Figure 1.10 : Diagram of the proposed Melt Dispersion Method mechanisms at the nanoscale. (a) A micron system in which the native shell fractures before Al melting and heals. (b) A nano system where, due to the high heating rate, the melting of thealuminum core creates pressure that stresses the shell causing it to spallate and eject molten core for reaction. **[98]**

A final work by Levitas *et al.*[100] studied the flame propagation speed for Al nanoparticles of 80 nm and microparticles from 3 to 4.5 μm in Al:MoO$_3$ thermites finding agreement with a theoretical model based on the flame speed as a function of M, as previously defined in Ref. 99. After combustion, a large reduction in particle size is observed by SEM for both micron and nano-scaled particles, consistent with MDM theory. However, some contradictions with this theory were recorded, including the presence of gaseous Al above temperatures of 2275 K. The fact that this occurs exclusively above the melting temperature of alumina, an indication that the shell does not fracture, directly contradicts MDM and earlier hypotheses of the alumina shell cracking to allow diffusion.

1.3.3   Reactive Sintering

In total contrast to the MDM concept, reactive sintering was first observed by Sullivan *et al.*[88] in 2010 using newly developed *in-situ* TEM images of before and after rapid heating of Al nanoparticles and Al:WO$_3$ nanothermites. Al particles of 50 nm were heated at a rate of 10^6

K/s with resulting images showing no spallation or dispersed molten Al as would indicate the presence of MDM, even under an extreme heating pulse from room temperature to 1473 K, held for 1 second. On the contrary, some particles are seen to undergo crystallization or show irregularities on the surface after heating, confirming the diffusion of aluminum through the native oxide shell. Under an SEM, with the advantages of backscattered electron imaging (BSE), thermites prepared at stoichiometric ratios of the same Al particles mixed with < 100 nm WO_3 particles were heated at an identical heating rate. The resulting images show clear surface contact between the fuel and oxide particles, and the authors propose that as the material is melted, a reactive interface is created between the two agglomerated species' particles where diffusion is aided by capillary and surface tension forces delivering molten material to the interface. WO_3 material that was far from any Al particles did not undergo morphological changes; however, the particles of opposing species in close proximity were hypothesized to react, leading to the exothermic reaction causing further sintering of adjacent particles, coined "reactive sintering".

This *in-situ* characterization method was continued and expanded in a 2011 study by Sullivan *et al.*[45] for different thermite couples in conjunction with T-Jump measurements of initiation temperature through optical emission analysis. They chose to investigate the reaction of Al:CuO, Al:Fe_2O_3, Al:WO_3, and Al:Bi_2O_3, where all Al nanoparticles are 50 nm, with oxide particle sizes for CuO, Fe_2O_3, WO_3, Bi_2O_3 at < 50 nm, < 50 nm, < 100 nm, and 90-210 nm, respectively. Additional tests were completed for thermites of Al with 6 nm CuO particles prepared by wet chemical synthesis. Using the classical T-Jump setup, as designed by Zhou *et al.*[101] to test the temperature for initiation at ~5 x 10^5 K/s, a medium heating rate, initiation is determined by emission captured by a photomultiplier tube (PMT). The resulting initiation temperatures are recorded in Table 1.3. All found temperatures are above or very close to the melting point of aluminum (933 K), corresponding to Al nanoparticle oxidation experimental results. The melting temperature of the oxidizer is also discussed, as certain oxides used, such as CuO and Fe_2O_3, decompose while melting releasing O_2 gas that increases reactivity.[58] A slight correlation is also observed between higher melting temperature for oxides resulting in higher initiation temperature, but WO_3 does not follow the trend, indicating that melting of both species is not necessary, although it may be a contributing factor to the runaway reaction.

Table 1.3: The initiation temperature of different aluminothermites as measured by a T-Jump experiment (5 x 10^5 K/s) with initation determined by PMT. Comparison with oxidizer bulk melting temperatures. The initiation temperatures are significantly closer to the Al fuel melting temperature (933 K). **[45]**

Thermite	Ignition Temperature (K, ± 40K)	Oxidizer Melting Temperature (Bulk values, K)
Al:CuO	1010	1599
Al:WO₃	1065	1746
Al:Fe₂O₃	1270	1735
Al:Bi₂O₃	857	1098

High heating, *in-situ* experiments were completed for Al:CuO, with 6 nm CuO particles, and Al:WO$_3$ nanothermites (50 nm, < 100 nm, respectively) within the TEM, at a heating pulse of 1473 K and held for 10 ms and 1 ms, respectively. It is important to note that these experiments are performed under vacuum, thus only condensed phase mechanisms occur. For certain thermite reactions known to have high gas production, such as Al:CuO, it is probable that the actual initiation is multiphase, as will be discussed in Section 3.4. This temperature (1473 K) corresponds to the necessary heat to observe morphological changes in the individual nano-Al particles as presented in Refs. 92-93. Interestingly, the products of reaction were a few nearly spherical pure copper particles with several large non-spherical aluminum aggregates, where it is clear that surface interaction has occurred between the original metal and oxide species. When compared with larger CuO particles heated by the same process, it is observed that, while sintering occurs, the newly formed aggregates are not fully reduced, but instead the intermediary Cu$_2$O product. This implies that it is indeed due to the exothermic redox reaction within the thermite that permits the full reduction of CuO to pure copper spheres.

A similar experiment was tested with both Al:WO$_3$ thermites and a secondary sample of independent WO$_3$ particles on the same slide; however, SEM imaging was preferred due to BSE showing great contrast between W-containing and Al-containing species due to their respective atomic weights. In the regions containing only tungsten oxide particles (melting point of 1746 K), minimal sintering was observed with no other morphological changes after heating to 1473 K. In contrast, the WO$_3$ particles in close proximity to the Al nanoparticles exhibit clear signs of reactive sintering. This difference indicates that the external heating alone was not enough to cause the clear agglomeration, but, instead, the exothermic redox reaction was necessary. An elemental linescan plotting of the intensity of W, O, and Al as of a function of position also indicates clear mixing of the fuel and oxide species, implying an interfacial condensed-phase reaction occurring at the surface interaction between particles.
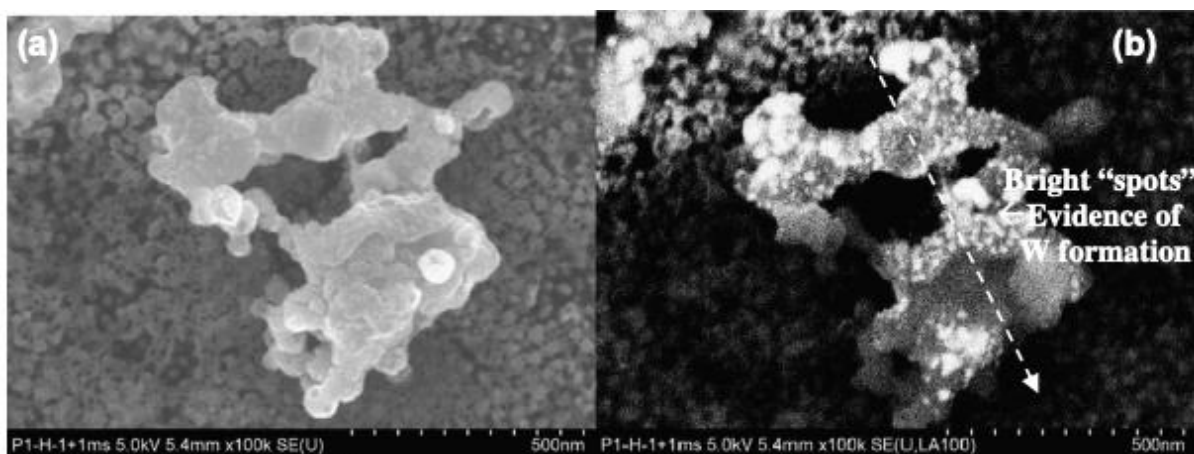
Figure 1.11 : Original (a) and BSE (b) post mortem images of an Al:WO$_3$ nanothermite after a second heating pulse with clear formation of solid tungsten (white spots, b). **[45]**

Further reflections on the final morphologies of the products in high heating rate nanothermite experiments indicate that the melting point of each product species is important to determine the resultant form. Copper, with a low melting point of 1356 K, forms nearly spherical agglomerates, whereas the pure tungsten, with a high melting temperature of 3680 K,

remains solid and thus, does not coalesce into spherical forms. This likely explains the bright spots in Figure 1.11 as clusters of solid tungsten. This explanation also corresponds to the observed morphology of alumina products for both experiment sets, as high-melting point Al_2O_3 (T_{melt} = 2327 K) cannot form a sphere within this reaction's timescale.

Sullivan *et al.* continued by investigating the importance of sintering to the reaction by calculating a theoretical "sintering timescale," defined by Equation 1.5 as the sum of the time to heat particles to their melting point and the time to fusion two particles of diameter, d_p.

$$\tau_{fusion} = \frac{\mu d_{eff}}{2\sigma_1} \tag{1.5}$$

where d_{eff} is the effective particle diameter ($\sim d_p$), μ is the size dependent liquid viscosity ($\sim$100 mPa·s), and σ_1 is the liquid surface tension ($\sim$0.7 J/m^2) for CuO particles. Treated as particles heated by convection in a hot gas environment above the Cu_2O temperature of fusion (1599 K), it is assumed that the temperature is constant within a single particle with negligible radiation losses. Additionally, it is assumed that no morphological changes occur below the melting temperature (as the timescale for fusion strongly increases after this point, despite prior fusion being possible through solid state grain boundary diffusion). A conservative ambient temperature, in addition to the lack of exothermic reaction energy contributions, is chosen to ensure overestimated sintering times. Thus, the particle is heated according to the convective heat transfer from the environment, given by:

$$\frac{dT_p}{dt} = \frac{hA}{\rho V C_p}(T_{gas} - T_p) \tag{1.6}$$

where T_p, A, V, and C_p are the temperature, surface area, volume, and temperature-dependent heat capacity of the particle and T_{gas} the surrounding gas temperature, held at 1700 K. The heat transfer coefficient h is defined by:

$$h = \frac{Nu k_g}{d_p} \tag{1.7}$$

with Nu, the Nusselt number, k_g, the thermal conductivity of the gas, and the particle diameter, d_p.

A comparison to a characteristic reaction timescale estimated to be 10 μs, taking 5% of the optically-measured burn time, is presented in Figure 1.12. The fusion time is extremely fast compared to the heating time, such that it is acceptable to reduce the total sintering time to equal the time to heat and melt the nanoparticles, finding good agreement with the estimated characteristic reaction timescale. The rapid timescale for fusion illuminates the importance of the heating method and rate on the characteristics of the combustion reaction. The authors propose that for some experimental setups at high heating rates, sintering may largely occur prior to combustion, whereas at lower heating rates, thermal losses may be great and permit

the particles to retain morphology during oxidation, leading to stronger size dependence on the speed of reaction.
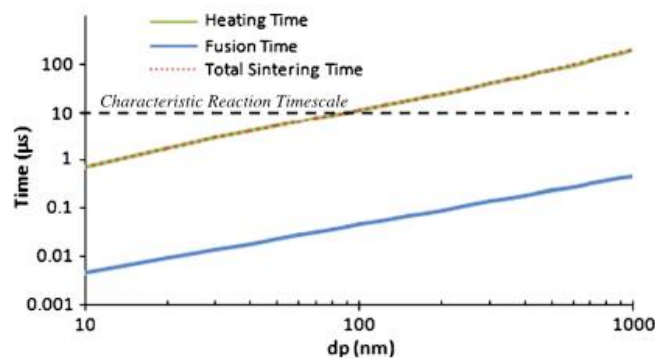
Figure 1.12 : Comparison of characteristic reaction timescale with estimated experimental timescale taking into account a theoretical timescale for the newly discovered process of reactive sintering. **[45]**

To investigate this effect on high heating rate experiments, Egan *et al.*[85] used the novel movie mode dynamic transmission electron microscopy method (MM-DTEM) to observe *in situ* heating of Al:CuO nanothermite materials, with Al nominal particle size of 80 nm and CuO particle of < 50 nm. The prepared samples were heated by a 532 nm laser pulse ($1/e^2$ diameter of 135 μm) for a duration of 12 ns at 0.3 kJ/m^2. A time-resolved image (Figure 1.13) of a 500 nm aggregate completely reacting within a period of 600 ns displays significant morphological changes after completion, including total loss of the original nanostructure.
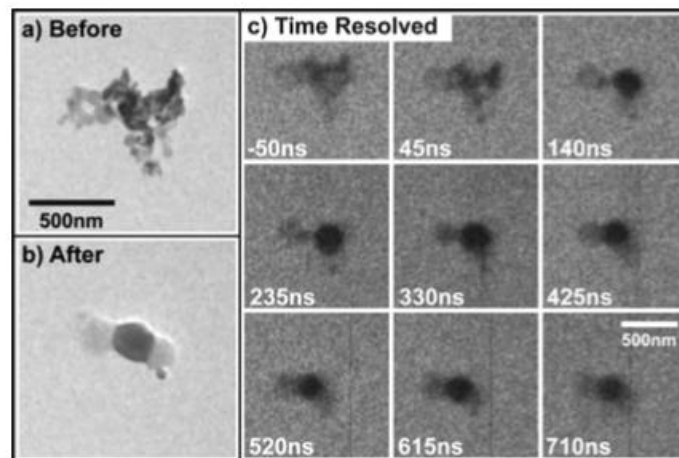
Figure 1.13 : MM-DTEM images of Al:CuO nanothermite heated by laser pulse and subsequent sintering reaction. **[85]**

The first loss of structure is observed around 45 ns, continuing with completed melting of central CuO around 235 ns while Al particles retain their form. At 425 ns, Al particles were observed to also lose their structure and coalesce towards the central CuO region, terminating the transformation at 615 ns with the final three species-segregated aggregates. An EDS line scan confirms condensed phase mixing within final reaction products from Al:CuO rapidly heated experiments (Figure 1.14). Significant oxidation is observed, as well as intermediary alloy products of Al and CuO. Importantly, despite the loss of the nanostructure, the Al nanoparticles do not display any sign of rupture of the oxide shell indicative of an MDM driven

reaction. Further images in Egan *et al.*[85] display a rapid loss of the initial morphology without spallation at heating rates up to 10^{11} K/s.
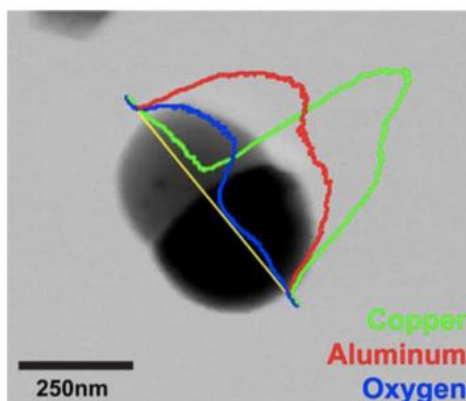
Figure 1.14 : Post-mortem SEM images of Al:CuO after heating and sintering with an overlaid EDS line scan. **[85]**

A size dependence is observed for larger aggregates, showing timescales for morphological changes in the CuO particles spanning up to ~6 μs. This is explained by absorption mechanics for larger particles, where the absorption efficiency per volume decreases with diameter for CuO particles above 175 nm. In addition, laser light absorption is not constant within the slide for densely packed subjects where upper layers may impede absorption for particles underneath.

Despite this nonuniform heating, the laser experiments correspond well when compared to Al:CuO nanothermite T-Jump experiments conducted with identical materials. It is calculated that 265 kJ are required to heat 2 Al and 3 CuO, a stoichiometric mixture, moles of reactant from ambient temperature to 1300 K, a point chosen well-above the Al:CuO initiation temperature. The heat of this reaction is ~1208 kJ, indicating that only 22% of the energy produced by the exothermic reaction is required to heat adjacent material of equal volume and promote the autonomous propagation of reaction. O_2 gas was also found to be present during the T-Jump experiments on isolated CuO nanoparticles, performed under vacuum, at slightly lower temperatures than the initiation temperature. Thus, it can be concluded that the full thermite reaction involves an already reduced phase of the oxidizer. Even when considering this loss of oxygen, only 38% of reaction enthalpy is required to heat adjacent material. Image comparison of the T-Jump products of reaction with the laser-induced system show a similar morphology, demonstrating that the DTEM observed reaction timescales are applicable to bulk combustion processes.

In studies of independent oxidation of Al nanoparticles in oxidizing environments, initiation delays are found to be on the scale of 100 μs; however, Al-containing nanothermites are found to burn in the range of 0.5 – 5 μs, with peak pressure achieved in ~10 μs, implying that condensed phase reaction mechanisms dominate the thermite initiation regime. As such, it is hypothesized that degree of mixing of the nanothermite material may play a very important role in determining reaction characteristics. A theoretical diffusivity of reaction, D, with the time scale of depletion, t, and length of region, l, is defined as:

$$t = \frac{(1.5l)^2}{D} \tag{1.8}$$

Using the time scale and lengths present in the DTEM experiments, D is ~5 x 10^{-4} cm^2/s, which corresponds to the time necessary to diffuse O in molten Cu for T > 3000 K. This could explain the difference in timescales for morphological changes seen for a sample with a large Al aggregate of ~1000 nm (~6 μs) and the sample displayed in Figure 1.13 with ~300 nm Al regions (600 ns).

In a recent paper from 2019, Wang *et al.*[44] introduce an innovative characterization and experimental platform to bridge the gap between high resolution imaging with *in-operando* fast response on the microscale. This allowed *in-operando* observation of nanothermite reactions at high enough resolution to perceive particle-sized phenomena such as reactive sintering in action. Using an innovative experimental setup consisting of a microscope objective coupled to a high-speed video camera, Al:CuO nanothermites are initiated showing a noticeable flame front of ~30 μm with a measured temperature of 3000 K, concordant with known Al:CuO reaction temperatures.

More importantly, reactive sintering was clearly evidenced in postmortem SEM images showing sintered particles of a mean diameter of ~20 μm, approximately three orders of magnitude greater than the initial particle size, after the flame front passes. Defined by a prominently apparent bright area, the sintering zone is found to match in dimension with the flame front, implying that the propagation of the reaction is carried by advection of heat produced by networks of sintering particles. The authors develop a relation between the sintering zone (D_r) and the final sintered size (or the diameter of the cooled area, D) such that $D \sim 0.69 D_r$ with an aggregate theoretical packing density of 33%, resulting in a three times decrease in volume.
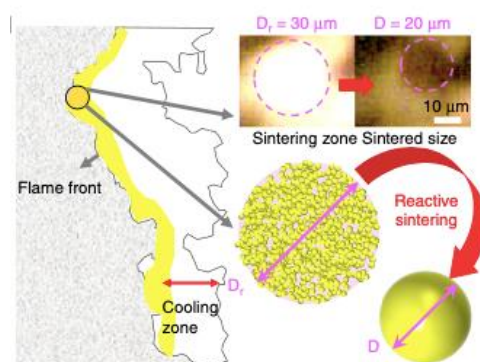
Figure 1.15 : Coupled analysis of post-mortem SEM images to a schematic showing the spatiotemporal relationship of sintering to the overall reaction propagation (from right to left) of Al:CuO powder combustion. **[44]**

Successfully coupling the position from the high-microscopy setup into SEM imaging for postmortem analysis, individual particles are studied and found to complete sintering within ~170 μs with a subsequent cooling period of ~350 μs. One sintered aggregate, principally composed of Al$_2$O$_3$ with smaller Cu particles, corresponds to the high-microscopy measured

sintering zone of ~30 μm. The propagation of the reaction zone of sintering is found to be larger and significantly quicker, ~50 cm/s, than the overall macroscopic flame propagation at 3.3 cm/s. This is best explained by the macroscopic propagation being limited by the thermal diffusivity between the sintered aggregates. Thus, the authors define a three-stage inhomogeneous macroscopic reaction front with different heat fluxes including the sintering, cooling, and final sintered product phases. Through tracking ten different points, a clear reactive sintering stage is apparent through flame front position jumps in a near-step function, as well as slight retractions as cooling begins and the spatial range is reduced.
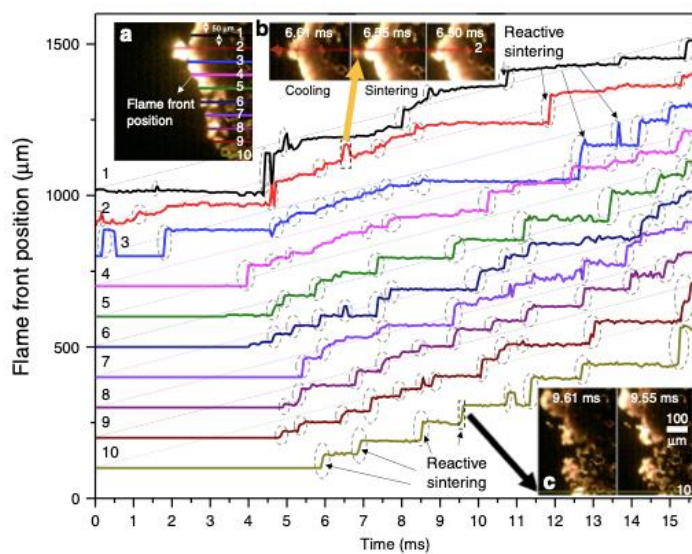
Figure 1.16 : Time-resolved flame front position extrapolated from post-mortem SEM images with annotations of major reactive sintering events. **[44]**

Overall, the past decade of research into the dominant mechanisms for initiating nanothermites has disproved the Melt Dispersion Method as a probability, while confirming diffusion mechanics and drawing a consensus that reactive sintering is apparent for all nanothermite pairs. This has interesting consequences on our understanding of the reaction characteristics' dependence on nominal particle size, instead implying that formed aggregate size and the degree of mixing may play a more important role, regardless of the external heating rate. While gas produced during initial heating likely still contributes to the initiation of the material for highly gaseous species, condensed phase mechanisms are sufficient for initiating most nanothermites.

1.4   Existing Approaches of Modelisation

Computer modeling is of particular importance in the energetic materials domain due to the potential danger in handling of the materials, particularly when interested in exploring new possible compositions. In addition to predicting performance, simulations can be used to investigate fundamental mechanisms or improve theoretical understanding of the reaction initiation, particularly to investigate the effect of experimentally observed phenomenon, such as reactive sintering as will be seen in this manuscript. It is important to choose a model scale

and method best adapted to the particular interest of the study. Models can be divided into macroscopic, microscopic, that spans from the atomic to the nanoscale, or mesoscopic groups, where each scale tends towards certain theoretical methods and uses, and each with their own advantages and disadvantages. Macroscopic models provide a full-system view, where the reaction is usually discretized into finite elements and characterized by thermo-chemical equations. At the other end of the spectrum, Molecular Dynamics (MD) and Density Functional Theory (DFT) are commonly used atomic-scale techniques that allow observation of microscopic phenomena, but severely limit the scope of the analysis at high computational cost. Mesoscopic models attempt to bridge the advantages and limitations of these divisions by exploring length-scales and time-scales that fall between atomistic and macroscopic scales.[102] Generally, there are three approaches to generate a mesoscopic model: 1) bottoms-up approach by adapting microscopic behavior into a larger scale model such as a Monte Carlo, which can limit the clear definition of the atomistic problem, 2) top-down approach through embedding by considering an inner region with great precision and an outer region with simplified treatment, 3) a phenomenological model that identifies building blocks based on observed features.

Combustion models of energetic materials exist in all three domains; however, they are generally not suitably adaptable to thermite reactions, which exhibit significantly more complex chemistries due to adiabatic temperatures over 2793 K that must account for melting, boiling and vaporization of reactants. On the macroscale, thermochemical codes such as CHEETAH[47,103] or NASA-CEA[46,104] are commonly utilized in both academic and industrial applications. As previously noted, these types of simulation rely on equilibrium thermodynamic estimates where the reaction is assumed to be completed. While adequate tools for the prediction of performance, there is a lack of consideration for the mechanisms at play that permit a fundamental study of the initiation and propagation reactions. Continuum-based simulations[105] begin to take into account the intricacies of reaction mechanics, but at very high computational cost. Some of these models can start to adopt mesoscopic principles, simplifying the macroscopic reaction while concentrating on one microscopic event, but still see limitations on the overall system size due to the complexity of the numerical methods utilized. On the microscale, molecular dynamics simulations[106] are also extremely expensive in terms of computing time and, thus, are most effectively utilized to investigate a single mechanism on smaller timescales. In the following two subsections, the principal modeling approaches to date at the atomic scale and, more recently, the mesoscopic scale are detailed.

1.4.1 Atomic scale

Density Functional Theory (DFT) and Molecular Dynamics (MD) are the most advanced techniques that allow a complete view of all combustion phenomena at the atomic scale. These approaches have primarily been applied to bi-metallic systems where many classical interatomic potentials were available from trustworthy publications.[107,108]

Simulations at the atomic scale have grown significantly in popularity as tools in material design as software packages based on Quantum Mechanics (QM) have become more accessible.

Conversely, this type of modeling is extremely expensive in terms of computing cost and resources, which leads to severe limitations on the scale of the simulation. This, of course, restricts the possibility of gaining a theoretical understanding of the key factors at play, as it restricts the ability to evaluate the dynamic evolution of the entire system. In recent years, atomic scale simulations have been optimized by using empirical force fields trained by QM structure and energy data that drastically reduce the computational cost. The original implementation of this idea is best suited to nonreactive interactions, yet insufficient for calculating changes in atom connectivity. In 2016, Senftle et al.[109] developed a reactive force-field (ReaxFF) that incorporates connection-dependent terms in the force-field definition that is capable of realizing reactive events through a bond-order formalism. This method allows an implicit treatment of reaction chemistry without explicitly considering QM, reducing computational costs in exchange of accuracy and increased simulation scale.

Thus, to simulate thermites, in which chemical reactions (redox) occur, it is necessary to utilize reactive force fields to avoid "heavier" ab initio MD calculations. Such modeling approaches have been employed with $Al:NiO$ and $Al:SiO_2$ thermite couples to study initiation of the reaction as a function of composition and structural aspects.[110,111] A DFT-based MD study looked at an $Al:Fe_2O_3$ multilayer system, with particular focus on the atomic scale mechanisms responsible for initiation in the reaction zone.[112] More recently, Xiong et al.[113,114] investigated the interface reaction processes of the $Al:CuO$ thermite at high temperatures through an ab initio MD simulation, as well as the transport mechanisms of interior oxygen atoms.

It is important to note that ab initio Molecular Dynamics remains limited to a duration on the order of a few tens of picoseconds (ps) while considering only a few thousands of atoms. The implementation of reactive force fields increases the scale to the nanosecond regime with a capacity to simulate significantly more atoms. Despite this optimization, the typical orders of magnitude relevant to thermite combustion are larger still, with initiation falling on the order of the millisecond regime and combustion fronts that reach the microscale in size. Ultimately, Molecular Dynamics is best suited to provide a detailed view of atomic scale processes, but full combustion simulations require continuum-level methods.

1.4.2 Mesoscopic

Over the past decade, the NEO team here at LAAS-CNRS has taken strides to probe the initiation process and overall behavior of different thermites (materials, format, and applications, etc.) through various model developments with complex mechanistic study at low computational cost.[48,49,115–120]

A first doctorate study by V. Baijot[115] established a gas-phase based model for $Al:CuO$ powder-based thermite combustion beginning with a local thermodynamic equilibrium model to calculate the production of gas during the reaction[116] and later extended to a micro-kinetic model predicting temperature, pressure, and species evolution of various Al-based thermites.[49,121] The original thermodynamic model considers a stoichiometric mixture with the

assumption that a local thermodynamic equilibrium, such as that assumed in the treatment of irreversible processes, is temporarily reached at each degree of completion of the reaction, defined as the extent of reaction, ζ. The global equilibrium is exclusively achieved at the end of the entire reaction. Thus, this local thermodynamic equilibrium assumption can be formulated as:

$$\frac{2b}{3}Al + M_aO_b \rightarrow \frac{b\zeta}{3}Al_2O_3 + a\zeta M + (1 - \zeta)\frac{2b}{3}Al + (1 - \zeta)M_aO_b \qquad (1.9)$$
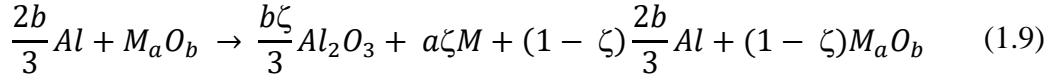
where M_aO_b is the metal oxide corresponding to the metal M with valency *2b/a* and ζ gives the fraction of thermite converted, while (1 - ζ) remains in unreacted form. Phase changes including melting, boiling, decomposition and condensation of alloys and oxides are taken into account using formation free energies from literature where values are adjusted for high pressure environments for gaseous species *i* through the relation :

$$P_i(T) = K_i \; x \; T^{\frac{3}{2}} \; x \; exp^{(\frac{\Delta U_i}{k_B T})} \qquad (1.10)$$

with $P_i(T)$, the partial pressure at temperature *T*, ΔU_i the vaporization energy, k_B the Boltzmann constant, and the pre-exponential factor K_i given theoretically by:

$$K_i = \frac{\sqrt{2\pi m_i k_B^3}}{s_i h} \qquad (1.11)$$

where m_i and s_i are the molecular mass and the surface unit cell area in condensed phase of species *i*, respectively, and *h* is the Planck constant. This formulation of the constant K_i can be calculated by equating the chemical potentials of species in the gas phase and the condensed phase or from experimental values of partial pressures at low temperatures, as used in this case due to the lack of accounting of the vaporization mechanism in the theoretical formulation.

All gases are considered to adhere to the perfect gas law, as the conservation of energy is utilized to calculate the temperature evolution as a function of the extent of reaction ζ where the exothermic reaction produces $Q_0 = \zeta(\%TMD)Q$ for the specific heat of reaction *Q*. Thus, the total heat required to heat the system from ambient T_0 to temperature *T* is:

$$q(T) = \int_{T_0}^{T} [C_v(T) + h(T)] \, dT \qquad (1.12)$$

$C_v(T)$ is the temperature dependent heat capacity for the system and the latent heat, $h(T)$, is a series of Dirac delta functions for all phase transitions, while all heat losses are neglected.

Simulations are thus completed by discretely increasing ζ, the extent of reaction, until the reaction has been completed. At each step, the released heat Q_0 is evaluated, followed by the calculation of the partial pressures of each species using Equation 1.10, with the composition determined by the perfect gas law. The vaporization heat is then calculated and applied to $q(T)$. When applied to Al:CuO thermites, the following pressures are determined as a function of the extent of reaction for different %TMD:
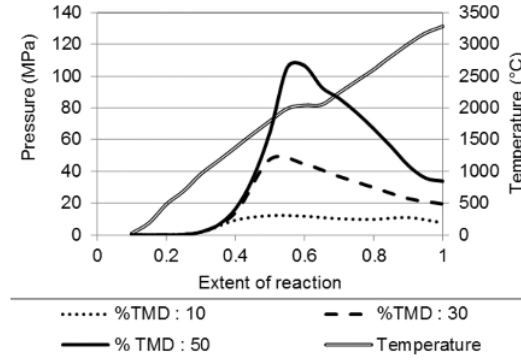
Figure 1.17 : Similated results of gas production as a function of the extent of the reaction, ζ, for an Al:CuO thermite from a model based on gas-phase mechanisms. **[116]**

This thermodynamic consideration was then combined with micro-kinetic diffusion, interphase exchange mechanisms, and DFT-based rate equations to predict temperature and pressure evolution as well as material compositions at low computational cost.[49] In this phenomenological model, the Al:CuO reaction is considered with multi-phase mechanisms including the diffusion of Al particles through the alumina shell towards the surface, where it then evaporates and either reacts in the gas-phase with gaseous oxygen or condenses on and reacts with the oxide particle. Freed oxygen from the reduction of the oxide species similarly reacts either by gas-phase mechanisms or through a gas surface exchange with the aluminum particle. All considered reactions are given in the following equations:

$$Al_{(sf)} \leftrightarrow Al_{(g)} \tag{1.13}$$

$$2Al_{(sf)} + \frac{3}{2}O_{2(g)} \rightarrow Al_2O_{3\,(c)} \tag{1.14}$$

$$Al_2O_{3\,(c)} \rightarrow 2Al_{(g)} + \frac{3}{2}O_{2(g)} \tag{1.15}$$

$$Al_xO_{y\,(g)} \rightarrow Al_2O_{3\,(c)} + Al_{(g)} or\, O_{2(g)} \tag{1.16}$$

$$2Al_{(g)} + 3CuO_{(c)} \rightarrow Al_2O_{3\,(c)} + 3Cu_{(c)} \tag{1.17}$$

$$2Al_{(g)} + 3Cu_2O_{(c)} \rightarrow Al_2O_{3\,(c)} + 6Cu_{(c)} \tag{1.18}$$
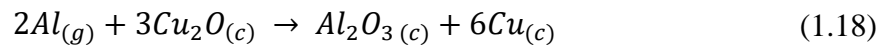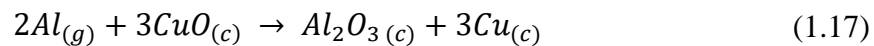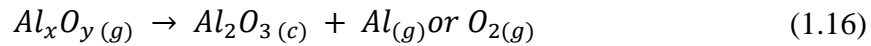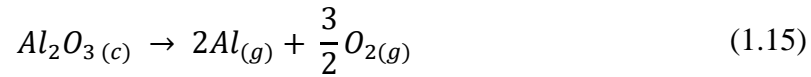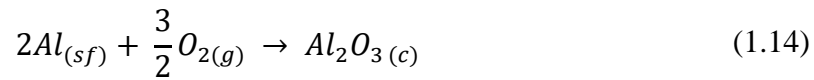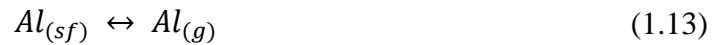
The primary beneficial results from this model include a study of the effect of the main parameters of reaction on the production of gas.[49] In Figure 1.18, the gas generation as a function of %TMD (Figure 1.18a) and the stoichiometric ratio (1.18b) are presented for a system of Al (100 nm) and CuO (240 nm) nanoparticles. The initialization procedure of the model, heating the system at a constant rate to a final temperature from room temperature, introduces a bias in respect to experiments where the system is initiated by a hot spot, causing overestimations in the pressure and temperature evolution. Thus, a correction was implemented to recalibrate the results that were then compared to experimental studies. The renormalized pressures in Fig. 1.18a are in good agreement with the experimental data. Better estimates may be possible by accounting for heat losses that would decrease the final temperature and pressure of the system.

As previously stated, many open air burn experiments have shown that the use of Al-rich mixtures improves the thermal properties of the reaction. In this configuration, ambient oxygen likely leads to an increase in performance that should not be seen by closed tube experiments. Thus, the effect of compaction on the movement of liberated oxygen from the reduced oxide was tested by comparing pressure generation for 1%TMD and 10%TMD thermites as a function of the stoichiometric ratio. For most compaction rates, the highest gas production is observed at the stoichiometric ratio ($\xi = 1.0$); however, the peak shifts for compaction lower than 1% TMD as only 2.7% of total oxygen present in the chamber comes from the ambient environment.
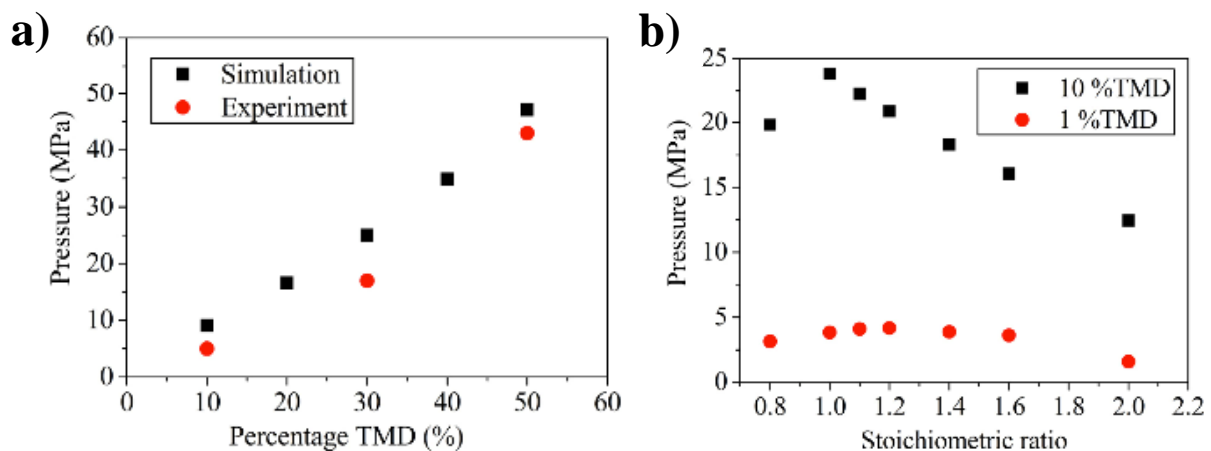
Figure 1.18 : Results of the pressure generated by an Al:CuO thermite system (100 nm, 240 nm respectively) as a function of a) the compaction rate (%TMD) and b) the stoichiometric ratio (ξ). **[49]**

This model also provides an overview of the temporal evolution of the reaction. Figure 1.19 presents simulated results for a system of 100 nm Al, with a 4 nm oxide shell, and 240 nm CuO nanoparticles. The mixture density is set to 50 %TMD with the rest of the simulated volume filled with oxygen at 20 kPa. The system is then heated at a constant rate of 2×10^6 K/s until reaching 1200 K. Analysis of the reaction illuminated five explicit stages of reaction:

1) The system is externally heated until the maximum temperature of 1200 K is achieved.

2) After the initial uniform heating, the temperature nearly plateaus, with only a slight 200 K increase in temperature as the diffusion of Al across the native shell is too low to allow significant Al oxidation; however, CuO decomposition continues.

3) At 1400 K (~0.65 ms), the Al diffusion outwards increases, increasing oxidation and causing a drastic temperature increase as the runaway reaction begins. The pressure simultaneously experiences a first slight increase before a rapid drop where the local maximum pressure corresponds to a large reduction of CuO into Cu_2O.

4) At 3100 K (~0.78 ms), the oxidation of the fuel outpaces the release of oxygen by decomposition. The aluminum begins to evaporate significantly, opening the oxidation to both condensed (on the surface) and gas phase pathways. This continues until alumina decomposition at the maximum temperature of 3524 K.

5) The decomposition of alumina stops the temperature increase and the system reaches a final equilibrium. At this point, the pressure is maximal at 111 MPa.
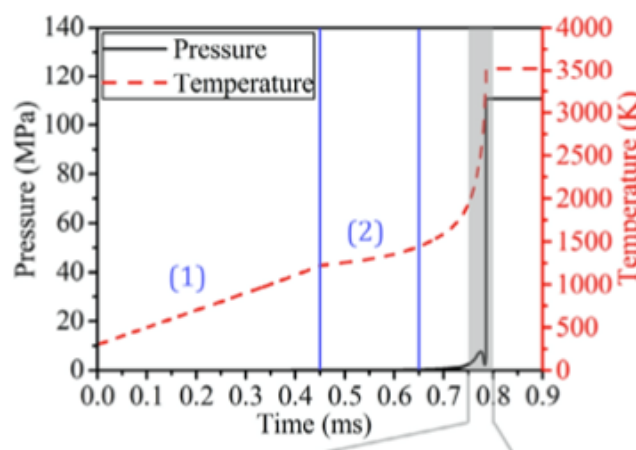
Figure 1.19 : The evolution of the temperature and pressure for an Al:CuO nanothermite (100 nm and 240 nm, respectively) at 50 %TMD displaying five explicit stages of reaction. **[49]**

Only a few modeling attempts have been proposed to extend a simple continuous approach developed for bimetallic reactives[122] based on the sandwich theory where overall mass transport and reaction is assumed to follow a single Arrhenius dependence on temperature, independent of the detailed chemical composition.

In this view, a second work began in 2016 completed by G. Lahiner[118] to develop a diffusion-based model of the ignition and self-propagating reaction in Al:CuO multilayered thin films. These thin film nanothermites, also known as a reactive multilayer, are composed of alternating nanoscale thick layers of at least two reactants, a metal fuel and the oxide, prepared by either a mechanical process or physical vapor deposition. Nanolaminates are particularly useful as micro-initiators[123–125], exploding foil initiators[126], and MEMS heat sources. While some experimental characterizations have demonstrated the effect of factors like the composition, amount, or thicknesses of the bilayers on the thermite performance, this was the first numerical tool designed to predict initiation and propagation behavior of thin film nanothermites. In this formulation, the microscale chemical reactions and mass transport mechanisms are coupled with the heat equation to evaluate the temperature evolution and account for heat losses on the macroscale. The chemical processes include the oxide

decomposition and the fuel oxidation, CuO and Al in this case, while considering the diffusion of oxygen atoms through Al_2O_3 and Cu_2O which drives the exothermic reaction.

The model is based upon the diffusion-reaction scheme developed by Deal and Grove[127] in 1965 for the thermal oxidation of silicon. In this framework, the diffusion mechanisms are treated as fluxes, which does not assume a certain mode migration (capillarity through grain boundaries, Fickian process, electromigration, etc.) As such, a one-dimensional diffusion/reaction scheme along the vertical axis is coupled with a one-dimensional thermal model along the propagation axis. This approach assumes a constant temperature within the vertically discretized layer structure, which is justified by the difference of an order of magnitude between the mass diffusivity in alumina ($< 10^{-8}$ m^2s^{-1}) and the lowest thermal diffusivity in the system, CuO (2.5×10^{-7} m^2s^{-1}). Due to computational costs, the system is discretized according to thermal diffusivity, neglecting diffusion between adjacent elements. The considered two-step reaction is as follows:

i)   CuO decomposes into Cu_2O at low temperature and the freed oxygen atoms diffuse across the interfacial layers to oxidize the Al layer nearest the interface, increasing the thickness of the alumina layer.

ii)   The remaining Cu_2O decomposes into its final product, Cu, and frees more oxygen atoms to further oxidate the Al.

During this process, phase transitions including melting and vaporization are taken into account. As the adiabatic reaction temperature, around 3136 K with phase changes, is well above most vaporization temperatures for the system's species, a vaporization temperature limit is imposed at 2090 K. This corresponds to the vaporization temperature of Cu_2O, the lowest in this system, where the nanostructure is lost, dispersing the materials into the ambient environment and favoring a gas-phased reaction, which is not considered in this model. The simulation is reduced to one half of an Al:CuO bilayer due to the periodic symmetry of the layers along the thickness. The flux approximation of mass conservation for the first step of reaction is given by:

$$\emptyset = \frac{D_{Cu2O}(C_{CuO/Cu2O} - C_{\frac{Cu2O}{Al2O3}})}{w_{Cu2O}} = \frac{D_{Al2O3}(C_{Cu2O/Al2O3} - C_{Al2O3/Al})}{w_{Al2O3}} = v \times C_{Al2O3/Al} \quad (1.19)$$

with $C_{i/j}$ the atomic concentration of oxygen at the interface between species i and j, D_i the diffusion coefficients of oxygen in species i, and w_j the thickness of layer j. This is directly equal to the speed of oxidation, v, at the interface between Al and the oxidized alumina as a function of the freed oxygen concentration at this barrier. This oxidation reaction rate is fixed at 3000 m/s, as it has been experimentally shown that the oxygen diffusion, and not the oxidation, is the limiting factor in thermite reaction. An Arrhenius law is applied to calculate the diffusion coefficients at temperature T, given the following prefactors and activation energies: $D_{Al2O3} = 9 \times 10^{-5}$ m^2s^{-1}, $D_{Cu} = D_{Cu2O} = 1.16 \times 10^{-6}$ m^2s^{-1}; $E_{a\ Al2O3} = 140$ $kJmol^{-1}$, $E_{a\ Cu} = E_{a\ Cu2O} = 67.3$ $kJmol^{-1}$. The values for copper-containing species were taken from a 1983

study of diffusivity in solid copper[128] and the alumina values were reported experimentally by Egan *et al.*[129]

The coupled thermal equation accounts for heat diffusion, exothermic thermite reaction, external input power, and heat losses by radiation, convection, and conduction through the substrate, respectively, in the following equation:

$$\frac{dH(x,t)}{dt} = \lambda_t \frac{d^2T(x,t)}{dx^2} + \frac{\phi \, x \, Q}{w/2} + \frac{P}{w_t} - \frac{\sigma(T^4(x,t) - T_a^4)}{w_t} - \frac{h_c(T(x,t) - T_a)}{w_t}$$
$$- \frac{\lambda_s}{w_t \, x \, w_s}(T(x,t) - T_a) \tag{1.20}$$

The thermal conductivity for the substrate, λ_s, can range from 0.1 to 100 W.m$^-$1.C^{-1} depending on the substrate material choice (polymer, glass, ceramic, highly conductive, etc.)

Finally, the total enthalpy, H, at position x at time t can be expressed as:

$$H(x,t) = H_{amb} + C_t(T(x,t) - T_{amb} + \sum_{T_i > T_{amb}} h_i \theta(T(x,t) - T_i) \tag{1.21}$$

where H_{amb} is the enthalpy at ambient temperature, T_{amb}, C_t is the average heat capacity of the film in J.m^{-3}.C^{-1}, and the final term is the Heaviside step function for the phase change with enthalpy h_i per unit volume undergoing the transition.

This model was then applied to predict the reaction performance of Al:CuO nanolaminates with high accordance with experimental values. Once validated, the tool was utilized to investigate the effect of bilayer thickness on the nanothermite performance. In Figure 1.20, the resultant steady-state propagation speed is presented as a function of the initial alumina barrier thickness (Fig. 1.20a) and the stoichiometric ratio (Fig. 1.20b). Both curves show a clear inverse relationship, with a steady decrease in propagation speed as the bilayer thickness increases. The propagation velocity reaches a maximum of 6 to 10 m/s at a bilayer thickness of approximately 25 nm, then sharply decreases caused by a lack of sufficient chemical energy with respect to the total heat capacity of the films. After this critical value (w > 25 nm), the surface contact area is the primary parameter to drive the performance: reducing the thickness of the bilayer increases the surface contact area and, thus, the reaction front velocity. The initial alumina thickness is shown to heavily influence the reaction characteristics. The propagation velocity is decreased by nearly half when the alumina thickness is multiplied by a factor of 4 (from 2 to 8 nm).

In regards to the stoichiometric ratio, the reaction front shows some performance improvements as the structure is moved into a fuel-rich regime. This is likely due to the high thermal conductivity of Al. As more Al is included in the overall system, the multilayer becomes more thermally conductive, aiding in the propagation of the reaction.
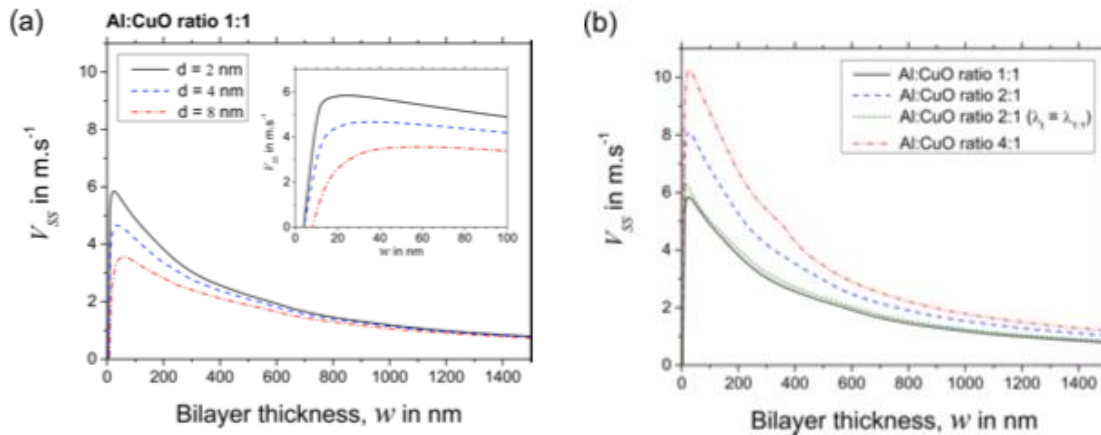
Figure 1.20 : Results of the reaction front propagation speed at steady state as a function of bilayer thickness (nm) as well as a) the initial alumina barrier layer thickness, and b) the stoichiometric ratio. **[48]**

Then, a novel study of the lifetime of these thermites was completed by simulating DSC experiments at low temperatures for extended time periods. In a recent work, Estève *et al.*[119] investigated the energy loss of an Al:CuO multilayer over time. Results from one of these tests is illustrated in Figure 1.21. First, Al:CuO multilayers were tested on their energy loss under 200°C aging conditions for 14 days. In Figure 1.21a, the temporal profiles are presented as a function of the stoichiometric ratio, attained by altering the bilayer thicknesses. As the stoichiometry increases, the percentage of energy loss decreases due to the fact that the reaction enthalpy is maximum at the stoichiometric ratio ($\xi = 1.0$) and decreases for fuel rich conditions. Figure 1.21b displays the temporal profile under the same conditions as a function of the bilayer thickness, while the stoichiometric ratio is held constant at $\xi = 2.0$. After 14 days, there is a large variation in energy loss from 5 to 40 % as the bilayer thickness decreases. Regardless of the bilayer thickness, the quantity of Al consumed to grow the amorphous alumina interface remains constant. As such, the increase in Al quantity in the nanolaminate dimishes the impact of interface evolution and aging.
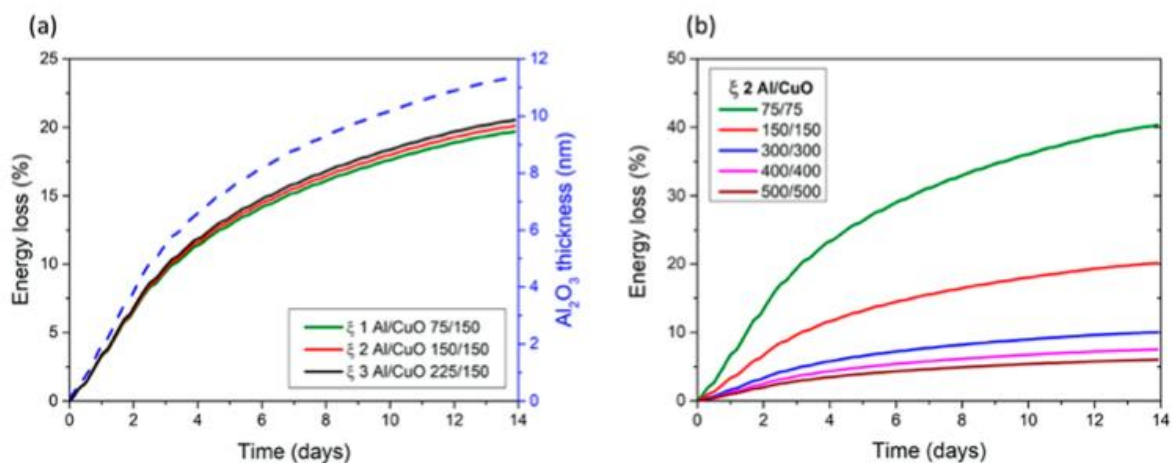
Figure 1.21 : Results of the aging study on the Al:CuO nanolaminate as a function of a) the stoichiometric ratio, and b) the bilayer thicknesses for a system at constant stoichiometry $\xi = 2.0$. **[119]**

This previous section presented the current simulation tools available in the nanothermite domain. At the macroscale, the majority analyze and predict the reaction based on thermochemical reaction rates which ignore the importance of geometry-based mechanisms

(*i.e.,* particle-based vs. bilayers). In general, macroscale approaches to nanothermites neglect an important degree of detail of the nanostructured components that has clearly been shown experimentally to affect thermite performance. On the other extreme, atomic scale simulations such as Molecular Dynamics concentrate exclusively on microscale dynamics, which make them difficult to extrapolate to macro timescales allowing full reaction simulation without extremely high computational cost.

New models on the mesoscale, combining the benefits of microscale mass transfer principles on macroscopic timescales begin to provide the information required for academic and industrial use. However, each model until now has either focused on gas-based mechanisms or certain nanostructured materials, like nanolaminates. With the recent discoveries of hypothesized mechanisms in nanothermite reactions, for example, reactive sintering, the need for a new generalized model based upon these observed condensed phase mechanisms in powder-based nanothermites is evident.

1.5   Conclusion

The past three decades have experienced a huge innovation in nanotechnology, both in theoretical understanding and practical manufacturing methods. The growth of this industry has consequently led to a mounting interest in nanothermites with novel applications demanding new material couples and computational tools to allow investigation into material design.

This chapter has presented the current state of the nanothermite domain. First, the basis for the reaction, the available methods of fabrication and mixing, and the importance of certain key parameters was explored. In a second part, more hypothetical works at the heart of the community debate on the dominant mechanisms and pathways of this reaction, hoping to augment the understanding and, therefore, manipulability of these systems was explained. On a whole, there is ample evidence that reactive sintering is a likely contributor to the self-sustaining thermite reaction, whereas recent works have mostly disproved the likelihood of a spallation type mechanism as the driving force. Finally, different modeling approaches currently available in the industry have been discussed, including the formulations, limitations, and exploitations of these numerical tools.

As the studies on reactive sintering are relatively new, none of the current simulations take into account this mechanism. Thus, this thesis aims to address this deficiency in analytical tools. The principal goal is to present a generalized efficient model for the initiation and propagation of nanoparticle-based thermites in powder form. Thermite couples with low gas production are of particular interest, as the importance of condensed phase mechanisms is more apparent. Given the growing demand for low-gas nanothermites for applications in the aerospatial, mining, and other domains, in addition to increasing research into thermites using new material species, the development of a phenomenological model with abstraction for customized species input is vital. This new model should allow easy comparison between

innovative thermite couples. However, a mesoscopic model also permits a view of the fundamental intermediate reactions and kinetics of this reaction. Therefore, this work is then exploited to investigate the newly postulated reactive sintering mechanism for initiation, in comparison to gas-phased driven reaction. The final goal is a study of the possible paths of heat transfer for propagation of these self-sustained reactions in condensed-phase dominant thermite couples, and the influence of common parameters of reaction on the complete thermite reaction. To accomplish this, a novel application of the Deal and Grove diffusion-reaction to spherical nanoparticle-based thermites is developed.

CHAPTER 2. Model Development & Mathematical Formulation

2.1 Introduction

In the previous chapter, after a presentation of the state of the art of current works in the nanothermite domain, different physico-chemical models were detailed, in addition to an overview of the possible reaction mechanisms at play for nanothermite initiation. It was noted that there is an undeniable lack of theoretical works in comparison with experimental studies, likely due to the complex mechanisms in a thermite reaction. Unfortunately, the models developed during the last 50 years for energetic materials such as CHNO are not applicable for thermites because of the completely different chemistry and behavior of these reactions. In what concerns thermite materials, pure condensed phase models were applied to nanolaminate structures. Emanating from bimetallic systems studies[131], first attempts involved very crude treatment of the chemistry driving the combustion, gradually evolving to develop models with more realistic oxido-reduction reaction mechanisms, which allowed predictions of initiation, propagation, as well as aging.[119] In systems composed of nanoparticles, after several conceptual proposals for the reaction fundaments (mostly gas phase versus condensed phase mechanisms), a micro-kinetic model was proposed in which gas phase reactions drives the overall thermite combustion.[49] This already complex zero dimensional model allowed simulation restricted to the prediction of pressure generation in closed vessels (using mixed Al/CuO nanoparticles), as propagation would require to extend the model to fluid dynamics considerations.[115,116] In view of the growing demand from emerging applications making use of nanoparticles for simple models allowing design parameter testing, this work proposes to establish a model formulation, as derived from previous work on nanolaminate systems. This formulation will focus on condensed phase mechanisms, with the goal to provide both fundamental exploration and predictive abilities for the entire self-sustaining combustion reaction. The objective of the model is not to quantify the combustion speed with accuracy, but rather to elaborate the general trends for flame propagation behavior in order to make an initial evaluation of design performance. It is clear that further progress in the comprehension of these reaction mechanisms is still required to develop more realistic and predictive physical models. The advent of advanced characterization techniques such as the direct observation of flame dynamics[41,44] will hopefully accelerate the speed of advancement in fundamental understanding.

Importantly, the proposed novel formulation considers, for the first time, the recent discovery of reactive sintering, and allows prediction of both the initiation and propagation of the combustion reaction. Additionally, explicit definition of parameters of interest, including diffusion coefficients, thermal conductivities, and degree of sintering, can provide clear information on their resultant effects on the reaction.

This chapter will elucidate the mathematical formulation of the model created to accomplish these goals. First, a study of the original basis of the flux approximation by Deal and Grove is presented. Next, the application of this theory to the specific powder-based nanothermite case is elaborated beginning with the base unit – a sintered pairing of a fuel and oxide particle. This first described implementation couples the diffusive flux of oxygen driven mass transfer and subsequent exothermic oxidation of the fuel with the heat equation and provides information on the initiation of a particle-based thermite reaction. Subsequently, a full burn-tube type apparatus formulation is presented where the system is fully homogeneously populated with identical base units and propagation is simulated. The description includes a discussion of different possible formulations of the macroscopic mechanisms that drive propagation.

2.2   Overview of the Deal and Grove Flux Approximation

In a 1965 paper by B.E. Deal and A.S. Grove, the authors proposed a simple model expressing the kinetics of the oxide layer growth associated with the thermal oxidation of silicon.[127] Even though the oxidation of silicon is a very exothermic reaction, similar to a conventional thermite reaction, this initial formulation was restricted to the diffusion-reaction scheme of the species, thus omitting the thermal piece. This was due to the fact that the oxidation was operated at high temperature ($> 1000°C$), without leading to a subsequent self-sustained reaction. In the context of microelectronics, the study was found to highly agree with experimental oxidation data on the grown oxide layer thickness for a wide range of temperatures.

The proposed formulation assumes movement of a species of oxidant that must go through three phases:

1) Transportation from the oxidizing atmosphere to the outer silicon surface where it reacts or is adsorbed.
2) Transportation across the growing oxide film towards the inner core silicon.
3) Reaction at the silicon interface to form a newly oxidized layer.

With the assumption that the initial transient period of oxidization has already passed, the oxidant flux (in mol of oxidant/unit time), F, at each of the three stages are identical at all times. A concentration of oxidant can then be determined at each phase interface creating a concentration gradient across the system. A linearized approximation to the transport rate with gas-phase transport coefficient, h, gives the flux from the gas environment to outer surface as

$$F_1 = h(C^* - C_0) \tag{2.1}$$

where C_0 is the concentration of oxidant at the outer surface and C^* is the equilibrium concentration of the oxidant in the oxide.

The flux across the oxide layer, currently positioned at $x_o(t)$ is then given by Fick's law as

$$F_2 = -D_{eff}(dC/dx) \qquad (2.2)$$

at any point x within the layer (x being the growth direction) with the effective diffusion coefficient, D_{eff} and the concentration gradient along the axis of reaction, dC/dx.

Finally, the oxidation reaction, of rate k, at the silicon surface gives a flux of

$$F_3 = kC_i \qquad (2.3)$$

Due to the steady-state condition, flux is constant across the system, leading to a resolved system of equations to calculate the flux.

$$F = F_1 = F_2 = F_3 = \frac{kC^*}{1 + \dfrac{k}{h} + \dfrac{kx_o}{D_{eff}}} \qquad (2.4)$$

At certain limits, the reaction is "diffusion controlled" as the diffusivity becomes very small relative to the rate constants (as $D_{eff}/kx_o \to 0$, $C_i \to 0$, and $C_0 \to 0$.) Thus, the growth of the oxide layer, for N_1 oxidant molecules incorporated into a unit volume of the oxide layer, is described by

$$\frac{dx_o}{dt} = \frac{F}{N_1} = \frac{kC^*/N_1}{1 + \dfrac{k}{h} + \dfrac{kx_o}{D_{eff}}} \qquad (2.5)$$

In the following adaptation of this model to the problem of a two-particle system, one fuel particle and one oxidizer particle, the first phase of the above-described process is considered to occur within the oxidizer nanoparticle. The liberated oxygen is then transported to the native oxide shell of the fuel particle. It is then identically transported across the oxide layer where the final flux oxidizes the fuel material, leading to the exothermic reduction-oxidation reaction. Next, the mathematical reworking of this novel application of the Deal-Grove model to powder-based nanothermites is presented.

2.3 Base Model Formulation

The basis for this model applies the previously described Deal and Grove flux approximation to the diffusion of oxygen in a similar construction to the nanolaminate model created by G. Lahiner[48] (See Section 1.4.2); however, in this model, the equations are adapted to nanoparticles with a spherical formulation. The model considers a base unit, a pairing of one nanoparticle of the fuel species pre-sintered to one nanoparticle of the oxide species. The degree of sintering is defined by a wetting contact angle, θ, such that the pairing contains a

contact interface between the oxide and the native oxide shell of the fuel particle. The system is thus defined by the following input parameters: the material species, the particle sizes or the stoichiometric ratio, the thickness of the native oxide layer, and the degree of sintering. This is demonstrated in Figure 2.1, see the oxide particle of radius R_{ox} and fuel particle of radius R_{fuel}. Reactive sintering causes the particles to coalesce such that their centers are separated by a distance $d_1 + d_2 < R_{ox} + R_{fuel}$ according to the wetting contact angle. In this view, oxygen, which is released through decomposition of the oxidizer, migrates from the oxidizer to the fuel particle where it reacts. Therefore, the initial interface layer between the fuel and oxidizer (denoted as S_{init}) propagates throughout the fuel particle; the associated surface is noted S_{ox} (*i.e.,* where the oxidation reaction occurs) leaving an oxide portion of thickness a_2. Similarly, a front of reduction propagates into the oxidizer particle (noted S_{reduc}, *i.e.,* where the reduction reaction occurs), which creates a reduced oxidizer portion of thickness b_1.

There is a preset of materials available to choose from for common nanothermite materials. For the fuel, aluminum, boron, magnesium, and zirconium are available.
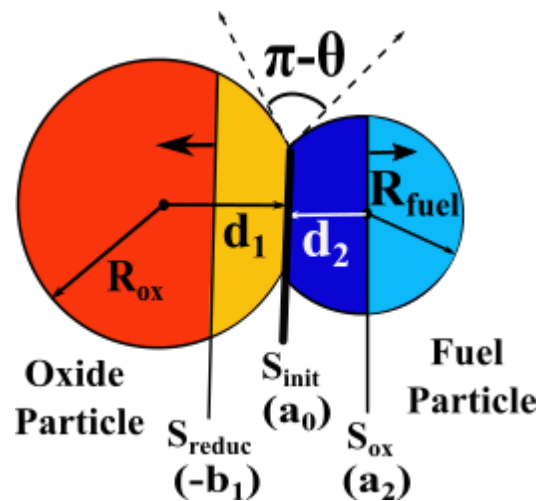
Figure 2.1 : The composition of the base model pairing of one oxide particle and one fuel particle, showing their interfaces and both oxidation and reduction reaction zones.

The provided oxide species include cupric oxide, ferric oxide, tungsten trioxide, and lead tetroxide. To define a species for this system, it is necessary to know the molecular weight, M_w (in kg.mol^{-1}), the density, ρ (in kg.m^{-3}), the melting temperature, T_{melt} (in K), the enthalpy of formation, H_{melt} (in J.mol^{-1}), and the diffusion coefficient of oxygen in the species, $D(T)$ defined by a pre-factor, D_0 (in m^2.s^{-1}), and the activation energy, E_a (in J.mol^{-1}). Additionally, a step index is defined that establishes a one or two-step reduction or oxidation process for the oxides and fuels, respectively. For example, CuO is well-known to undergo a two-step reduction with a first intermediary reduction to Cu_2O, then a final second reduction to Cu.[132] Similarly, some fuel species (not preset in this model software) such as tantalum (Ta) are known to undergo a two-step oxidation.[133,134] There are also some species for which the exact process remains unknown, and, thus, the flexibility to provide an intermediary reduced oxide or oxidized fuel allows the possibility to perform multiple simulations with varying reaction pathways for comparison with experimental results. Thus, the binary step index parameter must

be defined where 0 signifies a one-step process and 1, a two-step process. The relevant values for each species are reported in Table 2.1. Lastly, to fully generalize the overall code for easy adaptation to whatever species is required, one must define the number of atoms in the material molecule (*i.e.,* 5 atoms in one molecule of Al_2O_3) and the reaction coefficient. The latter is defined as the number of moles of the oxidizer required to free one atom of oxygen and moles of reduced oxide created (for oxides) or the number of moles of fuel and the oxidized fuel in complete reaction with one atom of oxygen (for fuels). For two-step processes, a second reaction coefficient must also be defined; in the case of a one-step process, the first and second reaction coefficients are the same. This value comes from the balanced equation for each species' individual reduction or oxidation, as seen in the following equations, and is listed for each preset species in Table 2.2.

$$2Al + 3CuO \rightarrow Al_2O_3 + 3Cu \qquad \Delta H = 397.5 \; kJ/mol \tag{2.5}$$

$$2Al + 6CuO \rightarrow Al_2O_3 + 3Cu_2O \tag{2.6}$$

$$2Al + 3Cu_2O \rightarrow Al_2O_3 + 6Cu \tag{2.7}$$

$$2Al + Fe_2O_3 \rightarrow Al_2O_3 + 2Fe \qquad \Delta H = 281.72 \; kJ/mol \tag{2.8}$$

$$2Al + 3Fe_2O_3 \rightarrow Al_2O_3 + 6FeO \tag{2.9}$$

$$2Al + 3FeO \rightarrow Al_2O_3 + 3Fe \tag{2.10}$$

$$2Al + WO_3 \rightarrow Al_2O_3 + W \qquad \Delta H = 277.58 \; kJ/mol \tag{2.11}$$

$$8Al + 3Pb_3O_4 \rightarrow 4Al_2O_3 + 9Pb \qquad \Delta H = 378.84 \; kJ/mol \tag{2.12}$$

$$2Al + 3Pb_3O_4 \rightarrow Al_2O_3 + 9PbO \tag{2.13}$$

$$2Al + 3PbO \rightarrow Al_2O_3 + 3Pb \tag{2.14}$$

$$2B + 3CuO \rightarrow B_2O_3 + 3Cu \qquad \Delta H = 104.14 \; kJ/mol \tag{2.15}$$

$$2B + 6CuO \rightarrow B_2O_3 + 3Cu_2O \tag{2.16}$$

$$2B + 3Cu_2O \rightarrow B_2O_3 + 6Cu \tag{2.17}$$

$$2B + Fe_2O_3 \rightarrow B_2O_3 + 2Fe \qquad \Delta H = 149.23 \; kJ/mol \tag{2.18}$$

$$2B + 3Fe_2O_3 \rightarrow B_2O_3 + 6FeO \tag{2.19}$$

$$2B + 3FeO \rightarrow B_2O_3 + 3Fe \qquad (2.20)$$

$$2B + WO_3 \rightarrow B_2O_3 + W \qquad \Delta H = 149.0 \, kJ/mol \qquad (2.21)$$

$$8B + 3Pb_3O_4 \rightarrow 4B_2O_3 + 9Pb \qquad \Delta H = 244.29 \, kJ/mol \qquad (2.22)$$

$$2B + 3Pb_3O_4 \rightarrow B_2O_3 + 9PbO \qquad (2.23)$$

$$2B + 3PbO \rightarrow B_2O_3 + 3Pb \qquad (2.24)$$

$$Zr + 2CuO \rightarrow ZrO_2 + 2Cu \qquad \Delta H = 394.26 \, kJ/mol \qquad (2.25)$$

$$Zr + 4CuO \rightarrow ZrO_2 + 2Cu_2O \qquad (2.26)$$

$$Zr + 2Cu_2O \rightarrow ZrO_2 + 4Cu \qquad (2.27)$$

$$3Zr + 2Fe_2O_3 \rightarrow 3ZrO_2 + 4Fe \qquad \Delta H = 275.52 \, kJ/mol \qquad (2.28)$$

$$Zr + 2Fe_2O_3 \rightarrow ZrO_2 + 4FeO \qquad (2.29)$$

$$Zr + 2FeO \rightarrow ZrO_2 + 2Fe \qquad (2.30)$$

$$3Zr + 2WO_3 \rightarrow 3ZrO_2 + 2W \qquad \Delta H = 248.33 \, kJ/mol \qquad (2.31)$$

$$2Zr + Pb_3O_4 \rightarrow 2ZrO_2 + 3Pb \qquad \Delta H = 370.55 \, kJ/mol \qquad (2.32)$$

$$Zr + 2Pb_3O_4 \rightarrow ZrO_2 + 6PbO \qquad (2.33)$$

$$Zr + 2PbO \rightarrow ZrO_2 + 2Pb \qquad (2.34)$$

It is important to note that certain parameters, like the diffusion coefficient, are not confidently known, especially for nanoparticles. Additionally, studies have proven that the melting temperature is size dependent at the nanoscale[83], therefore the use of bulk values is an estimation. The diffusion of oxygen within the original oxide species or in the initial oxidizer (for two-step reduction) is not important to the reaction, thus these values are not necessary. Likewise, for the final oxide, only the reaction coefficient value is required and, thus, these species are defined in a separate structure. While preset values are provided for the material attributes, it is also possible to customize these parameters, as described in the Software Architecture Document (see Appendix A). The preset values are presented in Table 2.1, including the material species, molecular weight, density, melting temperature, enthalpy of fusion and diffusion coefficients (prefactor and activation barrier).

Table 2.1 : Preset thermal and physical properties of the species provided automatically in the model including molecular weight (M_w) , density (ρ), melting temperature (T_{melt}), enthalpy of fusion (H_{melt}), prefactor (D_0) and activation energy (E_a) for oxygen diffusion in species.

Species	M_W (kg/mol)	ρ (kg/m³)	T_{MELT} (K)	H_{MELT} (J/mol)	D_0 (m²/s)	E_A (J/mol)	Ref
Al	0.027	2.7×10^3	933	10.79×10^3	-	-	[135]
Al₂O₃	0.102	3.95×10^3	1550	17.47×10^3	9×10^{-5}	1.5×10^5	[48,129]
B	0.011	2.34×10^3	2350	50.2×10^3	-	-	[136]
B₂O₃	0.07	2.46×10^3	723	24.56×10^3	2.5×10^{-6}	1.37×10^5	[137]
Mg	0.024	1.74×10^3	923	8.7×10^3	-	-	[138]
MgO	0.04	3.58×10^3	3125	77.3×10^3	1.9×10^{-8}	3.7×10^5	[139]
Zr	0.091	6.51×10^3	2128	16.9×10^3	-	-	[140]
ZrO₂	0.123	5.68×10^3	2988	93.65×10^3	9.73×10^{-7}	2.34×10^5	[141]
CuO	0.08	6.31×10^3	1550	17.47×10^3	-	-	[142]
Cu₂O	0.143	6×10^3	1550	17.47×10^3	1.16×10^{-6}	6.73×10^4	[48,128]
Fe₂O₃	0.16	5.25×10^3	1812		-	-	[143]
FeO	0.072	5.75×10^3	1650		6.3×10^{-2}	4.05×10^5	[139]
WO₃	0.232	7.16×10^3	1743	58.3×10^3	6.8×10^{-2}	1.25×10^5	[140,144]
Pb₃O₄	0.686	9.1×10^3	775		-	-	[145]
PbO	0.223	9.53×10^3	1161		$5. \times 10^{-9}$	9.37×10^4	[146]

One drawback of the base unit formulation of the model is that it limits the ability of the user to completely define the particle sizes and the stoichiometric ratio. With a single pairing of one fuel particle with one oxide particle, a relationship is forced between the particle sizes and their resultant mass equivalence ratio such that:

$$\left({m_{fuel}}/{m_{oxide}} \right)_{sample} = \frac{\rho_{fuel} R_{fuel}^3}{\rho_{ox} R_{ox}^3} \tag{2.35}$$

The subsequent stoichiometric ratio, calculated as the ratio between the mass equivalence ratio of the sample to the mass equivalence ratio of a stoichiometric mixture (as defined in Eq. 1.3), is thus similarly fixed according to the sizes of the materials.

$$\xi = \frac{\left({m_{fuel}}/{m_{oxide}} \right)_{sample}}{\left({m_{fuel}}/{m_{oxide}} \right)_{ST}} \tag{2.36}$$

This differs from an experimental setup where a larger amount of one species can be utilized in the thermite mixture to establish the desired stoichiometry. To account for this, the initialization of these parameters can be accomplished in three ways:

1. Define both species particle sizes and the stoichiometric ratio is calculated according to Equations 2.35 and 2.36.
2. Define the fuel species particle size and the desired stoichiometric ratio, and the oxide species particle size is calculated according to Equations 2.35 and 2.36.
3. Define the oxide species particle size and the desired stoichiometric ratio, and the fuel species particle size is calculated according to Equations 2.35 and 2.36.

The default (if all three parameters are provided by the user) is to consider the user-input fuel particle size and the desired stoichiometric ratio, adjusting the oxide particle size to fit the ratio. This was chosen as the default setting as the stoichiometric ratio has been shown to have a major effect on the reaction mechanics. The fuel particle size was chosen as there is a majority usage of aluminum nanoparticles that are spherical with a small dispersion around its nominal size; on the contrary, oxide particles are often non-spherical with much larger size distributions including large agglomerates.[89] It is, therefore, more logical to adjust the large diversity of oxide particle morphologies into an effective sphere of radius R_{ox} with the same relative quantity of material.

The thickness of the oxide shell establishes both the molar quantity of native oxide in the system, as well as the geometric placement of the native oxide/fuel interface. Finally, the degree of sintering is defined as a wetting contact angle in radians. The default angle is $\theta =$ 2.356 (135°) corresponding to TEM images from the original works on reactive sintering by Egan *et al.*[85], where a survey of imaged particles shows a tendency towards this degree of sintering. It is important to note that only convex-convex wetting is considered in this model, thus the angle must fall in the range $90° < \theta < 180°$.

After the initialization of the system, the geometry is described by the relations below:

$$d^2 > R_{ox}^2 - R_{fuel}^2 \tag{2.37}$$

$$d = d_1 + d_2 \tag{2.38}$$

$$R_{ox}^2 - R_{fuel}^2 = d_1^2 - d_2^2 \tag{2.39}$$

Working this system of equations allows the resolution of parameters d, d_1, and d_2 as follows:

$$d = \sqrt{R_{fuel}^2 + R_{ox}^2 - 2R_{fuel}R_{ox}\cos\theta} \tag{2.40}$$

$$d_1 = \frac{d^2 + R_{ox}^2 - R_{fuel}^2}{2d} \tag{2.41}$$

$$d_2 = \frac{d^2 + R_{fuel}^2 - R_{ox}^2}{2d} \tag{2.42}$$

The particles are assumed to retain their spherical form, as has been observed in high-heating rate experiments.[88] In these experiments, despite loss of the nanostructure when the materials coalesce into larger aggregates, a largely spherical nature is still maintained in post-mortem images. Additionally, the changes in volume attributable to differences in density between oxide and reduced oxide or fuel and oxidized fuel species are neglected. With these assumptions, all dimensional parameters remain constant throughout the simulation.

Thus, a two-dimensional system of two nanoparticles is established (Fig. 2.1), centered vertically on the middle of the particles and horizontally at the interface of the two particles, denoted a_o. In all cases considered in this work, the interface between particles, a_0, is held fixed at the origin, so the sintering is considered to have happened prior to the full reaction. This assumption is corroborated by the observed reaction times cited by Sullivan *et al.* where the sintering time lengths are negligible compared to the diffusion time lengths.[45] The second interface between the native oxide layer and the fuel core, $+ a_1$, is initialized to the oxide shell thickness within the fuel particle. As oxidation occurs during the reaction, this interface moves into the fuel particle along the +x axis. Finally, b_1, the interface between the initial oxide material and the final reduced product is initialized to the origin, such that $b_1^o = a_0 = 0$. If the reduction has an intermediary product, b_1 first represents the interface between the original oxide and the intermediary product, then the intermediary product and the final reduced oxide. It is assumed in this formulation that all the original material is first reduced to the intermediary product before the intermediary species begins to reduce to the final material. As the simulation commences and the oxide reduction begins, b_1 moves into the oxide particle along the -x axis. For a two-step reaction, this boundary is reset at the origin when the first oxide material has been completely reduced, and the absolute value of b_1 has surpassed the radius of the oxide particle. A two-dimensional schematic of the geometric setup at initiation is provided in Figure 2.2a, while Figure 2.2b shows a snapshot as the reaction has progressed.
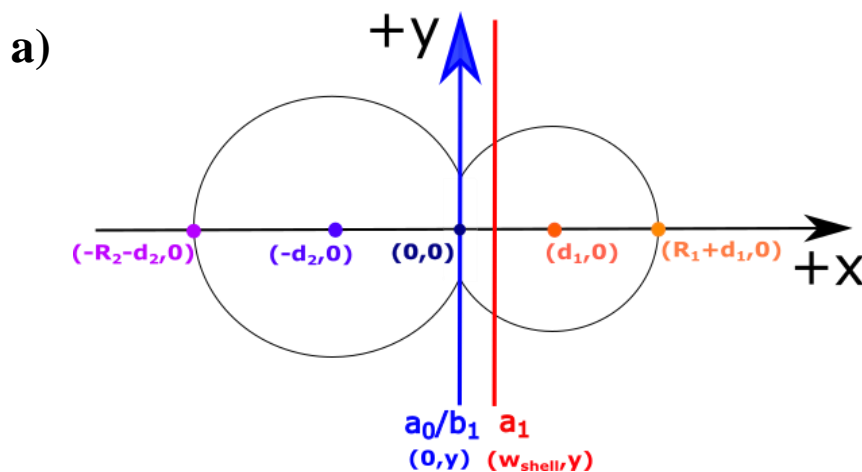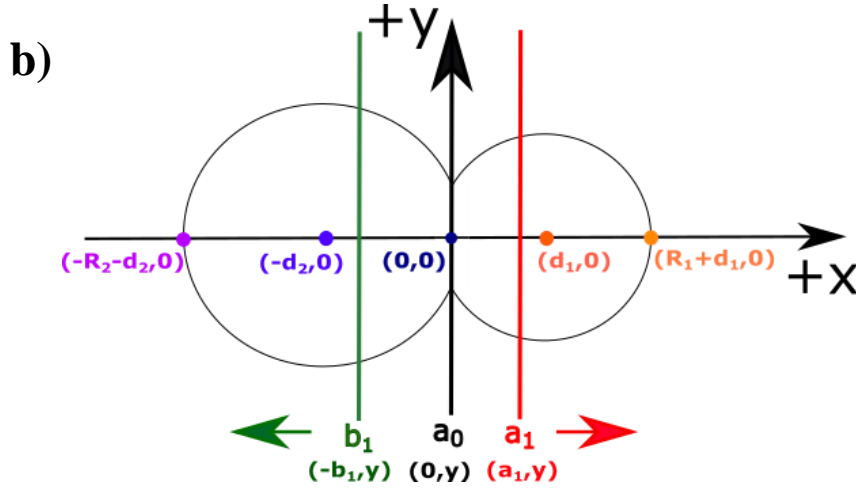
Figure 2.2 : Two-dimensional diagram of the system coordinates and interface positions at a) system initialization and b) once simulation has begun.

2.3.1   Mass Transport

Within this framework, the Deal and Grove approximation, assuming flat interfaces, gives the flux of atomic oxygen (mol.s^{-1}) across such an interface as

$$\Phi = -\text{D}\, S(x)\frac{\partial C}{\partial x} \qquad (2.43)$$

where D is the temperature-dependent diffusion coefficient and C is the oxygen concentration (mol.m^{-3}). $S(x)$ is the surface area of the flat interface at position x from the center of the sphere of radius R, expressed as

$$S(x) = \pi(R^2 - x^2) \qquad (2.44)$$

for this radial configuration. Differing from previous implementations of the Deal and Grove method for nanothermites[48], the surface area dynamically changes as the interfaces advance into the spherical particles. The diffusion coefficients of oxygen in the various materials in the system follow Arrhenius' law, such that

$$D(T) = D_o e^{-E_a/R_g T} \qquad (2.45)$$

with species-specific prefactor, D_o, and activation energy, E_a. These values for the numerous materials are provided in Table 2.1. In this work, R_g is the gas constant in J.K^{-1}.mol^{-1}.

The general solution for Equation 2.43 is logarithmic, of the form

$$C = -\frac{\Phi}{D}\frac{1}{2\pi R}\ln\frac{(R+x)(R-x_0)}{(R-x)(R+x_0)} + Cst \qquad (2.46)$$

In the flux approach, Φ is constant through the various interfaces, and successive oxygen concentrations can be deduced from the previous ones. During the first step of the reaction, the initial oxide component decomposes into either an intermediary reduced oxide or the final oxide product. This liberates oxygen that then diffuses across this product. Following the notations in Fig. 2.1-2.2, the oxygen concentration at b_1 is the solubility limit C_S. Due to a lack of reliable values for this solubility limit, particularly in light of possible defects in particles resulting from the manufacturing and mixing processes, this model imposes an upper atomic solubility limit of 10%. Thus, the oxygen concentration C_0 at a_0 is given by

$$C_0 = C_S - \frac{\Phi}{D_{ox}(T)} \frac{1}{2\pi R_{ox}} \ln\left(\frac{R_{ox} + d_1}{R_{ox} + d_1 - b_1}\right)\left(\frac{R_{ox} - d_1 + b_1}{R_{ox} - d_1}\right) \quad (2.47)$$

The freed oxygen arrives at the interface, a_0, between the two particles and then must diffuse across the oxidized fuel material. The atomic oxygen concentration in this material is then given by

$$C_1 = C_0 - \frac{\Phi}{D_{fuel}(T)} \frac{1}{2\pi R_{fuel}} \ln\left(\frac{R_{fuel} - d_2 + a_1}{R_{fuel} - d_2}\right)\left(\frac{R_{fuel} + d_2}{R_{fuel} + d_2 - a_1}\right) \quad (2.48)$$

In theory, the concentration at the plane of intersection, C_0, should not exceed the oxygen solubility limit. Nonetheless, this occurs frequently in practice and, if so, C_0 is automatically set to the solubility limit as previously defined. The postulated value for the solubility limit was supported by a theoretical study completed by Lahiner et $al.$ on Al:CuO nanolaminates, which showed that setting this limit even up to 100% solubility of oxygen in CuO and Cu_2O does not have a significant influence on the results.[48] This is most likely due to the significantly lower diffusion coefficient of oxygen in the oxidized fuel, which acts as the bottleneck interface in this model. Note that this assumption is applied regardless of the material species.

The second part of the redox reaction is the oxidation of the fuel. This is known to be very fast, particularly for the popular fuel choice, Al. It is possible to use an approximately infinite value for the reaction rate which would make $C_1 = 0$. Nevertheless, an approach using Arrhenius' law was preferred, despite the fact that oxidation of fuel materials in air is known to be spontaneous and thus requires zero activation energy.[147–149] The oxygen flux at the fuel/oxidized fuel interface is therefore expressed as

$$\Phi = \upsilon\pi\left(R_{fuel}^2 - a_2^2\right)C_1 \quad (2.49)$$

In this equation, the prefactor υ is the hopping rate of oxygen atoms (in m/s) in the first layer of the fuel/oxidized fuel interface. This prefactor is arbitrarily set to 3000 m/s, a high value that remains an order of magnitude lower than the maximum rate compatible with hopping rates and plane distances in solid lattices[150]. Simulations completed in this work have confirmed that

this is not the limiting factor for fuel oxidation, where the oxygen concentrations at the oxidated/non-oxidated fuel interface are very small, in all conditions and at all times.

Resolving these three equations calculates the flux at each time step. As such, for flux $\Phi(t)$, the reduction rate of the oxide moves the b_1 interface (first step of reduction) or b_1' interface (for second step reduction, if applicable) by

$$\frac{db_1}{dt} = \frac{\gamma_{ox}\Phi\Omega_{ox}}{\pi[R_{ox}^2 - (d_1 - b_1)^2]} \qquad (2.50)$$

$$\frac{db_1'}{dt} = \frac{\gamma_{int-ox}\Phi\Omega_{int-ox}}{\pi[R_{ox}^2 - (d_1 - b_1)^2]} \qquad (2.51)$$

with γ_{ox} and γ_{int-ox} , the stoichiometric reaction ratios of released oxygen from the molecular oxide and intermediate reduced oxide, respectively. Finally, the growth rate of the oxidized fuel material is given by the a_1 adjustment

$$\frac{da_1}{dt} = \frac{\gamma_{fuel}\Phi\Omega_{fuel}}{\pi[R_{fuel}^2 - (d_2 - a_1)^2]} \qquad (2.52)$$

Similarly, γ_{fuel} is the stoichiometric reaction ratio of the reacting oxygen with the fuel. All stoichiometric reaction ratios are provided in Table 2.2. Ω_i is the molar volume of species i.

Table 2.2 : Molecular properties of the provided species in the model including number of atoms per species molecule, and "reaction coefficients" for each species individual reduction or oxidation equation.

Species, x	Number of atoms, N_X	First reaction coefficient, γ_x^1	Second reaction coefficient, γ_x^2
Al	1	2/3	2/3
Al_2O_3	5	1/3	1/3
B	1	3/2	3/2
B_2O_3	5	3	3
Mg	1	2	2
MgO	2	2	2
Zr	1	2	2
ZrO_2	3	2	2
CuO	2	2	2
Cu_2O	3	1	1
Fe_2O_3	5	1	1
FeO	2	2	1
WO_3	4	3	3
Pb_3O_4	7	1	1
PbO	3	3	2

The moving boundaries resulting from any phase changes or chemical reactions induce mechanical stress inside the nanoparticles. These stresses are not taken into account in the simulations. In addition, the interface between particles, a_0, is considered constant as it is assumed that there is no diffusion of the initial fuel species and the degree of sintering is held constant. Thus, $\frac{da_0}{dt} = 0.$

2.3.2   Thermal Equation

For the base model, the mass diffusion is coupled to a simplified heat equation, neglecting all losses into the environment. The ambient temperature, $T_a = 300$ K, is considered the reference for all physical qualities. As such, the system is initialized to this temperature and only phase transformations occurring above this T_a are considered.

Given the high value of heat diffusivity with respect to mass diffusivity, in addition to the small size of the nanoparticles, the temperature can be considered uniform throughout the system while diffusion is taking place. Certain simulations at a rapid heating rate, such as the systems initiated by pulse laser, may not hold to this assumption, which is further discussed in Chapter 3. Additionally, this assumption fails if the two nanoparticles are not in contact, *i.e.,* before sintering occurs, which is not the case considered in this model. Thus, the general heat equation can be expressed as

$$C_v \frac{dT(t)}{dt} = \Phi(t)q + \sum h_j \delta(T - T_j) + P \qquad (2.53)$$

where C_v (in J.K^{-1}.m^{-3}) is the total heat capacity of the pair of two nanoparticles as a combination of their bulk heat capacities. In this model, the total heat capacity is calculated by the approximation

$$C_v = 3R(N_{fuel}n_{fuel} + N_{fuelShell}n_{fuelShell} + N_{oxide}n_{oxide}) \qquad (2.54)$$

where N_x is the number of atoms per molecule in the respective species x for the fuel, native oxide shell on the fuel, and oxide species. The number of moles of each species x given the physical dimensions of the particles and the native oxide shell thickness is given by n_x. The values of N_x for each species x are presented in Table 2.2.

The thermal evolution of the single pairing unit includes three terms. The first term on the right hand side represents the heat of reaction, with q, the molar heat of combustion in (J.mol^{-1} of atomic oxygen) multiplied by the flux of freed oxygen (mol of atomic oxygen.s^{-1}). The second term gathers all other internal enthalpy variations due to various phase changes such as the melting, evaporation, and decomposition of the species, with h_j the specific molar enthalpy of the mechanism for species j. T_j, is the temperature at which the mechanism occurs, and δ is the Dirac delta function. When the temperature of a phase change for a reactant or product is reached, the amount of energy required to melt all of that material species is deducted

from the total energy of the system. The third term P represents an external power density that is applied to initiate the system. Thermal losses are not considered in the thermal equation because they are characteristic of the whole macroscopic system and its geometry and here, the focus is on the isolated physico-chemical system composed of a two-nanoparticle pair.

2.4   Full Propagation Model

To elaborate a full burn-tube like system setup, the model is expanded to a one dimensional system of a discretized chain of identical cells where each elemental cell is homogeneously populated according to the compaction rate as a percentage of the Theoretical Max Density (%TMD) with N single fuel-oxidizer pairs. As such, the model corresponds to an open air line of thermite or a tube apparatus with an infinitesimally small wall thickness such that heat is not propagated along the wall.
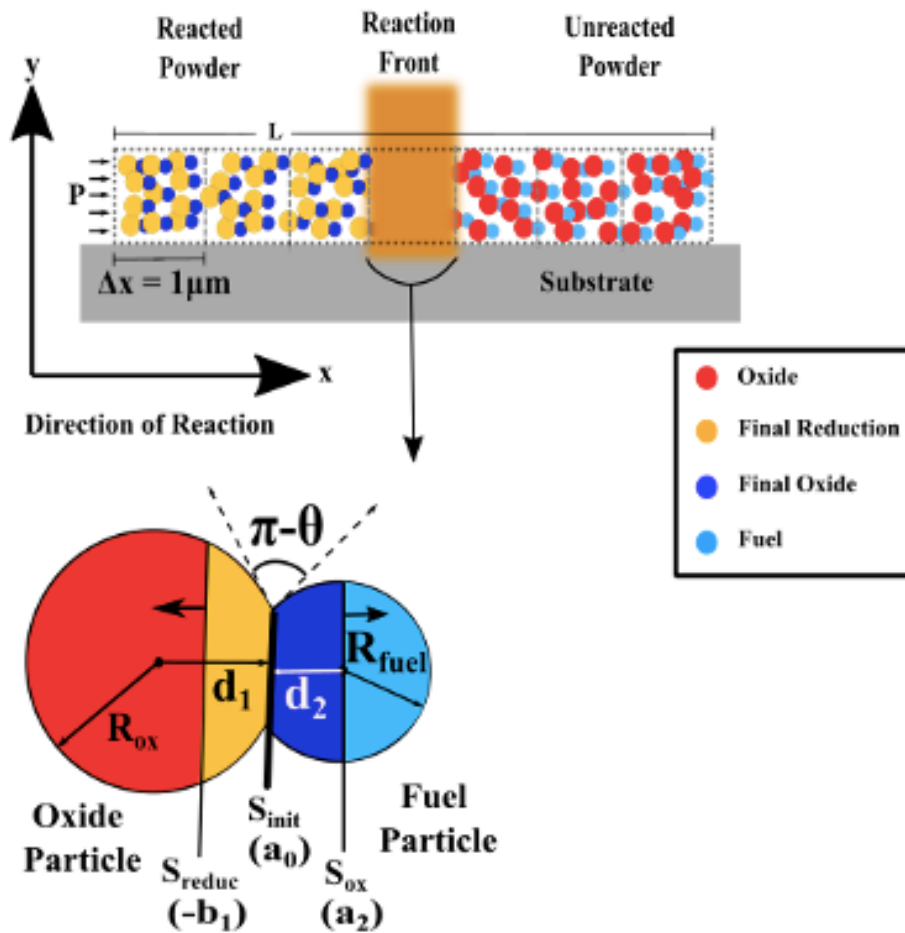
Figure 2.3 : Full system diagram for the final version of the propagation model. Reaction initiates at the far-left side and the reaction propagates from left to right

The thermite line is assumed to have a cylindrical geometry (a tube with no envelop) of radius R_{tube} and is divided into cells of a length dx giving an approximated cell volume $V_{cell} = \pi R_{tube}^2 dx$. Each cell is filled with completely geometrically identical particles, where all geometric parameters including R_{ox}, R_{fuel}, d, d_1, d_2, and the contact wetting angle, θ, as defined

in the base model, are constant (see Figure 2.3). Therefore, each individual thermite pair has a volume of

$$V_{thermite} = V_{ox} + V_{fuel} + V_{shell} \qquad (2.55)$$

where each material volume can be calculated by the following equations:

$$V_{ox} = \frac{\pi}{3} R_{ox}^2 (2R_{ox} + 3d_1) - d_1^3 \qquad (2.56)$$

$$V_{fuel} = \frac{\pi}{3} R_{fuel}^2 (2R_{fuel} + 3d_2) - d_2^3 \qquad (2.57)$$

$$V_{shell} = \frac{\pi}{3} [(R_{ox} - d_1 + a_1)^2 (2R_{ox} + d_1 - a_1) - (R_{ox} - d_1)^2 (2R_{ox} + d_1)] \qquad (2.58)$$

Therefore, the number of pairs per cell, N, can be established by

$$N = \%TMD \frac{V_{cell}}{V_{thermite}} \qquad (2.59)$$

Finally, the system is initiated by the application of a power density at the first cell at the left extremity of the one dimensional macroscopic system. This can be adjusted in future applications to account for a single point of external heating, but is not considered in the scope of the current work. The reaction front propagates from the left to the right side of the system. All pairs in each cell progresses simultaneously at the same rate, exactly as described in the base model description. In this case, all mass transfer equations are identical.

The propagation model differs only in the amount of heat produced by the exothermic redox reaction. This is due to the assumption of constant temperature across the cell and, thus, the identical progression of reaction in each particle pair. As such, the same equations for mass transfer are calculated for each cell, but the interface parameters $b_1(t)$ and $a_0(t)$ are equal for all pairs in the cell, giving a single flux, $\Phi(t)$, within each cell at each time step. The heat generated by the exothermic reaction inside cell i is now given by

$$Q_i = \Phi_i(t)qN \qquad (2.60)$$

However, since the increased amount of material is also taken into account in the volumetric heat capacity, C_v, this increase does not need to be explicitly expressed.

$$C_v N \frac{dT_i(t)}{dt} = P + N\Phi_i(t)q + \sum Nh_j\delta(T_i - T_j) \qquad (2.61)$$

For the reaction front to propagate, it is necessary to consider an interior heat transfer mechanism between the cells making up the tube. In reality, any system will transfer heat through all three possible pathways: conduction, convection, and radiation. This remains true

in nanothermite propagation where solid, not yet melted particles in contact will conduct heat between them, as well as the tube wall that will conduct heat the length of the apparatus. Produced gas and condensed phase material will convect heat down the tube. Radiation will be emitted by particles not in immediate contact with adjacent material. However, to attempt to better understand the fundamental mechanism of heat transfer for condensed-phase dominant nanothermites, each possibility was tested individually.

The following section presents three different formulations that were considered in the evolution of this work to try to better understand the mechanisms for heat transfer in low gas-producing nanothermites. The presentation of these ideas is chronological in their development, where the final proposition is the one considered the final and best formulation.

2.4.1   Cell Conduction by Radiation

The first attempt to model the heat transfer through the macroscopic apparatus was approached through a combined conductive/radiative schema. Taking a simple general thermal equation, neglecting losses into the environment,

$$C_V \frac{dT}{dt} = P + \phi q + \sum h_j \delta(T - T_j) + \lambda_{rad} \frac{d^2 T}{dx^2} \quad (2.62)$$

the macroscopic heat transfer is achieved through conduction from discretized element to element. This is the added fourth term when comparing Equation 2.62 to Equation 2.61. However, on the microscale within each cell, most material is not in solid contact for conduction. Thus, this formulation assumes that heat transferred from each particle pairing is given off by radiation, and this radiated heat is "conducted" to the adjacent cell. This is applied through an effective radiation-driven conduction coefficient, denoted λ_{rad}.

As the radiation given off in cell i is dependent upon the temperature in this cell, it is necessary to consider λ_{rad} temperature dependent and thus rewrite Equation 2.62 as

$$C_V \frac{dT}{dt} = P + \phi q + \sum h_j \delta(T - T_j) + \frac{d}{dx}\left(\lambda_{rad} \frac{dT}{dx}\right) \quad (2.63)$$

For a particle pair of combined length $D = R_{ox} + R_{fuel} + d$, the radiation can be given by

$$\lambda_{rad} = 4\sigma T^3 \frac{D}{\%TMD} \quad (2.64)$$

And thus, applying the finite method finds

$$\frac{d}{dx}\left(\lambda_{rad} \frac{dT}{dx}\right) = \frac{d}{dx}\left(4\sigma T^3 \frac{D}{\%TMD} \frac{dT}{dx}\right) = \frac{\sigma}{(\Delta x)^2} \frac{D}{\%TMD}[T_{i+1}^4 + T_{i-1}^4 - 2T_i^4] \quad (2.65)$$

where $\dfrac{D}{\%TMD}$ represents the empirical distance between particle pairs within a cell.

2.4.2 Gas Convection

A second proposition considers a macroscopic interpretation of convection by gas with an adiabatic reaction at uniform pressure within a closed tube system. Given that the speed of propagation is much smaller than the speed of sound, it can be assumed that the entire system is at constant pressure, P. As the element volume is held constant, the density of gas particles per element will adjust as they are propagated along the reaction axis, with the temperature finding equilibrium between the cell temperature due to the exothermic condensed-phase reaction and the gas particles' temperature. Thus, considering a cell x, with gas density (pressure), p_x, and gas transfer from cell x to cell $x + 1$, Y_x, the total heat generated is given by two equations

$$Q_x(t) = qN\Phi_x(t)dt + C_p(Y_{x-1}T_{x-1}(t) - Y_xT_x(t)) \tag{2.66}$$

$$Q_x(t) = (C_{mat} + C_pp_x)dT_x(t) - V_{air}dP \tag{2.67}$$

where $C_p(Y_{x-1}T_{x-1}(t) - Y_xT_x(t))$ is the convective component driving the propagation of the gas molecules in a general heat equation. Equation 2.67 analyzes the gas convection in the system in terms of enthalpy. The variables include C_p, the specific heat capacity of the gas particles, C_{mat} the total volumetric heat capacity per cell, and the volume of air in the system, given by the following formulas

$$C_p = \frac{\gamma}{1-\gamma}\frac{R}{M_{air}}V_{air} \tag{2.68}$$

$$C_{mat} = NC_{part} = NC \tag{2.69}$$

$$V_{air} = 1 - \%TMD \tag{2.70}$$

Equations 2.66 and 2.67 can be resolved to a form $Y_N = \alpha_N - \beta_N dP$ when considering the closed tube assumption such that $\sum dp_x = \sum Y_{x-1} - Y_x = 0$ and $\dfrac{dT_x}{T_x} = \dfrac{dP}{P} - \dfrac{dp_x}{p_x}$, where

$$\alpha_x\left(\frac{C_{mat}}{p_x} + 2C_p\right)T_x = \alpha_{x-1}\left[\left(\frac{C_{mat}}{p_x} + C_p\right)T_x + C_pT_{x-1}\right] + qN\Phi_x dt \tag{2.71}$$

$$\beta_x\left(\frac{C_{mat}}{p_x} + C_p\right)T_x = \beta_{x-1}\left[\left(\frac{C_{mat}}{p_x} + C_p\right)T_x + C_pT_{x-1}\right] + \frac{\gamma}{\gamma-1} + \frac{C_{mat}}{p_x\left(\frac{R}{M_{air}}\right)} \tag{2.72}$$

Finally, these recursive equations find the total increased system pressure, P'(t), each cell's partial pressure, p'_x (t), and each cell's equilibrium temperature, T'_x (t) by

$$P' = P + dP = P+ = \frac{\alpha_N}{\beta_N} \tag{2.73}$$

$$p'_x = p_x + dp_x = p_x + (\Upsilon_{x-1} - \Upsilon_x)$$
$$= p_x + \left(\frac{\alpha_{x-1}\beta_N - \alpha_N\beta_{x-1}}{\beta_N} - \frac{\alpha_x\beta_N - \alpha_N\beta_x}{\beta_N} \right) \tag{2.74}$$

$$T'_x = T_x + dT = \frac{P + dP}{\left(\dfrac{R}{M_{air}} \right)(p_x + dp_x)} \tag{2.75}$$

As the system is considered closed, this model iteration includes an enveloping cylindrical wall which directly conducts heat in two dimensions. The wall thickness is given by the input tube parameters, r_{in}, the inner tube radius, and r_{out}, the outer tube radius. This wall can then be discretized into N_{wall} partitions with an irregular radial distribution, for $j = [1 - N]$.
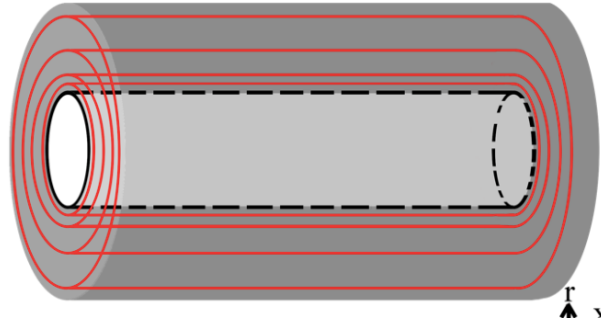
Figure 2.4 : Diagram of concentric radial discretization.

$$r_j = r_{in} + (r_{out} - r_{in}) \frac{\exp(i)}{\exp(N_{wall})} \tag{2.76}$$

The chosen distribution provides a temperature profile inversely exponentially proportional to the radius.

The conductive term of the thermal equation can therefore be rewritten in cylindrical coordinates to account for conduction in the system through the metal walls, at position i, along the propagation axis and position j along the tube shell.

$$C_{mat} \frac{\partial T_{ij}}{\partial t} = \lambda_{wall} \left[\frac{T_{i+1,j} + T_{i-1,j} - 2T_{i,j}}{\Delta x^2} + \frac{T_{i+1,j} + T_{i-1,j} - 2T_{i,j}}{\Delta r^2} + \left(\frac{1}{r_j} \right) \frac{T_{i,j+1} - T_{i,j-1}}{2\Delta r} \right] \tag{2.77}$$

The innermost layer of the envelope is assumed to be at the same temperature as the inner reaction cell, while the outermost layer is constant with the ambient temperature, giving boundary conditions:

$$T_{i,1} = T_{i,0} \quad and \quad T_{i,N} = T_{amb}$$

2.4.3   Direct Material Conduction

The final version utilized throughout the tests presented in this study considers conduction from cell to cell explicitly, as though there is a thread of material in contact throughout the apparatus. This is, of course, an assumption that is shown to be acceptable to predict thermite performances (see Section 4.4). The thermal conductivity of the cell is defined as some mathematical estimation taking into account the ratio of materials and their bulk conductivities. Four different possible calculations of this effective conduction coefficient, denoted λ_{eff}, were explored. In this formulation, the conductive heat transfer drives propagation, while radiation and convection are considered losses into the environment, with no envelope considered at the system boundaries. Additionally, the radial dependence of the temperature is neglected, as the conductivity is much higher compared to losses. The radius of the system is always much smaller than the ratio λ_{eff}/h_c.

In this model construction, the macroscopic thermal equation is written as

$$C_V \frac{dT}{dt} = P + \phi q + \sum h_j \delta(T - T_j) + \lambda \frac{d^2T}{dx^2} - \frac{2\sigma}{r_{cyl.}}(T^4 - T_{amb}^4) - \frac{2h_c}{r_{cyl.}}(T - T_{amb}) \qquad (2.78)$$

With three terms added to account for the conduction $\lambda \frac{d^2T}{dx^2}$, with the conduction coefficient, λ, in W.m^{-1}.K^{-1}, radiation, $\frac{2\sigma}{r_{cyl.}}(T^4 - T_{amb}^4)$, with the Stephen-Boltzmann constant, $\sigma = 5.67$ x 10-8 W.m^{-2}.K^{-4}, and convection, $\frac{2h_c}{r_{cyl.}}(T - T_{amb})$, with convective coefficient h_c in W.m^{-2}.K^{-1}. The factor $2/r_{cyl.}$ accounts for the fact that radiative and convective losses occur at the boundaries of the cylindrical system. Thus, with conduction as the main source of heat transfer, that term is adapted with λ_{eff}. The radiative and convective terms are considered heat losses into the environment. This system is supplemented by the following initial and boundary conditions, where the ends are considered thermally isolated:

T(t$_0$) = T$_{amb}$ = 300 K   T(x=0) = T(cell 1)   T(x=L) = T(cell n)
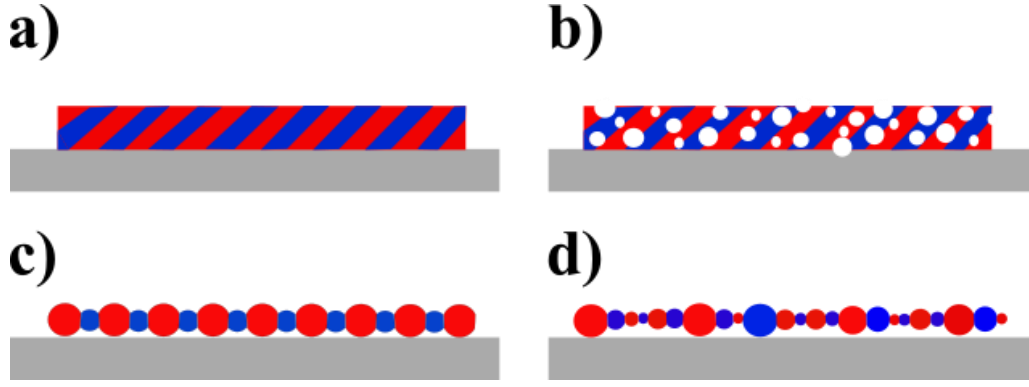
Figure 2.5 : One-dimensional diagrams of the "effective" material structure given by a) bulk material with combined thermal properties. b) bulk material with voids filling space to %TMD. c) single 1D chain of identical alternating fuel and oxide particles. d) a single 1D chain of various sized alternating fuel and oxide particles.

With these considerations in mind, the first, obvious formulation for λ_{eff} considers a continual heat flow through the compressed powder, which corresponds to a bulk material with the combined thermal properties of the fuel and the oxide species (o, oxidizer; f, fuel) as depicted in Figure 2.5a. This estimation was utilized by Montgomery *et al.*[151] in a customized thermochemical code for pressed pyrotechnic compositions. The estimation, adapted from a structural model for thermal conductivity of heterogenous materials in parallel[152] is given as

$$\lambda_{eff}^a = \varepsilon_o \lambda_o + (1 - \varepsilon_o)\lambda_f \qquad (2.79)$$

Considering the two heterogeneous materials the fuel and oxide species, with their respective bulk conduction coefficients λ_f and λ_o, an effective conduction coefficient can be calculated relative to the mass fraction of each species. ε_o and $(1 - \varepsilon_o)$ give these values for the oxide and fuel species, respectively, in a fully compacted system (100 %TMD). Note that Montgomery *et al.*[151] denote this fraction as θ_s and $(1 - \theta_s)$. This gives a value that is the maximum theoretical value for the effective conduction coefficient, yet there will always be voids present even in highly compacted nanothermite powders.

To modify this value to account for an actual experimental %TMD, the formula is slightly adjusted to

$$\lambda_{eff}^b = \varepsilon_o \lambda_o + (\%TMD - \varepsilon_o)\lambda_f \qquad (2.80)$$

In this case, the material is still treated as a bulk heterogeneous material, but which now fills the apparatus to the set %TMD with voids (Figure 2.5b). Both of these approaches do not take into account the geometric factors that form the basis of this model, the sintered particle pair, in addition to simulating a %TMD that is rarely seen in particle-based nanothermites ($> 60\%$). Note also that the effective conductive coefficient ignores the interfacial regions formed by the wetted contact between the fuel-oxide pairing, whose bottlenecking aspect is important at the scale of the diffusion/reaction equations in our model.

The third formulation proposes a novel method of calculating an effective conduction coefficient by considering a single one-dimensional chain of alternating fuel and oxide particles, seen in Figure 2.5c. In this configuration, most oxide species of low conductivity will act as a bottleneck to the overall heat conduction and, thus, initiation and propagation of the system. Due to the quick melting of most reactant species or their reduced forms, this configuration could also be representative of a solid matrix of one species with embedded individual particles of the other. Taking into account the geometry and bulk conductivities λ_{fuel} and λ_{ox} for the fuel and oxide species, respectively, the total effective conduction coefficient is

$$\frac{1}{\lambda_{eff}^c} = \frac{d_{ox}(3R_{ox}^2 - d_{ox}^2) + d_{fuel}(3R_{fuel}^2 - d_{fuel}^2)}{\%TMD \times 6d^2} \times [\frac{1}{\lambda_{ox}R_{ox}} ln \frac{(R_{ox} + d_{ox})}{(R_{ox} - d_{ox})}$$
$$+ \frac{1}{\lambda_{fuel}R_{fuel}} ln \frac{(R_{fuel} + d_{fuel})}{(R_{fuel} - d_{fuel})}$$

(2.81)

This equation is obtained by expressing the heat flux across the two-particle interface as a function of the temperature difference between the centers of the particles. The heat flux is calculated in the same manner as the mass transport flux. The same logarithmic behaviour is thus observed.

A final proposition elaborates Equation 2.81 to allow a realistic diversity of non-constant particle sizes, as seen in the size distribution of an actual nanopowder, as well as the assortment of different sized agglomerates formed after reactive sintering. This formulation is shown in Figure 2.5d and is given by Equations 2.82 and 2.83. When this effective conduction coefficient is used, the particle size distribution is exclusively accounted for in the conduction, while the particle sizes considered for all mass transfer mechanisms remain constant. Manipulation of this size distribution can effectively simulate voids in the packed tube apparatus by creating a large bottleneck in the heat transfer at particles of large size and low bulk conductivity. This is useful for addressing the effects of the voids that will naturally occur due to irregularities in mixing and filling methods for this type of experiment, or to have a better effective conduction coefficient for low compaction rates. This will be further discussed in Section 4.3.

$$\frac{1}{\lambda_{eff}^d} = \frac{1}{6 * \%TMD} \Sigma \frac{1}{R_i \lambda_i} ln \left[\frac{R_i + d_i^+}{R_i - d_i^+} * \frac{R_i + d_i^-}{R_i - d_i^-}\right]$$
$$\times \frac{\Sigma[d_i^+(3R_i^2 - d_i^{+2}) + d_i^-(3R_i^2 - d_i^{-2})]}{(\Sigma(d_i^- + d_i^+))^2}$$

(2.82)

where

$$d_{i,i+1}^2 = (d_i^+ + d_{i+1}^-)^2 = R_i^2 + R_{i+1}^2 - 2R_iR_{i+1}cos\, \theta_{i,i+1} \qquad (2.83)$$

Here, the heat flux is again expressed as a function of the temperature difference along a chain of sintered nanoparticles. For this reason, Eq. 2.82 contains a sum representing all

discrete interfaces between nanoparticles, which can be modified depending on the actual structure considered. Again, the different particle sizes are only considered during the initial calculation of the effective conduction and not for the mass transfer calculations or subsequent simulation. Various half-Gaussian distributions around common nominal particle sizes were utilized and will be presented and discussed in Section 4.3.

2.5 Conclusion

This chapter has provided the theoretical basis for the mathematical formulation of the Deal & Grove diffusion-reaction scheme and its adaptation to energetic materials through the coupling with a thermal equation. First, the base model pairing of a single fuel particle with a single oxide particle that is used for initiation-only results is presented. This model was then expanded into a full propagation model within a one dimensional cylindrical burn-line like simulated apparatus. Different strategies to allow the transfer of the heat produced by exothermic redox reaction were elaborated in the chronological order of their development. The following chapters will show and discuss the application and exploitation of these models to simulate different nanothermite initiation and propagation experiments. Additionally, the comparison of the different heat transfer formulations with the motivation for the choice of the final version will be discussed.

CHAPTER 3. Base Model Validation & Exploitation to Investigate Nanothermite Initiation

3.1 Introduction

Two different theoretical model formulations were presented in the preceding chapter in their chronological order of development. First, a base model was elaborated that simulates a single particle pair externally heated until initiation to investigate and quantify the effects of condensed phase mechanisms on the initiation delay. This limitation of the model to exclusively consider the condensed phase was chosen to contribute to the current debate in the nanothermite domain on whether the dominant mechanism for initiation is condensed or gas phase. Recent experimental evidence indicates that the so-called "reactive sintering" plays an important role in the initiation of the self-sustained exothermic redox reaction, but no work in numerical models around this phenomenon exist. Additionally, the recent call for computationally efficient models in the nanothermite industry to provide fast, valid estimates of thermite performance motivated the desire to determine if condensed phase mechanisms alone (permitting a simpler and quicker simulation) could accurately approximate the desired results.

Thus, there were three main objectives for the simulated experiments of initiation. The first was to validate the model formulation through comparison with established experimental results. Then, once the model was confidently found to predict acceptable initiation results with only condensed-phase mechanisms, to utilize the program to compare the results with a purely gas-phase model to investigate the fundamental mechanisms at play in initiation. Finally, the base model was exploited to investigate the effect of different parameters (size, degree of coalescence, stoichiometry), as well as to complete a benchmark study, estimating the initiation reaction characteristics for couples of interest in recent gasless applications.

The first two sections are devoted to the validation of this model by two different sets of experiments, from Ref. 85. One experiment features nanoparticles heated at a very fast heating rate ($\sim 10^{11}$ K/s) in a DTEM environment. A second T-jump experiment considers the same initial nanoparticles heated at a medium rate ($\sim 10^{5}$ K/s). Further simulations of these two experimental setups are then presented looking at the effect of particle size, up to the micron scale, the degree of sintering, and the stoichiometric ratio between the fuel and oxide material. A final exploitation of the Al:CuO T-Jump experiment is used to compare the results directly with an identical simulation based on dominant gas-phase mechanisms. Then, the model is extended for more unique thermite couples that are seeing increasing interest in gasless applications.

3.2 High Heating Rate Initiation

This section is dedicated to simulations associated with a specific high heating rate experimental setup, as described in Ref. 85, in which laser heating is utilized to initiate a thermite mixture. A 532 nm monochromatic wavelength laser with pulse durations of 12 ns and a peak fluence of 0.3 kJ.m^{-2} imposes a high heating rate on the order of 10^{11} K/s. The thermite is composed of a set of Al:CuO nanoparticles placed on a TEM grid, under ultra-high vacuum. The chamber is equipped with a dynamic TEM setup allowing *in-situ* image acquisition for a period of a few hundreds of nanoseconds following the laser initiation.

In the following calculations, it is assumed that the thermite system does not endure any thermal losses. The heating rate is such that the oxygen diffusion is negligible within this the timescale of the sintering process, as corroborated by the theoretical calculations of sintering time versus reaction time in Ref. 45. To recreate this situation *in silico,* the simulations are not begun by heating the samples from room temperature, but rather are assigned an initial temperature as a function of the experimental setup including the laser characteristics, the heating duration, the radius of the nanoparticles and the material properties. The system consists of 80 nm Al and 50 nm CuO nanoparticles. This is a highly fuel-rich system ($\xi = 8.0$) that was chosen to correspond to numerous experimental setups for validation and comparison. A rough estimation of the experimental heating procedure leads to a temperature regime on the range of 10^3 K. Thus, a range of initial temperatures from 1000 to 1500 K are first simulated to investigate the effect of the imposed initial temperature on the subsequent temperature evolution and initiation of the system. The results of these initial simulations are provided in Figure 3.1. Note that the contact angle between Al and CuO particles is fixed, reflecting the sintering process taking place at the very initial stage of heating, at $\theta = 135°$, corresponding to the observed angle on post-mortem TEM images in Ref. 85. Finally, in these first experiments where the major goal is to exclusively analyze the initiation of the system, vaporization temperature limits are not imposed as the gas-phase material does not propagate and, thus, does not affect the part of interest of the reaction.

For almost all of the curves, a three-step profile is observed. The first step displays a slight increase in temperature up to an inflexion point from which an initiation temperature can be derived. A sharp temperature rise, constituting the second phase of the reaction, is then observed up to a saturation of the temperature (the final phase) that remains constant over time, as no losses are present in the simulations. Depending on the initial temperature, the temperature saturates from 3297 K ($T_o = 1000$ K) to 3795 K ($T_o = 1500$ K). Evidently, the initiation delay decreases with increasing initial temperature but remains below 18 μs (except for $T_o = 1000$ K), which corresponds to the order of magnitude of the experimentally observed

delay. Finally, lowering the initial temperature below 800 K induces initiation delays into the ms regime.
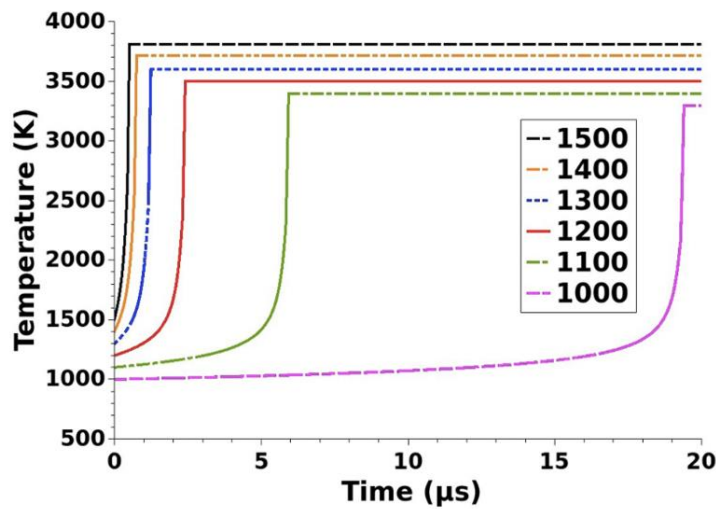
Figure 3.1 : Temperature evolution for the various applied initial temperatures, at a contact angle $\theta = 135°$, in the 1000-1500 K range for an Al:CuO system.

The species' temporal evolution for a high initiation temperature, $T_o = 1500$ K, is presented in Figure 3.2, which provides a clarifying view of how the overall combustion scenario operates as a function of temperature. The first reaction step corresponds to the release of oxygen from CuO (black curve), which leads to aluminum oxidation (slight and continuous Al drop, see the orange curve). Concurrently, Cu_2O is generated as CuO decomposes (blue curve). During the sharp temperature increase (second phase), the oxygen reservoir produced by the Cu_2O reduction is rapidly consumed, giving rise to pure copper (red curve), alumina formation (green curve), and a sharp drop in Al. This second stage of reaction takes approximately 0.08 μs. Note that at this extremely fuel rich stoichiometric ratio ($\xi = 8.0$), only a small percentage of the Al is consumed after 1 μs, while all of the oxidizer is reduced.
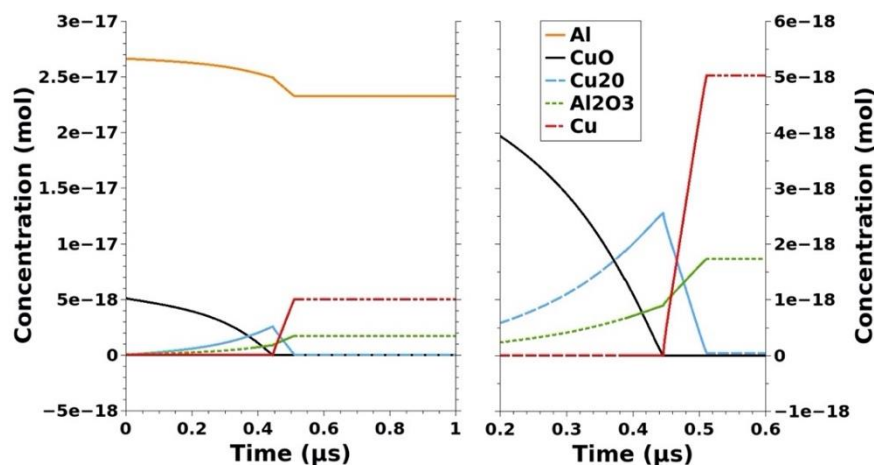
Figure 3.2 : The evolution of the species' molar concentrations as a function of time, for the Al:CuO reaction at $T_o = 1500$K and $\theta = 135°$: left side, for all species, right side, a zoom of the CuO, Cu_2O, Al_2O_3, and Cu region, on the period of high reactivity.

A second example of the evolution of the species for a longer initiation delay is illustrated by Figure 3.3. In this case, an initial temperature $T_o = 1000$ K, leading to a delay of ~20 μs according to Figure 3.1, is applied to the same nanothermite system.
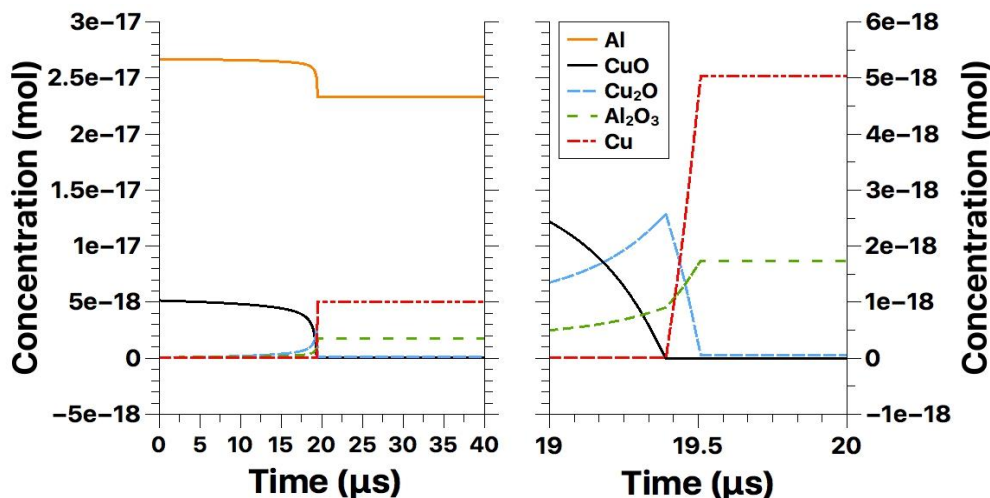
Figure 3.3 : The evolution of the species' molar concentrations as a function of time, for the Al:CuO reaction at $T_o = 1000$ K and $\theta = 135°$: left side, for all species, right side, a zoom of the CuO, Cu$_2$O, Al$_2$O$_3$, and Cu region, on the period of high reactivity.

It is clear that as long as the initial temperature is high enough to lead to the initiation of the exothermic redox reaction, it does not affect the behavior of the evolution of the species. The overall pattern resembles that of the quicker initiation example. Within the timescale of the initiation delay, initial reduction and oxidation reaction occur until around 20 μs. As the self-sustained exothermic reaction initiates, the material composition of the system evolves very rapidly. The time for this second stage to occur is approximately 0.12 μs, a duration very close to that of quicker initiations (~0.08 μs).

Continuing with the same *in-silico* setup, the effect of the degree of sintering on initiation delays was studied as a function of the nanoparticles' initial temperature (see Figure 3.4). The initiation delay shows a major dependency on the contact angle for almost all initial temperatures. Importantly, only the highest considered temperatures, accompanied by low contact angles, in the 90-110° range, show an initiation delay on the order of a few tens of nanoseconds. These simulated results can then be interpreted in light of the experimental findings. From the data available in Ref. 85, it is difficult to extrapolate quantitative values for the initiation delay, temperatures, and species within the condensed phase. However, orders of magnitude are given: (1) the coalescence of melted CuO nanoparticles takes ~45 ns for 50 nm CuO in diameter, (2) the melting of the Al core-shell structures is evidenced at 425 ns, (3) the complete sintering and mixing is observed after 600 ns. In this process, the coalescence of small particles occurs continuously with both CuO and Al nanoparticles, resulting in the full reaction operating in the condensed phase with larger structures.

Overall, the simulated experiments with an initial temperature of at least 1300 K correspond well to the main experimental observations. Additionally, the adoption of an effective initial temperature was supported by the authors' hypothesis that, with this

experimental setup, the CuO melts before Al due to the higher absorption of the monochromatic laser source. An earlier work by the same team suggests that the native oxide shell on the Al nanoparticles may also cause a delay of the coalescence of this species.[42] These two propositions oppose the classical interpretation, based on experiments initiated by heating at a medium rate by the Joule effect, that the whole Al nanoparticle melts before the CuO.
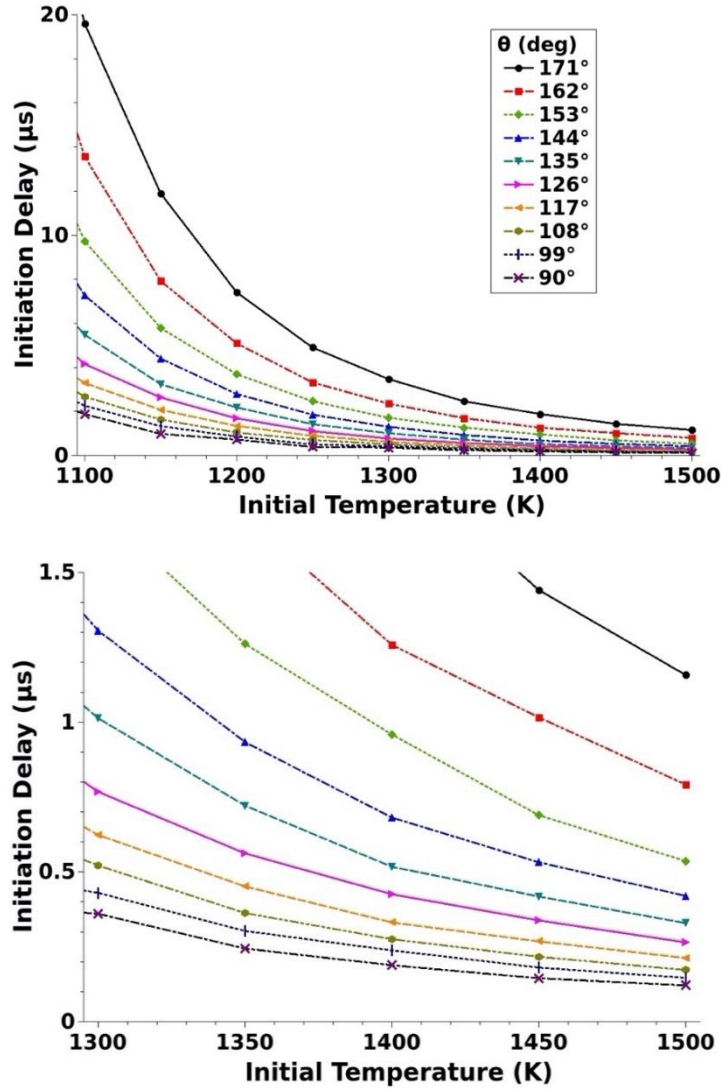
Figure 3.4 : Initiation delays as a function of the Al:CuO nanothermite initial temperature for different values of the contact angle: upper, for all initial temperatures tested; lower, zoom view of the low initiation delay regime.

Thus, to get further insight into this high-heating initiation process, the initial temperature, T_o, reached upon the laser heating can be roughly estimated from the emissivities ε of the nanoparticles as follows:

$$\Delta T = T_o - 300 = \frac{3W_{abs}}{4\pi\rho C_v R^3} \quad \text{with} \quad W_{abs} = \varepsilon\pi R^2 P_{laser}\Delta t \qquad (3.1)$$

where P_{laser} (W.m^{-2}) is the applied laser power density, R, the particle's radius, ε, the emissivity, and Δt (s), the heating duration. Considering the assumption that the two nanoparticles are in thermal equilibrium, the total absorbed heat is distributed in the bulk which gives the initial temperature, T_o, as

$$T_o = 298 + P_{laser}\Delta t \frac{3(\varepsilon_{Al}R_{Al}^2 + \varepsilon_{CuO}R_{CuO}^2)}{4(\rho_{Al}C_{V-Al}R_{Al}^3 + \rho_{CuO}C_{v-CuO}R_{CuO}^3)} \tag{3.2}$$

The emissivities 0.25 and 0.75 are chosen for the Al and CuO, respectively (roughly estimated from Refs. 153-155.

Table 3.1: Calculated initial temperature of the Al:CuO system after 12 ns laser heating accounting for the heating of both Al:CuO mixture or CuO considered alone.

CuO Diameter (nm)	Al Diameter (nm)	Initial Temperature, T_o (K)	
		Al:CuO System	Single CuO nanoparticle
50	80	1241	2312
100		1190	1305
150		960	969
200		805	802
300		500	499
1000		399	398

Table 3.1 provides the temperature T_o reached after the laser heating by the Al:CuO system or CuO alone according to Equation 3.2 as a function of different CuO diameters, as the authors' themselves observe great variations in CuO sizes. The estimation clearly evidences the significant impact of respective CuO nanoparticle sizes on the temperature reached after the heating period. Given the melting temperatures for both copper oxides considered (1599 K and 1505 K for CuO and Cu_2O, respectively), only isolated CuO nanoparticles with the smallest size (50 nm in diameter) surpass these temperatures within the pulse duration. The maximum temperature that can be reached for the Al:CuO system with the smallest CuO is 1241 K.

Looking exclusively at this theoretical analysis, it can be concluded that the formation of a wetted interfacial region and subsequent reactive sintering as described in Ref. 85 cannot be achieved by laser heating while assuming a homogeneous temperature through thermal conduction between the Al and CuO in contact. However, if instead the CuO particles are, at first, considered to act as a thermally isolated species, it is possible that the temperature reached by the smallest size CuO in contact with Al could induce either partial melting or at least sufficient pre-melting to induce the formation of a wetting contact angle. This corresponds to the calculations of isolated CuO nanoparticles with smaller diameters heated to temperatures well above the CuO melting point (2312 K). This suggests that the system may be inhomogeneous with very hot points composed of small melted CuO nanoparticles that fall into contact with and wet other nanoparticles, either CuO or Al, of larger size. In Ref. 85, the authors also tested individual CuO nanoparticles that, with no possibility of exothermic reaction, were expected to either melt immediately during the laser pulse or not at all. On the contrary, they found that size dependent delays occurred similarly to the Al:CuO thermite

experiment. These delays were attributed to laser-induced reduction of the CuO and this hypothesis was confirmed with selected area diffraction patterns that both Cu_2O and Cu were also present in the product.

The original results from Egan *et al.*[85] also show large discrepancies in initiation delays, from the nanosecond regime discussed above to a few μs, possibly due to the inhomogeneity of CuO particles both in shape and in size. Theoretical calculations consistently show that CuO particles exceeding 50 nm in diameter will not melt after the 12 ns laser heating pulse leading to an increase in *de-facto* initiation delays. Therefore, further tests were completed to simulate the reaction of larger CuO particles (100 nm and 200 nm in diameter) with 80 nm Al particles at a large wetting contact angle (θ = 171°), which corresponds to cases where the temperature reached by laser heating will not be sufficient to initially melt and sinter the particles. The results for this setup as a function of initiation temperature are presented in Figure 3.5. Taking the theoretical temperature achieved from the laser heating in Table 3.1 for the 100 nm CuO (1190 K) gives an initiation delay of 13.8 μs. For the 200 nm CuO (805 K), the initiation delay is 31.5 ms. The importance of the impact of CuO particle size is clear and shows that CuO particles with a size of ~100 nm best fit the experimental findings. Thus, it is likely that Egan *et al.* have an inhomogeneous population of CuO nanoparticles (with additional differences in the shape) that may be composed of nominal 50 nm CuO with larger sized aggregates, exhibiting initiation delays in the microsecond regime. In this case, the melting of small CuO nanoparticles (~50 nm in diameter and less) can support the melting of larger size particles, as well as boosting, through reactive sintering, the redox reaction at the interfaces with aluminum nanoparticles. This would explain the drop in initiation delays to a few μs when aggregates of less than 500 nm are present in the energetic Al:CuO mixture.
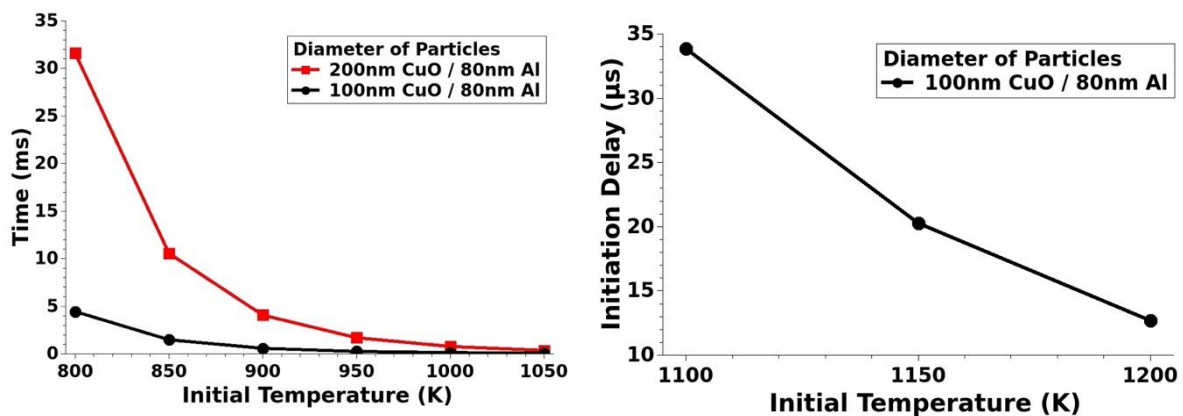
Figure 3.5 : The initiation delay as a function of the Al:CuO initial temperature with θ = 171°: left side, for two system sizes: (black curve, circles) 80:100 nm in diameter, (red curves, squares), 80:200 nm in diameter; right side, zoomed view of 80:100 nm system in the high temperature region.

3.3   Medium Heating Rate Initiation (T-Jump Experiment)

In this section, a lower, medium heating regime is utilized to initiate the nanothermites through the Joule effect. The T-Jump/TOFMS (time-of-flight mass spectrometer) experimental

setup was developed by Zhou *et al.*[101] to study condensed state reactions after initiation from a rapidly heated wire where the reactants are within the ion-extraction region of a time-of-flight mass spectrometer. The probe consists of a 76 μm Pt wire that is coated in a thin layer of the energetic mixture that is then resistively heated at a rate up to ~10^6 K/s. In Ref. 85, T-Jump experiments of Al:CuO nanoparticle mixtures were performed, heated at 5 x 10^5 K/s under high vacuum. The connection to mass spectrometry equipment allows *in-situ* measurement of the nature of gas released (O_2 and aluminized molecules such as AlO, Al_2O, etc.) as the temperature increases. In the reported experiment, a photodiode captures the light emission *in situ* concomitantly with the mass spectrometer.

To reconstruct these experiments *in silico*, the same program framework is used with an applied heating rate of 5 x 10^5 K/s to analyze the temperature and species' evolution in the system. The resultant simulated temperature evolution as a function of the degree of sintering (θ) to observe its effects on the initiation delay are illustrated in Figure 3.6. Multiple wetting contact angles are applied to validate the theoretical formulation in face of the reality of these experiments where both particle size and the wetting contact angle see a continuous change during sintering.
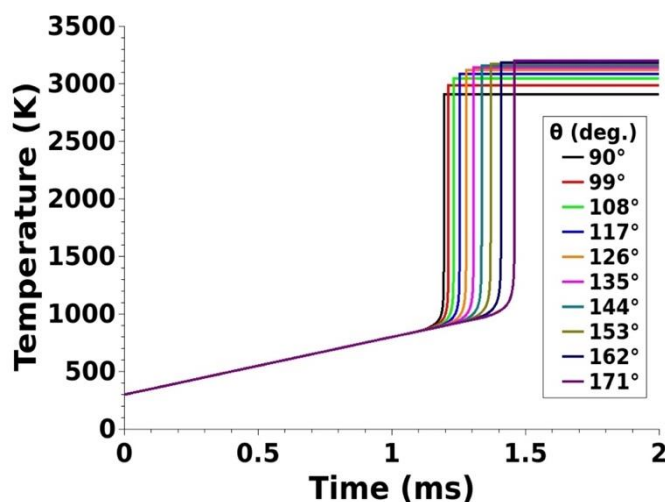
Figure 3.6 : The Al:CuO temperature evolution as a function of time for the T-Jump experiment with various wetting contact angles with a ramp set at 5 x 10^5 $K.s^{-1}$ as in Ref. 85

As in the DTEM experiment, the temperature evolution exhibits three clear phases. The first stage shows an increase in temperature resulting nearly exclusively from the external constant heating rate for a duration of ~1 ms. All contact angles display the same slope for this period, as the early redox reactions have a negligible effect at this point of experiment. A second phase is defined by the highly exothermic redox reaction until a final third phase reaches a constant temperature as all reactive material is exhausted. Initiation is first obtained for the lowest contact angle (90°) with an initiation delay of 1.1 ms. At the minimum degree of sintering, therefore for the largest wetting contact angle of 171°, this delay increases to 1.4 ms. Thus, varying the contact angle leads to only moderate modification of the initiation time (a 0.3 ms difference), indicating that the degree of sintering, or the time until full coalescence, if valid for medium heating rate experiments, will have a limited effect on initiation delays. This,

again, confirms the proposition by Sullivan *et al.*[45] that the timescale of reactive sintering is negligible in light of the full initiation timescale (see Figure 1.12).

Note that the initiation temperatures (ranging from roughly 850 to 1050 K) are much lower than those applied in the rapid heating experiments (around the melting point of CuO nanoparticles), which indicates that at the initiation point, it is possible that only the aluminum has melted. This corroborates the absence of a firm correlation between initiation times and temperatures. The results from these simulated experiments calculate initiation delays that are of the order of magnitude of experimental observations that range from roughly 1.5 to 1.7 ms depending on the detection method. The slightly higher initiation times observed experimentally may be due to the different modes of detection, either by gas phase species detection via spectrometer or from optical detection of ionized species, possibly emanating from gaseous species in contact with or not far from the surface.

3.4   Comparison with Gas Phase Model

After validation of the model by experimental results, it was further exploited to quantifiably analyze the respective role of gas versus condensed phase mechanisms for the initiation of aluminothermites. Results of a T-Jump-like experiment are compared to simulations from an existing reaction model based exclusively on gas-phase mediated reactions, described in Section 1.4.2. As explained, this model considers a more complex mechanistic scenario in its treatment of the reaction, where all exothermic processes are mediated by the gas phase. To summarize:

1) Low temperature diffusion is dominated by the migration of core Al atoms to the outer surface of the shell (*i.e.,* diffusion of Al across the alumina shell).
2) The liberated Al can oxidize, either on the surface or in the gas phase after evaporation, if the temperature is sufficient for this process.
3) Gaseous oxidizing species can emanate either from an open-air condition and/or from the decomposition of CuO.
4) An equilibrium of intermediate gas phase species (O, Al_2O, AlO, etc.) is established at each time step.

Thus, these mechanisms assume two major exothermic processes:

i)   gaseous oxidation of evaporated aluminum with oxidizing species
ii)   aluminum oxidation (after the Al diffusion from the core of Al nanoparticles to the surface) in contact with the gas phase oxidizing species

It is, therefore, necessary to consider a nominal confinement of the gas phase to allow for reaction in the gas phase model. To reproduce the vacuum conditions in the T-Jump experiment, a very low compaction is chosen (0.1 %TMD) to prevent high pressures in the combustion chamber in the gas phase model. It is important to note and keep in mind that these assumptions

should lead to underestimated initiation delays for the gas phase model. To correctly compare the two models, the experimental protocol from the previous sections (3.1-2) is equivalently applied here. The parameters are summarized in Table 3.2.

Table 3.2 : The main input parameters both the condensed phase and gas phase based models utilized for comparison in Figure 3.7. The initiation-only base model of the condensed phase formulation does not account for chamber/macroscale properties.

Parameter	Condensed Phase Model Value	Gas Phase Model Value
Diameter of Al particles	76 nm	
Diameter of CuO particles	50 nm	
Native Oxide Shell Thickness	2 nm	
Stoichiometric Ratio	1.0	
Initial Temperature	300 K	
% TMD	-	0.1 %TMD
Heating Power	-	1.4 kW
Heating Duration	-	2.5 ms
Chamber Length	-	0.7 mm
Chamber Diameter	-	4 mm

Figure 3.7 presents a comparison of the temporal evolution for these two models. Observing the initiation times calculated at 1.19 – 1.46 ms for 171° and 90° contact angles, respectively, it is evident that mass transport and the resulting exothermic reactions in the condensed phases are more efficient than those mediated through the gas phase.
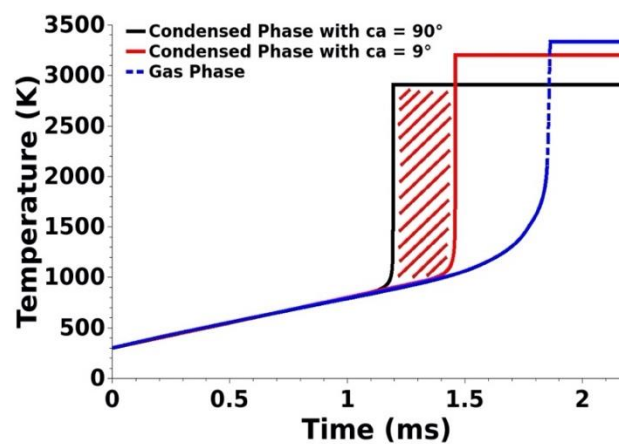
Figure 3.7 : The Al:CuO temperature evolution from ambient to point of initiation as calculated via a gas-phase reaction model (dotted blue) and via a condensed-phase reaction model, with consideration of all contact angles (dashed portion) from a contact angle of 171° (solid black) to 90° (solid red). For both simulations, the heating ramp is 5 x 10^5 K/s.

While remaining on the same order of magnitude, the gas phase driven model finds an initiation delay at 1.83 ms. The nominal difference in initiation delays for the two extremes of the contact angle range (minimum, 171°, maximum, 90°) again confirms the minimal impact of sintering on a medium heating rate setup.

Increasing or decreasing the confinement of gaseous species, by varying the %TMD, does not show a strong influence on the initiation delay; the lowest initiation delay is obtained for 50 %TMD at 1.8 ms, constituting a saturated minimum value for the initiation delay (see Figure 3.8). Ultimately, the initiation through the condensed phase, while slightly more efficient and quicker, exhibits a comparable timescale to the initiation delay through a gas-condensed heterogeneous reaction. As both fall into accordance with the general range of initiation delay found experimentally, it is concluded that potentially both are present and make an important contribution during the initiation phase.
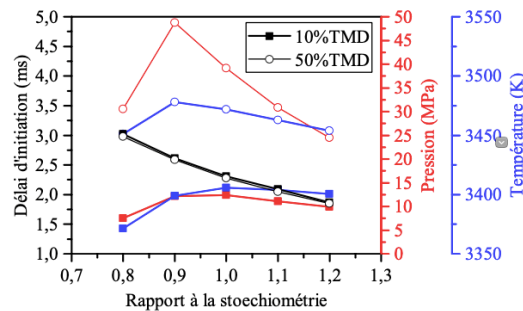
Figure 3.8 : Comparison of the initiation delay (black), pressure (red), and temperature (blue) for two %TMD (solid, 10% ; hollow, 50%) as a function of the stoichiometry simulated using a gas-phase based model formulation. **[118]**

3.5   Effect of Key Parameters on Initiation

Previous sections validate the predictive nature of our approach based on explicit treatment of the condensed phase mechanisms for simulation of the initiation stage of Al:CuO thermite materials in the form of nanoparticle mixtures. Given this preliminary validation of the model by the general agreement of predictions with both experimental initiation delays and a previously corroborated gas-phase based model, the model was further exploited to attempt to look at common variables in experimental design. However, a major limitation in this model formulation is the co-dependence of the stoichiometric ratio and the particle sizes due to the single particle pairing design. Given that one oxide particle is always paired with one fuel particle, the stoichiometric ratio will always be fixed as the ratio between these two particle sizes. As outlined in Section 2.3, it is therefore up to the user to either define both particle sizes or to fix a stoichiometric ratio and one of the particle sizes, with the other particle size adjusted to meet the stoichiometric ratio. Despite this restriction on normally independent variables, it is possible to investigate the effects of them within this limited context. Additionally, all results from this point take into account the vaporization temperature limit to restrict the simulation to a temperature range corresponding to condensed phase reactions.

3.5.1   Stoichiometric Ratio

First, the initiation delay is tested for the Al:CuO couple as a function of the stoichiometric ratio while holding the diameter of the Al fuel particle constant. To coordinate with many experimental studies, this diameter is fixed at 80 nm. The resultant CuO oxide particle size is then determined for each simulation according to the stoichiometric ratio. Table

3.3 presents the parameters for these simulations, where all couples have the same wetting contact angle at $\theta = 135°$.

\

Table 3.3 : Resultant CuO oxide particle diameters as a function of the stoichiometric ratio and the constant Al fuel particle diameter = 80 nm with θ = 135°.

Stoichiometric Ratio	Diameter of Al fuel particle	Diameter of CuO oxide particle
0.8	80 nm	107 nm
0.9		103 nm
1.0		99 nm
1.1		96 nm
1.2		93 nm
1.3		91 nm
1.4		89 nm
2.0		79 nm

The resultant initiation delays for these tests are presented in Figure 3.9. In comparable experimental studies, it has been found that mixtures with a stoichiometric ratio of 1.2 produces the fastest burning rates, and, in some cases, the shortest initiation delay.[77] Generally, multiple studies have shown optimal thermite performance (*i.e.,* low initiation delay with a high burning rate) for slightly fuel-rich mixtures with stoichiometric ratios ranging from $1.2 – 1.5$.[43,81,94,95]
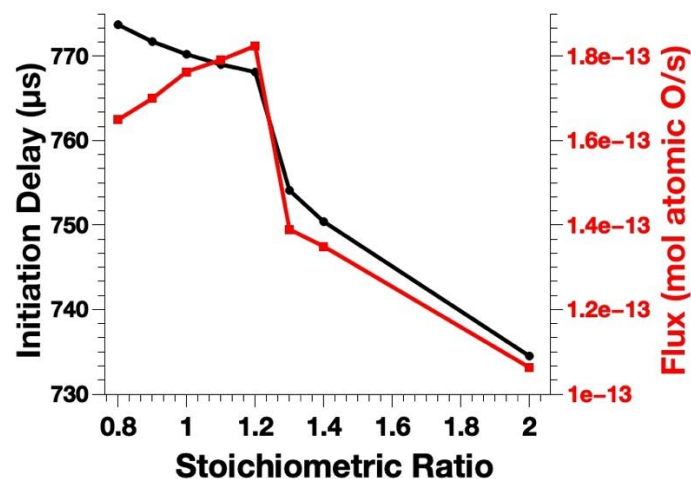
Figure 3.9 : The initiation delay and flux (mol of atomic O/s) of the Al:CuO thermite system with constant D_{Al} = 80 nm and varying D_{CuO} as a function of the stoichiometric ratio.

Observing the simulated results, in the case of various CuO particle sizes, there are two linear regimes: 1) a first linear reduction of the initiation delay up to $\xi = 1.2$ followed by a large reduction to 2) a steeper linear reduction for fuel rich mixtures of $\xi > 1.2$. However, looking at the flux of moles of atomic oxygen entering the fuel particle at initiation, the maximum value is found for $\xi = 1.2$. There is a nearly linear increase in the flux from $\xi < 1.2$, followed by a

large reduction in this value after $\xi = 1.2$ with a linear reduction as a function of increasing stoichiometric ratio for $\xi \geq 1.3$.

Table 3.4 : Resultant Al fuel particle diameters as a function of the stoichiometric ratio and the constant CuO oxide particle diameter = 100 nm with $\theta = 135°$..

Stoichiometric Ratio	Diameter of Al fuel particle	Diameter of CuO oxide particle
0.8	75 nm	100 nm
0.9	78 nm	
1.0	81 nm	
1.1	83 nm	
1.2	86 nm	
1.3	88 nm	
1.4	90 nm	
2.0	102 nm	

This experimental setup was also simulated in the other direction, holding the CuO oxide particle to the standard size of 100 nm while varying the Al fuel particle diameter to achieve different stoichiometric ratios. The Al particle diameters range from 74.9 nm, which is slightly under the nominal particle size at 80 nm, to 101.69 nm (Table 3.4).
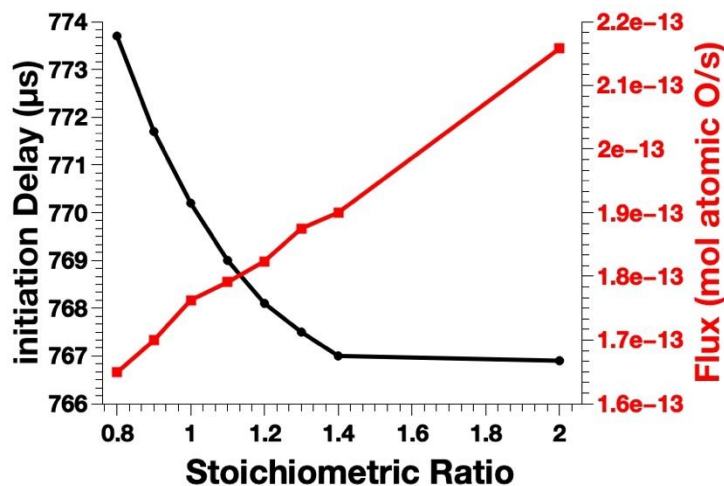
Figure 3.10 : The initiation delay and flux (mol of atomic O/s) of the Al:CuO thermite system with constant D_{CuO} = 100 nm and varying D_{Al} as a function of the stoichiometric ratio.

In Figure 3.10, there is a nearly linear reduction in initiation time as a function of stoichiometric ratio up to the fuel-rich regime ($\xi = 1.4$). This generally corresponds to the experimental studies that show the lowest initiation delay for slightly fuel-rich mixtures.[77] After this stoichiometric ratio, the initiation delay does not increase as seen experimentally, but does not significantly decrease for $\xi = 2.0$. Interestingly, in this case the flux of moles of atomic oxygen arriving to oxidate the fuel particle increases linearly as a function of the stoichiometric ratio.

To better investigate the possible cause, further simulations were completed to better investigate the role of each material's particle size. The following results present different fuel and oxide particle sizes that are held to the same stoichiometric ratio.

3.5.2   Particle Size

In an experimental study of Al:MoO$_3$ nanothermites by Granier *et al.*[77], it was found that varying the Al particle diameter for a fuel-rich stoichiometric ratio ($\xi = 1.2$) showed a 99.8% reduction in initiation delay for Al-nano thermites compared to micrometer composites. For particles within the nanoscale, there appears to be a minimal value under which there is no further reduction in initiation time. The authors hypothesize that at this critical limit around 50 nm in diameter, the increased ratio of native oxide relative to the other materials limits the performance improvements.
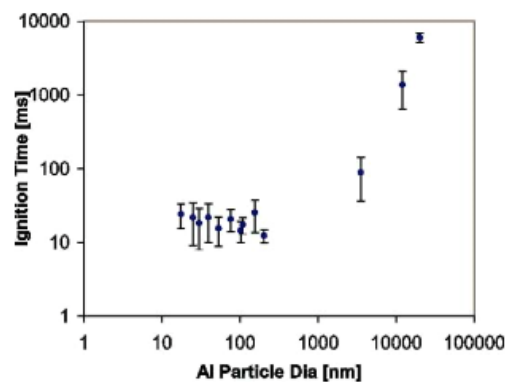
Figure 3.11 : Ignition time of Al:MoO$_3$ nanothermites, $\xi = 1.2$, as a function of the Al particle diameter. **[77]**

The simulated results emulate a similar set-up for Al:CuO thermites where the Al fuel particle size and the stoichiometric ratio are set, with a corresponding calculated CuO oxide particle size. The resultant initiation times for this set-up are presented in Figure 3.12 on a logarithmic scale. There is a clear proportional relationship with a reduction in initiation times as a function of the decreasing Al diameter; however, the implication of a critical minimum size is not apparent in the simulated results. This is not surprising given the previously stated limitations due to the single particle pair. In the experimental study, the MoO$_3$ oxide particle diameter is constant, while the stoichiometric ratio is achieved as a function of the total quantities of each material in the final mixture. As such, there is a potential effect of the oxide particle size that inhibits the individual study of the fuel particle diameter. However, the significant reduction in initiation delay between microscale and nanoscale components is evident for the simulated results. For a reduction in particle size from 1 μm to 100 nm, there is a corresponding reduction of ~38% in initiation delay. This difference increases to an approximately 50% reduction considering nanoparticles of 50 nm and smaller.
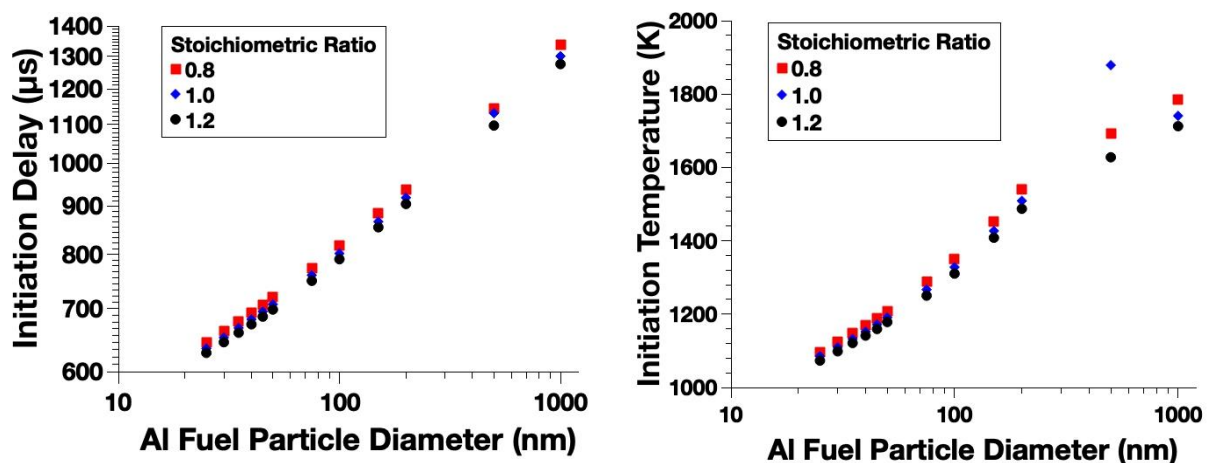
Figure 3.12 : The initiation results of Al:CuO thermites as a function of Al fuel particle diameter for three stoichiometric ratios: 0.8 (red squares), 1.0 (blue diamonds), 1.2 (black circles); left, initiation delays, right, initiation temperatures.

Huang *et al.*[83] completed a literature review of different studies of the initiation of Al particles alone as a function of their diameter in oxygen-containing environments. They determined two regimes: 1) an exponential increase in initiation temperature as a function of particle diameter for particles smaller than 10 – 100 μm, 2) a stagnation in initiation temperature for particles greater than 10 – 100 μm. Looking at the simulation results of the initiation temperature as a function of the fuel particle size, a similar relation is found where the initiation temperature decreases exponentially for smaller fuel particle sizes. While different stoichiometric ratios present slightly different results for larger particles, the general results correspond well with Huang *et al.* that also showed variable discrepancies to the general relation in the micron-regime (Figure 1.4). In any case, the overall performance improvements seen experimentally for nanoscale components is equally reflected in the simulation results.

3.5.3   Native Oxide Shell Thickness

The final factor that can significantly affect the characteristics of initiation is the thickness of the native oxide shell of the Al fuel particle. It is possible to control the formation of the oxide layer during the fabrication process. As detailed in Chapter 1, a study of the effect of this shell was produced by Chowdhury *et al.*[87] by comparing the initiation delay of ~50 nm Al nanoparticles with an original native shell of ~2 nm, with some particles further oxidated at 773 K until obtaining a shell thickness of 3 or 4 nm, mixed with < 100 nm particles of CuO in a T-Jump experimental setup. It was found that there is a nearly linear increase in initiation time as a function of the native oxide shell thickness, according to the detection of Cu by mass spectrometry (see Fig. 1.8).

This experimental setup was adapted and simulated with the model, with the caveat that the stoichiometric ratio of the base mixture will be affected as the calculation is a slight estimation that does not account for the native oxide shell alumina. Thus, the system is designed as a 50 nm in diameter Al particle paired to a ~60 nm CuO particle, for $\xi = 1.2$, and a 62 nm

CuO particle, for $\xi = 1.0$, where only the native alumina shell thickness varies from 1 nm to 4 nm. The results from these simulations are displayed in Figure 3.14.
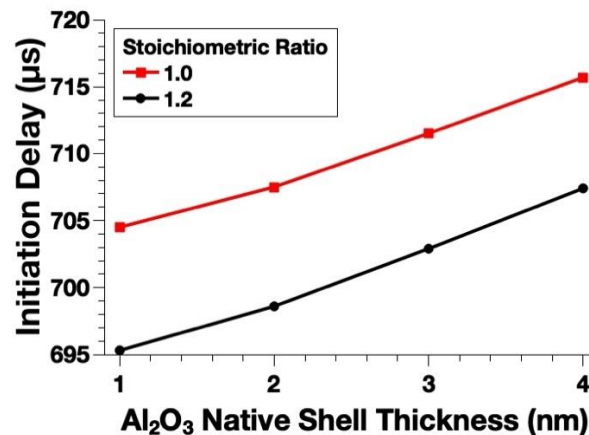
Figure 3.14 : The initiation delay of the Al:CuO nanothermite as a function of the native alumina oxide shell for two stoichiometric ratios: 1.0 (red squares) and 1.2 (black circles).

At a stoichiometric ratio of 1.0, the initiation delay has a range of 705 μs to 715 μs as the shell thickness varies from 1 nm to 4 nm, with a similar difference of 10 μs in initiation delay (695 μs to 705 μs) for $\xi = 1.2$; however, at $\xi = 1.2$, the black curve shows a slightly steeper increase in initiation delay from 1 to 2 nm shell thickness. Given the significantly smaller CuO particles within the simulation when compared to the experimental setup to maintain the stoichiometric ratio, it is not surprising that the simulated initiation delays, while on an order of magnitude of the experimental study results, are a bit higher. Still, the simulated results are extremely consistent with the pattern found by Chowdhury *et al.*[87], showing a very nearly linear dependence of the initiation delay on the native oxide shell thickness. A thicker native oxide shell will limit the oxygen flux arriving at the native oxide shell/fuel material interface which will slow the initiation of the system. In most thermite couples, the diffusion through the oxide shell is the limiting factor instead of the diffusion of the freed oxygen through the already-reduced oxide material; thus, the shell thickness is a parameter that should be heavily considered in thermite design. Additionally, the thicker the shell, the less unoxidized fuel material is available to produce the exothermic reaction necessary for applications that require a higher heat production. In this case, the final temperature attained is constant regardless of the oxide shell thickness, due to its restriction by the applied vaporization temperature limit to consider only condensed-phase reaction. However, in real life applications, the oxide shell thickness is an important tunable factor to optimize the nanothermite performance according to the desired application.

3.6   Benchmark Study of Different Materials

After the validation of the model for Al:CuO nanoparticles, giving a good estimation of initiation delays in comparison to experimental results, and an examination of the effects of important parameters, the model was further exploited to explore material pairs that are growing in interest for new applications, yet lack experimental study. The varied fuel and oxide materials were chosen to highlight pairs that produce minimal gas, thus making them better

suited choices for a model considering only condensed-phase reactions. Aluminum, boron, magnesium, and zirconium were considered as choices for fuels, while oxides including cupric oxide (CuO), ferric oxide (Fe_2O_3), tungsten trioxide (WO_3), and lead tetroxide (Pb_3O_4) were proposed. The fuel species were chosen based on novel application propositions, while the oxide choices were based upon low gas-producing species.[59,116] Unfortunately, some of these materials are not fitting choices for a purely condensed-phase reaction due to low vaporization temperatures, such as magnesium (1373 K) or the intermediate reduced oxide of lead tetroxide, lead monoxide (PbO, 1808 K) in certain combinations. The final difficulty in applying this model to new materials is the low amount of information available on the diffusion coefficients of composite materials, as well as thermal parameters for these species on the nanoscale. Additionally, the reaction pathways for these different thermite couples are not certain. For example, some species, such as Fe_2O_3, have been hypothesized to follow a two-step reduction with an intermediate reduced oxide product of FeO or Fe_3O_4.[153–155] There are also examples of fuel species that undergo a two-step oxidation, such as tantalum, which is not considered in this benchmark study.[133,134] The model is generalized to allow a user to define the reaction pathway according to their desired sources by the inclusion of an input parameter for each species defining it as a one or two-step oxidation/reduction, respectively, and the explicit definition of intermediary reaction species. All relevant values taken from the currently available literature are presented in Tables 3.5 and 3.6.

Table 3.5: Oxygen diffusion coefficient pre-factors and activation energies in various fuel species including aluminum, boron, and zirconium.

Fuel Species	Oxide Species	Diffusion Coefficient, D_0 ($m^2.s^{-1}$)	Activation Energy, E_a ($kJ.mol^{-1}$)	Sources
Al	Al_2O_3	9×10^{-5}	140	48,129
B	B_2O_3	2.5×10^{-6}	137	137
Zr	ZrO_2	9.73×10^{-7}	234	141

Table 3.6: Oxygen diffusion coefficient pre-factors and activation energies in various oxide species including CuO, Fe_2O_3, WO_3, and Pb_3O_4.

Oxide Species	Diffusion Coefficient, D_0 ($m^2.s^{-1}$)	Activation Energy E_a ($kJ.mol^{-1}$)	First Reduced Species	Final Reduced Species	Sources
CuO	1.16×10^{-6}	67.3	Cu_2O	Cu	48,128
Fe_2O_3	6.3×10^{-2}	405	FeO	Fe	139
WO_3	6.82×10^{-6}	125	-	W	144
Pb_3O_4	5.39×10^{-9}	94	PbO	Pb	146

To standardize the results to allow for qualitative comparison between the different species, the fuel species particle is consistently 80 nm in diameter, while the oxide particle size varies in accordance to a stoichiometric ratio of 1.2. The wetting contact angle is also held constant at 135°. The thermite couples have an applied external heating ramp of 10^3 K/s that is maintained until the exothermic reaction overcomes this heating rate following the T-Jump experimental setup. The heating ramp was reduced to a lower heating rate (compared to the ramp applied in the rest of this chapter, $\geq 10^5$ K/s) to account for the variability in volumetric heat capacity and the resultant heat produced by the redox reaction for each pairing. Each individual thermite coupling has a customized disruption or vaporization temperature limit that is set as the minimum of all vaporization temperatures of the fuel, oxidized fuel, oxide, and intermediate oxide (if two-step reaction) materials. As previously stated, given the uncertainty of the diffusion coefficients of oxygen in each material, particularly on the nanoscale, as well as the reaction pathways for each species' reduction or oxidation, the goal of this model is to provide qualitative more so than quantitative results to aid in system design. The resultant initiation delays for these different nanothermite couples are presented in Table 3.7.

Table 3.7 : Initiation delays and temperatures for different nanothermite couples with D_{fuel} = 80 nm, ξ = 1.2, and θ = 135°

Fuel Species	Oxide Species (size in nm)		Heat of Reaction (kJ)	Vaporization Temperature (K) (Species)		Initiation Delay (ms)	Initiation Temperature (K)
Al	CuO	(93)	397.5	2070	(Cu_2O)	48	847
	Fe_2O_3	(87)	281.7	2743	(Al)	152	1956
	WO_3	(88)	277.6	1975	(WO_3)	52	896
	Pb_3O_4	(106)	378.8	1808	(PbO)	88	1417
B	CuO	(121)	104.1	2070	(Cu_2O)	75	1183
	Fe_2O_3	(112)	149.2	2130	(B_2O_3)	163	2080
	WO_3	(114)	149.0	1973	(WO_3)	76	1192
	Pb_3O_4	(138)	244.3	1808	(PbO)	108	1690
Zr	CuO	(92)	394.3	2070	(Cu_2O)	135	1826
	Fe_2O_3	(85)	275.5	3135	(Fe)	156	2033
	WO_3	(87)	248.3	1973	(WO_3)	147	1972
	Pb_3O_4	(105)	370.6	1808	(PbO)	138	1765

On a qualitative basis, there are clear patterns that emerge. Obviously, the corresponding size of the lead oxide particles are always the greatest (> 100 nm) due to the density of lead atoms. All other oxide species had relatively similar particle diameters, in the 80-90 nm range. For each fuel species, the iron oxide thermite has the longest initiation delay and initiation temperature. This is most likely due to the low diffusivity of oxygen in iron oxides, as well as the high temperature of decomposition of Fe_2O_3 (1573 K). All iron oxide couples show an initiation temperature significantly higher than this decomposition temperature. Generally, the thermites containing WO_3 initiate on a similar order of magnitude

as CuO, while Pb_3O_4 thermites show a tendancy to longer initiation times and significantly higher initiation temperatures.

Comparing the results further based on the fuel species, aluminum-based thermites are the most efficient and systematically exhibit the lowest initiation delay as well as the lowest initiation temperature for all tested oxidizers. This fuel species also has the lowest melting point at 933 K, lending itself well to a purely condensed phase reaction. The lowest initiation delay is obtained with CuO and WO_3 with a temperature of initiation around 850-900 K, which corresponds to the activation energy of oxygen migration through the alumina barrier layer ($E_a = 140$ kJ.mol^{-1}). Therefore, the reaction is limited by this specific diffusion event indicating that decomposition and diffusion through the oxidizer occur at or below this temperature. The $Al:Pb_3O_4$ thermite also shows a tendency to longer initiation delay with a significantly higher initiation temperature. Given the strong performance of all other aluminothermites, it is possible that this case may instead be limited by the slow diffusion of oxygen through the intermediate reduced oxide, PbO, with an oxygen diffusion on the scale of 10^{-10} m^2/s for the temperature range of reaction.

The boron-based thermites show a slight increase in initiation delay and temperature when compared to the aluminum-based. This can likely be attributed to the lower heat of reaction (*i.e.,* 104 kJ/mol of atomic oxygen reacting with B compared to 397.5 kJ/mol of atomic oxygen reacting with Al), as the migration of oxygen species across the growing oxidized fuel barrier layer show similar activation energies (137 and 140 kJ/mol for B_2O_3 and Al_2O_3, respectively) leading to relatively close diffusion coefficients in the reaction temperature range (10^{-8} m^2/s at 2000 K for Al_2O_3 and 3000 K for B_2O_3, see Figure 4.10).

The zirconium-based thermites are the least performant with long initiation delays and significantly higher initiation temperatures across the board. This is due to the much higher activation energy that is necessary for the oxygen atoms to migrate towards the fuel (234 kJ/mol) leading to low oxygen diffusivity (10^{-10} m^2/s) until around 3000 K. Interestingly, this hindered migration is such that all initiation delays fall into the same range (or slightly lower) than that of iron oxide, 130 to 160 ms range. In addition, the initiation temperature is observed to be closer to the vaporization limit. Therefore, it is possible that the initiation of these thermites is partially dominated by gas-phase reactions.

A final simulation was performed to determine if the degree of sintering affects a thermite couple with very different initiation characteristics than the original $Al:CuO$ study. To test this, a simulation was completed for the $Al:Fe_2O_3$ thermite pairing with 80 nm Al and 87 nm Fe_2O_3 particles ($\xi = 1.2$) with a heating ramp of 10^5 K/s.

Figure 3.15 displays a zoomed in view of the temperature profiles as a function of time for this thermite couple with a wetting contact angle ranging from 90° to 171°. The resultant initiation delays range from 1.82 ms (90°) to 2.04 ms (171°). Comparably to the $Al:CuO$ results (Figure 3.6), varying the contact angle shows only moderate modification of the initiation time

with a difference of 0.2 ms. This again indicates that the sintering timescale is likely significantly shorter than the overall initiation timescale, thus, its effect on the initiation kinetics is not transformative, as observed with more reactive thermites such as Al:CuO.
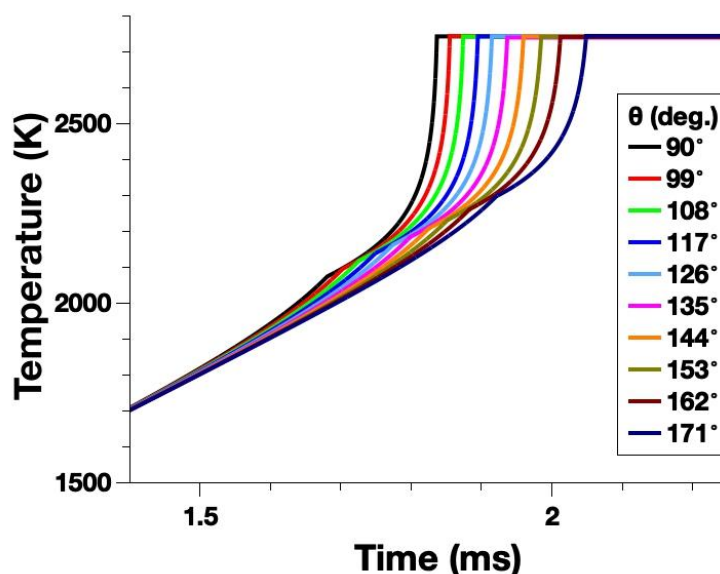
Figure 3.15 : The temporal profiles of the Al:Fe$_2$O$_3$ nanothermite (D_{Al} = 80 nm, ξ = 1.2) as a function of the wetting contact angle, θ.

3.7 Conclusion

In this chapter, the results of the first formulation of the model consisting of a single fuel particle paired to an oxide particle and initiated through different external heating regimes is presented. First, this model was validated by comparing simulated results of an Al:CuO nanothermite couple under medium and high heating rates with experimental results from Ref. 85. The model gives satisfactory determination of initiation delays for both high and medium heating rates. The impact of the degree of sintering on initiation was specifically addressed for both heating regimes, showing contrasting effects. The high heating rate (10^{11} K/s) experiment, initiated through laser heating, was replicated *in silico* by the application of an initial temperature as a function of the size and absorptivity of the nanoparticles. For these experiments, the contact angle heavily influenced the initiation delay, showing initiation delays similar to the experimentally observed morphological changes (~ hundreds of ns) for only the most pre-sintered pairs (90° ≤ θ ≤ 117°). In this case, the initiation of the reaction is dominated by the temperature rise in CuO nanoparticles because of its absorption of the laser power density, more than the sintering itself. In contrast, all other experiments presented follow the T-Jump experiment protocol by applying a constant heating rate (from 10^3 to 10^5 K/s) until the self-sustaining exothermic reaction exceeds the applied ramp. Utilizing this medium heating rate experiment, the effect of the wetting contact angle was investigated. Contrary to the high heating rate experiments, it showed a minimal influence of the degree of sintering on the initiation delay, as previously hypothesized by the calculation of timescales for both sintering and the overall reaction by Sullivan *et al.*[45] In response to the strong debate in the literature to identify gas phase versus condensed phase mechanisms in thermite combustion, a direct comparison with a gas phase-based model was also utilized to study the dominant mechanisms

at play in the initiation of nanothermites. While slightly lower initiation delays are obtained when using condensed phase mechanisms, gas phase reactions remain plausible in the initiation at medium heating rate. These simulations provided a quantitative validation of the model basis when compared to the experimental results, finding initiation delays of ~1.5 ms for medium heating rates.

Given this confirmation of the simplified condensed phase model, it was then extrapolated to probe the effect of varying key parameters of the system including the particle sizes, into the microscale, the native oxide shell thickness, and the stoichiometric ratio. The discrete formulation of a single particle pairing does limit the quantitative comparison with experimental results, yet overall patterns of improvements in performance are observed as the particle size is reduced. Additionally, slightly fuel-rich mixtures ($1.2 \leq \xi \leq 1.5$) are found to produce lower initiation delays and temperatures. It is important to note that, given the limitations of the model, simulated results for very small particles or increasingly fuel-rich mixtures may underestimate the initiation delays.

Finally, the model was exploited to complete a benchmark study of qualitative comparison of different nanothermite couples. With the increasing availability of nanoscale fabrication methods, novel applications are calling for new, tunable thermite couples that will produce the desired reaction. Some of these innovations specifically require low or no gas production due to the environment or apparatus, and, thus, this model can be a useful tool for system design in comparing materials quickly and at low computational cost. For all fuel species, ferric oxide (Fe_2O_3) is found to produce the longest initiation delays and highest initiation temperatures, while cupric oxide (CuO) leads to the fastest initiation, closely followed by tungsten trioxide (WO_3). Aluminum-based thermites show the best performance, while zirconium-based are the least performant when regarding the fuels. Vaporization temperature limits are applied in these cases to contain the reactions to the condensed phase only. If a simulated couple does not appear to initiate below these temperatures, it is possible that gas-phase mechanisms are dominant in the initiation of that nanothermite.

In the next chapter, the development of a second model formulation that extends the model to simulate the complete propagation of a discretized tube or burn line populated by the base unit single particle pairing presented in this chapter is detailed. Once established, the model is similarly exploited to determine the effect of parameters such as the particle sizes, compaction as a percentage of Theoretical Maximum Density (%TMD), and stoichiometric ratio on the macroscopic initiation delay and steady-state propagation speed. A benchmark study of the same materials explored in Section 3.5 is developed.

92

CHAPTER 4. Full Model Validation & Exploitation to Study Nanothermite Propagation

4.1 Introduction

Chapter 2 provided the detailed formulation of a purely condensed phase model for nanothermites based upon the diffusion of freed oxygen from the reduced oxide material to oxidate the fuel species. This extremely exothermic reduction-oxidation reaction becomes self-sustaining as the heat produced after initiation can propagate the reaction along an apparatus. The previous chapter detailed the validation and exploitation of a base model considering a single particle pair. This limits the evaluation of simulated results to the initiation of the nanothermite, whereas most applications will require a self-sustained propagation of the reaction along either a tube or an open channel. To provide an analytical tool for full propagation system design, the base model was extended into a coupled mesoscopic formulation that permits consideration of the chemical reactions and mechanisms at the nanoscale, while calculating the macroscopic reaction on longer dimensional and time scales.

The main challenge in the development of this coupled model was to determine the correct driving force of heat transfer that could provide accurate simulations of the steady-state propagation of nanothermites. In the first section, an evaluation of the three proposed mechanisms, as described in Section 2.4.1 - 2.4.3, for this heat transfer is presented. Laid out chronologically, the models include a combination of microscopic radiation from the particle pairs with a macroscopic conduction between adjacent cells, a second proposal integrating a macroscopic treatment of convection through a gaseous environment, and, finally, a purely conductive heat transfer through contact between particle pairs. Once the chosen formulation is validated, four different mathematical constructions of an effective conduction coefficient were compared to best represent the geometrical factors in a system with reactive sintering, while providing good qualitative measurements of thermite performance. Next, the model was further explored in light of recent experimental findings by Wang *et al.*[79]. The novel *in-operando* high-speed microscopy technology allows observation of the reaction with -μs time and -μm spatial resolution, and, thus, direct observation of the reactive sintering process.

In the final section, the validated model is exploited to test the effect of varying key parameters, such as the particle sizes, the rate of confinement (%TMD), and the stoichiometric ratio. This chapter concludes with a benchmark comparison of the different materials as tested for initiation in Section 3.6, and a look into the enhancements of the simulation when an envelope is considered.

4.2 Comparison of Macroscopic Heat Transfer Mechanisms

To determine which macroscopic heat transfer method would be suitable in the final complete propagation model, a direct comparison was made by studying a classic Al:CuO system. This entails a stoichiometric ratio of $\xi = 1.0$ at 60 % TMD with 80 nm Al nanoparticles including a 2 nm native shell. Correspondingly determined by Equations 2.35 and 2.36, the CuO nanoparticles are 99 nm in diameter. This mixture is placed in a 3 mm long open air line or tube, depending on the implementation. For tube apparatuses (radiative with envelope and gas convection simulated experiments), the inner diameter is 2 mm with a 3 mm thick wall. Thermal losses (conductive, convective, and radiative) have been systematically considered. All systems are initialized at the ambient temperature, 300 K, with an imposed limit of disintegration and loss of the condensed phase structure at 2070 K, the vaporization temperature of Cu_2O. All other material and reactive properties of importance can be referenced in Table 2.1 and Table 2.2. Additionally, it is important to note that two of the four tests include an envelope, while the other two are considered open air simulations. Those that consider a confining element are the second radiative/conductive heterogeneous mechanism test and the gas convective formulation. The equations for each model construction can be found in Section 2.4.

The results from all simulated systems are presented in Table 4.1. It is quickly clear that the best approach to find propagation speeds on the correct order of magnitude with respect to the experimental tests is the direct conduction method. The following subsections go further into detail on the faults or limitations of all of the theoretical formulations considered, providing a glimpse into the developmental process of the propagation model as it followed during the course of this thesis.

Table 4.1 : A summary of reaction characteristics for the three heat transfer methods tested in the development of the full propagation model including cell conduction of radiated heat from particles, a macroscopic treatment of propagation through gas convection, and direct particle conduction.

Formulation	Initiation Delay (ms)	Initiation Temperature (K)	Propagation Speed
Radiative	3.73	990	0.08 mm/s
Radiative w/ Envelope	13.6	997	80.66 mm/s
Gas Convective w/ Envelope	1030	1007	22.3 mm/s
Direct Conduction	59.3	944	61 cm/s

4.2.1 Radiative/Conductive Environment

As outlined in Section 2.4.1, the first approach to the macroscopic heat transfer along the experimental apparatus considers the conduction of heat driven by radiation from the particle pairs, due to their exothermic reduction/oxidation, as a contribution to the total heat in the cell. Practically, this heat is propagated between adjacent cells through a conduction-like treatment of the radiation. To construct this concept numerically, an effective conduction coefficient was

defined according to the formula for radiative heat loss and integrated into the conduction term of the heat equation.

$$\lambda_{rad} = 4\sigma T^3 \frac{D}{\%TMD} \qquad (4.1)$$

where D is the effective diameter of the pair, *%TMD* is the compaction rate, and σ is the Stephen-Boltzmann constant.

Two different *in-silico* experimental setups are explored with this formulation. The first considers an open air environment as with an open channel filled with a nanothermite mixture; however, an assumption is made that the radiated heat is not lost to the environment, but, instead, is exclusively conducted to heat the adjacent material. The resulting propagation velocity is extremely low at 80 µm/s, despite the fact that radiative losses are not considered. This implies that the radiative contribution marginally affects propagation. A second formulation now considers an envelope, closing the environment as in a burn tube experiment. In this case, to complete the thermal equation, two-dimensional conduction through the tube wall is added. The wall is discretized into concentric cylinders with a length of *dx*, as defined for the inner tube cells. The radii of each concentric cylinder are defined according to Eq. 3.44. This addition to the formulation increases the propagation velocity to 80.66 mm/s, which falls within the order of magnitude of the overall macroscopic propagation rate found in Ref. 44 (3.3 cm/s); however, it remains lower by almost an order of magnitude than the experimental microscopic propagation (50 cm/s), which is supposed to be governed by condensed phase processes (sintering). Clearly, radiation, even combined with conduction through the envelope, is not the best representation of a system with reactive sintering.

Looking at the system as described in the introduction of Section 4.2, the effective diameter of the two particle pair is estimated to $D = 172.38$ nm. Thus, considering a temperature range from the ambient to the vaporization limit (300 – 2070 K) leads to an effective conduction coefficient ranging from 1.76×10^{-6} (at 300 K) to 5.78×10^{-4} (at 2070 K). While a simple estimation, the values found are at minimum four order of magnitude smaller than the effective conduction coefficients calculated by the direct conduction method (~ 2 W/mK). In hindsight, it is apparent that another strategy must be considered, as this very low conduction rate does not propagate enough heat to lead to realistic propagation speed simulation. As a sidenote, while this formulation is not more costly in terms of computational resources than the final method, the slow propagation speed naturally leads to a longer calculation time.

4.2.2 Macroscopic Gas Convection Formulation

The second proposal considered changing the overall formulation to a heterogeneous reaction with a macroscopic treatment of gas produced during the chemical reactions, leading to heat propagation through convection. This hybrid conception of the nanothermite reaction would likely provide a more realistic simulation, providing the desired focus on the effects of reactive sintering and condensed phase reaction on the initiation, while gas phase mechanisms

would dominate in the propagation regime. Given the high temperatures reached during the continued exothermic reaction as it propagates, it is valid to assume many species could pass into the gas phase.

The process of this closed tube experiment, as previously defined in Section 2.4.2, can be summarized by the following. An external heating regime is applied to the leftmost discretized cell, with the added heat augmenting the temperature. This is followed by a calculation of the overall change in pressure in the tube due to this temperature increase, as species are heated and some vaporize, followed by a recursive analysis of every cell to determine the new distribution of heated gas particles in the cells of the system. This movement of heated particles is the mechanism by which the heat is propagated to further heat subsequent cells and initiate their own self-sustaining exothermic redox reaction.

Regarding the results in Table 4.1, the gas-based system was found to propagate the reaction at 22.3 mm/s. This value is somewhat closer to the overall macroscopic propagation rate found in Ref. 44; however, combined with the very long initiation delay, these values clearly prove that this system is not a good estimation of realistic nanothermite reactions. Even by the time of initiation of the first cell, heated externally, the change in the overall pressure in the tube due to the temperature increase was only on the magnitude of 10^{-10} Pa, which only managed to heat the adjacent second cell by approximately 3 K.

Despite the slight improvement in the propagation results, the major concern with this model formulation remains the computational cost. Given the recursive nature of the calculations for the macroscopic pressure change and redistribution of the heated material in the system, the simulation requires a significantly longer execution time, on the scale of weeks. Other model conceptions can turn out results in a matter of days. In particular, the computational time to reach initiation of the first cell is more than ten times that of other approaches. This naturally also leads to a strain on computational resources, where it is extremely difficult to define the time period to write results to sufficiently observe the reaction, but avoid overwriting before the initiation of the self-sustaining reaction. One of the major goals for this work was to provide a rapid, low-cost analytic tool for pre-system design considerations, thus, the gas convection based mechanism does not deliver on this simulation design goal. It was, again, necessary to reconsider the numerical construction of the macroscopic heat transfer mechanism.

4.2.3 Direct Particle Conduction Formulation

In the previous subsections, the results of two attempted strategies for the treatment of macroscopic heat transfer were insufficient in comparison with the experimental data available for validation. The next logical step was a proposition considering direct conduction between particles in contact, as outlined in Section 2.4.3. Different calculations of an effective conduction coefficient were proposed, each corresponding to a certain configuration of nanoparticles according to a %TMD, *i.e.,* fully compacted thermite solid, embedded particles in a matrix, or low %TMD particle chain. The results presented in Table 4.1 correspond to the

third proposition, with a constant-sized alternating chain of nanoparticles (see the discussion in Section 4.3 for the motivation of this choice).

Performing the simulation for comparison, the direct conduction formulation leads to a calculated steady state propagation speed of approximately 60 cm/s. This corresponds well to newer experimental results, falling within the order of magnitude for the speed of the microscopic propagation of the main front flame under reactive sintering. A larger discussion taking a focus on these fundamentals of the reaction in light of this novel experimental work is laid out in Section 4.4.

Additionally, this model structure is extremely efficient in terms of computational cost, with most simulations terminating in a span of a few days maximum. Certain adjustments to test extreme parameters such as very highly compacted systems (%TMD > 70%) or very large particle sizes (μm scale) can increase the calculation time to about a week. Due to the highly optimizable nature of this approach, the direct conduction model remains significantly faster than the other suggested methods of heat transfer. Considering this and the positive correlation of results with comparison to experimental methods, this was the final choice of macroscopic heat transfer method for the development of the full propagation model formulation.

4.3   Comparison of Different Conduction Formulations

After deciding upon the direct particle conduction formulation as the driving mechanism of macroscopic heat transfer in the system, four different possible methods to calculate an effective conduction coefficient as detailed in Section 2.4.3 were considered. The basis for these formulations comes from an experimental and numerical study completed by Montgomery *et al.*[151] to study $Si:Pb_3O_4$ and $Si:MnO_2$ thermites for gasless mining applications. To compare, a classical Al:CuO setup with 80 nm Al particles and corresponding 99 nm CuO particles ($\xi = 1.0$) at 60 %TMD in a 3mm long burn line was simulated with each conduction method. Table 4.2 provides the reaction characteristics for each of these tests. The final analysis of this Al:CuO system simulated with each of these conduction coefficients leading to the choice of the generalized use of the third construction will be detailed in the following subsection.

Table 4.2 : The nanothermite reaction characteristics for an 80 nm Al : 99 nm CuO system ($\xi = 1.0$) at 60 %TMD with different effective conduction coefficient formulas.

Formulation	Effective Conduction Coefficient (W/mK)	Initiation Delay (ms)	Initiation Temperature (K)	Propagation Speed
1	83.3	85.3	1003	22 m/s
2	50.2	68.8	997	11 m/s
3	2.94	59.3	944	61 cm/s
4	0.599 – 1.21	23.1 – 42.3	943	17 – 30 cm/s

.

The first effective conduction coefficient was defined according to the formula proposed in Ref. 151. It considers a continual heat flow through the compressed powder, which corresponds to a completely dense (100% TMD) bulk material with a joint conductivity calculated as a proportional combination of the bulk thermal conductivities of the fuel and oxide species (see Equation 2.79). This corresponds well to the systems studied by Montgomery *et al.* that have very high compaction rates (> 75 % TMD). This composite bulk material-like formulation found a thermal conduction coefficient of 83.3 W/mK. This is a very high conductivity and, thus, drives the propagation at the fast rate of 22 m/s. Ultimately, this approach is not the best choice when simulating powder-based thermites, which generally have compaction rates ranging from 25 – 75 % TMD on average. The numerical consideration of the powder thermite as a new composite bulk material cannot accurately reflect the influence of the geometrical features of a particle-based system.

Next, the second effective conduction coefficient contains only a slight adjustment to the first formula. In this case, the coefficient is defined as a combination of the bulk conductivities for each species as a composite material of variable compaction, like a bulk material with voids (see Equation 2.80). These vacancies act as a bottleneck on the propagation of the reaction and will limit the conductivity. Thus, the second formulation finds a conduction coefficient of 50.2 W/mK for the previously described system and a corresponding propagation velocity of 11 m/s. This reaction speed remains too high compared to recent experimental results, but, most importantly, while allowing an abstract treatment of the reduction in speed due to voids, this model formulation does not account for the specific surfaces of contact through which direct particle conduction can actually occur.

The third formulation of a chain of alternating fuel and oxide particles was a novel approach to take into account the importance of the interfacial region between particles due to the geometric features of the defined system (Equation 2.81). The conductivity through the interfaces into large oxide particles that traditionally have a smaller bulk thermal conductivity can bottleneck the heat propagation, slowing the overall propagation of the self-sustained reaction. As such, this could also be representative of an embedded matrix of oxide particles within a more conductive condensed material fuel. The resultant initiation delays and propagation speeds found with this model variant have been validated and discussed in view of recent experimental findings in Section 4.4. While remaining an estimation, this numerical construction of the effective conduction coefficient gives a propagation speed of 60 cm/s for the described system, which falls within the order of magnitude of best agreement with experiments so far.

The fourth and final approach to calculate an effective conduction coefficient is an elaboration of the third formulation that allows a distribution of different sized particles in the chain (Equation 2.82 and 2.83). The goal of this method was to find a better estimation of the speed of propagation by simulating the realistic variability of particle sizes seen in actual fabricated powders. Additionally, the numerous studies of *in-sitio* observation of reactive

sintering has shown that the formation of microscale components due to agglomeration occur on a faster timescale than that of the overall reaction, meaning some nanoscale material coalesces before reaction initiation and propagation.[45] It is important to note that the consideration of diverse particle sizes is considered exclusively within the definition of the effective conduction coefficient, whereas the particles are fixed at a constant size for all mass transfer and thermal calculations within the model structure. Essentially, an effective conduction coefficient is computed at the initiation of the model before the actual simulation occurs.

Thus, using the general system parameters as described in the introduction to this section, multiple size dispersions of either just the fuel particles, just the oxide particles, or both were tested. The dispersion was set up as a half-Gaussian distribution with the mean set to the average particle size utilized in these studies (*i.e.,* 80 nm for aluminum, 100 nm for cupric oxide). Each effective conduction coefficient presented for a certain variance was defined as the average of three calculations of this variance with a different seed value utilized to generate the random diameter samples. This led to a variety in effective conduction coefficients that were simulated to find their corresponding reaction characteristics. A summary of these system features and resultant behavior is provided in Table 4.3.

Table 4.3 : Summary of the dispersion characteristics and resultant effective conduction coefficients, initiation delays and temperatures, and propagation speeds for these systems considering possible dispersions of 1) only Al fuel particles, 2) only CuO oxide particles, and 3) customized dispersions for each species.

Variable Species	Variance	Effective Conduction Coefficient (W/mK)	Initiation Delay (ms)	Initiation Temperature (K)	Propagation Speed (cm/s)
Al	80 nm – 700 nm	1.074	38	944	28
	80 nm – 1 μm	0.599	23	943	17
CuO	100 nm – 700 nm	1.089	39	944	28
	100 nm – 1 μm	0.707	27	943	20
Both	80 nm – 1.2 μm (Al) 100 nm – 1.2 μm (CuO)	1.21	42	944	31

Beginning with a look at the tested variances for the Al fuel particle, exclusively, two variations were tested, both spanning from the mean particle size commonly found in purchased Al nanopowder, 80 nm, up to either 700 nm (variance = 150) or 1 μm (variance = 250). The smaller distribution (80 nm – 700 nm) paired with constant 100 nm CuO nanoparticles led to a conduction coefficient of 1.074 W/mK, whereas the larger distribution with the same CuO particles dropped this coefficient to only 0.599 W/mK. Figure 4.1 shows the Al particle size distributions for these two variances.

Figure 4.1 : The Al particle diameter distributions calculated by a random sampling restricted to a half-Gaussian curve for variances of a) 250 and b) 150.

A symmetrical study was completed by sampling a random distribution of CuO particle sizes with variances of 150 and 250. The mean particle diameter considered in this case was 100 nm. Thus, a variance of 150 provides a span from 100 nm to 700 nm, and a variance equal to 250 spans from 100 nm to 1 μm, as illustrated in Figure 4.2. This corresponds to effective conduction coefficients of 1.089 W/mK and 0.707 W/mK, respectively.

Figure 4.2 : The CuO particle diameter distributions calculated by a random sampling restricted to a half-Gaussian curve for variances of a) 250 and b) 150.

The final test observed the variation in the effective conduction coefficient while varying the sizes of the particles for both the fuel and oxide species. A larger variance of 300 was considered, leading to a distribution from 80 nm to 1.2 μm for Al and from 100 nm to 1.2 μm for the CuO (see Figure 4.3). The effective conduction coefficient calculated with these distributions was 1.21 W/mK. It is interesting to note that, contrary to the isolated distributions for Al or CuO, the larger particle size distribution leads to a relatively high conductivity. This is a direct consequence of taking into account the geometric factors in the formulation, as two larger particles in contact will share a larger interfacial region through which heat can propagate at a faster rate.

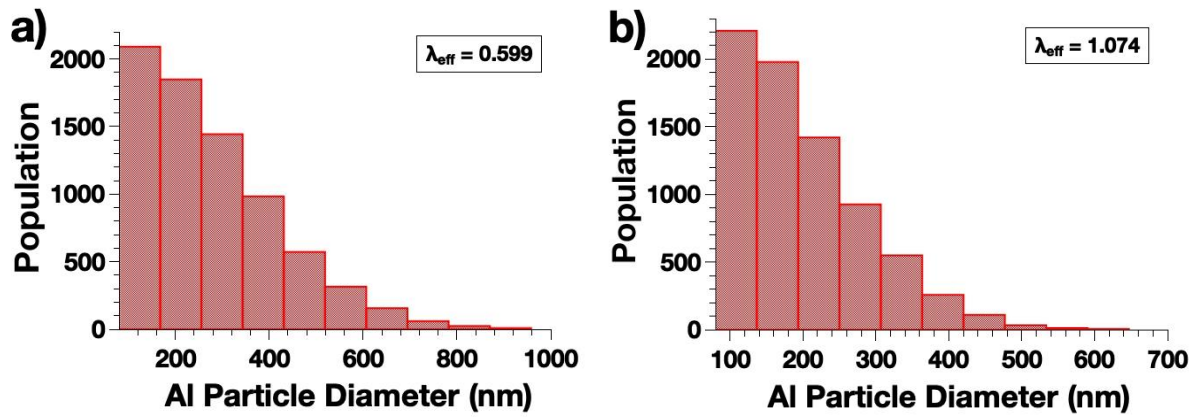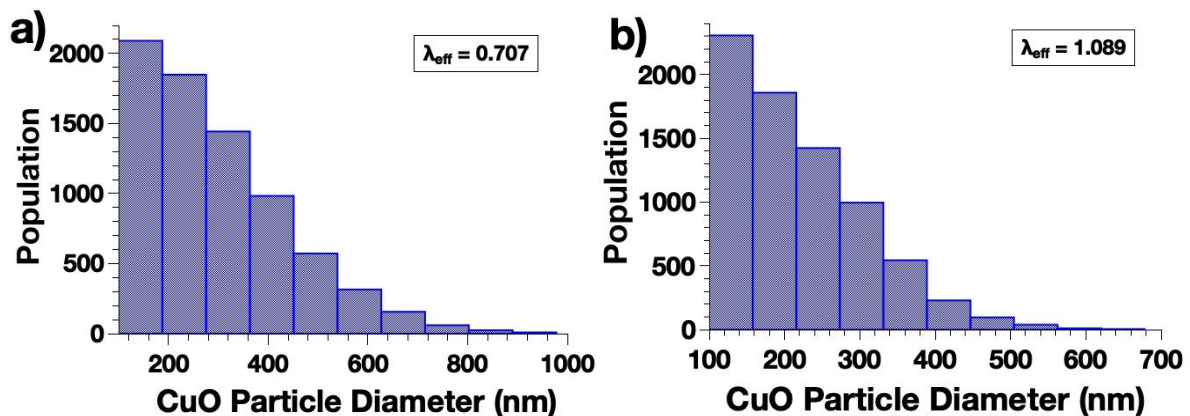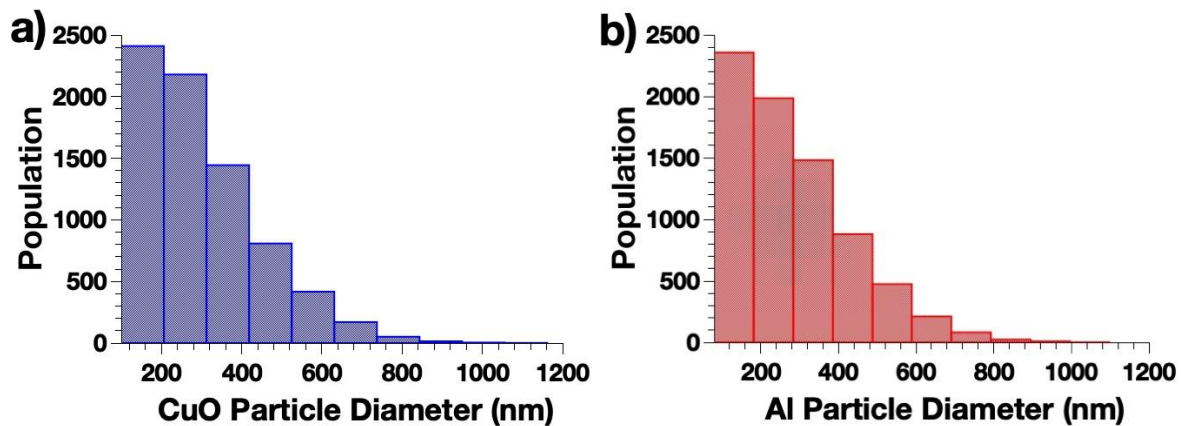**Figure 4.3 :** The a) CuO particle diameter and b) Al particle diameter distributions calculated by a random sampling restricted to a half-Gaussian curve for a variance of 300.

In regards to the speed of propagation for these varied systems, all fall within an acceptable order of magnitude in relation to the recent studies on the nanothermite reaction from Wang *et al.*[44] From the lowest conductivity (0.599 for a variance of 250 on the only Al-particles) to the highest (1.2 for a variance of 300 on both fuel and oxide particles), the difference in the propagation velocity is around 15 cm/s. Additionally, the difference between the speed of propagation for the system where both particle sizes are randomly distributed and for the system under the third formulation where both particles sizes are considered fixed is only around 30 cm/s. Ultimately, all of these values fall within a reasonable margin of error for a qualitative study of nanothermite propagation. Therefore, it can be concluded that the size dispersion does not severely influence the initiation nor the propagation phenomena. For simplicity, the third formulation was retained for all other tests as it was proved a reasonable approximation of more complex, dynamic systems.

4.4 Validation of the Direct Particle Conduction Formulation

As seen in the Section 4.2, the direct particle conduction formulation found the only steady state propagation speed approaching agreement with recent experimental work on Al:CuO thermites. It was thus decided to utilize this numerical construction as the basis for the full propagation model, concentrating on the third proposition of a constant chain of alternating fuel and oxide particles for comparison with experimental results. The most common experimental setup includes 80 nm Al spherical nanoparticles from ALEX with 25 – 100 nm CuO particles of more random form, sometimes rods. *In silico*, the simulated experiment for comparison is as described in Section 4.2, utilizing 80 nm Al particles (2 nm native shell thickness) with ~50 nm CuO particles, for $\xi = 1.0$, at 60 %TMD. This mixture is placed in a 3mm long open air channel. The system is initialized at the ambient temperature, 300 K, with an imposed limit of disintegration and loss of the condensed phase structure at 2070 K, the lowest vaporization temperature of all considered species, namely Cu_2O. The resultant propagation speed was found to be approximately 61 cm/s after installation of the steady state regime.

Regarding all of the literature reporting propagation speeds of Al:CuO thermites, many see speeds on the order of hundreds of meters per second. In particular, Sanders *et al.*[89] (see Section 1.2.3) found an average velocity of 525 m/s for an 80 nm Al: ~21 x 100 nm CuO rods and Glavier *et al.*[121] recorded a propagation speed of 340 m/s for 80 nm Al spherical particles (4 nm alumina shell thickness) mixed with ~240 nm CuO powder of random shape. The results of the Al:CuO simulation speed of approximately 70 cm/s is not in quantitative agreement with many of these earlier open burn line experiments. This is most likely explained by the lack of ambient oxygen in the simulated experiments. Free oxygen available from the ambient environment can significantly aid in the oxidation of the fuel species through gas-phase mechanisms and, thus, remains outside of the consideration of this work. Additionally, it is largely agreed that the overall thermite reaction is heterogeneous, likely dominated in the early stages by condensed phase reactions but passing to a gas dominant regime as the exothermic reaction raises the temperature above the boiling point of most reactant species. This, combined with a low to medium compaction rate of the thermite material generating gases and/or possible pressurization of the burning material (tube experiment) may also dramatically impact the propagation properties. This then leads to a self-sustained looping heterogeneous reaction where material at a very high temperature will be ejected by the release of gas from the oxidizer towards material further along the tube, heating it by advection and continuing the cycle. A new study by Jacob *et al.*[41] evidenced this mechanism through high speed two-dimensional temperature measurements with a combination of high speed spectrometry and high-speed color camera pyrometry of three systems including $Al:Fe_2O_3$, $Al:Fe_2O_3:70\%$ WO_3, and $Al:WO_3$ initiated on a hot wire under an argon environment. A comparison of the high speed pyrometry images showed that the inclusion of a high gas production oxidizer (Fe_2O_3) can augment the propagation speed of a low gas production, high adiabatic temperature oxidizer (WO_3) through a three-component thermite mixture. This was clearly shown in the pyrometry images where the $Al:Fe_2O_3$ showed a decent sized cloud of ejected material, the $Al:WO_3$ displayed extremely limited ejected material, and the $Al:Fe_2O_3:70\%$ WO_3 had the largest cloud of ejected material of the three, with a corresponding highest propagation speed. It can thus be understood that the production of gas and pressurization of heated material is indeed an important factor in the propagation of nanothermites through increased advection.

Despite the disagreement in propagation speeds with many experimental works, a recent study by Wang *et al.*[44] using a novel observation technique that allows μs timescale resolution with μm spatial resolution found interesting results in better correlation with the simulated propagation speed. Utilizing a microscope objective (x40) coupled to a high-speed color video camera (~55 μs per frame), a 512 μm x 512 μm region of thermite mixture composed of ~85 nm Al nanoparticles and ~40 nm CuO particles was observed. The overall goal was to observe the reaction propagation, and more specifically, the reactive sintering of the material *in operando*. As previously discussed in Section 1.3.3, the authors observe an inhomogeneous reaction with discontinuous flame fronts, with the principal front defined as a so-called sintering zone of ~30 μm with a propagation of the microscopic sintering reaction at approximately 50 cm/s. The sintering takes place in around 170 μs, with a subsequent cooling period of 265 μs in a zone of ~60 μm, terminating in a final sintered product. This leads to

images showing extremely bright spots that discontinuously propagate the reaction, but show consistent temperatures of 3000 – 3500 K, corresponding to previously measured reaction temperatures for Al:CuO thermites, regardless of the front location. After passage of the flame front, the final sintered product is observed to be agglomerated particles of ~20 μm. The authors establish a relationship between the sintering zone (denoted D_r) and the final sintered product (denoted D), such that with an aggregate packing density of 33 %TMD, $D \approx 0.69 D_r$. Thus, the sintering zone can be considered the effective thickness of the reaction zone or flame front, representing the local volume of material reacting simultaneously. At the macroscale, the overall flame front is found to propagate at a speed of ~3 cm/s. This allowed the authors to estimate heat fluxes for the sintering flame front of ~10^9 W.m^{-2}, corresponding to an estimated thermal conductivity of 60 W.m^{-1}.K^{-1}, and for the cooling regions of ~10^6 W.m^{-2}, with a corresponding thermal conductivity of gas from this region of 0.1 W.m^{-1}.K^{-1}. As such, the reaction shows local rapid reaction that is then slowed by low conductivity zones leading to the relatively slow macroscopic propagation rate.

It is now interesting to analyze the simulated results in light of these new experimental findings. First, the original simulation had a speed of 61 cm/s, on the same order of magnitude as the sintering flame front propagation found by Wang et $al.$[44] Considering the spatial discretization in the simulation, with $dx = 1$ μm, it is expected to find a propagation velocity in the range of that found within the sintering range (30 μm). Additionally, the experimental setup does not constrain the direction of propagation, as it instead observes a zone of disposed material onto a square slide. It is, therefore, applicable to assume that propagation in a burn channel or tube will exhibit behavior most similar to the dominant flame front in a more abstract deposition pattern.

A second simulation was completed integrating the estimated aggregate density and thermal conductivity of the macroscopic reaction observed with the same material properties. With a compaction rate of 33 %TMD and an imposed conductivity of 0.1 W.m^{-1}.K^{-1}, the propagation speed fell to 8.5 cm/s. Even considering direct particle conduction instead of a more realistic gas convection or advection (as observed from the cooling regions in experiment), the adjusted propagation velocity is a good estimation of the macroscopic propagation rate as seen in Ref. 44.

In general, the speed of propagation of nanothermites is very sensitive to the experimental setup, as well as the material characteristics. Given the variability and scarcity of experimental studies specifically reporting propagation velocities, it is difficult to create a numerical tool to quantitively simulate the reaction for any possible apparatus and conditions. Yet, in this subsection, the calculated propagation speeds of the model were validated by novel experiments under an argon environment, and particularly in light of the newer understanding of the importance of reactive sintering. While the simulated propagation speeds were lower than open burn line experimental values, the direct particle conduction mechanism can accurately estimate the propagation of the flame front for experimental setups where condensed phase mechanisms are dominant.

4.5 Exploitation of the Direct Particle Conduction Formulation

4.5.1 Effect of Key Parameters

a. Compaction Rate (%TMD)

As seen in Chapter 1, from both experimental and numerical model results, the rate of compaction (given as a percentage of the Theoretical Maximum Density) has a very marked effect on both the initiation delay and the steady state propagation speed of the thermite reaction. Generally speaking, considering systems at the nanoscale, the initiation delay augments as the system is increasingly compacted.

A study by Stamatis *et al.*[156] tested this effect on a highly fuel-rich $Al:MoO_3$ system compressed into 0.635 cm in diameter cylindrical pellets from a powder synthesized by Arrested Reactive Milling. The pellet is then initiated using a defocused CO_2 laser beam (10.6 μm wavelength) heating on one side in a combustion chamber. The results, presented in Figure 4.4, are coupled with a simple heat transfer model to analyze the heating and thermal initiation of the pellets. While the study at hand considers very high compaction rates due to the nature of compressed pellets, both the scattered data points and the trend line as found by the numerical model show a mostly proportional relation between the initiation delay and the compaction of the pellet.
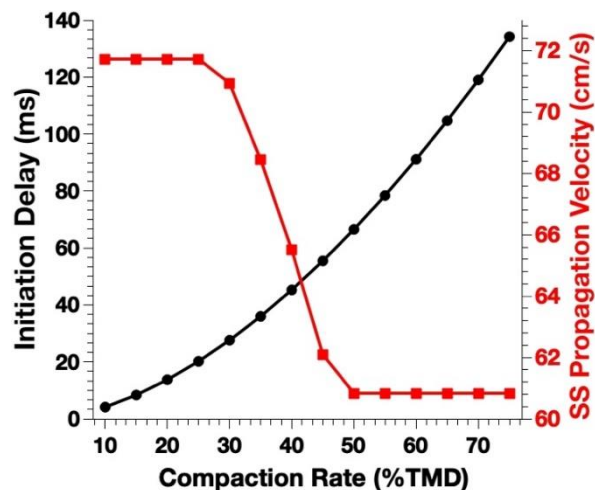
Figure 4.4 : The initiation delay of a fuel-rich $Al:MoO_3$ compressed pellet thermite as a function of the compaction rate (%TMD) with experimental results (hollow squares) and a simulated trendline (solid line)**. [156]**

A simulation of an Al:CuO system at the stoichiometric ratio ($\xi = 1.0$) with 80 nm Al particles, with a 2 nm alumina shell, and 99 nm CuO particles in a 3 mm long open burn line was completed to study the effects of the compaction rate according to the condensed phase propagation model. The initiation delays and propagation speeds as a function of %TMD are

displayed in Figure 4.5. In regards to the initiation delay, a pattern similar to the experimental results by Stamatis *et al.*[156] is found. The initiation delay increases with the compaction rate, spanning from 4 ms at 10 %TMD to 134 ms at 75 %TMD. A slightly exponential relation is found, but it is important to note that the trend becomes linear at high %TMD.
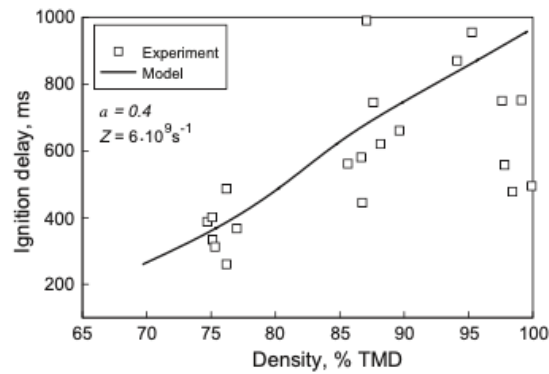
Figure 4.5 : The initiation delay and steady-state propagation speed for an Al:CuO system (80 nm Al, 99 nm CuO, ξ = 1.0) as a function of the compaction rate.

Looking at the steady state propagation speed in Figure 4.5, three regimes were found as a function of the compaction rate. For systems at 25 %TMD and under, the propagation velocity is constant at approximately 72 cm/s. Similarly, at a compaction rate of 50 %TMD or greater, the reaction propagates at a steady rate of 61 cm/s. The third regime is a relatively linear decrease in propagation speed from 25 %TMD to 50 %TMD. The overall qualitative pattern seen in the simulated tests for > 25 %TMD corresponds to recent experimental results: the steady state propagation velocity decreases inversely with increasing compaction. This pattern is confirmed by Pantoya *et al.*[157] in a study on Al:MoO$_3$ pellets initiated by laser in an ambient environment (see Figure 1.9). Figure 4.6 displays the same experimental results reconfigured on a linear scale as a function of %TMD, converted from a logarithmic scale of explicit density in g/cm^3. On this linear scale, there is a clear inverse exponential relationship between the propagation velocity and the compaction rate. The three regimes defined on the modified image correspond to 0 to 0.6 g/cm^3 for regime I, between 0.6 g/cm^3 and 2 g/cm^3 for regime II, and from 2 g/cm^3 to 3 g/cm^3 for regime III.
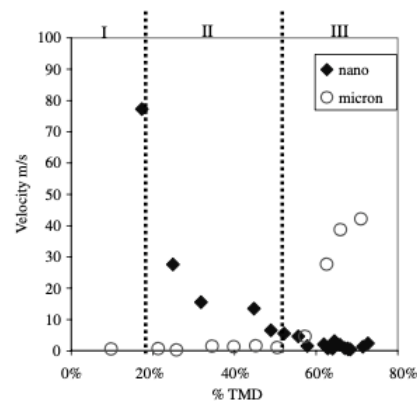
Figure 4.6 : Flame velocity as a function of the compaction rate (%TMD) for nano (black diamond) and micron (hollow circle) Al particles mixed with nano-MoO$_3$ compressed into thermite pellets and initiated by laser. **[157]**

On the contrary, the stabilized propagation rate for a compaction rate under 25 % TMD does not match the improved performance observed experimentally. This is most likely attributable to the fact that at low compaction, the combustion regime is probably driven by more dominant gas phase mechanisms, rather than purely condensed phase phenomena.

b. Stoichiometric Ratio

Experimental studies on the effect of the stoichiometric ratio, ξ, on the initiation delay and the speed of propagation of the self-sustained thermite reaction surprisingly showed that the most performant (*i.e.,* fastest propagation with the lowest initiation delay) mixtures are fuel-rich. In Section 1.2.3, Granier *et al.*[77] found that a ratio of $\xi = 1 - 1.5$, depending on the Al particle size, led to the highest burn rate with a correspondingly low initiation delay on a study of Al:MoO$_3$ nanothermites (see Figure 1.2). This was further corroborated by a study of Al:WO$_3$ by Prentice *et al.*[81] that found optimum performance at $\xi = 1.4$. Most studies on this effect have been performed on open air experiments, such as a burn line or channel, thus, it could be concluded that the excess fuel in these mixtures is then oxidized by oxygen from the ambient environment, leading to improved performance. In this case, an experiment or simulation in vacuum or under a different gaseous environment would be expected to find an optimization closer to the stoichiometric ratio ($\xi = 1.0$). This would then indicate that the model, which is currently incapable of replicating a stoichiometric ratio with fixed particle sizes, would not see improved performance at fuel-rich stoichiometry.

However, the system conductivity is another potential cause of the slight shift in the maximum propagation peak from the stoichiometric ratio towards a more fuel-rich regime. Increasing the conductivity (through the inclusion of a higher proportion of more conductive fuel material) may pre-heat the upfront of the flame, thus accelerating its propagation. Additionally, a fuel-rich experimental system, where all particle sizes remain the same and it is instead the quantity of each powder in the mixture that determines the stoichiometric ratio, experiencing better performance could support the general understanding that the limiting step of the nanothermite reaction is the diffusion of the freed oxygen through the oxidized fuel layer. In theory, given that the amount of diffusion possible through this layer is determined by a solubility limit, having more particles available to oxidize in parallel could augment the speed of the reaction. This is a possible explanation for the study on Al:MoO$_3$ thermites in burn tube experiments (thus, without additional ambient oxygen) that also found the highest propagation velocity for slightly fuel-rich mixtures.[79]

To better investigate this effect, it is interesting to perform a study *in silico* with the full propagation model, as it also does not account for any ambient environment or gas phase interactions. In this case, oxygen apart from that freed by the oxide species reduction cannot contribute to the oxidation of the fuel and it is not possible for multiple fuel particles to receive freed oxygen from one oxide particle. Thus, multiple simulations were completed with 80 nm in diameter Al, with the CuO particle size adjusted to correspond to a stoichiometric ratio ranging from 0.8 to 5.0. It is important to again note that given the formulation of this model,

with a base two-particle pair, the adjustment of the stoichiometric ratio is achieved by finding a corresponding CuO particle size. This is not necessarily a correct representation of the experimental conditions. In these setups, the stoichiometric ratio is attained by modifying the amount of each powder included in the final thermite mixture, and this difference in representation of the stoichiometric ratio could affect the quantitative simulation results. Therefore, it is important to analyze the results while considering that some differences could be attributable to the oxide particle size. The contact angle is consistently fixed at $\theta = 135°$. The results of this study are displayed in Figure 4.7.
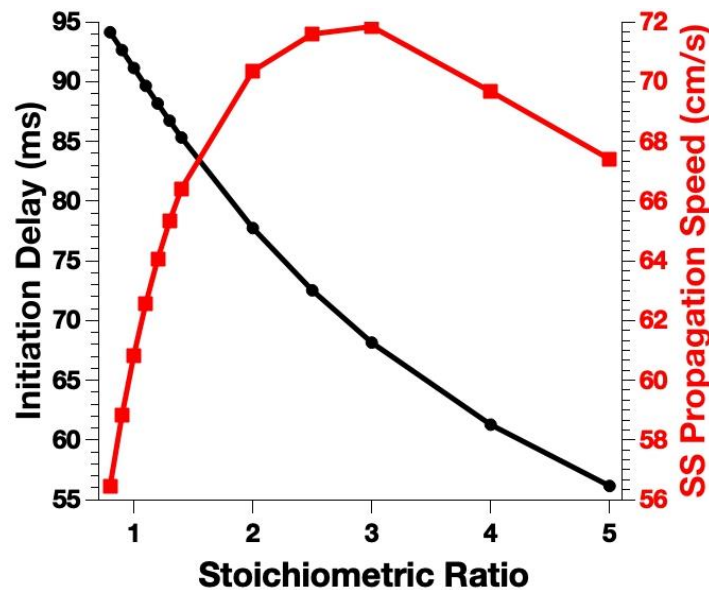
Figure 4.7 : The initiation delay and steady state propagation speed of an Al:CuO nanothermite ($\theta = 135°$) as a function of the stoichiometric ratio. The system contains 80 nm Al particles with CuO particle size determined to meet the stoichiometric ratio as calculated by Equations 2.35 and 2.36.

It is immediately clear that, similar to the closed burn tube experiment performed by Son *et al.*[79], as the stoichiometric ratio becomes increasingly fuel-rich, the initiation delay decreases nearly linearly and the propagation velocity increases. However, the simulation does not find the commonly found maximum around $\xi = 1.2 - 1.4$. On the contrary, the propagation speed continues to increase with the stoichiometric ratio at least up to $\xi = 3.0$. This implies that the possible presence of ambient oxygen, while likely contributing to the reaction propagation, is not the only explanation for the performance improvements seen with fuel-rich mixtures. Again, this is very possibly due to the boost in conductivity in a mixture with a larger percentage of fuel material, of which traditional materials have higher bulk conductivity. Slightly increasing the conductivity allows preheating of the flame upfront, facilitating oxido-reduction reactions, yet, continually increasing the conductivity further as the stoichiometric ratio increases to more and more fuel-rich can possibly quench the reaction through conductive losses along the system, causing a maximum somewhere in the fuel-rich regime, generally below $\xi = 3.0$. However, moving into the extremely fuel-rich domain at $\xi = 4.0$ in the simulation does lead to a slight decrease in propagation speed to about 68 cm/s, while experimental studies have shown that a much more significant reduction is expected. Additionally, the initiation delay continues to decrease drastically in a manner that indicates that the model likely overestimates performance

characteristics for very fuel-rich mixtures. A study of the possible mechanisms by which propagation of the self-sustaining reaction is improved by the presence of more fuel is necessary.

In consideration of the limitations of the system, the presence of larger CuO particles to fulfill the desired stoichiometric ratio does not explain the improved performance. Larger particles that are reduced in the linear manner of the formulation may provide more freed oxygen to facilitate the exothermic reaction, but, given that the limiting diffusion step is the passage into the fuel particle, a larger reservoir of freed oxygen should not increase reactivity. This implies that another mechanism is responsible for the performance enhancements in this case, requiring further study to determine the nature of the increased propagation speed and lower initiation delay.

c. Particle Size

In Section 1.2.3b, numerous experimental studies on the effect of the particle size, for both the fuel and oxide species found a general pattern of a reduction in the speed of propagation of the reaction as particle sizes increased.[78,83,84,86] Certain results also pointed to a critical limit in the reduction of the fuel particle size where under 50 nm the benefits of the nanostructure are outweighed by the diluting effect of a large percentage of alumina.[84] Similar to the initiation study on this effect, it is important to remember that the model is limited by the intercoupling of the definition of the particle sizes and the stoichiometric ratio while analyzing the following results.

Table 4.4 : The Al fuel and corresponding CuO oxide particle diameters for a 60 %TMD system at $\xi = 1.2$.

Diameter of Al Fuel Particle (nm)	Diameter of CuO Oxide Particle (nm)
10	12
30	35
50	58
75	87
100	117
200	233
500	582
1000	1166

The simulations are based on a classic Al:CuO setup fixed at a slightly fuel-rich stoichiometric ratio, $\xi = 1.2$, at 60 %TMD. The CuO particle diameters are calculated as a function of the Al particle size and the set stoichiometric ratio as defined in Equations 2.35 and 2.36. The corresponding CuO particle sizes are outlined in Table 4.4.

The steady-state speed of propagation and initiation delays for these simulations are presented in Figure 4.8. As in the study on the effect of the particle diameter on the initiation delay completed with the base model, the simulated results do not show evidence of the critical limit, indicating that the model probably overestimates the performance (lower initiation delay, higher propagation speed) for extremely small particle sizes. However, the overall pattern in the thermite behavior found corresponds well to the literature review established by Huang *et al.*[83]. For the common nanoscale regime of particles from 30 nm to 1 μm, the propagation speed ranges from ~ 80 cm/s to ~ 7 cm/s, a 91% difference. Correspondingly, the initiation delay and the initiation temperature increase from 59 ms to 185 ms and from 900 K to 1300 K, respectively, for the same range. The initiation temperatures are relatively close to the trend line found in the literature review displayed in Figure 1.4.
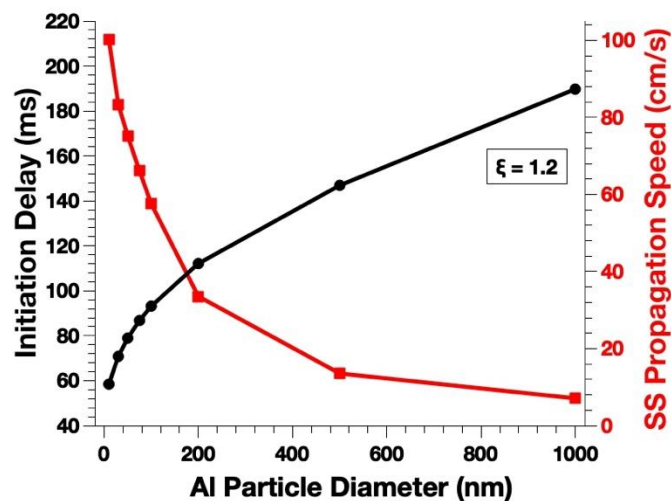
Figure 4.8 : A study of the initiation delays and steady-state propagation speeds of the thermite reaction as a function of the Al fuel particle diameter, at a fixed stoichiometric ratio of ξ = 1.2 at 60 %TMD. The CuO oxide particle diameters are determined according to Equations 2.35 and 2.36.

Nevertheless, it is also important to consider the role of the size of the corresponding oxide particle. At a fixed stoichiometric ratio, given the limitations of the system, the CuO diameter also shrinks proportionally with the fuel particle diameter. Weismiller *et al.*[86] established in a study on the effect of nano- versus micro-sized components on the propagation of Al:CuO and Al:MoO$_3$ thermites that the oxide size has a stronger influence on the propagation speed. For both thermite couples, it was found that the inclusion of microscale oxide components with nanoscale fuel reduced the propagation velocity significantly more than the inverse, with microscale fuel and nanoscale oxide. This particular effect is not possible to study in the simulation, but purely microscale thermites were also tested. For all nanoscale components in the Al:CuO system, the authors found a propagation speed of ~ 990 m/s. For the Al:CuO microthermite, this speed dropped to only ~180 m/s, reducing the linear burning rate by 81%, which is close to the same percentage of reduction seen for the 1μm Al: 1.17 μm CuO simulation. One of the main perspectives for the continuation of this work is the elaboration of a model allowing multiple particles of one species (fuel or oxide) to coagulate to a single particle of the opposing species to permit a better investigation into the fundamental influence of each particle size on the propagation reaction.

d. Native Oxide Shell Thickness

There is a limited amount of experimental study on the effect of the native oxide shell on nanothermite performance. Most commercially available aluminum nanoparticles have an active aluminum content of ~70–90%, corresponding to a natural oxide shell of 1 to 2 nm in thickness. It is possible to increase this through custom Al particle fabrication or by further oxidation of the particles at a temperature under the Al melting point for various timescales depending on the desired thickness.

In Section 1.2.3, a study by Chowdhury et al.[87] on the effect of the native shell thickness on the initiation delay of Al:CuO thermites was discussed. This study was then used for comparison with the base pair initiation model in Section 3.5.3. Both the experimental and theoretical simulation works show a directly proportional decrease in the time for initiation as the shell gets increasingly thicker.

A similar full propagation simulation was performed with 80 nm Al mixed with CuO particles of 99 nm (for $\xi = 1.0$) and 92 nm (for $\xi = 1.2$). The results of both the initiation delays and the propagation velocities are presented in Figure 4.9. Looking at the initiation delays (black circles), the same pattern is seen for both stoichiometric ratios, which matches with the experimental results found by Chowdhury et al.[87], as well as the base model simulation results. Regardless of the stoichiometric ratio, the initiation delay shows a slight linear increase as the oxide shell grows larger; however, the initiation delay in a fully populated experiment, as opposed to a single base pair, has augmented by an order of magnitude. Again, this is logical as increasing the original oxide corresponds to a thicker barrier to the diffusion of freed oxygen arriving to oxidate the fuel species. Additionally, the larger the native shell, the less unoxidized fuel material is available for oxidation.
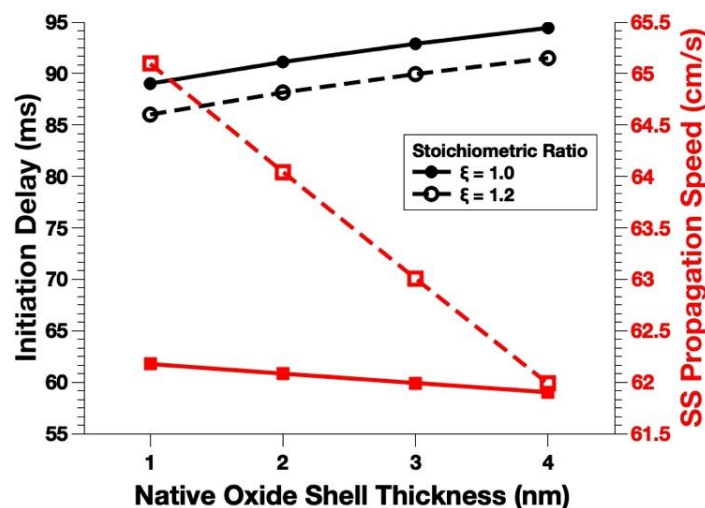
Figure 4.9 : The initiation delay (black circles) and steady state propagation speed (red squares) of Al:CuO nanothermites as a function of the native oxide shell thickness for a stoichiometric ratio of $\xi = 1.0$ (solid) and $\xi = 1.2$ (hollow).

Interestingly, observing the propagation speeds (red squares) shows a significant difference in the importance of the native shell thickness according to the stoichiometric ratio. For both ratios,

the propagation speed declines as a function of increasing native oxide shell thickness. As the rate of diffusion through the native oxide layer is most commonly the limiting step of the reaction, a thicker barrier will further reduce the amount of oxygen arriving to oxidize the fuel at each time step. At a stoichiometric ratio of $\xi = 1.0$, the shell thickness only slightly influences the propagation speed, with a light reduction in the speed as the thickness increases. In comparison, the propagation velocity has a more consequential reduction ($\sim$ 3 cm/s) for thicker oxide shells at a ratio of $\xi = 1.2$. The only difference in these two systems is the adjusted CuO particle size to achieve the stoichiometric ratio. The larger oxide particle will increase the surface area of the contact interface between the two particles, thereby allowing more oxygen diffusion through the native oxide layer. It is then possible that the increased surface area and subsequent oxygen diffusion is more sensitive to the thickness of the barrier with a more substantial limitation of the oxidation of the fuel, leading to a slower propagation of the overall reaction.

4.5.2 Benchmark Study of Different Materials

In a similar goal to the initiation study, a full benchmark study of the preset materials listed in Section 2.3 was completed. The initiation delay, initiation temperature and burn rate for a full propagation system was calculated for each combination of fuel and oxide species, with the results presented in Table 4.5. The important material properties that drive this reaction are summarized in Tables 3.5 and 3.6. The third direct conduction formulation of a constant alternating chain of particles is utilized for all thermite couples in this comparison. A physically standardized system was implemented in a 3 mm long burn channel at 60 %TMD with an 80 nm fuel particle (2 nm native oxide shell) and a corresponding oxide diameter for a stoichiometric ratio of 1.0 calculated for each species. The diffusion coefficients of oxygen in all reactant species considered in this study are presented in Figure 4.10 over a temperature range of 300 K to 5000 K.
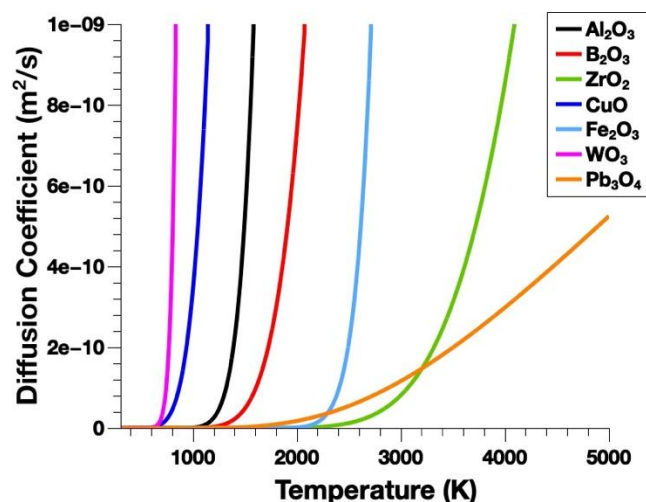
Figure 4.10 : The oxygen diffusion coefficient as a function of temperature for all species considered in this benchmark study (the oxides listed are the initial oxide material, while the values are for the final or intermediary reduced species, when possible). The diffusion coefficient is calculated by an Arrhenius' equation $D(T) = D_0 e^{(-Ea/RT)}$ with the prefactor D_0 and activation energy E_a provided for each species in Table 2.1.

Overall, the best performances are obtained with aluminum as the fuel. Apart from iron oxide, which shows specific behavior across all fuels tested, aluminothermites (thermites with Al as the fuel) are the only fuel group tested that exhibit initiation delays below 100 ms. The corresponding initiation temperatures are also the lowest in the range of 900-1000 K (with the exception of iron oxide). Lastly, the aluminothermites also have high burn rates, notably in combination with the CuO oxidizer, which was found to have the highest burn rate of all tested cases (60 cm/s). Thermite reactions can be primarily governed by the oxygen diffusivity through its oxidized fuel, the reaction product, which may act as a barrier for the reacting species to meet and react. Even though the oxidizer is usually chosen for its relative metastability, its decomposition or simply its ability to provide an easy pathway for migrating oxidizing species towards the fuel and its oxide may temper the role of the oxidized fuel barrier layer as the leading parameter, as will be seen for most cases apart from CuO. Obviously, the thermal conductivity as well as the reaction enthalpy are other important parameters. This multiplicity of components makes it very difficult, if not impossible, to quantitatively predict *a priori* the reaction behavior of a given thermite. A more detailed look on each considered thermite is presented in the following subsections.

Table 4.5 : Main guideline properties and results in terms of calculated initiation delays and propagation velocities for Al, B and Zr fuel based nanothermites.

Fuel Species	Oxide Species	Vaporization Temperature Limit (K)	First Vaporized Species	Conductivity (W/m.K)	Initiation Delay (ms)	Burn rate (cm/s)	Initiation Temp (K)
Al	CuO	2070	Cu_2O	2.9	91	60	943
	Fe_2O_3	2743	Al	6.7	350	38	1994
	WO_3	1973	WO_3	1.6	63	17	718
	Pb_3O_4	1808	PbO	1.6	127	2.1	1194
B	CuO	2070	Cu_2O	2.4	192	4.3	1285
	Fe_2O_3	2130	B_2O_3	5	360	17	1577
	WO_3	1973	WO_3	1.4	186	14.5	1228
	Pb_3O_4	1808	PbO	1.3	165	8	1192
Zr	CuO	2070	Cu_2O	2.6	270	6.7	1643
	Fe_2O_3	3135	Fe	6.8	334	37	1957
	WO_3	1973	WO_3	1.5	245	14.3	1862
	Pb_3O_4	1808	PbO	1.5	*	*	*

* Did not initiate

a. Al-based Nanothermites

The high abundance of aluminum with a highly exothermic oxidation process when coupled with most oxide materials has led it to be the dominant, inexpensive choice for many

thermite preparations. Due to this, aluminothermites have been extensively investigated experimentally, but an exact and quantified understanding of the series of mechanisms of initiation and propagation remains debated. One goal of this mechanistically-restricted model, that considers only condensed phase reaction, is to be able to discuss this complexity further through comparison with other materials. The aluminothermite reaction kinetics have been determined to be primarily driven by the oxygen diffusivity through the growing alumina layer, characterized by its diffusion pre-factor and activation energy barrier, $D_o = 9 \times 10^5$ m^2/s and $E_a = 140$ kJ/mol, respectively.

Beginning with an analysis of the Al:CuO system, likely the most studied nanothermite couple in powder form, Chapter 3 showed that the simplified condensed phase-driven model can accurately predict the thermite initiation when heated under common initial conditions (10^5 K/s). Additionally, Section 4.3 evidenced that the propagation among a monodispersed and regular alternation of Al and CuO nanoparticles along a chain, as designed in our model, is a good basis for treating propagation. The results from the full propagation simulation found an initiation delay of 91 ms at a temperature of 943 K, which is approximately one order of magnitude higher than for the initiation-only base model for identical nanoparticles.
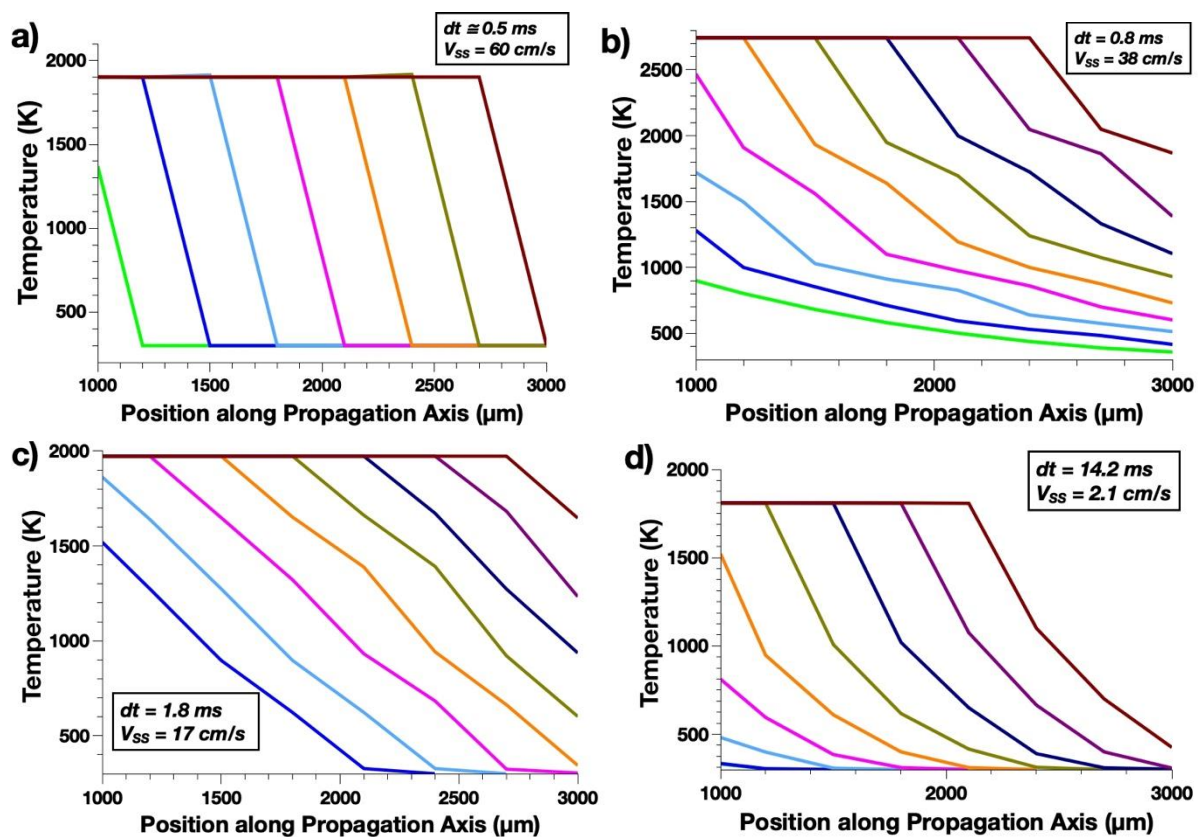
Figure 4.11 : Temperature profiles along the axis of propagation (+x) of the system taken at intervals of time, *dt*, for a) Al:CuO, b) Al:Fe$_2$O$_3$, c) Al:WO$_3$, and d) Al:Pb$_3$O$_4$.

In that base model, the neglect of all heat losses, both towards an adjacent cell for propagation and into the environment, leads to a higher heat ramp with all energy produced from external heating and the resultant redox exothermic reaction contributing only to the

initiation of the runaway thermite reaction. In the full propagation version, the model contains an explicit treatment of losses due to conduction, convection, and radiation that slows down the temperature rise due to external heating and, consequently, the chemistry of initiation. The calculated steady-state propagation speed was found to be 60 cm/s for the system with parameters of the benchmark study. This propagation speed agrees fairly well with the new work completed by Wang *et al.* where high-speed microscopy permitted *in-operando* observation of the propagation reaction on a local and macroscopic scale (see Section 4.4). This novel characterization technique has provided important insight into the combustion process within the flame front, which was found to be of a thickness of ~30 μm for the Al:CuO particle system. In this study, the authors distinguish two regimes: 1) a rapid (50 cm/s) microscopic combustion process due to sintering within the flame front, *i.e.*, a purely condensed phase process, and 2) a significantly slower macroscopic heterogeneous propagation at 3.3 cm/s.

Following the kinetics of the various species in a given reacting unit cell of the system it is observed that at the disruption temperature, only 22% of the Al reservoir has been consumed (Figure 4.12a). This is consistent with the fact that Al:CuO is known to produce a lot of gases and possibly fragments or aggregates that will continue burning in the atmosphere between the remaining condensed phases.
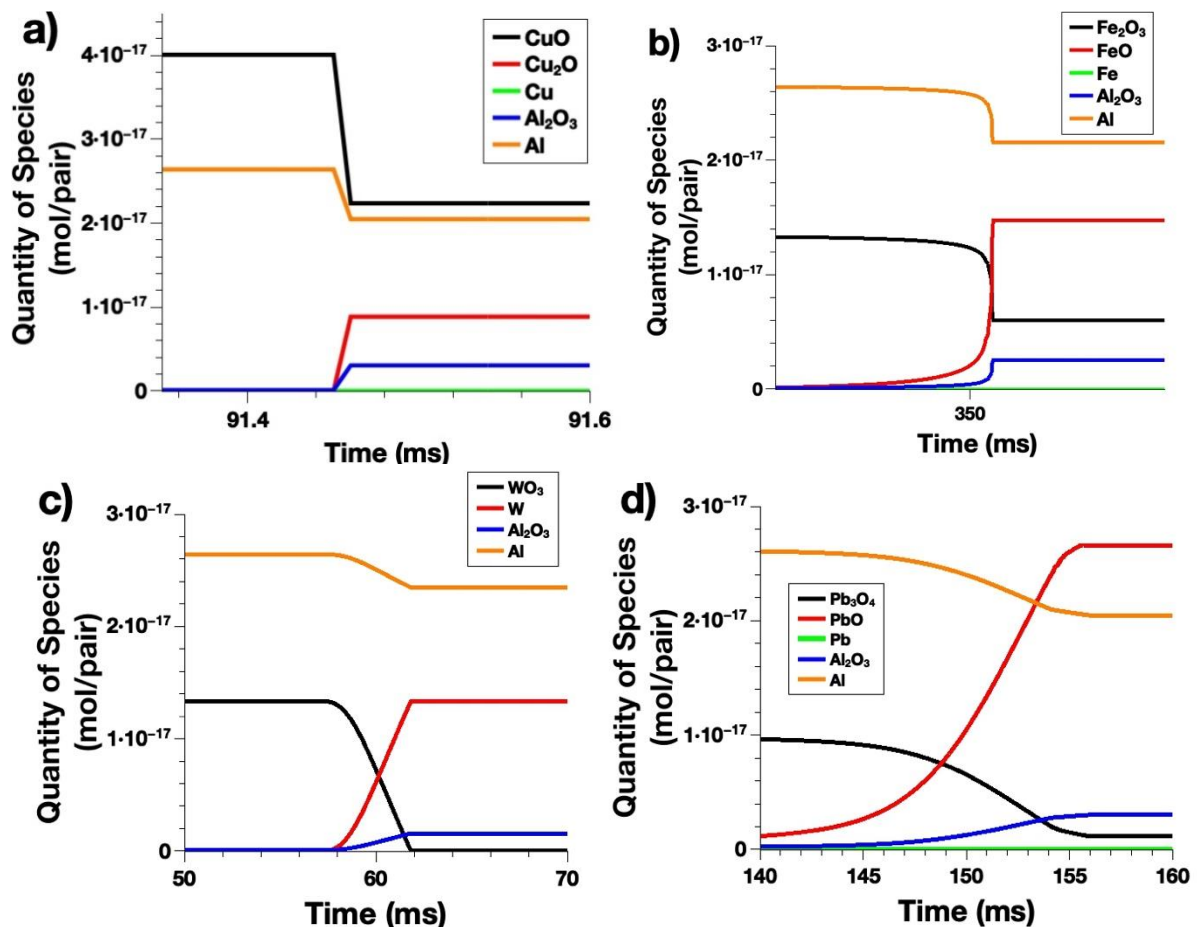
Figure 4.12 : The kinetic evolution of the quantites of each species in one discretized cell for the a) Al:CuO, b) Al:Fe$_2$O$_3$, c) Al:WO$_3$, and d) Al:Pb$_3$O$_4$ thermites.

Ferrous oxide (Fe_2O_3) is another oxide material of great technological interest due to its high exothermic performance with reduced gas production in thermite couples. The Al:Fe_2O_3 thermite couple produces only 0.14 moles of gas per 100g of thermite mixture compared to the Al:CuO thermite couple at 0.54 moles of gas per 100g of thermite mixture.[50] Extensive studies have characterized the Al:Fe_2O_3 thermite reactions or isolated Fe_2O_3 reduction finding complex decomposition scenarios that were not found to vary with the stoichiometry of the system.[153–155] One study in particular by Duraes *et al.*[155] used X-ray diffraction and spectroscopy to analyze the intermediate products present in the reaction. While the main products found were alumina and iron, the significant presence of $FeAl_2O_4$, among other intermediate components, led the authors to propose a reduction scheme where Fe_2O_3 reduces first to both Fe_3O_4 and FeO, before a final reduction to pure iron. Excess Al that is not oxidized is then hypothesized to form iron-aluminates during the intermediary reduction phase. Therefore, similarly to the Al:CuO thermite, this model assumes a two-step decomposition in which Fe_2O_3 first decomposes into FeO and then further reduces to Fe (see individual reaction Equations 2.8 – 2.10). Looking at the propagation simulation results, the Al:Fe_2O_3 system shows a significantly greater initiation delay (350 ms) and temperature (1994 K) compared to Al:CuO. This is not surprising considering that the diffusion of oxygen species within these species have distinct diffusion kinetics; in this model, the decomposition of the oxidizers follows inner oxygen diffusion characteristics (see Table 4.10), which is assumed to be consistent with their decomposition kinetics. Iron oxide is known to have a decomposition temperature (1808 K) significantly higher than that of CuO (933 K for the bare oxidizer, 1050 K for Al:CuO thermite)[161], with a similar difference established for the oxygen diffusivity (see Figure 4.10), which likely causes this delay in initiation. In summary, the ability of iron oxide to release oxygen species and the facility of oxygen diffusion through the reduced intermediary oxide dominate the initiation performance, which is radically different from the Al:CuO reaction that is driven by oxygen transport through the aluminum oxide barrier layer.

In regards to the propagation behavior, the Al: Fe_2O_3 system has a burn rate calculated to be 38 cm/s, in the same general range as Al:CuO, with a well-established steady state regime. Considering the lower enthalpy of reaction (281.7 kJ per mol of atomic oxygen) compared to that of Al:CuO (397.5 kJ per mol of atomic oxygen), some other effects are probably playing an active role in sustaining a relatively high flame velocity. For one, the Al:Fe_2O_3 combustion can endure a much higher flame temperature due to the high disruption temperature (Al vaporization), which *de facto* increases all mechanisms kinetics; this effect of the disruption temperature increase leading to a higher burn rate is well-documented in Refs. 40 and 49 for nanothermites in the form of nanolaminates. Additionally, the thermal conductivity is approximately three times that of Al:CuO, which causes preheating of the non-reacted thermite during the long period of initiation. This process is clearly visible in Figure 4.11b, as a spatial spreading of the flame front temperature is visible in comparison to that of Al:CuO. For Al:Fe_2O_3, the flame extends over ~800 µm while it is only 200 µm for Al:CuO (defined as the spatial extension between temperature at its maximum and its upfront thermalization, at a given time of the steady state propagation). To quantify the role of this later process, the conductivity of the iron oxide-based thermite was artificially reduced to the same value as that of Al:CuO. The calculated burn rate of this Al:Fe_2O_3 thermite with λ_{AlCuO} was 19.7 m/s, roughly one-third

of the Al:CuO thermite burn-rate, and with minimal change to the initiation delay. Importantly, this indicates that conductivity, rather than the flame temperature, allows a reasonably high burn rate in Al:Fe$_2$O$_3$. From Figure 4.12b, it was calculated that 19% of the Al was consumed during the reaction.

The third couple, Al:WO$_3$, presents another low gas-producing option with only 0.14 moles of gas produced per 100g of thermite mixture.[50] It is interesting to note that this is the only oxide currently simulated undergoing a single step reduction reaction. The initiation temperature is calculated at 718 K, the lowest value of all of the considered Al-based thermites, just below that of the Al:CuO couple. WO$_3$ exhibits a higher inner diffusion rate for oxygen atoms to diffuse towards aluminum and its oxide. As a consequence, this thermite falls within the same category as Al:CuO, *i.e.,* thermites in which initiation is governed by the mass transport across the aluminum oxide barrier layer. This allows an initiation delay as low as 63 ms, the lowest of all considered thermites. It is lower even than that of Al:CuO, which is likely due to the larger amount of elementary exothermic reactions in this delay, as more oxygen is provided by the oxidizer at equivalent temperature. In addition, the slightly lower conductivity (1.6 *vs* 2.9 for stoichiometric Al:CuO) is a means to locally concentrate the energy into hot points, leading to quick initiation, but low propagation. The burn rate shows a well-established steady state (see Figure 4.11c) at the value of 17 cm/s, lower than that of both Al:Fe$_2$O$_3$ and Al:CuO cases, principally because of this poor thermal conductivity. With the enthalpy of reaction being in the range of Al:Fe$_2$O$_3$ (277 kJ per oxygen atom), a higher burn rate is expected, but the significantly lower disruption temperature, 1973 K, 100 K lower than Cu$_2$O, is inhibiting. Similarly, this low disruption temperature also leads to the lowest amount of fuel consumption before loss of the nanostructure, with only 11% of the Al utilized (Fig. 4.12c).

While an uncommon oxide choice due to the dangerous consequences of human ingestion, lead continues to see use in nanothermites within the mining sector.[151,162,163] Thus, Al:Pb$_3$O$_4$ remains of interest within the thermite domain with a total gas production slightly less than Al:CuO at 0.4215 moles of gas produced per 100g of thermite mixture.[50] The enthalpy of reaction is remarkably high at 378.8 kJ per atom of oxygen. However, the vaporization temperature that limits the overall system temperature during combustion is the lowest of all considered aluminothermites, corresponding to the vaporization of PbO at 1808 K. Interestingly, this thermite offers a sort of compromise between the Al:Fe$_2$O$_3$ and Al:CuO cases. The enthalpy of reaction and conductivity are more in the range of Al:CuO, while the oxygen supply is limited by the oxidizer, as in Al:Fe$_2$O$_3$. The oxygen diffusivity in the reduced oxide, PbO, is much lower than that of Al$_2$O$_3$, in the range of 10^{-9} m^2.s^{-1} (versus 10^{-4} m^2.s^{-1} for alumina) even though it is thermally activated at lower temperature with an activation energy of 93.7 kJ.mol^{-1} (versus 140 kJ.mol^{-1} for alumina). The dual effect of low activation, but with a limited oxygen flux leads to an initiation time of 127 ms, higher than the Al:CuO thermite, but still much lower than that of Al:Fe$_2$O$_3$. The limited burn rate value, 2 cm/s, is associated with a poor thermal conductivity that does not allow for much preheating of the unreacted material before system disruption at the relatively low vaporization temperature. Note that in all Al-based thermites tested, the steady state is always achieved. In addition, they all reach their disruption temperature. As Al:Pb$_3$O$_4$ possesses the lowest disruption temperature, corresponding to the

vaporization of PbO (1808 K), the burning of the remaining thermite materials is operated in the gas phase, which is consistent with the high level of gas production reported for this thermite (0.84 g of gas per g of thermite), almost at the level of $Al:I_2O_5$, which is one of the best known thermites for gas generation.[50] The amount of Al consumed was most comparable to the Al:CuO system, with 23% used (Fig. 4.12d).

b. Boron-based Thermites

Generally, boron thermites have attracted less attention despite higher gravimetric as well as volumetric energy densities than other fuels like aluminum.[50,164] While the gas produced by the B:CuO couple (0.45 moles per 100g of thermite mixture) remains comparable with Al:CuO, the $B:Fe_2O_3$ thermite is actually found to produce a negligible amount of gas, making it a high contender for gasless thermite applications.[50] Isolated boron nanoparticles are known to be difficult to initiate for combustion, possibly due to its native oxide shell that exhibits low oxygen diffusivity compared to aluminum oxide despite its low melting temperature (700 K). The boron thermites also have the overall lowest heat of reactions of all the thermite reactions considered in this study (104 – 244 kJ/mol of atomic O depending on the couple), which, in combination with the slower oxygen diffusivity through boron oxide, leads to the expectation of low propagation speeds and high initiation delays. The high vaporization temperatures of boron and its oxide permits the assumption to a higher extent that combustion processes will occur in the condensed state compared to other fuels, making it a fitting selection for this model. Due to the difficulties in initiating usual boron-based thermites, the literature available for experimental comparison is rather sparse compared to aluminothermites. Most of the documentation is based on the addition of boron to other thermites as additives.[165] Overall, Table 4.5 shows that initiation times largely increase (~0.1 s) and flame front velocities decrease (~cm/s range) by roughly an order of magnitude compared to aluminothermites having the same metal oxidizer. The effective conductivities of the boron couples follow the same pattern and are quantitively comparable to those of the aluminothermites.

Surprisingly, the B:CuO couple offers one of the weakest performances of the boron-based thermites with the second longest initiation delay and the slowest propagation speed. For B:CuO, the simulation gives an initiation time of 192 ms, which is more than twice the initiation time of Al:CuO, with a consistently higher temperature (1285 K for B:CuO). This value corresponds to experimental values found by Huang *et al.*[164] with initiation delays of 125 ms for a stoichiometric mixture of particles of 500 nm and 50 nm in diameter for boron and CuO, respectively, as a compressed pellet in a constant-volume vessel. The burn rate is low at 4.3 cm/s. Both the high initiation time and low burn rate values are driven by the limited oxygen flux through the B_2O_3 oxide supplying the thermite exothermic reaction as the thermal conductivity value is not very different from that of Al:CuO. The low reaction enthalpy is also contributing to the weaker thermite performance.

With iron oxide, the initiation time for the boron-based thermite is multiplied by a factor of two compared to B:CuO, with an ensuing rise in the initiation temperature to 1577 K. The value of 360 ms, which qualitatively corresponds well with the similar increase seen

experimentally, makes it the slowest in reactivity of all tested thermite couples. This illustrates the experimental difficulty to initiate these types of thermites and, particularly, $B:Fe_2O_3$, because of both limitations in oxygen delivery by the iron oxide reservoir and the poor oxygen diffusion through the barrier layer. Once self-sustained reaction is reached, this couple has the highest flame velocity for this fuel at 17 cm/s, which corroborates the fact that thermal conductivity is a crucial factor in the burn rate property, allowing the preheating of the upfront reaction zone. In terms of the initiation time, the simulated performance for B:CuO and $B:Fe_2O_3$ correspond well with the trends seen in Ref. 164 with an improved initiation when CuO is used as the oxidant as compared to Fe_2O_3.
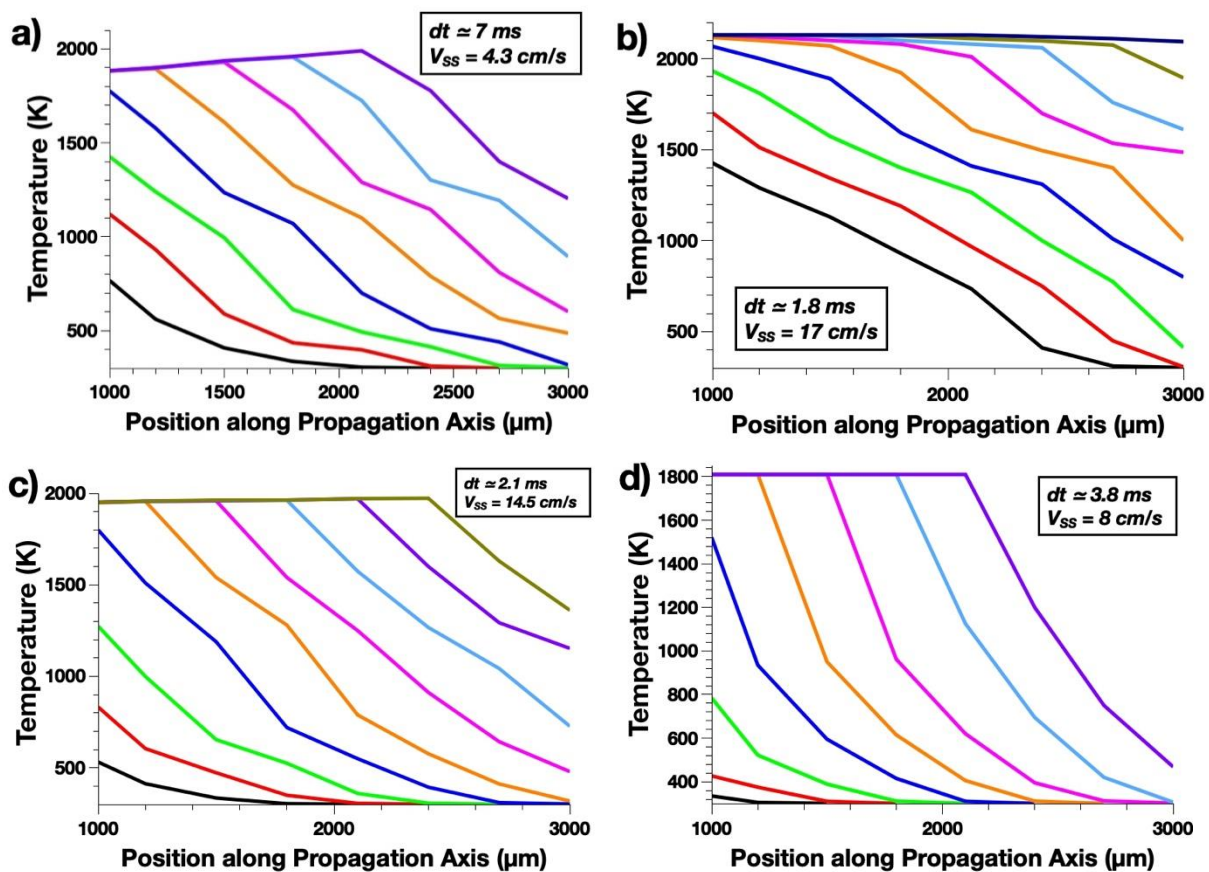
Figure 4.13 : Temperature profiles taken at intervals of *dt* for a) B:CuO, b) $B:Fe_2O_3$, c) $B:WO_3$, and d) $B:Pb_3O_4$ systems at ξ = 1.0 with 80 nm boron particles.

With nearly equivalent thermal conductivity, tungsten and lead oxides show similar initiation delays (186 and 165 ms, respectively), slightly lower than that of B:CuO (~192 ms), with comparable initiation temperatures (~1200 K). The burn rate of $B:WO_3$, 14.5 cm/s, is almost twice that of $B:Pb_3O_4$, 8 cm/s, despite $B:Pb_3O_4$ having the highest enthalpy of reaction of all tested cases with boron as a fuel. Thermites utilizing lead as the oxidant have the highest energy production per atom of freed oxygen for any of the considered chemical reactions in this study, so these couples would be expected to show high performance. However, as in the case of $Al:Pb_3O_4$, with the extremely low diffusivity of oxygen within the reduced PbO oxide (see Figure 4.10), it is likely that this becomes the limiting step of the reaction, particularly before the system disruption at the low temperature of 1808 K (PbO). Further experimental study will be required to process the validity of these results. Similar to aluminothermites, all

boron-based couples show a clear steady state propagation, reaching their disruption temperature (see Figure 4.13) once the steady state regime is established.

c.   Zirconium-based Thermites

In a similar capacity to boron metal, nanosized zirconium has been proposed as an additive to improve the properties of conventional Al micron-sized fuel, with these three-material composite thermites showing higher reactivity in terms of initiation time, increased energy delivery and longer duration of combustion.[60] Importantly, the poor oxygen diffusivity across ZrO_2, the lowest of all considered fuels (see Figure 4.10) is a strong limit to the reactivity of thermites using only Zr as the fuel, even more limiting than the case of boron, which also exhibits difficulties for initiation for the same reason. This leads to longer initiation times and temperatures despite similar thermal conductivities compared with aluminothermites. The initiation times exceed 200 ms for all systems. Note that $Zr:Pb_3O_4$ cannot be initiated under these conditions, requiring an initiation/propagation formulation that relies solely on gas phase mechanisms for systems brought to the disruption temperature. At this time, there are no studies explicitly studying the reaction characteristics of purely zirconium based systems, and so the results will be discussed in comparison with the other fuel propositions.

Immediately upon comparison of the temperature profiles for the $Zr:CuO$, $Zr:Fe_2O_3$, and $Zr:WO_3$ simulations (Figure 4.14) with the profiles from the preceding fuels (Al, Fig. 4.11; B, Fig. 4.13), the limiting effect of the low oxygen diffusivity in ZrO_2 is apparent. All of the profiles show a difficulty in initiation of the self-sustaining regime, also reflected in the long initiation times. Instead, the systems are steadily heated with good conductivity along the tube, leading to a pre-heating effect that can contribute to higher propagation speeds. It is interesting to note that the $Zr:CuO$ couple is again the slowest propagating reaction for this fuel at 6.7 cm/s. It is probable that the relatively low vaporization limit for this system at 2070 K (Cu_2O) is not sufficiently hot enough to allow enough freed oxygen to escape into the fuel particle until just before being cutoff due to system disintegration. CuO is generally a high gas-producing oxidizer, and, thus, this couple would likely see enhanced performance in experimental studies or in multiphasic simulations including gas phase reactions.

The $Zr:Fe_2O_3$ thermite couple shows comparable behavior to the other thermite couples utilizing this oxide. The reaction remains dominantly driven by the decomposition of Fe_2O_3 at the high temperature of 1957 K. This is similar to $Zr:CuO$, in that it does not allow the high influx of oxygen into the Zr fuel that is necessary for the runaway reaction to initiate until this high temperature. However, this system is limited by a much higher vaporization temperature at 3135 K for the final Fe product, which allows more time for the oxidation of the fuel, and more activation for diffusion, after this high decomposition point but before the disintegration of the system. This couple was found to have the highest propagation rate at 37 cm/s, likely owed to the preheating of the system due to the high conductivity and the high vaporization limit allowing the system to overcome the negative effects of low oxygen diffusivity in ZrO_2. It is interesting to note that this propagation velocity is nearly as performant as that of the

Al:Fe_2O_3 thermite, despite the large difference in oxygen diffusivity between Al_2O_3 and ZrO_2 and the very similar heats of reactions (275 kJ/mol of atomic oxygen and 281 kJ/mol of atomic oxygen for Zr:Fe_2O_3 and Al:Fe_2O_3, respectively).
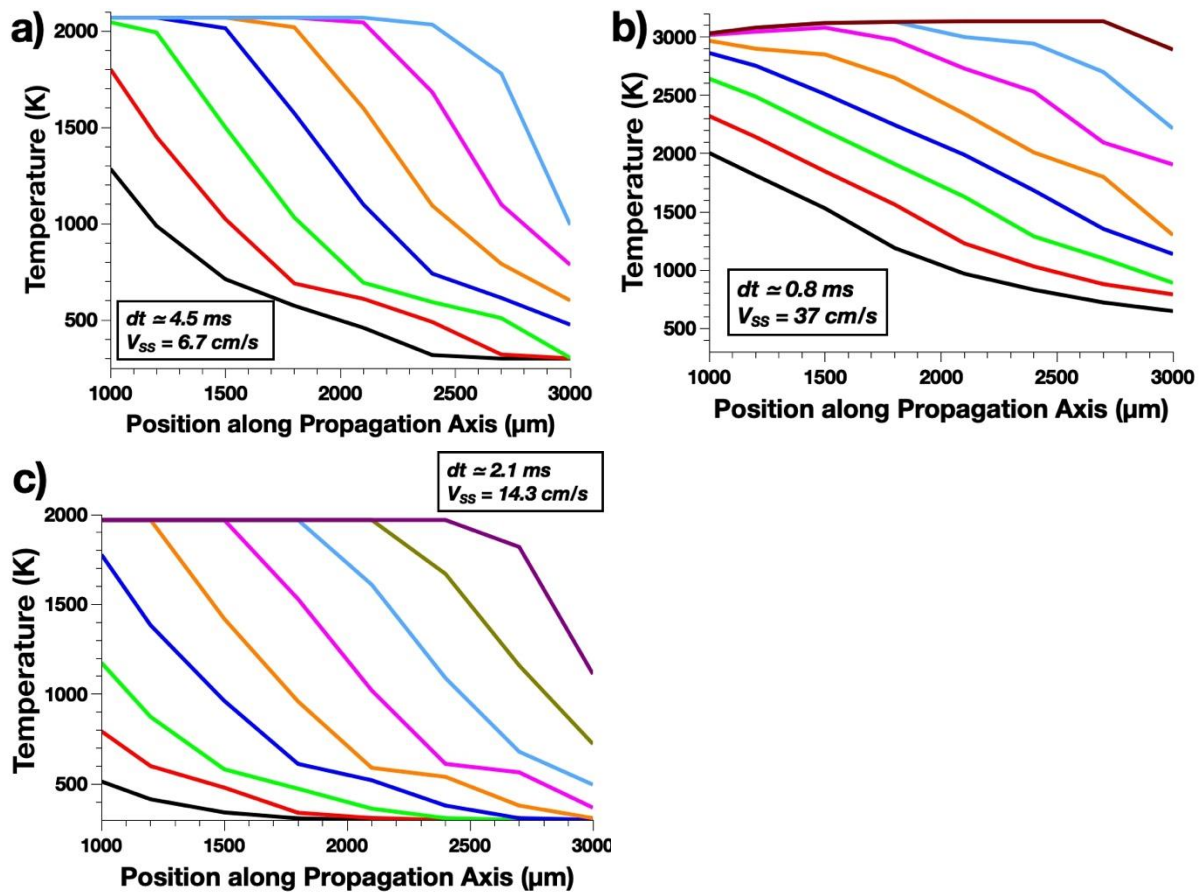
Figure 4.14 : Temperature profiles taken at intervals of *dt* for a) Zr:CuO, b) Zr:Fe_2O_3, and c) Zr:WO_3, systems at ξ = 1.0 with 80 nm zinc particles.

On the contrary to the limitation of the Zr:CuO system, the very high oxygen diffusivity in WO_3 at low temperature likely moderates the deficit caused by limited diffusion through the native oxide layer. The freed oxygen reservoir is available in this case to maximize the oxidation of the fuel from about 800 K. This is still significantly smaller than the comparative temperature gradients of this oxide coupled with the other fuels.

Finally, the Zr:Pb_3O_4 couple was the only thermite considered that does not manage to initiate under the simulated conditions. This is ultimately unsurprising given the extremely low oxygen diffusivity in both species acting as a complete bottleneck to the initiation of the self-sustaining reaction. Combined with the very low vaporization temperature of PbO (1808 K), the diffusivity of oxygen in ZrO_2 and Pb_3O_4 only reach a maximum of 1.7 x 10^{-13} and 9.88 x 10^{-12}, respectively, before the dissolution of the nanostructured system.

Overall, the results of this benchmark study highlight the role of oxygen mass transport and thermal conductivity on the initiation time and burn rate. It is observed that mass transport has a major impact on both properties, while conductivity more specifically affects the burn

rate. However, the simulated losses are largely underestimated compared with most experimental set ups. Additionally, the effects of the substrate or envelope, which are known to play an essential role, are not taken into account here.

4.5.3 Addition of an Envelope

A final test was completed to attempt to better simulate a realistic experimental setup with the inclusion of a conductive envelope, at low computational cost. In lieu of an explicit definition of two-dimensional conduction through the tube, as utilized in the radiation-conduction heat transfer formulation, the model was simplified to recalculate an effective conduction coefficient representative of the reactive material as well as the envelope. To accomplish this, a geometric parameter K is defined as

$$K = \left(\frac{r_{ext}}{r_{int}}\right)^2 - 1 \qquad (4.2)$$

where r_{int} is the internal radius containing the reactive material and r_{ext} is the external envelope radius. The newly adjusted conduction coefficient is the sum of the direct particle conduction coefficient and the geometric factor, K, multiplied by the bulk thermal conductivity of the material of the envelope.

$$\lambda' = \lambda + \lambda_{envelop} K \qquad (4.3)$$

It is also necessary to modify the volumetric heat capacity of the entire experimental setup by similarly multiplying the geometric factor by the volumetric heat capacity of the envelop material. This volumetric heat capacity is estimated at 2.5 J/cm^3, a typical average value for a metal.

$$C_v' = C_v + \left(\rho \times C_p\right)_{envelop} \times K \qquad (4.4)$$

With the consideration of an envelope material with an approximated conductivity of 100 W/mK, representative of a metal, the overall effective conduction coefficient is increased to 303 W/mK for an 80 nm Al (2 nm Al_2O_3 shell): 99 nm CuO couple at a stoichiometric ratio of 1.0 and 60 % TMD. This is about 100 times greater than the effective conductivity of the symmetrical system without an envelope. Simulated in a tube 3 mm long, with an inner diameter of 2 mm and an outer diameter of 4 mm, the steady-state propagation speed increases to 2.2 m/s. This is interesting as it moves the simulation into the regime of the higher experimental values seen on the order of meters per second. Unsurprisingly, the heavily augmented thermal conductivity also significantly increases the initiation delay to 732 ms.
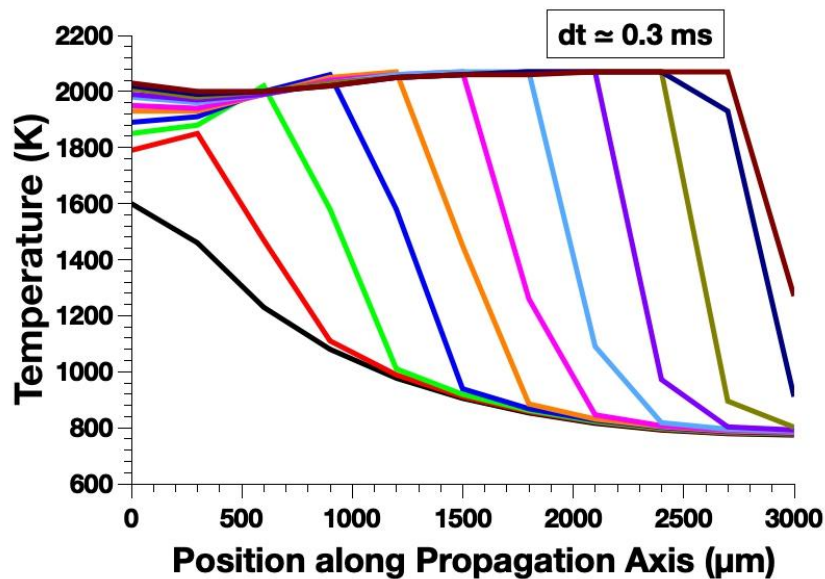
Figure 4.15 : Temperature profiles along the enveloped burn tube experiment over the span of the Al:CuO reaction at intervals of approximately 0.3 ms.

The addition of an envelope aids in propagation as the walls of the tube conduct the heat generated through the thermite redox reaction very quickly. The results attained are completely realistic in light of experimental values, however, in reality, a contained tube experiment would also be significantly affected by the production of gas and subsequent advection and convection. While a valid estimation of the thermite process, the addition of an envelope would not be applicable for thermite reactions that are possibly driven by a gas-dominated regime.

4.6 Conclusion

This chapter has presented the chronological development, validation, and exploitation of a full propagation model to simulate the macroscopic behavior of nanothermites driven by condensed phase mechanisms. The main goal was to create an analytical tool that can provide a qualitative evaluation of the thermite reaction, including initiation and propagation, to guide material design for new gasless applications quickly and at low cost. As such, both the validity of results as well as the computational cost on resources and calculation time were very important in the choice of the final formulation.

First, three different heat transfer methods were considered including a mixed radiation/conduction scheme, a macroscopic gas convection treatment, and direct conduction through particle contact. Both the radiative and convective methods found propagation speeds far below experimental values, and, in the case of the gas convection treatment, required extremely high computational cost and time. Thus, the direct particle conduction model was retained as the final formulation utilized to study the fundamental reaction parameters at play and the effects of key parameters and different thermite couples on the reaction behavior. Following this decision, another evaluative comparison was completed between four different formulations of an effective conduction coefficient to drive the conduction through particle

contact. The first two numerical constructions were directly pulled and adapted from a mixed experimental/theoretical study on $Si:Pb_3O_4$ nanothermites for mining applications. These provide a conduction coefficient that is representative of a composite bulk material, which does not take into account the geometrical factors of the particle contact. Thus, given the newly proven importance of reactive sintering and the goal of providing a model that considers the effect of this mechanism, a novel formulation was constructed as a chain of alternating fuel and oxide particles of a constant size. The final method improved the third formulation by allowing a distribution of particle sizes as seen in actual nanoparticle fabrication. The analysis showed that all of the effective conduction coefficients found propagation speeds on the order of magnitude of new experimental results, so it was decided to utilize the third formulation of a constant-sized alternating chain as an acceptable estimation of more diverse systems, while still being based on the pathway through the interfacial regions of contact between the particles. Once the final model formulation was decided, the model was available for validation by comparison with experimental results and further exploitation to fundamentally explore different parameters of the thermite propagation reaction.

The results of a generic stoichiometric Al:CuO mixture with a median compaction rate of 60 %TMD was studied in light of a recent fundamental study of the Al:CuO thermite with *in-operando* observation of the microscopic and macroscopic reaction. The simulation provided a propagation rate of approximately 61 cm/s, which found good correlation with the experimental flame front propagation at ~ 50 cm/s. However, the authors also found an overall macroscopic propagation velocity of 3 cm/s, confirming that for a powder arrayed on a glass slide, the flame front is discontinuous with clear heterogeneous pathways for heat transfer through the powder. When the estimated compaction rate and thermal conductivity of the system were integrated into a simulation, the consequent propagation rate was found to be approximately 8 cm/s. This again fell into good agreement with the macroscopic reaction regime elaborated in the experimental study.

Following the validation of a direct particle conduction propagation model, the effects of different system parameters such as the compaction rate, particle size, stoichiometry, and native oxide shell thickness were studied. Similar to the initiation base model, it is not possible within the current formulation to separate the effects of particle size and stoichiometry explicitly, as they are intimately linked in the definition of the base particle pairing at the heart of the system. Regardless, as a qualitative study, the patterns seen as a function of these parameters correspond to past experimental investigations into their importance. An increase in the compaction rate generally reduces the propagation speed and increases the initiation delay. The stoichiometric ratio is found to cause an increase in propagation speed in direct proportion, with a similar decrease in the initiation delay. However, it is also clear that the model probably overestimates the advantage of a fuel-rich mixture as the classic maximum peak around $\xi = 1.2 - 1.4$ was not found, instead showing improved behavior up to a stoichiometric ratio around 2.0 and only finding a slight decrease in the propagation speed for $\xi = 5.0$. In regards to the particle size, while not completely representative of an experimental setup, the model found an experimental increase in the flame front propagation speed as the

particle size decreases. An inversely symmetrical relation is found for the initiation delay, with an exponential reduction as the particle size increases. Finally, while lacking in experimental values for comparison, a logical pattern was found as a function of increasing native oxide shell thickness. As this is often the limiting step in the thermite reaction, a thicker oxide shell will further reduce the diffusion of freed oxygen arriving per time step to the fuel for oxidation, reducing the reaction's speed of propagation and increasing the time for initiation.

As with the base initiation model, a benchmark study of different materials of interest for new thermite applications with a focus on gasless thermite couples was completed. While remaining estimations, a qualitative comparison of the results of these simulations allowed an investigation of the importance of the diffusion rates of oxygen in different species versus the conductivity of the material. Aluminothermites remain highly performative in comparison with more diverse species, but as manufacturing and nanoparticle fabrication methods improve and evolve, some couples that produce negligent gas could become a better choice for certain applications.

Finally, a last adjustment was added to the model to consider a system enveloped by a conductive material. This better represents many nanothermite experimental setups like burn tubes that are commonly used. As to be expected, the inclusion of a conductive wall in the effective conduction coefficient significantly increases the conductivity and, thus, the speed of propagation of the reaction. It is important to note in this case, however, that any couple known to produce gas could very likely have the performance further improved in experiments due to the constriction of the gas with subsequent advection or convection contributing to the macroscopic heat transfer.

Together, the macroscopic direct conduction thermal treatment coupled to the diffusion/reaction scheme originally outlined by Deal and Grove form a complete condensed-phase initiation and propagation model for powder nanothermite systems. In particular, this is the first numerical model that explicitly takes into account the experimentally observed reactive sintering mechanism. The combination of both the base initiation model and the full propagation version provides an analytical tool for both fundamental research and industrial system design in the nanothermite domain. A Software Architecture Document outlining the computational organization of the program is available in Appendix A.

Conclusion & Future Perspectives

This doctoral work was completed as one axe of a larger project on energetic materials within the NEO team at LAAS-CNRS, which features research on the development, fabrication, integration, characterization, and modelling of different nanothermites and their applications. Innovative applications in new domains such as aerospatial engineering or MEMS devices call for tunable nanothermite performance with specific heat release, propagation speed, and gas generation to achieve the desired combustion for each domain. As manufacturing methods, integration and structuring techniques, and general nanotechnology continue to improve, the need for efficient numerical models that can aid in system design of these tunable materials grows as well. Additionally, mesoscopic simulations that focus on certain phenomenological mechanisms can be utilized to investigate the kinetics of nanothermite combustion and to help interpret experimental findings. Finally, validated models can provide quick, vital insight into the effects of key parameters such as the system compaction rate, particle sizes and materials, and the stoichiometric ratio of thermite mixtures. In light of this emergent need, and in complement of previous works on a gas-phase powder-based model and a condensed-phase nanolaminate model, this thesis details the development, mathematical formulation, and exploitation of a novel condensed-phase model for powder-based nanothermites that also accounts for the recently discovered reactive sintering mechanism. This numerical package has allowed both qualitative performance prediction as a function of the described key parameters as well as insight into the fundamental mechanisms at play in both the microscopic chemical combustion and the macroscopic propagation behavior.

The first chapter presents a general state of the art on the domain of nanothermites, beginning with an overview of the chemistry of the reaction, the available manufacturing and fabrication methods, and the principal parameters at play. In particular, some general patterns are established including:

- An optimal thermite performance for slightly fuel-rich mixtures with $\xi = 1.2 - 1.4$ on average.
- A reduction in the initiation delay and increase in the propagation speed as the particle size is reduced, up to a critical limit estimated to be ~$50 - 80$ nm.
- A linear increase in initiation delay as a function of increasing native oxide shell thickness on the fuel particle.
- An increase in propagation speed as the compaction rate is reduced, entering a regime where gas-phase mechanisms are favored.
- A possible larger influence of the oxide particle size on the overall nanothermite performance, as the relative amount of native oxide to fuel material grows as the particle size is reduced, diluting the beneficial effects of the size reduction.

Next, a presentation of the current state of understanding of nanoparticle-based thermite initiation is provided. In the last couple of decades, three major hypotheses have been proposed as the driving behavior during the early stages of combustion. The most general involves a

heterogeneous condensed and gas phase mechanism beginning with a diffusive regime until shell fracture of the fuel particle due to volumetric changes as the particle oxidizes and the core melts. Through the resultant fissures, the fuel material is also released to diffuse and interact in both phases with the oxidizer material or an oxidizing environment as the temperature increases due to the redox reaction. A second theory, called the Melt Dispersion Method, was suggested after post-mortem images of combustion products showed hollow, yet intact fuel particles. This led the team to propose that, at the nanoscale, the tensile stresses in the shell cause it to undergo dynamic spallation and disperse clusters of fuel material into the environment for reaction. The final hypothesis was proposed after development of *in-situ* imaging allowed direct observation of an agglomeration of the fuel and oxide particles. The authors proposed that as the material melts, a reactive interface is formed between the particles with diffusion occurring as capillary and surface tension forces deliver fuel material to the interface. This would imply that condensed-phase mechanisms play a dominant role in the initiation regime of nanothermite combustion. Additional studies on this mechanism also made clear the importance of the external heating method on the thermite performance. Finally, a further improvement on characterization technology that permits both spatial and temporal microscale resolution has shown the effect of reactive sintering on propagation behavior. The study finds microscale, discontinuous flame fronts where a fast propagation of reactive sintering occurs at ~50 cm/s, with a slower overall macroscopic propagation at ~3 cm/s.

This section is completed by a look at the current models available for nanothermites and, more generally, energetic materials. While macroscopic, thermodynamic simulations are well-suited to simulate more conventional energetic materials such as RDX, the assumption of a complete reaction and negligence of microscopic mechanisms limit their applicability to nanothermites. On the microscale, Molecular Dynamics and Density Functional Theory based simulations can illustrate complex microscopic phenomenon, but at extremely high computational cost. This cost limits these types of models to small systems at short timescales which do not allow easy simulation of the full nanothermite initiation and propagation. Models at this scale are more appropriate for explicit investigation of one or two mechanisms. Mesoscopic, phenomenological simulations fill this gap between the macro and microscale offers by using building blocks of specific, important microscopic mechanisms combined with a more generalized macroscopic treatment of the overall reaction. The NEO team has previously offered two such models. The first uses a gas-phase dominant formulation to simulate the gas and pressure generation of powder-based Al:CuO thermites. This model was ultimately limited to the pressure and temporal evolution of the system, without providing information about the propagation of the reaction. A second proposal utilized the Deal and Grove diffusion/reaction scheme to establish a condensed-phase simulation of the initiation, propagation, and aging of Al:CuO nanolaminates. This led to a desire to create a similar treatment for powder-based nanothermites, with a high customizability to allow simulations of new materials of interest, as well as a numerical analysis of the newly observed reactive sintering mechanism.

Thus, the second chapter features the development of such a model with a full initiation and propagation simulation package based on the Deal and Grove diffusion/reaction scheme.

After an overview of the original implementation of this scheme applied to the oxide layer growth of silicon oxidation, the formulation of the building block base model of one single fuel particle paired with one oxide particle is detailed. This basic model, suitable for initiation simulations only, involves a spherical implementation of the treatment of oxygen diffusion through the system as a flux due to the concentration gradient of oxygen at each interface. At initialization, the two particles are considered already sintered according to an input wetting contact angle and the interface between the oxide and reduced oxide is set at the contact interface. The interface between the fuel and initial native oxidized fuel is set at a distance equal to the oxide shell thickness into the oxide particle. As the simulation begins, the concentrations of oxygen at each interface, the resultant gradient, and resultant oxygen flux are calculated. Then, the interface positions are adjusted with the oxide/reduced oxide interface moving into the oxide particle, while the fuel/oxidized fuel interface progresses inversely into the fuel particle. Finally, this mass transfer schema is coupled to a simplified thermal equation that does not account for losses, where the oxygen flux is multiplied by the heat of reaction for the thermite couple per mole of atomic oxygen. An external power density is applied until the energy produced from the reduction-oxidation of the species overcomes that of the external energy source, defined as the point of initiation of the runaway exothermic nanothermite reaction. It is important to note that the major limitation of this system is a forced dependence between the particle sizes and the initiation due to the 1:1 pairing.

The second half of the chapter describes the extension of this base model to a full propagation model where a burn line-like cylindrical apparatus is discretized into cells with each being filled with an identical quantity of building block base pairs according to the compaction rate. The progression of the mass transfer and temperature evolution are considered constant within each cell. The system is initiated with an external power density applied exclusively at the leftmost cell. The principal difficulty in the development of this model was to determine an accurate method of macroscopic heat transfer between cells that corresponds to experimental results. Three possible pathways are presented in their chronological order of development beginning with a heterogeneous radiative-conduction formulation, a macroscopic gas convection treatment, and, finally, direct conduction. As the direct conduction method corresponded best with experimental results, four different equations to calculate an effective conduction coefficient between cells were described. As in the base model, the mass transfer module is coupled to a more complex thermal equation that takes into account all phase changes including melting and vaporization, as well as radiative, convective, and conductive losses into the environment. The combination of the initiation and propagation models provides the full nanothermite simulation package that offers both a fundamental study of the thermite reaction, as well as performance predictions at low computational cost.

In Chapter 3, the base model is exploited to simulate multiple experimental setups for validation and investigation into the driving mechanisms of initiation, the effects of key parameters, and a comparison of qualitative performances for different common thermite couples including Al, B, and Zr as fuels in combination with CuO, Fe_2O_3, WO_3, and Pb_3O_4 as oxides. Simulations of a classic 80 nm Al:99 nm CuO system at a stoichiometric ratio of $\xi = 1.0$, with a 2 nm native oxide shell were validated by comparison of simulated results with

medium (10^5 K/s) and high (10^{11} K/s) heating rate experiments from Ref. 85. Importantly, the degree of sintering was found to moderately to highly affect the initiation delay under a high heating rate, while having little effect on the delay at a medium heating rate. In the high heating rates experiments, the system is initiated by laser, with a novel characterization through *in-situ* TEM imaging. To simulate this, an initial temperature calculated as a function of the size and absorptivity of the nanoparticles is applied. Only the most pre-sintered pairs ($90° \leq \theta \leq 117°$) were determined to have initiation delays in the range of the experimentally observed morphological changes (~ hundreds of ns). This is likely due to the absorption characteristics of the material, as CuO absorbs nearly three times as much energy at 532 nm wavelength, making the temperature increase in the CuO nanoparticles dominant.

Conversely, the medium heating rate T-Jump experiments, recreated *in silico* through the application of a constant heating ramp, found initiation delays in accordance with experimental values (~1.5 ms) for all considered degrees of sintering with the initiation delay spanning 1.19 – 1.46 ms for contact angles from 171° - 90°. As there remains a strong discussion on whether gas or condensed phase mechanisms dominate the initiation regime, the same setup was simulated with a purely gas phase model for comparison. Despite the condensed phase mechanisms clearly leading to a more efficient initiation, the gas phase results were also found to agree pretty well with the experimental results at ~1.8 ms.

Once proven a valid model for both medium and high heating rates, the initiation simulation was further extrapolated to test the influence of variation in several key parameters of the system including particle size, into the microscale, the native oxide shell thickness, and the stoichiometric ratio. As previously stated, the formulation of a single particle pairing does limit the capacity for explicit quantitative comparison with experimental works, but the overall patterns established in Chapter 1 are also found in the simulations, with the exception of the stoichiometric ratio. This is the parameter the most affected by the single particle pairing and, thus, improved performance is calculated up to a larger fuel-rich stoichiometry ($\xi = $ ~3). Similarly, the simulation overestimates performance enhancements for extremely small particle sizes.

A final exploitation of the base model provided a benchmark study comparing sixteen nanothermite couples. Overall, aluminum-based thermites report the best performance with zirconium-based showing the weakest performance. Comparing the oxides, couples with Fe_2O_3 are found to lead to the longest initiation delays and highest initiation temperatures, while CuO couples show the fastest initiation. Temperature limits were imposed on these simulations to a vaporization temperature (lowest vaporization temperature of all species in the system) at which the system's nanostructure is disrupted and condensed phase mechanisms are no longer dominant. If a simulated couple does not appear to initiate below these temperatures, it is possible that gas-phase mechanisms are dominant in the initiation of that nanothermite.

The fourth and final chapter of this work details extensive exploitation of the full propagation model for a determination of the best macroscopic propagation formulation,

validation with recent experimental studies, and a look at the effects of the compaction rate, particle sizes, stoichiometric ratio, and material species on the propagation behavior of thermite combustion. In a first section, the direct conduction formulation is proven to simulate propagation behavior in the best accordance with experimental works, at the lowest computational cost of the three methods proposed. All four formulations of an effective conduction coefficient, representing a fully dense composite material, a highly compacted material with vacancies, a chain of constant-sized alternating fuel and oxide species, and a chain of variable-sized alternating particles, were found to produce propagation speeds comparable to recent experimental results. The third formulation, a chain of constant-sized alternating particles, is retained as the most efficient numerical construction that also takes into account the important geometric factor of the sintered interface. This interface between a highly conductive fuel particle and an oxide particle of low conductivity can significantly bottleneck the propagation of the flame front.

This development was followed by validation with a recent fundamental study with *in-operando* observation of the microscopic and macroscopic reaction of an Al:CuO thermite. For a simulated system at a median compaction rate (60 %TMD) where condensed phase mechanisms are dominant, a propagation rate was found to be ~60 cm/s, in good correlation with the experimentally observed flame front propagation at ~50 cm/s. As this study investigated a thermite powder arrayed on a TEM grid, the authors also found an overall macroscopic propagation velocity of 3 cm/s where the flame front is discontinuous with clear heterogeneous pathways for heat transfer through the powder. A simulation was completed integrating the estimated compaction rate and thermal conductivity of this macroscopic system with a resultant propagation rate of ~8 cm/s,

Next, a study of the effects of the key parameters of the reaction are found to display the same general patterns observed experimentally. The limitation of the single particle pairing again limits a strict quantitative comparison. For the compaction rate, the propagation speed decreases and the initiation delay increases as the system is more compacted. An increase in the stoichiometric ratio causes a directly proportional increase in the propagation speed, but, again, the limitation likely causes an overestimation of the performance for fuel-rich mixtures with $\xi > 2$. The flame front propagation speed is found to increase as the particle size decreases, while the initiation delay decreases exponentially. Furthermore, a logical pattern is found with an increase in initiation delay with a reduction of the propagation speed as the thickness of the native oxide shell is increased, limiting the diffusion of freed oxygen arriving to oxidize the fuel material.

Finally, the model was extended for a benchmark study of different materials of interest for new thermite applications with a focus on gasless thermite couples. Aluminothermites remained the most performative in comparison with the more diverse couples, but as manufacturing and nanoparticle fabrication methods improve and evolve, some couples that produce negligent gas could become a better choice for certain applications. This study also, despite remaining a qualitative comparison, allowed an investigation of the importance of the diffusion rates of oxygen in different species versus the conductivity of the material. The very

low diffusivity of oxygen through the ZrO_2 shell causes the Zr-based thermites to be the least performant, with the combination with Pb_3O_4 unable to initiate a self-sustaining reaction. The accuracy of the prediction of propagation performance for innovative nanothermite couples can continue to be improved as new studies provide further observation of the reaction and new characterization can lead to values for specific reaction parameters like diffusion coefficients with higher corroboration.

The continued research and integration of these types of parameters or new mechanisms into the model remains the primary perspective for the future of this work. In particular, more sources of study on the diffusion pre-factor and activation energy for oxygen diffusion in new species of interest is vital. Similarly, there are very few values of confidence reported for the thermal conductivity of nanoparticles of different species, and, thus, the current version of the simulation must estimate using bulk thermal conductivities. Eventually, an available library of common nanothermite materials is desired to allow a full software package for use in both academic and industrial system design.

Within the model construction itself, while already validated for a good qualitative assessment of performance, new geometric formulations of the mass transfer mechanisms could allow a low computational cost increase in system complexity for improved accuracy, particularly in conjunction with higher confidence parameter values. In particular, two to four oxide or fuel particles agglomerated around a single fuel or oxide particle, respectively, would allow a decoupling of the forced relation between the particles' sizes and the stoichiometric ratio. If each cell of the apparatus is filled with a random sampling of these various base geometries, it is also possible for a couple of fuel particles to utilize the freed oxygen reservoir from a single oxide particle, increasing the amount of fuel consumed before the system is disrupted, and consequently, the amount of heat produced.

The full macroscale propagation model can be similarly improved by a more explicit construction of an enveloped tube or the substrate of a burn line. Overall, the simulation package currently underestimates the losses into the environment which leads to an overestimation of the thermite performance. Another axe of interest is to integrate this model as the chemical and thermodynamic building block of reaction into a Finite Element Analysis software such as ANSYS or COMSOL. In this case, the analysis of the thermal conduction through an envelope or substrate, as well as thermal losses into the environment, is determined by FEA, with the interior temperature along the tube provided from the customized nanothermite combustion simulation. In such an approach, 3D complex environments, beyond simple cylindrical envelops, could be envisaged, which should find interest in the perspective of PYROMEMs design.

More fundamentally, one step ahead for modelling nanothermites in the form of mixed powder is to couple the developed condensed phase formulation with gas phase processes, as proposed by Vincent Baijot and co-workers in Ref. 115. This integrated approach, in the frame of a computational fluid dynamic methodology would certainly represent the most ambitious way to confront all elementary processes of the thermite combustion, within each other. In this

way, the correct balance between gas and condensed phase mechanisms could be operated to arrive at an unprecedented level of predictability in the combustion of thermite materials.

Concurrently with these improvements to the software package, the model can continue to be used as a validated numerical tool to both probe fundamental mechanisms at the heart of this complex reaction, as well as aid in system design for new gasless nanothermite applicates. An additional user interface would be the final complement to render the software package complete for easy use and adaptability for all users' projects.

APPENDIX A

Software Architecture Document

This program has been designed to simulate the initiation and propagation of the self-sustaining combustion of a nanoparticle powder-based thermite mixture including a metallic fuel and an oxide. The *in-silico* experiment is designed as a non-confined radial system, comparable to an open burn line experiment (with the option to consider an envelope), with a homogeneously distributed mixture with the following characteristics:

- The dimensions (length, inner diameter and outer diameter if contained within an envelope) of the experimental apparatus
- The degree of compaction of the mixture as a function of %TMD
- The fuel and oxidizer species, with certain pre-defined materials available
- Material geometry and properties (radii, native oxide thickness, stoichiometric ratio)

Additional parameters are pre-defined according to available literature, however many are not confidentally known, particularly at the nanoscale, and thus these can be adjusted as further studies become available. These parameters include:

- Diffusion coefficients for either the fuel or oxide species
  - o Pre-factor, D_0 in [m^2/s]
  - o Activation energy, E_a in [J/mol]
- Thermal conduction coefficient for either the fuel or oxide species i, λ_i in [W/m.K]
- Heat of reaction, $Q_{reaction}$ in [J/mol of atomic Oxygen]
- Thermal conductivity of the substrate, $\lambda_{substrate}$ in [W/m.K]
- External power density applied for initiation in [W/m^3]

The pre-defined materials include aluminum, boron, magnesium, and zinc as fuel options and cupric oxide (CuO), ferric oxide (Fe$_2$O$_3$), tungsten trioxide (WO$_3$), and lead tetroxide (Pb$_3$O$_4$). This system is then initiated through application of the external power density until the reaction becomes self-sustaining (the exponential temperature increase from exothermic reaction renders the external power input as negligible.) The simulation continues until either all fuel or oxide material in the system has been utilized, a final time has been reached, or the temperature stabilizes or is lost for a certain amount of time (i.e thermite does not achieve initiation or does not complete propagation.)

The program then provides the following output results:

- The evolution of the temperature profile of the system

- Final summary of results including the initiation delay, the average initiation temperature, the steady-state propagation temperature, the total external energy required to initiate the system

1   Program Architecture

The software package, written in C, includes all files necessary for a full simulation of pre-defined materials.

Source Files
- main.c
  - Initiation(System *system)
  - MassTransfer(System *system)
  - HeatTransfer(System *system)
- IO.c
  - initResults(System *system)
  - writeResults(System *system)
  - writeProp(System *system, int i)
- Species.c

Header Files
- System.h
- IO.h

Export Files
- Input Parameters.txt
  - Summary of all initial parameters passed into the system from input.txt
- Final Results.txt
  - Summary at final time with most important result parameters recorded including initiation delay, initiation temperature, and propagation speed
- System View.txt
  - Temperature overview of system written at user-defined intervals for certain cells at a different user-defined intervals (pre-defined as N_element/10)
- Flux at Initiation.txt
  - The flux in each cell as it initiaties
- Propagation.txt
  - The time speed of propagation for each cell's initiation
- Cell0.txt
  - Comprehensive overview of thermal heat quantites (qCond, qReact, qLoss) at intervalled time steps in first cell

Structures

System :

Species parameters

Species fuel, oxidFuel, oxide, reducOxide
oxSpecies finOxide
- Fuel, oxidized fuel, original oxide, intermediate reduced oxide, final reduced oxide
double M0, M1, M2, M3, rho0, rho1, rho2, rho3, Nmol0, Nmol1, Nmol2, Nmol3, Nmol4
- species 0: reduced oxide, species 1: oxide, species 2: fuel, species 3: oxidized fuel, species 4: final oxide
- Molecular weight, density, molar quantity, of each species, respectively
double Hf0, Hf1, Hf2, Hf3, Hfus0, Hfus1, Hfus2, Hfus3, Tfus0, Tfus1, Tfus2, Tfus3
- Molar enthalpy of fusion, total enthalpy of fusion for initial molar quantities, temperature of fusion

Geometric parameters

double Rfuel, Roxide, theta, dd, d1, d2, V1, V2, V3, V_thermite
- Radius of fuel particle, radius of oxide particle, contact angle, distance between sintered particle centers, distance from contact interface to oxide particle center, distant from contact interface to fuel particle center, volume of oxygen particle, volume of fuel particle, volume of native oxide shell, total volume of a sintered pair

Macroscopic system parameters

double chamberL, innerD, outerD, TMD, V_chamber, V_element, dx, N_element, N_pair
- Tube length, inner diameter, outer diameter, %TMD, total tube volume, volume of one elemental cell, length of elemental cell, number of elemental cells, number of particle pairs per elemental cell

Temporal parameters

double time, dTime, t_final, timeToWrite, lastWrite
- Time, time step, final time, time step for writing export files, last time of writing export files

Mass transfer parameters

double v, D01, D03, E1, E3
- Speed of oxidation reaction, diffusion coefficient prefactor of oxygen in intermediate/final oxide species, diffusion coefficient prefactor of oxygen in

oxidized fuel species, diffusion coefficient activation energy in intermediate/final oxide species, diffusion coefficient activation energy in oxidized fuel species

Thermal parameters

double T_amb, dTmin, dTmax, T_init
- Ambient temperature, minimum temperature change, maximum temperature change, minimum temperature for self-sustained reaction initiation

double C, q, P, qInput
- Effective volumetric heat capacity, heat of reaction per atom oxygen, input power density, input energy

double s1, s2, Cs1, Cs2
- Solubility (mol/mol), concentration at maximum solubility (mol/m^3)

double lambda, hConv
- Effective conduction coefficient, convection coefficient

Reaction parameters

double initDelay, flameSpeed
- Initiation delay, propagation speed

int flagNoOxide, flagNoRedOx, flagNoFuel, flagUpOp
- Flags for no more oxide, no more reduced oxide (for two-step reaction), no more fuel, for first cell that fulfills upper optimization criterion

int noMassIndex, vapIndex, lowOpIndex, upOpIndex, stepIndex
- Maximum cell with no more reactive material, maximum cell that has vaporized,

Element :

Species Parameters

double Nmol0, Nmol1, Nmol2, Nmol3, Nmol4
- Molar quantities of each species, respectively, in this cell

Mass Transfer Parameters

double a0, a1, b1, da1, db1
- Contact interface, fuel/oxidized fuel interface, oxide/reduced oxide interface, oxidized fuel growth, oxide/reduced oxide reduction

double dif1, dif2, flux1, flux2, brack
- Cell-specific diffusion coefficient for reduced oxide/final oxide, diffusion coefficient for oxidized fuel, flux in reduced oxide/final oxide, flux in oxidized fuel, logarithmic piece of the flux calculation

Thermal Parameters

double temp, dTemp, Tmax

- Current temperature, change in temperature, maximum temperature in this cell

double qCond, qCondTot, qReactTot, qLoss, qLossTot, qTot

- Heat due to conduction at this time step, total heat due to conduction, total heat due to exothermic reaction, heat due to convective and radiative losses at this time step, total heat due to convection and radiative losses, total heat at this time step

double Hfus0, Hfus1, Hfus2, Hfus3, Hfus4

- Total energy to melt each respective species given current molar quantities

int flagOxideMelt, flagRedOxMelt, flagFuelMelt, flagOxFuelMelt

- Flag for if the oxide, reduced oxide, fuel, oxidized fuel has already been completely melted

Reaction Parameters

int flagNoOxide, flagNoRedOx, flagNoFuel

- Flag when all oxide, reduced oxide, or fuel species, respectively, has been used in the reaction

double t_init, Tinit

- Time of cell initiation, temperature of cell initiation

Species:

   int steps

- 0 : for one-step reaction, 1: for two-step reaction

   double M, rho, Tfus, Hfus, massCoeff, massCoeff2

- Molecular weight, density, temperature of fusion, enthalpy of fusion, mass coefficient for first reaction step, mass coefficient for second reaction step

   double D0, Ea, lambda, numAtoms

- Prefactor for diffusion coefficient, activation energy for diffusion coefficient, bulk conduction coefficient, number of atoms in one molecule
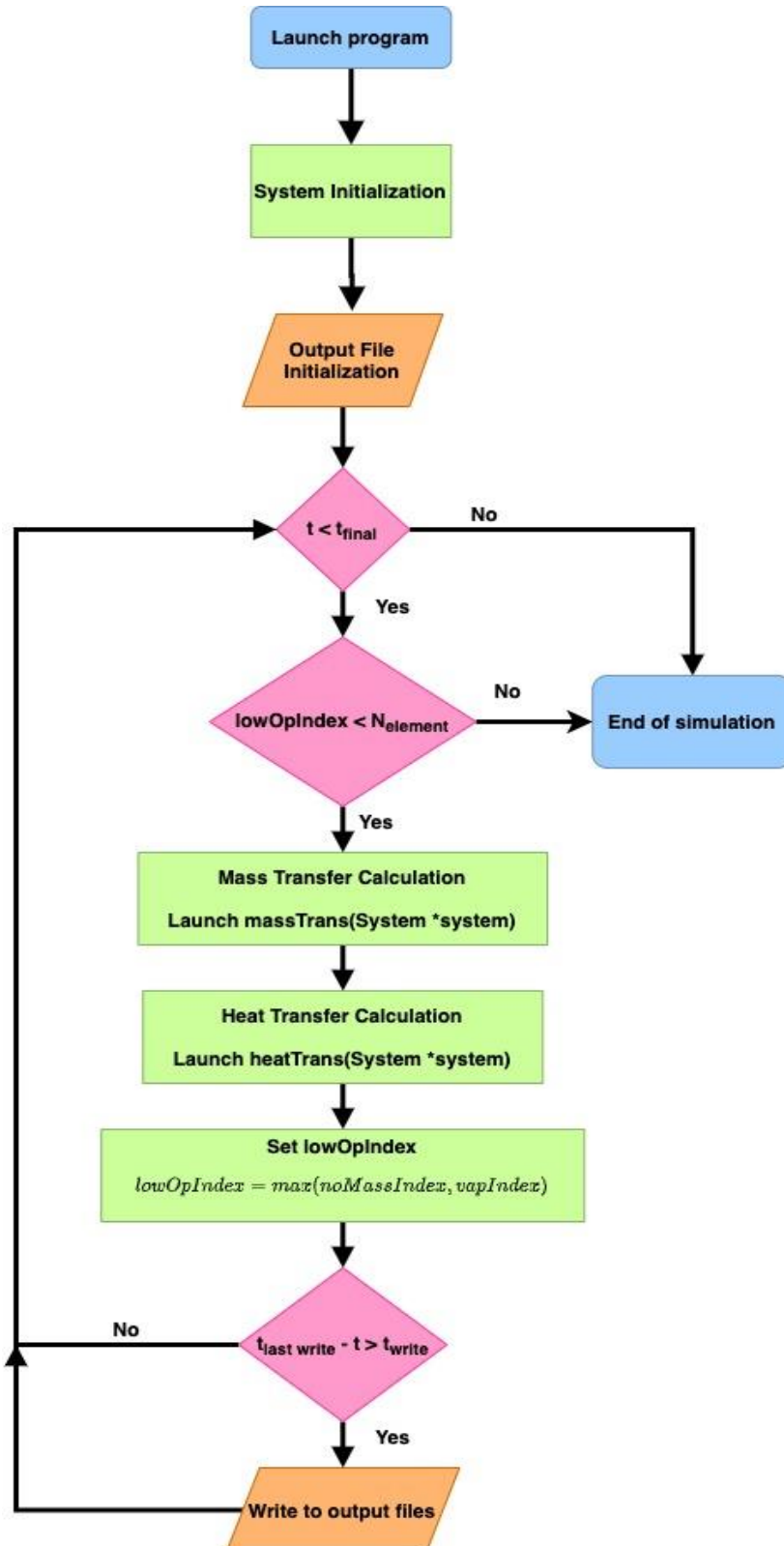
oxSpecies

   double massCoeff

- Mass coefficient for final reduction step of reaction

Program Breakdown

The program is divided into modules for the initiation, mass transfer, and heat transfer to allow easy adaptability to customize the nature of the heat transfer mechanisms. The following section will elaborate the layout of the program.

Within the initialization module, all geometric parameters are defined according to the given material, particle and system parameters. The stoichiometric ratio or the effective particle diameters are calculated and set according to the rules established in Chapter 2 (Equations 2.35 and 2.36). The effective conduction coefficient is calculated according to Equation 2.81.

Mass Transfer Module
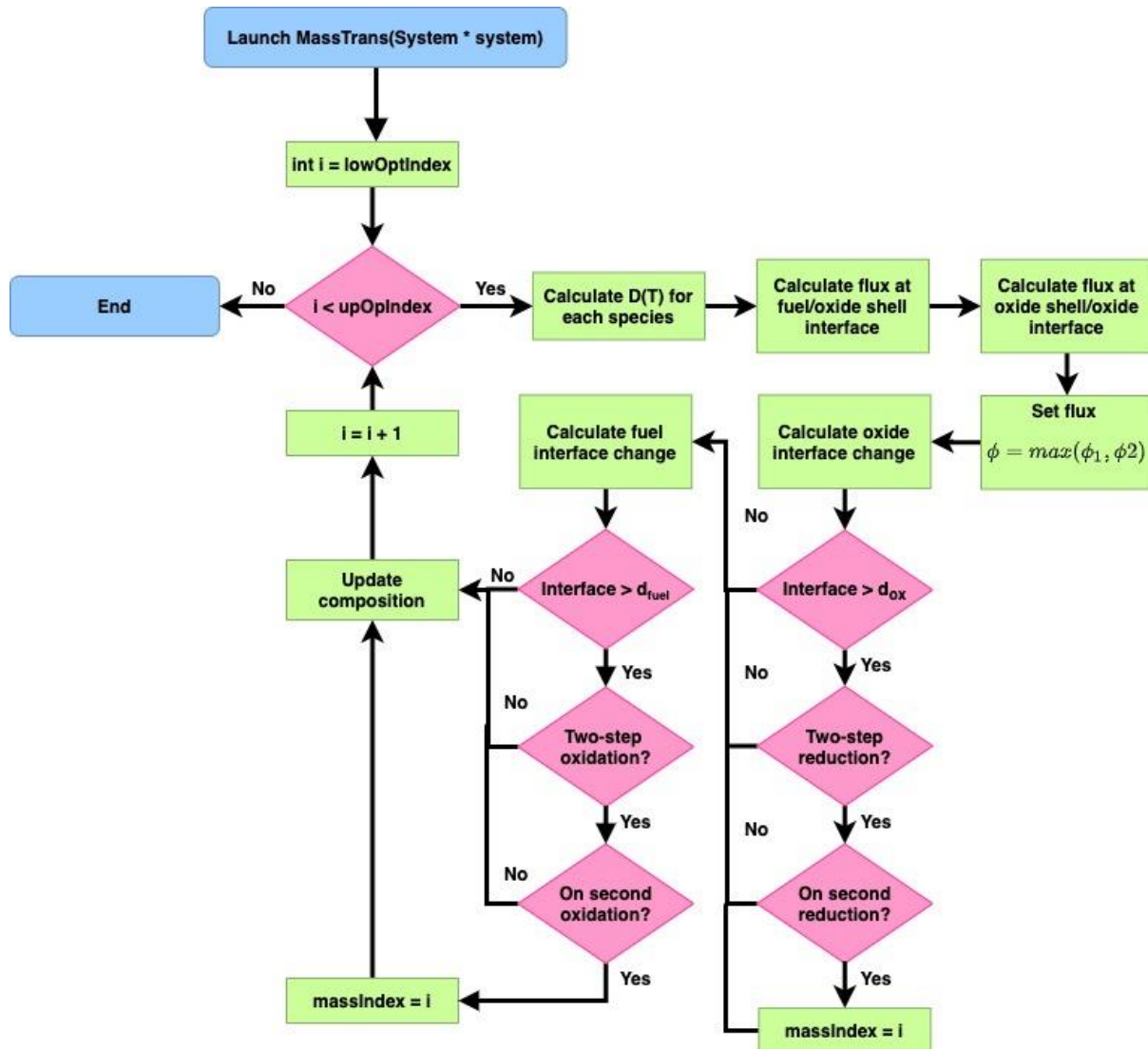
When the mass transfer function is launched, a loop begins at the low optimization index. Each cell in the loop then undergoes the described theoretical calculation of the changes in interface as the freed oxygen from the reduced oxide is transferred across the reduced oxide and oxidized fuel layers to oxidate the fuel material.

This begins by the calculation of the temperature-dependent diffusion coefficient in the cell for the reduced oxide and the oxidized fuel species. Then, two fluxes are calculated: one at the reduced oxide/oxide shell interface and one at the oxide shell/oxide interface. These calculations are the implementation of the resolved equations of the flux approximation, as

described in the theoretical model description (see Section 2.3.1) The minimum of these two values is preserved as the limiting flux for this time step.

The resultant reduction of the oxide due to this flux is calculated and applied through the adjustment of the oxide/reduced oxide interface, b_1. If the new position of this interface extends further than the limit of the oxide particle, if the reduction is a one-step reaction, or the particle is on the second stage of the reduction reaction, then the oxide material has been consumed. The no mass index is then set to this cell index. If this is only the first stage of a two-step reduction, then the interface is reset to the particle contact interface for the reaction to continue. Next, a similar calculation is completed for the oxidized fuel/fuel interface, a_1, to account for the new growth of the oxidized fuel into the fuel particle. Likewise, if this interface position exceeds the limit of the fuel particle, for a one-step oxidation reaction or the final stage of a two-step reaction, the fuel material is completely exhausted. In this case, the no mass index is set to this cell index. If this is the initial stage of a two-step oxidation, then the a_1 interface is reinitialized to the contact interface.

Finally, the material compositions of the cell are updated, and the new positions of the interfaces are stored. This process is repeated for each cell in the system up to the upper optimization index. The individually calculated flux retained as a global variable in each Element structure will be utilized in the thermal equation.

Heat Transfer Module

Once the mass transfer has been calculated for all cells still containing reactive material, the simulation passes into the heat transfer module. The initialized index for this looped function is the vaporization index, as cells where the reactive material has been completely expended retain their nanostructure and can be considered to remain in the chain of conduction.

The first calculation takes the time-dependent flux and calculates the heat created by the exothermic reaction, according to the standard enthalpy of reaction.

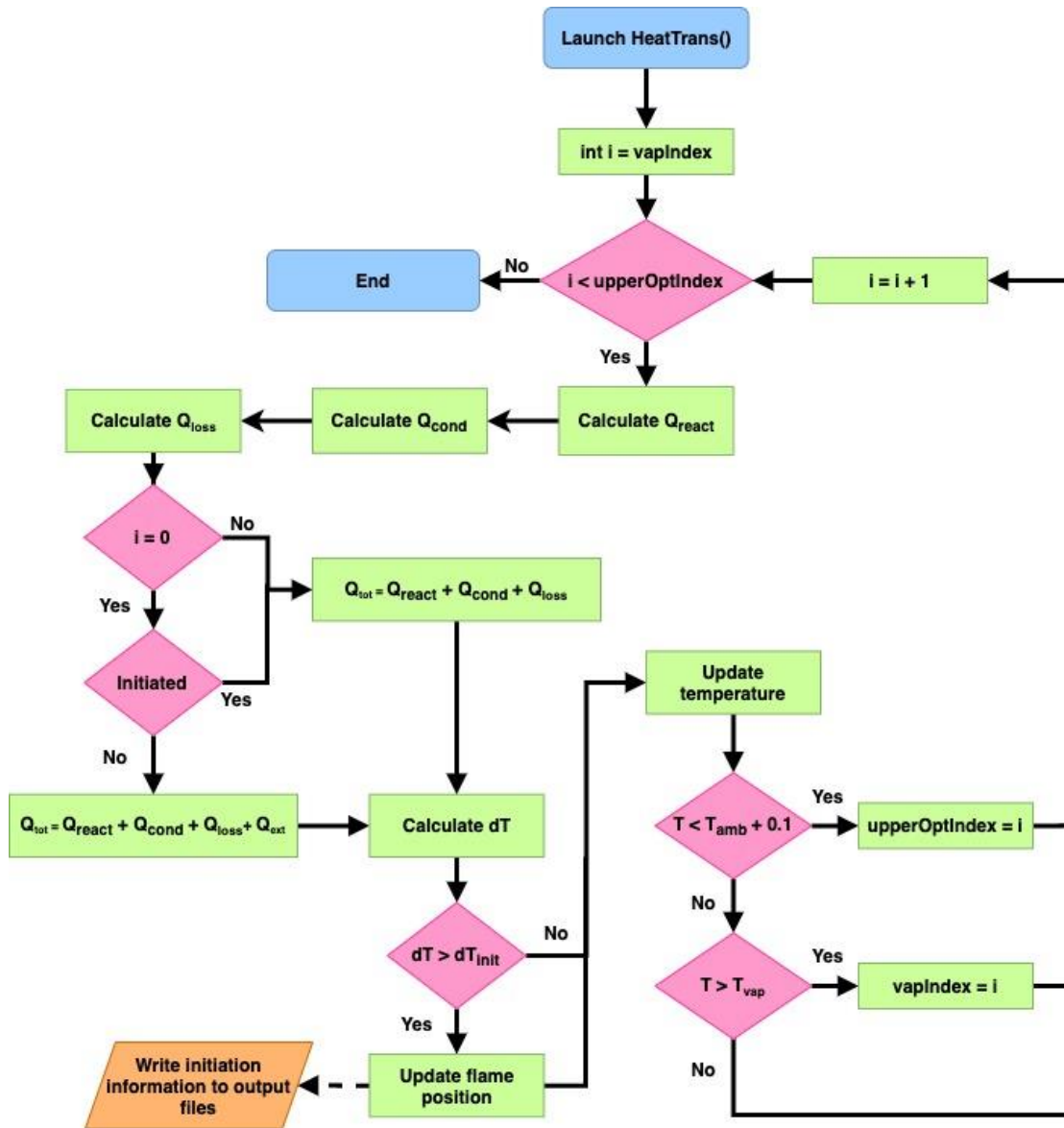$$dQ_{react} = q\Phi(t)dt$$

Next, a finite difference solution to the second-order derivative finds the change in heat due to conductivity.

$$dQ_{cond} = \lambda_{eff}\frac{T_{i+1} + T_{i-1} - 2T_i}{dx^2}dt$$

The heat losses into the environment by radiation and convection are then evaluated in this cell.

$$dQ_{loss} = \left(\frac{2}{r_{inner}}(T_i^4 - T_{amb}^4) + h_{conv}(T_i - T_{amb})\right)dt$$

These values are then combined into a total change in enthalpy. If the current cell under evaluation is the first cell on the left of the system ($i = 0$), and the cell has not yet initiated the self-sustaining reaction, the total dQ_{tot} is supplemented by the external heat input, here applied as a power density, P [W/m^3].

$$dQ_{tot} += Pdt$$

These time-dependent calculations are then added to the global variables of total heat generated or lost by each of these mechanisms during the simulation. The final change in temperature is calculated as the total enthalpy change divided by the volumetric heat capacity.

$$dT = \frac{dQ_{tot}}{C_V}$$

At this point, the cell is assessed for initiation according to the conditions defined during initiation. Generally, the self-sustaining reaction is considered achieved when the heat

generated by the exothermic redox reaction surpasses the input energy from the external initiation method. The default value is an increase in the change in temperature, *dT*, of at least one order of magnitude from the recorded value due to the applied power density. If this condition is met, and the cell index is greater than the current flame position, then the propagation speed is determined and recorded in the propagation export file (Propagation.txt.)

$$V_{flame} = \frac{dx}{t_{init}(i) - t_{init}(i-1)}$$

The steady-state flame temperature is assumed to be achieved by the center point of the system; this has been confirmed and, thus, the flame propagation speeds from $N_{element}/2$ until the end of the system are averaged to find the overall value, V_{ss} to account for minute differences due to the numerical method.

Lastly, the cell temperature is updated. For changes in temperature less than 0.1 K, the temperature change is considered negligible for optimization and the first cell to exhibit this change is set as the upper optimization index. The heat transfer calculation of the rest of the system is ignored for this time step. On the contrary, if the updated temperature exceeds the vaporization limit (the minimum vaporization temperature of all materials in this system,) then it is assumed that the vaporization of this species causes an explosive loss of the nanostructure. This would cause gas-phase mechanisms, which are neglected in this model, to become the dominant pathway for both mass and heat transfer. The cell farthest along the propagation to surpass this temperature of system disruption is set as the vapIndex.

Optimization

As previously stated, the program is optimized to speed-up calculations within certain boundaries. The system contains multiple indices for optimization including noMassIndex, vapIndex, lowOpIndex, and upOpIndex. The mass transfer module evaluates the system from the lowOpIndex to the upOpIndex, while the heat transfer module only considers the system from the vapIndex to the upOpIndex.

The first, noMassIndex, is triggered for cells that have utilized all of either the oxide, intermediate oxide, or fuel material available for reaction. This is determined within the mass transport module. If only this index is activated, the cell can still be considered in heat transfer mechanisms, as the nanostructure necessary for heat conduction remains intact. The second index, vapIndex, is switched when the given cell has surpassed the minimum vaporization temperature of all materials considered in the simulation. After this point, the nanostructure of the material in this cell is considered lost due to the vaporization of this material. The temperature remains fixed at the vaporization limit, but all behavior within the vaporized section is assumed to be gas-dominant. As such, the last such cell, of *i = vapIndex*, is considered a hot point that will continue contributing to the overall conduction.

Both the loss of reactive material and the vaporization of a species and resultant loss of nanostructure render the cell outside of the scope of this model; thus, the combined lower optimization index, lowOpIndex, is defined as the maximum of the noMassIndex and vapIndex. The final index, the upper optimization index, is evaluated during the heat transfer module to limit unnecessary calculations at the beginning of the simulation when the heat in the system has been minimally dispersed. At this stage, cells further along the system will see minimal heating from conduction and, thus, minimal diffusion to encourage the initiation of the self-sustaining reaction.

Export Files and Termination Criterion

A time interval, timeToWrite, is defined to establish when to write to the export files providing results. If the time since the last write to memory is greater than this interval, then general results, such as the temperature view of the system, are recorded.

There are three possible scenarios for the termination of the simulation. If the design parameters are not sufficient to elicit the self-sustaining propagation reaction, a stagnation or loss in the temperature for a defined amount of time or a final time limit is reached and the program exits. Otherwise, the simulation concludes when the reaction has fully propagated throughout the entire system. This occurs once the lower optimization index reaches the end of the appartus, either indicating that all of the reactive material in the last cell is consumed or the cell's temperature has reached the vaporization limit.

Computational Considerations

The numerical scheme of the system is driven by a finite difference scheme applied to the second-order differential equations. The major assumptions include that all reactions within one cell are constant for each pairing, and, thus, that there is a uniform temperature across not only each particle pairing, but the entire cell. This is validated by the high value of heat diffusivity with respect to mass diffusivity, in addition to the small scale of the nanoparticles and the length of a cell. This was also corroborated by experimental works showing a flame front of ~30 μm when compared to the cell length (1 μm). Additionally, this assumption could cause higher margins of error in calculation for systems initiated with extremely high heating rates, as previously discussed in Section 3.2.

Certain computational limits must be taken into account to avoid divergence of the model. In particular, a stabilization criterion requires a certain proportion between the time step, Δt, and the cell length, Δx, given by

$$\Delta t \ll \frac{\Delta x^2}{D_{thermal}}$$

where $D_{thermal}$ is the thermal diffusivity. Generally, this requires a time step of 10^{-7} s or lower.

Bibliography

(1)   Rossi, C. Nanoenergetic Materials for MEMS: A Review. *Journal of Microelectromechanical Systems* **2007**, *16* (4), 919–931.

(2)   Howard, R. A. *Realities and Perceptions in the Evolution of Black Powder Making*; Routledge, 2016; pp 45–65.

(3)   McLachlan, S. *Medieval Handgonnes: The First Black Powder Infantry Weapons*; Bloomsbury Publishing, 2011.

(4)   Jorpes, J. E. Alfred Nobel. *Br Med J* **1959**, *1* (5113), 1–6.

(5)   Goldschmidt, H. Obtaining Chromium. US578868A, March 16, 1897. Washington, DC: U.S. Patent and Trademark Office.

(6)   Goldschmidt, H.; Brewitt, W. Process of Uniting Rails. US1246909A, November 20, 1917. Washington, DC: U.S. Patent and Trademark Office.

(7)   Saita, K.; Ueda, M.; Yamamoto, T.; Karimine, K.; Iwano, K.; Hiroguchi, K. Trends in Rail Welding Technologies and Our Future Approach. *NIPPON STEEL & SUMITOMO METAL TECHNICAL REPORT* **2013**, No. 105, 9.

(8)   Rossi, C.; Briand, D.; Dumonteuil, M.; Camps, T.; Pham, P. Q.; Rooij, N. F. de. Matrix of 10×10 Addressed Solid Propellant Microthrusters: Review of the Technologies. *Sensors and Actuators A: Physical* **2006**, *126* (1), 241–252.

(9)   Tanaka, S.; Hosokawa, R.; Tokudome, S.; Hori, K.; Saito, H.; Watanabe, M.; Esashi, M. MEMS-Based Solid Propellant Rocket Array Thruster. *Transactions of the Japan Society for Aeronautical and Space Sciences* **2003**, *46* (151), 47–51.

(10)   Teasdale, D.; Milanovic, V.; Chang, P.; Pister, K. S. J. Microrockets for Smart Dust. *Smart Mater. Struct.* **2001**, *10* (6), 1145–1155.

(11)   Lonsdale, C. P. Thermite Rail Welding: History, Process Developments, Current Practices and Outlook for the 21st Century. **2000**, 18.

(12)   Trache, D.; M. Klapötke, T.; Maiz, L.; Abd-Elghany, M.; T. DeLuca, L. Recent Advances in New Oxidizers for Solid Rocket Propulsion. *Green Chemistry* **2017**, *19* (20), 4711–4736.

(13)   Rossi, C. *Al-Based Energetic Nanomaterials: Design, Manufactoring, Properties, and Applications*; ISTE Ltd, John Wiley & Sons, Inc., 2015; Vol. 2.

(14)   Wang, H.; Julien, B.; Kline, D. J.; Alibay, Z.; Rehwoldt, M. C.; Rossi, C; Zachariah, M.R. *Probing the Reaction Zone of Nanolaminates at ~µs Time and ~µm Spatial Resolution*, J. Phys. Chem. C **2020**, 124 (25), 13679–13687.

(15)   Rossi, C.; Estève, A.; Vashishta, P. Nanoscale Energetic Materials. *Journal of Physics and Chemistry of Solids* **2010**, *71* (2), 57–58.

(16)   Rossi, C. Two Decades of Research on Nano-Energetic Materials. *Propellants, Explosives, Pyrotechnics 39* (3), 323–327.

(17)   Petrantoni, M.; Rossi, C.; Salvagnac, L.; Conédéra, V.; Estève, A.; Tenailleau, C.; Alphonse, P.; Chabal, Y. J. Multilayered Al/CuO Thermite Formation by Reactive Magnetron Sputtering: Nano versus Micro. *Journal of Applied Physics* **2010**, *108* (8), 084323.

(18)   Wu, T.; Sevely, F.; Julien, B.; Sodre, F.; Cure, J.; Tenailleau, C.; Esteve, A.; Rossi, C. New Coordination Complexes-Based Gas-Generating Energetic Composites. *Combustion and Flame* **2020**, *219*, 478–487.

(19)   Benhammada, A.; Trache, D. Thermal Decomposition of Energetic Materials Using TG-FTIR and TG-MS: A State-of-the-Art Review. *Applied Spectroscopy Reviews* **2020**, *55* (8), 724–777.

(20) Nicollet, A. De l'étude de l'initiation de nanolaminés réactifs Al/CuO par point chaud à l'intégration de pyroMEMS pour la sécurité. phdthesis, Université Paul Sabatier - Toulouse III, 2018.

(21) Elbasuney, S.; Yehia, M.; Ismael, S.; El-Shaer, Y.; Saleh, A. Catalyzed Nitrocellulose Nanocomposite: A Novel Energetic Composition with Superior Decomposition Kinetics for Advanced Microchips. 17.

(22) Sharma, P.; Kumar, V.; Singh, A. Pyro MEMS Design for Fuze. *International Journal of Electrical, Electronics and Data Communication* **2015**, Special Issue - I, 136-138.

(23) Rossi, C. Engineering of Al/CuO Reactive Multilayer Thin Films for Tunable Initiation and Actuation. *Propellants, Explosives, Pyrotechnics* **2019**, *44* (1), 94–108.

(24) Chaalane, A.; Chemam, R.; AZZOUZ, I.; Dkhissi, A.; Djillali, M.; Houabes, M.; Esteve, D. *Enhanced Chemical Micro-Thrusters for Maneuvering Nano-Satellites*; 2017.

(25) Rossi, C.; Larangot, B.; Pham, P.-Q.; Briand, D.; de Rooij, N. F.; Puig-Vidal, M.; Samitier, J. Solid Propellant Microthrusters on Silicon: Design, Modeling, Fabrication, and Testing. *Journal of Microelectromechanical Systems* **2006**, *15* (6), 1805–1815.

(26) Rodríguez, G. A. A.; Suhard, S.; Rossi, C.; Estève, D.; Fau, P.; Sabo-Etienne, S.; Mingotaud, A. F.; Mauzac, M.; Chaudret, B. A Microactuator Based on the Decomposition of an Energetic Material for Disposable Lab-on-Chip Applications: Fabrication and Test. *J. Micromech. Microeng.* **2008**, *19* (1), 015006.

(27) Pezous, H.; Rossi, C.; Sanchez, M.; Mathieu, F.; Dollat, X.; Charlot, S.; Conédéra, V. Fabrication, Assembly and Tests of a MEMS-Based Safe, Arm and Fire Device. *Journal of Physics and Chemistry of Solids* **2010**, *71* (2), 75–79.

(28) Nicollet, A.; Charlot, S.; Baijot, V.; Estève, A.; Rossi, C. Ultra-Rapid and Fully Integrated Active Pyrotechnic Safety Switches Integrating Nanothermites. In *2017 Materials Research Society Fall Meeting & Exhibit*; Boston, MA, United States, 2017.

(29) Marín, L.; Nanayakkara, C. E.; Veyan, J.-F.; Warot-Fonrose, B.; Joulie, S.; Estève, A.; Tenailleau, C.; Chabal, Y. J.; Rossi, C. Enhancing the Reactivity of Al/CuO Nanolaminates by Cu Incorporation at the Interfaces. *ACS Appl. Mater. Interfaces* **2015**, *7* (22), 11713–11718.

(30) Kwon, J.; Ducéré, J. M.; Alphonse, P.; Bahrami, M.; Petrantoni, M.; Veyan, J.-F.; Tenailleau, C.; Estève, A.; Rossi, C.; Chabal, Y. J. Interfacial Chemistry in Al/CuO Reactive Nanomaterial and Its Role in Exothermic Reaction. *ACS Appl. Mater. Interfaces* **2013**, *5* (3), 605–613.

(31) Mursalat, M.; Huang, C.; Julien, B.; Schoenitz, M.; Esteve, A.; Rossi, C.; Dreizin, E. L. Low-Temperature Exothermic Reactions in Al/CuO Nanothermites Producing Copper Nanodots and Accelerating Combustion. *ACS Appl. Nano Mater.* **2021**, *4* (4), 3811–3820.

(32) Abdallah, I.; Zapata, J.; Lahiner, G.; Warot-Fonrose, B.; Cure, J.; Chabal, Y.; Esteve, A.; Rossi, C. Structure and Chemical Characterization at the Atomic Level of Reactions in Al/CuO Multilayers. *ACS Appl. Energy Mater.* **2018**, *1* (4), 1762–1770.

(33) Marín, L.; Gao, Y.; Vallet, M.; Abdallah, I.; Warot-Fonrose, B.; Tenailleau, C.; Lucero, A. T.; Kim, J.; Esteve, A.; Chabal, Y. J.; Rossi, C. Performance Enhancement via Incorporation of ZnO Nanolayers in Energetic Al/CuO Multilayers. *Langmuir* **2017**, *33* (41), 11086–11093.

(34) Zapata, J.; Nicollet, A.; Julien, B.; Lahiner, G.; Esteve, A.; Rossi, C. Self-Propagating Combustion of Sputter-Deposited Al/CuO Nanolaminates. *Combustion and Flame* **2019**, *205*, 389–396.

(35) Marin, L.; Warot-Fonrose, B.; Esteve, A.; Chabal, Y. J.; Rodriguez, L. A.; Rossi, C. Self-Organized Al2Cu Nanocrystals at the Interface of Aluminum-Based Reactive

Nanolaminates to Lower Reaction Onset Temperature. *ACS Appl. Mater. Interfaces* **2016**, *8* (20), 13104–131113.

(36) Julien, B.; Cure, J.; Salvagnac, L.; Josse, C.; Esteve, A.; Rossi, C. Integration of Gold Nanoparticles to Modulate the Ignitability of Nanothermite Films. *ACS Appl. Nano Mater.* **2020**, *3* (3), 2562–2572.

(37) Julien, B.; Wang, H.; Tichtchenko, E.; Pelloquin, S.; Esteve, A.; Zachariah, M. R.; Rossi, C. Elucidating the Dominant Mechanisms in Burn Rate Increase of Thermite Nanolaminates Incorporating Nanoparticle Inclusions. *Nanotechnology* **2021**, *32* (21), 215401.

(38) Wang, H.; Kline, D.; Rehwoldt, M.; Wu, T.; Zhao, W.; Wang, X.; Zachariah, M. R. Architecture Can Significantly Alter the Energy Release Rate from Nanocomposite Energetics. *ACS Applied Polymer Materials* **2019**.

(39) DeLisio, J. B. Understanding the Relationships Between Architecture, Chemistry, and Energy Release of Energetic Nanocomposites. Phd. Thesis, University of Maryland, College Park, College Park, Maryland, 2017.

(40) Nicollet, A.; Lahiner, G.; Belisario, A.; Souleille, S.; Djafari-Rouhani, M.; Estève, A.; Rossi, C. Investigation of Al/CuO Multilayered Thermite Ignition. *Journal of Applied Physics* **2017**, *121* (3), 034503.

(41) Jacob, R. J.; Kline, D. J.; Zachariah, M. R. High Speed 2-Dimensional Temperature Measurements of Nanothermite Composites: Probing Thermal vs. Gas Generation Effects. *Journal of Applied Physics* **2018**, *123* (11), 115902.

(42) Egan, G. C.; Sullivan, K. T.; LaGrange, T.; Reed, B. W.; Zachariah, M. R. In Situ Imaging of Ultra-Fast Loss of Nanostructure in Nanoparticle Aggregates. *Journal of Applied Physics* **2014**, *115* (8), 084903.

(43) Jian, G.; Piekiel, N. W.; Zachariah, M. R. Time-Resolved Mass Spectrometry of Nano-Al and Nano-Al/CuO Thermite under Rapid Heating: A Mechanistic Study. *J. Phys. Chem. C* **2012**, *116* (51), 26881–26887.

(44) Wang, H.; Kline, D. J.; Zachariah, M. R. In-Operando High-Speed Microscopy and Thermometry of Reaction Propagation and Sintering in a Nanocomposite. *Nature Communications* **2019**, *10*, 3032.

(45) Sullivan, K. T.; Piekiel, N. W.; Wu, C.; Chowdhury, S.; Kelly, S. T.; Hufnagel, T. C.; Fezzaa, K.; Zachariah, M. R. Reactive Sintering: An Important Component in the Combustion of Nanocomposite Thermites. *Combustion and Flame* **2012**, *159* (1), 2–15.

(46) Gordon, S.; Mcbride, B. J. *Computer Program for Calculation of Complex Chemical Equilibrium Compositions and Applications. Part 1: Analysis*; NASA Technical Report; NASA, 1994.

(47) Fried, L. E. *CHEETAH: A Fast Thermochemical Code for Detonation*; UCRL-ID-115752; Lawrence Livermore National Lab., CA (United States), 1993.

(48) Lahiner, G.; Nicollet, A.; Zapata, J.; Marín, L.; Richard, N.; Rouhani, M. D.; Rossi, C.; Estève, A. A Diffusion–Reaction Scheme for Modeling Ignition and Self-Propagating Reactions in Al/CuO Multilayered Thin Films. *Journal of Applied Physics* **2017**, *122* (15), 155105.

(49) Baijot, V.; Djafari-Rouhani, M.; Rossi, C.; Estève, A. A Multi-Phase Micro-Kinetic Model for Simulating Aluminum Based Thermite Reactions. *Combustion and Flame* **2017**, *180*, 10–19.

(50) Fischer, S. H.; Grubelich, M. C. *Theoretical Energy Release of Thermites, Intermetallics, and Combustible Metals*; SAND-98-1176C; CONF-980728-; Sandia National Labs., Albuquerque, NM (US), 1998.

(51) Monk, I.; Schoenitz, M.; Dreizin, E. L. Combustion of a Rapidly Initiated Fully Dense Nanocomposite Al–CuO Thermite Powder. *Combustion Theory and Modelling* **2019**, *23* (4), 651–673.

(52) Orieux, S.; Rossi, C.; Estève, D. Compact Model Based on a Lumped Parameter Approach for the Prediction of Solid Propellant Micro-Rocket Performance. *Sensors and Actuators A: Physical* **2002**, *101* (3), 383–391.

(53) Larangot, B.; Rossi, C.; Camps, T.; Berthold, A.; Pham, P.; Briand, D.; Puig-Vidal, M.; Miribel, P.; Esteve, D.; Rooij, N. D.; Montanes, E.; Macias, G.; Samitier, J. Solid Propellant Micro Rockets - Towards a New Type of Power MEMS. In *NanoTech 2002 - "At the Edge of Revolution";* American Institute of Aeronautics and Astronautics: Avignon, France, 2002.

(54) Larangot, B.; Conédéra, V.; Dubreuil, P. Solid Propellant MicroThruster: An Alternative Propulsion Device for Nanosatellite. In *NanoTech 2002 - "At the Edge of Revolution";* 2002; p 5756.

(55) Trache, D.; DeLuca, L. T. Nanoenergetic Materials: Preparation, Properties, and Applications. *Nanomaterials* **2020**, *10* (12), 2347.

(56) Nicollet, A.; Salvagnac, L.; Baijot, V.; Estève, A.; Rossi, C. Fast Circuit Breaker Based on Integration of Al/CuO Nanothermites. *Sensors and Actuators A: Physical* **2018**, *273*, 249–255.

(57) Medina, F.; Preaud, L. Shaped Charge and Application for Separating Two Stages of an Aeronautical Craft or Neutralizing the Same. US10288391B2, May 14, 2019.

(58) Zhou, L.; Piekiel, N.; Chowdhury, S.; Zachariah, M. R. Time-Resolved Mass Spectrometry of the Exothermic Reaction between Nanoaluminum and Metal Oxides: The Role of Oxygen Release. *J. Phys. Chem. C* **2010**, *114* (33), 14269–14275.

(59) Jian, G.; Chowdhury, S.; Sullivan, K.; Zachariah, M. R. Nanothermite Reactions: Is Gas Phase Oxygen Generation from the Oxygen Carrier an Essential Prerequisite to Ignition? *Combustion and Flame* **2013**, *160* (2), 432–437.

(60) Wainwright, E. R.; Dean, S. W.; Vummidi Lakshman, S.; Weihs, T. P.; Gottfried, J. L. Evaluating Compositional Effects on the Laser-Induced Combustion and Shock Velocities of Al/Zr-Based Composite Fuels. *Combustion and Flame* **2020**, *213*, 357–368.

(61) Luo, G.; Wang, X.; Zachariah, M. R.; Mishra, R. Ignition Threshold of Perovskite-Based Oxides for Solid Fuel Oxidation from First-Principles Calculations. *J. Phys. Chem. C* **2019**, *123* (29), 17644–17649.

(62) Wang, X.; Wu, T.; Zachariah, M. R. Doped Perovskites To Evaluate the Relationship between Fuel–Oxidizer Thermite Ignition and Bond Energy, Electronegativity, and Oxygen Vacancy | The Journal of Physical Chemistry C. *Journal of Physical Chemistry C* **2017**, *121* (1), 147–152.

(63) Wang, H.; Jian, G.; Zhou, W.; DeLisio, J. B.; Lee, V. T.; Zachariah, M. R. Metal Iodate-Based Energetic Composites and Their Combustion and Biocidal Performance. *ACS Appl. Mater. Interfaces* **2015**, *7* (31), 17363–17370.

(64) Weihua Jiang; Yatsui, K. Pulsed Wire Discharge for Nanosize Powder Synthesis. *IEEE Transactions on Plasma Science* **1998**, *26* (5), 1498–1501.

(65) Sarathi, R.; Sindhu, T. K.; Chakravarthy, S. R. Generation of Nano Aluminium Powder through Wire Explosion Process and Its Characterization. *Materials Characterization* **2007**, *58* (2), 148–155.

(66) Sedoi, V. S.; Ivanov, Y. F. Particles and Crystallites under Electrical Explosion of Wires. *Nanotechnology* **2008**, *19* (4), 145710.

(67) Higa, K. T.; Johnson, C. E.; Hollins, R. A. Preparation of Fine Aluminum Powders by Solution Methods. US5885321A, March 23, 1999.

(68) André, B.; Coulet, M.-V.; Esposito, P.-H.; Rufino, B.; Denoyel, R. High-Energy Ball Milling to Enhance the Reactivity of Aluminum Nanopowders. *Materials Letters* **2013**, *110*, 108–110.

(69) Marioth, E.; Kroeber, H.; Loebbecke, S. Comparison of Nanoparticulate Thermite Mixtures Formed by Conventional and Supercritical Fluid Processes. In *Fraunhofer-Institut für Chemische Technologie*; Karlsruhe, 2006.

(70) Kim, S. H.; Zachariah, M. R. Enhancing the Rate of Energy Release from NanoEnergetic Materials by Electrostatically Enhanced Assembly. *Advanced Materials* **2004**, *16* (20), 1821–1825.

(71) Malchi, J. Y.; Foley, T. J.; Yetter, R. A. Electrostatically Self-Assembled Nanocomposite Reactive Microspheres. *ACS Appl. Mater. Interfaces* **2009**, *1* (11), 2420–2423.

(72) Séverac, F.; Alphonse, P.; Estève, A.; Bancaud, A.; Rossi, C. High-Energy Al/CuO Nanocomposites Obtained by DNA-Directed Assembly. *Advanced Functional Materials* **2012**, *22* (2), 323–329.

(73) Calais, T.; Baijot, V.; Djafari Rouhani, M.; Gauchard, D.; Chabal, Y. J.; Rossi, C.; Estève, A. General Strategy for the Design of DNA Coding Sequences Applied to Nanoparticle Assembly. *Langmuir* **2016**, *32* (37), 9676–9686.

(74) Calais, T.; Bancaud, A.; Estève, A.; Rossi, C. Correlation between DNA Self-Assembly Kinetics, Microstructure, and Thermal Properties of Tunable Highly Energetic Al–CuO Nanocomposites for Micropyrotechnic Applications. *ACS Appl. Nano Mater.* **2018**, *1* (9), 4716–4725.

(75) Calais, T.; Bourrier, D.; Bancaud, A.; Chabal, Y.; Estève, A.; Rossi, C. DNA Grafting and Arrangement on Oxide Surfaces for Self-Assembly of Al and CuO Nanoparticles. *Langmuir* **2017**, *33* (43), 12193–12203.

(76) Calais, T.; Playe, B.; Ducéré, J.-M.; Veyan, J.-F.; Rupich, S.; Hemeryck, A.; Djafari Rouhani, M.; Rossi, C.; Chabal, Y. J.; Estève, A. Role of Alumina Coatings for Selective and Controlled Bonding of DNA on Technologically Relevant Oxide Surfaces. *J. Phys. Chem. C* **2015**, *119* (41), 23527–23543.

(77) Granier, J.; Pantoya, M. Laser Ignition of Nanocomposite Thermites. *Combustion and Flame* **2004**, *138*, 373–383.

(78) Bockmon, B. S.; Pantoya, M. L.; Son, S. F.; Asay, B. W.; Mang, J. T. Combustion Velocities and Propagation Mechanisms of Metastable Interstitial Composites. *Journal of Applied Physics* **2005**, *98*, 064903-064903–064907.

(79) Son, S. F.; Asay, B. W.; Foley, T., J.; Yetter, R. A.; Wu, M. H.; Risha, G. A. Combustion of Nanoscale Al/MoO3 Thermite in Microchannels. *Journal of Propulsion and Power* **2007**, *23* (4).

(80) Sullivan, K. T.; Kuntz, J. D.; Gash, A. E. The Role of Fuel Particle Size on Flame Propagation Velocity in Thermites with a Nanoscale Oxidizer. *Propellants, Explosives, Pyrotechnics* **2014**, *39* (3), 407–415.

(81) Prentice, D.; Pantoya, M. L.; Gash, A. E. Combustion Wave Speeds of Sol-Gel-Synthesized Tungsten Trioxide and Nano-Aluminum: The Effect of Impurities on Flame Propagation. *Energy and Fuels* **2006**, *20* (6), 2370–2376.

(82) Dutro, G. M.; Yetter, R. A.; Risha, G. A.; Son, S. F. The Effect of Stoichiometry on the Combustion Behavior of a Nanoscale Al/M0O3 Thermite. In *Proceedings of the Combustion Institute*; Elsevier Limited, 2009; Vol. 32 II, pp 1921–1928.

(83) Huang, Y.; Risha, G. A.; Yang, V.; Yetter, R. A. Effect of Particle Size on Combustion of Aluminum Particle Dust in Air. *Combustion. & Flame* **2009**, *156* (1), 5–13.

(84) Pantoya, M. L.; Granier, J. J. Combustion Behavior of Highly Energetic Thermites: Nano versus Micron Composites. *Propellants, Explosives, Pyrotechnics* **2005**, *30* (1), 53–62.

(85) Egan, G. C.; LaGrange, T.; Zachariah, M. R. Time-Resolved Nanosecond Imaging of Nanoscale Condensed Phase Reaction. *The Journal of Physical Chemistry C* **2015**, *119*, 2792–2797.

(86) Weismiller, M. R.; Malchi, J. Y.; Lee, J. G.; Yetter, R. A.; Foley, T. J. Effects of Fuel and Oxidizer Particle Dimensions on the Propagation of Aluminum Containing Thermites. *Proceedings of the Combustion Institute* **2011**, *33* (2), 1989–1996.

(87) Chowdhury, S.; Sullivan, K. T.; Piekiel, N.; Zhou, L.; Zachariah, M. R. Diffusive vs Explosive Reaction at the Nanoscale. *Journal of Physical Chemistry C* **2010**, *114* (20), 9191–9195.

(88) Sullivan, K. T.; Chiou, W.-A.; Fiore, R.; Zachariah, M. R. In-Situ Microscopy of Rapidly Heated Nano-Al and Nano-Al/WO. *Applied Physics Letters* **2010**, *97* (13), 133104.

(89) Sanders, V. E.; Asay, B. W.; Foley, T. J.; Tappan, B. C.; Pacheco, A. N.; Son, S. F. Reaction Propagation of Four Nanoscale Energetic Composites (Al/MoO3, Al/WO3, Al/CuO, and B12O3). *Journal of Propulsion and Power* **2007**, *23* (4), 707–714.

(90) Ahmad, S. R.; Cartwright, M. *Laser Ignition of Energetic Materials*; John Wiley & Sons, 2014.

(91) Rozenband, V. I.; Vaganova, N. I. A Strength Model of Heterogeneous Ignition of Metal Particles. *Combustion and Flame* **1992**, *88* (1), 113–118.

(92) Rosenband, V. Thermo-Mechanical Aspects of the Heterogeneous Ignition of Metals. *Combustion and Flame* **2004**, *137* (3), 366-375.

(93) Trunov, M. A.; Schoenitz, M.; Dreizin, E. L. Effect of Polymorphic Phase Transformations in Alumina Layer on Ignition of Aluminium Particles. *Combustion Theory and Modelling:* **2007**, *10* (4).

(94) Rai, A.; Park, K.; Zhou, L.; Zachariah, M. R. Understanding the Mechanism of Aluminium Nanoparticle Oxidation. *Combustion Theory and Modelling* **2006**, *10* (5), 843–859.

(95) Zhang, S.; Dreizin, E. L. Reaction Interface for Heterogeneous Oxidation of Aluminum Powders. *J. Phys. Chem. C* **2013**, *117* (27), 14025–14031.

(96) Coulet, M.-V.; Rufino, B.; Esposito, P.-H.; Neisius, T.; Isnard, O.; Denoyel, R. Oxidation Mechanism of Aluminum Nanopowders. *J. Phys. Chem. C* **2015**, *119* (44), 25063–25070.

(97) Vorozhtsov, A. B.; Lerner, M.; Rodkevich, N.; Nie, H.; Abraham, A.; Schoenitz, M.; Dreizin, E. L. Oxidation of Nano-Sized Aluminum Powders. *Thermochimica Acta* **2016**, *636*, 48–56.

(98) Levitas, V. I.; Asay, B. W.; Son, S. F.; Pantoya, M. Mechanochemical Mechanism for Fast Reaction of Metastable Intermolecular Composites Based on Dispersion of Liquid Metal. *Journal of Applied Physics* **2007**, *101* (8), 083524.

(99) Levitas, V. I.; Pantoya, M. L.; Dikici, B. Melt Dispersion versus Diffusive Oxidation Mechanism for Aluminum Nanoparticles: Critical Experiments and Controlling Parameters. *Appl. Phys. Lett.* **2008**, *92* (1), 011921.

(100) Levitas, V. I.; Pantoya, M. L.; Dean, S. Melt Dispersion Mechanism for Fast Reaction of Aluminum Nano- and Micron-Scale Particles: Flame Propagation and SEM Studies. *Combustion and Flame* **2014**, *161* (6), 1668–1677.

(101) Zhou, L.; Piekiel, N.; Chowdhury, S.; Zachariah, M. R. T-Jump/Time-of-Flight Mass Spectrometry for Time-Resolved Analysis of Energetic Materials. *Rapid Communications in Mass Spectrometry* **2009**, *23* (1), 194–202.

(102) Harding, J. H. Mesoscopic Modelling. *Current Opinion in Solid State and Materials Science* **1997**, *2* (6), 728–732.

(103) Fried, L.; Souers, P. *CHEETAH: A next Generation Thermochemical Code*; UCRL-ID-117240; Lawrence Livermore National Lab., CA (United States), 1994.

(104) Gordon, S.; Mcbride, B. J. *Computer Program for Calculation of Complex Chemical Equilibrium Compositions, Rocket Performance, Incvident and Reflected Shocks, and Chapman-Jouguet Detonations. Interim Revision.*; NASA Technical Report 19780009781; NASA, 1976.

(105) Epps, J. Continuum Modelling of Al/CuO Nanothermite Pellet Combustion. Phd. Thesis, Univesity of Waterloo, Waterloo, Ontario, Canada, 2020.

(106) Baras, F.; Politano, O. Molecular Dynamics Simulations of Nanometric Metallic Multilayers: Reactivity of the Ni-Al System. *Physical Review B: Condensed Matter and Materials Physics* **2011**, *84*, 024113.

(107) Turlo, V.; Politano, O.; Baras, F. Modeling Self-Sustaining Waves of Exothermic Dissolution in Nanometric Ni-Al Multilayers. *Acta Materialia* **2016**, *120*, 189–204.

(108) Turlo, V.; Politano, O.; Baras, F. Alloying Propagation in Nanometric Ni/Al Multilayers: A Molecular Dynamics Study. *Journal of Applied Physics* **2017**, *121* (5), 055304.

(109) Senftle, T. P.; Hong, S.; Islam, M. M.; Kylasa, S. B.; Zheng, Y.; Shin, Y. K.; Junkermeier, C.; Engel-Herbert, R.; Janik, M. J.; Aktulga, H. M.; Verstraelen, T.; Grama, A.; van Duin, A. C. T. The ReaxFF Reactive Force-Field: Development, Applications and Future Directions. *npj Computational Materials* **2016**, *2* (1), 1–14.

(110) Jin-Ping Z.; Yang-Yang Z.; Hui L.; Jing-Xia G.; Xin-Lu C. Molecular dynamics investigation of thermite reaction behavior of nanostructured Al/SiO2 system. *wlxb* **2014**, *63* (8), 086401–086401.

(111) Zeng, H.-D.; Zhu, Z.-Y.; Zhang, J.-D.; Cheng, X.-L. Diffusion and Thermite Reaction Process of Film-Honeycomb Al/NiO Nanothermite: Molecular Dynamics Simulations Using ReaxFF Reactive Force Field. *Chinese Phys. B* **2017**, *26* (5), 056101.

(112) Shimojo, F.; Nakano, A.; Kalia, R. K.; Vashishta, P. Enhanced Reactivity of Nanoenergetic Materials: A First-Principles Molecular Dynamics Study Based on Divide-and-Conquer Density Functional Theory. *Appl. Phys. Lett.* **2009**, *95* (4), 043114.

(113) Xiong, G.; Yang, C.; Zhu, W. Interface Reaction Processes and Reactive Properties of Al/CuO Nanothermite: An Ab Initio Molecular Dynamics Simulation. *Applied Surface Science* **2018**, *459*, 835–844.

(114) Xiong, G.; Yang, C.; Feng, S.; Zhu, W. Ab Initio Molecular Dynamics Studies on the Transport Mechanisms of Oxygen Atoms in the Adiabatic Reaction of Al/CuO Nanothermite. *Chemical Physics Letters* **2020**, *745*, 137278.

(115) Baijot, V. Modélisation et simulation multi-niveaux de la combustion d'une thermite composée de nanoparticules Al/CuO : des phénomènes microscopiques à la simulation du système en combustion. Phd. Thesis, Université Paul Sabatier - Toulouse III, Toulouse, France, 2017.

(116) Baijot, V.; Glavier, L.; Ducéré, J.-M.; Djafari Rouhani, M.; Rossi, C.; Estève, A. Modeling the Pressure Generation in Aluminum-Based Thermites. *Propellants, Explosives, Pyrotechnics* **2015**, *40* (3), 402–412.

(117) Baijot, V.; Ducéré, J.-M.; Rouhani, M. D.; Rossi, C.; Estève, A. Effect of Temperature and O2 Pressure on the Gaseous Species Produced during Combustion of Aluminum. *Chemical Physics Letters* **2016**, *649*, 88–91.

(118) Lahiner, G. Etude Théorique Du Vieillissement des Nanolaminés Al/CuO. Phd. Thesis, Université Paul Sabatier - Toulouse III, Toulouse, France, 2021.

(119) Estève, A.; Lahiner, G.; Julien, B.; Vivies, S.; Richard, N.; Rossi, C. How Thermal Aging Affects Ignition and Combustion Properties of Reactive Al/CuO Nanolaminates: A Joint Theoretical/Experimental Study. *Nanomaterials* **2020**, *10* (10), 2087.

(120) Tichtchenko, E.; Estève, A.; Rossi, C. Modeling the Self-Propagation Reaction in Heterogeneous and Dense Media: Application to Al/CuO Thermite. *Combustion and Flame* **2021**, *228*, 173–183.

(121) Glavier, L.; Taton, G.; Ducéré, J.-M.; Baijot, V.; Pinon, S.; Calais, T.; Estève, A.; Djafari Rouhani, M.; Rossi, C. Nanoenergetics as Pressure Generator for Nontoxic Impact Primers: Comparison of Al/Bi2O3, Al/CuO, Al/MoO3 Nanothermites and Al/PTFE. *Combustion and Flame* **2015**, *162*.

(122) Alawieh, L.; Weihs, T. P.; Knio, O. M. A Generalized Reduced Model of Uniform and Self-Propagating Reactions in Reactive Nanolaminates. *Combustion and Flame* **2013**, *160* (9), 1857–1869.

(123) Taton, G.; Lagrange, D.; Conedera, V.; Renaud, L.; Rossi, C. Micro-Chip Initiator Realized by Integrating Al/CuO Multilayer Nanothermite on Polymeric Membrane. *J. Micromech. Microeng.* **2013**, *23* (10), 105009.

(124) Ahn, J. Y.; Kim, S. B.; Kim, J. H.; Jang, N. S.; Kim, D. H.; Lee, H. W.; Kim, J. M.; Kim, S. H. A Micro-Chip Initiator with Controlled Combustion Reactivity Realized by Integrating Al/CuO Nanothermite Composites on a Microhotplate Platform. *J. Micromech. Microeng.* **2015**, *26* (1), 015002.

(125) Zhu, P.; Shen, R.; Ye, Y.; Fu, S.; Li, D. Characterization of Al/CuO Nanoenergetic Multilayer Films Integrated with Semiconductor Bridge for Initiator Applications. *Journal of Applied Physics* **2013**, *113* (18), 184505.

(126) Zhou, X.; Shen, R.; Ye, Y.; Zhu, P.; Hu, Y.; Wu, L. Influence of Al/CuO Reactive Multilayer Films Additives on Exploding Foil Initiator. *Journal of Applied Physics* **2011**, *110* (9), 094505.

(127) Deal, B. E.; Grove, A. S. General Relationship for the Thermal Oxidation of Silicon. *Journal of Applied Physics* **1965**, *36* (12), 3770–3778.

(128) Narula, M. L.; Tare, V. B.; Worrell, W. L. Diffusivity and Solubility of Oxygen in Solid Copper Using Potentiostatic and Potentiometric Techniques. *MTB* **1983**, *14* (4), 673–677.

(129) Egan, G. C.; Mily, E. J.; Maria, J.-P.; Zachariah, M. R. Probing the Reaction Dynamics of Thermite Nanolaminates. *J. Phys. Chem. C* **2015**, *119* (35), 20401–20408.

(130) Brotman, S.; Rouhani, M. D.; Rossi, C.; Estève, A. A Condensed Phase Model of the Initial Al/CuO Reaction Stage to Interpret Experimental Findings. *Journal of Applied Physics* **2019**, *125* (3), 035102.

(131) Picard, Y. N.; McDonald, J. P.; Friedmann, T. A.; Yalisove, S. M.; Adams, D. P. Nanosecond Laser Induced Ignition Thresholds and Reaction Velocities of Energetic Bimetallic Nanolaminates. *Appl. Phys. Lett.* **2008**, *93* (10), 104104.

(132) Pike, J.; Chan, S.-W.; Zhang, F.; Wang, X.; Hanson, J. Formation of Stable Cu2O from Reduction of CuO Nanoparticles. *Applied Catalysis A: General* **2006**, *303* (2), 273–277.

(133) Voitovich, V. B.; Lavrenko, V. A.; Adejev, V. M.; Golovko, E. I. High-Temperature Oxidation of Tantalum of Different Purity. *Oxid Met* **1995**, *43* (5), 509–526.

(134) DeLisio, J. B.; Wang, X.; Wu, T.; Egan, G. C.; Jacob, R. J.; Zachariah, M. R. Investigating the Oxidation Mechanism of Tantalum Nanoparticles at High Heating Rates. *Journal of Applied Physics* **2017**, *122* (24), 245901.

(135) Burgess, Donald R. Jr. Aluminum Thermochemical Data in **NIST Chemistry WebBook, NIST Standard Reference Database Number 69**, Eds. P.J. Linstrom and W.G. Mallard, National Institute of Standards and Technology, Gaithersburg MD, 20899, https://doi.org/10.18434/T4D303, (retrieved May 30, 2021).

(136) Burgess, Donald R. Jr. Boron Thermochemical Data in **NIST Chemistry WebBook, NIST Standard Reference Database Number 69**, Eds. P.J. Linstrom and W.G. Mallard, National Institute of Standards and Technology, Gaithersburg MD, 20899, https://doi.org/10.18434/T4D303, (retrieved May 30, 2021).

(137) Tokuda, T.; Ito, T.; Yamaguchi, T. Seif Diffusion in a Glassformer Melt Oxygen Transport in Boron Trioxide. *Zeitschrift für Naturforschung A* **1971**, *26* (12), 2058–2060.

(138) Burgess, Donald R. Jr. Magnesium Thermochemical Data in **NIST Chemistry WebBook, NIST Standard Reference Database Number 69**, Eds. P.J. Linstrom and W.G. Mallard, National Institute of Standards and Technology, Gaithersburg MD, 20899, https://doi.org/10.18434/T4D303, (retrieved May 30, 2021).

(139) Reddy, K. P. R.; Cooper, A. R. Oxygen Diffusion in MgO and α-Fe2O3. *Journal of the American Ceramic Society* **1983**, *66* (9), 664–666.

(140) Burgess, Donald R. Jr. Zirconium Thermochemical Data in **NIST Chemistry WebBook, NIST Standard Reference Database Number 69**, Eds. P.J. Linstrom and W.G. Mallard, National Institute of Standards and Technology, Gaithersburg MD, 20899, https://doi.org/10.18434/T4D303, (retrieved May 30, 2021).

(141) Keneshea, F. J.; Douglass, D. L. The Diffusion of Oxygen in Zirconia as a Function of Oxygen Pressure. *Oxidation of Metals* **1971**, *3* (1), 1–14.

(142) Burgess, Donald R. Jr. Copper Oxide Thermochemical Data in **NIST Chemistry WebBook, NIST Standard Reference Database Number 69**, Eds. P.J. Linstrom and W.G. Mallard, National Institute of Standards and Technology, Gaithersburg MD, 20899, https://doi.org/10.18434/T4D303, (retrieved May 30, 2021).

(143) Burgess, Donald R. Jr. Iron Oxide Thermochemical Data in **NIST Chemistry WebBook, NIST Standard Reference Database Number 69**, Eds. P.J. Linstrom and W.G. Mallard, National Institute of Standards and Technology, Gaithersburg MD, 20899, https://doi.org/10.18434/T4D303, (retrieved May 30, 2021).

(144) Sikka, V. K.; Rosa, C. J. The Oxidation Kinetics of Tungsten and the Determination of Oxygen Diffusion Coefficient in Tungsten Trioxide. *Corrosion Science* **1980**, *20* (11), 1201–1219.

(145) National Center for Biotechnology Information. "PubChem Compound Summary for CID 16685188, Lead tetroxide" PubChem, https://pubchem.ncbi.nlm.nih.gov/compound/Lead-tetroxide. Accessed 6 July, 2021.

(146) Thompson, B. A.; Strong, R. L. Self-Diffusion of Oxygen in Lead Oxide1. *J. Phys. Chem.* **1963**, *67* (3), 594–597.

(147) Lanthony, C.; Ducéré, J.; Rouhani, M.; Hemeryck, A.; Estève, A.; Rossi, C. On the Early Stage of Aluminum Oxidation: An Extraction Mechanism via Oxygen Cooperation. *The Journal of chemical physics* **2012**, *137*, 094707.

(148) Lanthony, C.; Guiltat, M.; Ducéré, J. M.; Verdier, A.; Hémeryck, A.; Rouhani, M. D.; Rossi, C.; Esteve, A. Elementary Surface Chemistry during CuO/Al Nanolaminate-Thermite Synthesis: Copper and Oxygen Deposition on Aluminum (111) Surfaces. *ACS Appl. Mater. Interfaces* **2014**, *6* (17), 15086–15097.

(149) Lanthony, C.; Ducéré, J.-M.; Estève, A.; Rossi, C.; Djafari-Rouhani, M. Formation of Al/CuO Bilayer Films: Basic Mechanisms through Density Functional Theory Calculations. *Thin Solid Films* **2012**, *520* (14), 4768–4771.

(150) Kittel, C. *Introduction to Solid State Physics, 8th Edition*, 8th ed.; John Wiley & Sons, 2004.

(151) Montgomery, Y. C.; Focke, W. W.; Kelly, C. Measurement and Modelling of Pyrotechnic Time Delay Burning Rates: Method and Model Development. *Propellants, Explosives, Pyrotechnics* **2017**, *42* (10), 1161–1167.

(152) Mujumdar, A. S. *Handbook of Drying Materials*, 3rd ed.; Taylor & Francis Group, L.L.C, 2006.

(153) Mei, J.; Halldearn, R. D.; Xiao, P. Mechanisms of the Aluminium-Iron Oxide Thermite Reaction. *Scripta Materialia* **1999**, *41* (5), 541–548.

(154) Monazam, E. R.; Breault, R. W.; Siriwardane, R. Reduction of Hematite (Fe2O3) to Wüstite (FeO) by Carbon Monoxide (CO) for Chemical Looping Combustion. *Chemical Engineering Journal* **2014**, *242*, 204–210.

(155) Durães, L.; Costa, B. F. O.; Santos, R.; Correia, A.; Campos, J.; Portugal, A. Fe2O3/Aluminum Thermite Reaction Intermediate and Final Products Characterization. *Materials Science and Engineering: A* **2007**, *465* (1), 199–210.

(156) Stamatis, D.; Dreizin, E. L. Thermal Initiation of Consolidated Nanocomposite Thermites. *Combustion and Flame* **2011**, *158* (8), 1631–1637.

(157) Pantoya, M. L.; Levitas, V. I.; Granier, J. J.; Henderson, J. B. Effect of Bulk Density on Reaction Propagation in Nanothermites and Micron Thermites. *Journal of Propulsion and Power* **2009**, *25* (2), 465–470.

(158) Grapes, M. D.; Reeves, R. V.; Fezzaa, K.; Sun, T.; Densmore, J. M.; Sullivan, K. T. In Situ Observations of Reacting Al/Fe2O3 Thermite: Relating Dynamic Particle Size to Macroscopic Burn Time. *Combustion and Flame* **2019**, *201*, 252–263.

(159) Fan, R.-H.; Lü, H.-L.; Sun, K.-N.; Wang, W.-X.; Yi, X.-B. Kinetics of Thermite Reaction in Al-Fe2O3 System. *Thermochimica Acta* **2006**, *440* (2), 129–131.

(160) Shin, M.-S.; Kim, J.-K.; Kim, J.-W.; Moraes, C. A. M.; Kim, H.-S.; Koo, K.-K. Reaction Characteristics of Al/Fe2O3 Nanocomposites. *Journal of Industrial and Engineering Chemistry* **2012**, *18* (5), 1768–1773.

(161) Jian, G.; Chowdhury, S.; Sullivan, K.; Zachariah, M. R. Nanothermite Reactions: Is Gas Phase Oxygen Generation from the Oxygen Carrier an Essential Prerequisite to Ignition? *Combustion and Flame* **2013**, *160* (2), 432–437.

(162) Montgomery, Y. C.; Focke, W. W.; Kelly, C. Measurement and Modelling of Pyrotechnic Time Delay Burning Rates: Application and Prediction of a Fast Burning Delay Composition. *Propellants, Explosives, Pyrotechnics* **2017**, *42* (11), 1289–1295.

(163) Focke, W. W.; Tichapondwa, S. M.; Montgomery, Y. C.; Grobler, J. M.; Kalombo, M. L. Review of Gasless Pyrotechnic Time Delays. *Propellants, Explosives, Pyrotechnics* **2018**, *0* (0).

(164) Huang, S.; Deng, S.; Jiang, Y.; Zheng, X. Experimental Effective Metal Oxides to Enhance Boron Combustion. *Combustion and Flame* **2019**, *205*, 278–285.

(165) Sullivan, K.; Young, G.; Zachariah, M. R. Enhanced Reactivity of Nano-B/Al/CuO MIC's. *Combustion and Flame* **2009**, *156* (2), 302–309.

(166) Wu, T.; Lahiner, G.; Tenailleau, C.; Reig, B.; Hungría, T.; Estève, A.; Rossi, C. *Unexpected enhanced reactivity of aluminized nanothermites by accelerated aging.* Chemical Engineering Journal **2021,** 418, 129432.